Faculdade de Engenharia da Universidade do Porto

Aerodynamic Performance Optimization of Portuguese High-Speed Trains Using CFD

Gonçalo Semblano



Master's in Mechanical Engineering

Supervisor: Professor Delmar Jorge

Co-supervisor: Professor Abílio de Jesus

October 6, 2026

Aerodynamic Performance Optimization of Portuguese High-Speed Trains Using CFD

Gonçalo Semblano

Master's in Mechanical Engineering

October 6, 2026

Abstract

The constant development of high-speed railway has led to more attention shifting towards aerodynamic performance. It is a key factor influencing stability, energy efficiency and infrastructure loading. Aerodynamic phenomena including complex wakes, significant variations in aerodynamic forces and pressure distribution and critical values of drag and lift represent significant concerns for a project of this magnitude. Understanding said phenomena is essential for the design of modern trains and for ensuring compliance with current norms and legislations.

This dissertation presents a numerical research (using Computational Fluid Dynamics (CFD)) on key operating conditions, such as circulation under crosswinds and the passing of vehicles. The study was carried out within the scope of the *TrainSolutions Portugal* project, whose goal is to boost the Portuguese railroad. The numerical simulations were performed using ANSYS Fluent, employing different Reynolds-Averaged Navier–Stokes (RANS) turbulence models, to analyse its effect on the results; every computational investigation was carried out within the scope of the EN 14067 standard.

After a brief introduction to the project and a detailed literature review on the topic of this thesis, benchmark tests were conducted; the results obtained for the new train were compared to an InterCity Express (ICE) model. This made it possible to infer which of the CFD configurations tested was the most suited one, as well as allowing for future comparison of data. Various mesh refinements and RANS turbulence models ($k-\epsilon$ and SST $k-\omega$) were tested, with the latter demonstrating better reliability.

During an extensive crosswinds study, the aerodynamic coefficients were obtained for several points across a wide range of yaw angles. To complement this analysis, graphical results were examined to identify the aerodynamic phenomena present and determine critical areas of the train's geometry. In doing so, it was demonstrated that the vehicle met the design requirements; moreover, the formation of vortexes was noticed, which led to the identification of geometrical features whose modification could improve the design.

The passing manoeuvre generates a transient fluid flow whose unpredictability must be considered. Unsteady CFD simulations were performed, which enabled the visualization of the event (through animations recorded in ANSYS Fluent) and the analysis of the development of aerodynamic coefficients over time, to conclude that the train's behaviour is stable during this operation.

The outcomes of this dissertation show the capacity of modern CFD techniques in aerodynamics. In the end, the results provide a solid framework for the certification of the *TrainSolutions Portugal*'s model and leave room for further developments in the field.

Keywords: Aerodynamics, CFD, Crosswinds, EN 14067, High-Speed Trains, Transient Flow

Acknowledgments

First and foremost, I would like to thank the people, without whom this project would never have come to be.

I want to thank Professors Abílio de Jesus and Delmar Jorge for proposing this dissertation and for all the help provided during these months. I also appreciate Eduardo's help, as he was the one who followed my work closer every day. All three provided me with the assistance needed to succeed in finishing this thesis in terms of engineering expertise and project guidance.

Furthermore, I am grateful to FEUP for granting me the opportunity to take part in such an interesting project as *TrainSolutions Portugal*, while supporting me with the necessary means to conceive a robust thesis.

Finally, I am deeply thankful for all the support my family and friends offered me during this time. Completing this thesis and my master's degree was no easy task, but their help along the way made the challenge feel lighter. Knowing there was always someone to reach out to during the difficult times was essential.

Gonçalo Semblano

This work is a result of Agenda “PRODUCING RAILWAY ROLLING STOCK IN PORTUGAL”, nr. C645644454-00000065, investment project nr. 55, financed by the Recovery and Resilience Plan (PRR) and by European Union - NextGeneration EU.



Contents

1 Introduction **1**
- 1.1 The Portuguese Railroad System . . . 2
- 1.2 Framing of the Project . . . 5
- 1.3 Objective . . . 7
- 1.4 Structure of the Dissertation . . . 7

2 Literature Review **9**
- 2.1 Railway Aerodynamic Standards . . . 9
  - 2.1.1 Development of the EN 14067 Series . . . 11
  - 2.1.2 Overview of the EN 14067 - Parts 4 and 5 . . . 12
  - 2.1.3 Overview of the EN 14067 - Part 6 . . . 13
  - 2.1.4 Discussion and Relevance to the Present Work . . . 16
- 2.2 Computational Fluid Dynamics . . . 17
  - 2.2.1 Introduction to Computational Fluid Dynamics . . . 17
  - 2.2.2 Governing Equations of Fluid Flow . . . 18
  - 2.2.3 Turbulence Modelling . . . 20
  - 2.2.4 Numerical Methods and Mesh Generation . . . 21
  - 2.2.5 Advantages, Limitations and Relevance to Railway Aerodynamics . 23
- 2.3 Computational Fluid Dynamics on Railway Aerodynamics . . . 25
  - 2.3.1 Development of CFD in Railway Aerodynamics . . . 25
  - 2.3.2 Aerodynamic Flow Around Trains . . . 26
  - 2.3.3 Crosswind Aerodynamics . . . 27
  - 2.3.4 Train Passing Aerodynamics . . . 30
  - 2.3.5 Summary and Research Gap . . . 34

3 Headwinds and Model Testing **37**
- 3.1 Train Geometry . . . 37
- 3.2 Headwind Simulations . . . 39
  - 3.2.1 Mesh Generation . . . 41
  - 3.2.2 ANSYS Fluent Parameterization . . . 46
- 3.3 ICE - Benchmark Testing . . . 52
  - 3.3.1 Benchmark Results . . . 55

4 Crosswinds **57**
- 4.1 Geometry and Mesh . . . 58
- 4.2 ANSYS Fluent Parameterization . . . 61
- 4.3 Results . . . 62
  - 4.3.1 Transient Simulation . . . 67

5 Passing of Vehicles **69**
5.1 Preliminary Test Configurations 70
5.2 Final Transient Configuration 80
5.3 Advanced Configurations and Further Developments 85

6 Results and Analysis **87**
6.1 Headwinds Simulations 87
6.2 Crosswinds Simulations 91
6.2.1 Aerodynamic Coefficients 92
6.2.2 Pressure and Velocity Distributions 97
6.3 Train Passing Simulations 107
6.3.1 Aerodynamic Coefficients 107
6.3.2 Pressure and Velocity Distributions 114

7 Conclusions **123**
7.1 Summary of the Thesis 123
7.2 Conclusions 124
7.2.1 Importance of the Results 124
7.2.2 Challenges and Limitations 125
7.3 Future Works 126

References **129**

A User-Defined Function (UDF) for the Transient Simulations **135**
A.1 UDF File "prime" for the Movement of the Main Vehicle (Along the x-Direction) 135
A.2 UDF File "secondary" for the Movement of the Second Vehicle (Opposite to the x-Direction) 136

B Contours of Absolute Pressure Around the Train (Crosswinds Study) **137**

C Pathlines Around the Train (Crosswind Study) **143**

D Velocity Magnitude Contours Around the Train's Cross-Section (Crosswind Study) **149**

E Aerodynamic and Pressure Coefficients over Time during the Passing Manoeuvre **155**

F Graphical Results from the Passing Manoeuvre **163**
F.1 Velocity Magnitude Contour on the XZ Plane 163
F.2 Pathlines Around the Train 165
F.3 Contour of Absolute Pressure on the XY Plane 168
F.4 Contour of Absolute Pressure Around the Trains 172

List of Figures

1.1 Share of Total Final Consumption (TFC) by sector over the years [1]. . . . 2
1.3 Evolution of the highway system in Portugal in the last 5 decades [2]. . . . 3
1.4 Evolution of the railway system in Portugal in the last 5 decades [2]. 3
1.2 Portuguese railway system as of 2020 [3]. 4
1.5 High-speed projects in Portugal for the next years [4]. 5
1.6 First preview of the "portuguese train" [5]. 6

2.1 Visual representation of the apparent velocity [6]. 15

3.1 First preview of the "portuguese train" [5]. 38
3.2 Front view of the first carriage of *TrainSolutions*'s model. 38
3.3 Side view of the first carriage of *TrainSolutions*'s model. 39
3.4 Side view of the computational domain. 40
3.6 Axis system. 40
3.5 Front view of the computational domain. 41
3.7 Side view of the smaller volume of the domain. 42
3.8 Front view of the smaller volume of the domain. 42
3.9 View of the finest mesh from the symmetry plan. 44
3.10 Closer view of the finest mesh from the symmetry plan, focusing on the separation zone. 44
3.11 Closer view of the finest mesh from the symmetry plan, focusing on the train. 44
3.12 View of the mesh from a section plane. 45
3.13 Closer view of the mesh from a section plane. 45
3.14 Evolution of drag coefficient for the different meshes for the `S_1_0` configurations. 50
3.15 Evolution of drag coefficient for the different meshes for the `S_2_0` configurations. 50
3.16 Evolution of drag coefficient for the different meshes for the `S_1_E` configurations. 51
3.17 Evolution of drag coefficient for the different meshes for the `S_2_E` configurations. 51
3.18 Drag coefficients for different meshes and convective schemes. 52
3.19 Front view of the carriage of ICE's model. 53
3.20 Side view of the carriage of ICE's model. 53
3.21 Close view of the mesh of ICE's model from the symmetry plane. 54
3.22 Close view of the mesh of ICE's model from a section plane along the width of the train. 55

4.1 Front and side view of the geometry of the domain for the crosswinds study at 0°. 58
4.2 Isometric view of the domain at 0° and 90°. 59
4.3 Isometric view of the domain at 30° and 45°. 59
4.4 Close-up side view of the mesh for crosswinds with a 0° yaw angle. 60
4.5 Close-up front view of the mesh for crosswinds with a 0° yaw angle. 60
4.6 Graphic of C_x for corresponding yaw angle. 65
4.7 Graphic of C_y for corresponding yaw angle. 66
4.8 Graphic of C_z for corresponding yaw angle. 67

5.1 Front and isometric view of the geometry of the domain for the train passing study. 74
5.2 Front and isometric view of the geometry around the vehicles for the train passing study. 74
5.3 Side view of the train volume without the air pocket. 75
5.4 Perspective view of the 2 vehicles and their initial positions in the domain (only the floor is represented). 75
5.5 Close side view of the mesh of the domain, allowing to distinguish the different layers of element sizes. 76
5.6 Side view of the mesh of train volume. 76
5.7 Front and isometric view of the geometry of the domain for the final configuration of the train passing study. 81
5.8 Front and isometric view of the geometry around the vehicles for the final configuration of the train passing study. 81
5.9 Side view of the train volume without the air pocket. 81
5.10 Perspective view of the 2 vehicles and their initial positions in the domain. 82
5.11 Close side view of the mesh of the domain for the final configuration. 83
5.12 Side view of the mesh of train volume. 84

6.1 Values of C_x plotted with number of elements in each mesh. 89
6.2 Close side view of the meshes used for both models in this experiment, to verify the volume of the region near the train. 90
6.3 Graphic of C_x for both models for each yaw angle. 92
6.4 Graphic of C_y for both models for each yaw angle. 93
6.5 Graphic of C_z for both models for each yaw angle. 95
6.6 Graphic of C_{Mx_lee} for both models for each yaw angle. 96
6.7 Contours of absolute pressure around the train for the crosswind study at a yaw angle of 0°, viewed from the leeward (left) and windward (right) sides. 98
6.8 Contours of absolute pressure around the train for the crosswind study at a yaw angle of 30°, viewed from the leeward (left) and windward (right) sides. 98
6.9 Contours of absolute pressure around the train for the crosswind study at a yaw angle of 45°, viewed from the leeward (left) and windward (right) sides. 99
6.10 Contours of absolute pressure around the train for the crosswind study at a yaw angle of 60°, viewed from the leeward (left) and windward (right) sides. 99
6.11 Contours of absolute pressure around the train for the crosswind study at a yaw angle of 90°, viewed from the leeward (left) and windward (right) sides. 100
6.12 Pathlines around the train (coloured by velocity magnitude) for the crosswind study at a yaw angle of 0°, viewed from the leeward side from above (left) and below (right). 100

6.13 Pathlines around the train (coloured by velocity magnitude) for the crosswind study at a yaw angle of 30°, viewed from the leeward side from above (left) and below (right). 101
6.14 Pathlines around the train (coloured by velocity magnitude) for the crosswind study at a yaw angle of 45°, viewed from the leeward side from above (left) and below (right). 101
6.15 Pathlines around the train (coloured by velocity magnitude) for the crosswind study at a yaw angle of 60°, viewed from the leeward side from above (left) and below (right). 102
6.16 Pathlines around the train (coloured by velocity magnitude) for the crosswind study at a yaw angle of 90°, viewed from the leeward side from above (left) and below (right). 102
6.17 Velocity magnitude contours around the train on a YZ cross-sectional plane for the crosswind study at a yaw angle of 0°. 103
6.18 Velocity magnitude contours around the train on a YZ cross-sectional plane for the crosswind study at a yaw angle of 10°. 103
6.19 Velocity magnitude contours around the train on a YZ cross-sectional plane for the crosswind study at a yaw angle of 30°. 104
6.20 Velocity magnitude contours around the train on a YZ cross-sectional plane for the crosswind study at a yaw angle of 45°. 104
6.21 Velocity magnitude contours around the train on a YZ cross-sectional plane for the crosswind study at a yaw angle of 60°. 105
6.22 Velocity magnitude contours around the train on a YZ cross-sectional plane for the crosswind study at a yaw angle of 90°. 106
6.23 Values of C_x over time for the main vehicle. 109
6.24 Values of C_y over time for the main vehicle. 110
6.25 Values of C_z over time for the main vehicle. 112
6.26 Values of C_p over time for the midpoint of the intersection. 113
6.27 Velocity magnitude contour on the XZ plane at $t = 0.305$s. 115
6.28 Velocity magnitude contour on the XZ plane at $t = 0.652$s. 116
6.29 Pathlines around the train at $t = 0.150$s. 116
6.30 Pathlines around the train at $t = 0.395$s. 117
6.31 Contour of absolute pressure on the XY plane at $t = 0.365$s. 118
6.32 Contour of absolute pressure on the XY plane at $t = 0.435$s. 118
6.33 Contour of absolute pressure on the XY plane at $t = 0.909$s. 119
6.34 Contour of absolute pressure around the vehicles at $t = 0.255$s. 120
6.35 Contour of absolute pressure around the vehicles at $t = 0.420$s (front view). 120
6.36 Contour of absolute pressure around the vehicles at $t = 0.500$s. 121

B.1 Contours of absolute pressure around the train for the crosswind study at a yaw angle of 0°, viewed from the leeward (left) and windward (right) sides. 137
B.2 Contours of absolute pressure around the train for the crosswind study at a yaw angle of 5°, viewed from the leeward (left) and windward (right) sides. 137
B.3 Contours of absolute pressure around the train for the crosswind study at a yaw angle of 10°, viewed from the leeward (left) and windward (right) sides. 138
B.4 Contours of absolute pressure around the train for the crosswind study at a yaw angle of 15°, viewed from the leeward (left) and windward (right) sides. 138
B.5 Contours of absolute pressure around the train for the crosswind study at a yaw angle of 20°, viewed from the leeward (left) and windward (right) sides. 138

B.6 Contours of absolute pressure around the train for the crosswind study at a yaw angle of 25°, viewed from the leeward (left) and windward (right) sides. 138
B.7 Contours of absolute pressure around the train for the crosswind study at a yaw angle of 30°, viewed from the leeward (left) and windward (right) sides. 139
B.8 Contours of absolute pressure around the train for the crosswind study at a yaw angle of 35°, viewed from the leeward (left) and windward (right) sides. 139
B.9 Contours of absolute pressure around the train for the crosswind study at a yaw angle of 40°, viewed from the leeward (left) and windward (right) sides. 139
B.10 Contours of absolute pressure around the train for the crosswind study at a yaw angle of 45°, viewed from the leeward (left) and windward (right) sides. 139
B.11 Contours of absolute pressure around the train for the crosswind study at a yaw angle of 50°, viewed from the leeward (left) and windward (right) sides. 140
B.12 Contours of absolute pressure around the train for the crosswind study at a yaw angle of 55°, viewed from the leeward (left) and windward (right) sides. 140
B.13 Contours of absolute pressure around the train for the crosswind study at a yaw angle of 60°, viewed from the leeward (left) and windward (right) sides. 140
B.14 Contours of absolute pressure around the train for the crosswind study at a yaw angle of 70°, viewed from the leeward (left) and windward (right) sides. 140
B.15 Contours of absolute pressure around the train for the crosswind study at a yaw angle of 80°, viewed from the leeward (left) and windward (right) sides. 141
B.16 Contours of absolute pressure around the train for the crosswind study at a yaw angle of 90°, viewed from the leeward (left) and windward (right) sides. 141

C.1 Pathlines around the train (coloured by velocity magnitude) for the crosswind study at a yaw angle of 0°, viewed from the leeward side from above (left) and below (right). 143
C.2 Pathlines around the train (coloured by velocity magnitude) for the crosswind study at a yaw angle of 5°, viewed from the leeward side from above (left) and below (right). 143
C.3 Pathlines around the train (coloured by velocity magnitude) for the crosswind study at a yaw angle of 10°, viewed from the leeward side from above (left) and below (right). 144
C.4 Pathlines around the train (coloured by velocity magnitude) for the crosswind study at a yaw angle of 15°, viewed from the leeward side from above (left) and below (right). 144
C.5 Pathlines around the train (coloured by velocity magnitude) for the crosswind study at a yaw angle of 20°, viewed from the leeward side from above (left) and below (right). 144
C.6 Pathlines around the train (coloured by velocity magnitude) for the crosswind study at a yaw angle of 25°, viewed from the leeward side from above (left) and below (right). 145
C.7 Pathlines around the train (coloured by velocity magnitude) for the crosswind study at a yaw angle of 30°, viewed from the leeward side from above (left) and below (right). 145
C.8 Pathlines around the train (coloured by velocity magnitude) for the crosswind study at a yaw angle of 35°, viewed from the leeward side from above (left) and below (right). 145

C.9 Pathlines around the train (coloured by velocity magnitude) for the crosswind study at a yaw angle of 40°, viewed from the leeward side from above (left) and below (right). . . . 146
C.10 Pathlines around the train (coloured by velocity magnitude) for the crosswind study at a yaw angle of 45°, viewed from the leeward side from above (left) and below (right). . . . 146
C.11 Pathlines around the train (coloured by velocity magnitude) for the crosswind study at a yaw angle of 50°, viewed from the leeward side from above (left) and below (right). . . . 146
C.12 Pathlines around the train (coloured by velocity magnitude) for the crosswind study at a yaw angle of 55°, viewed from the leeward side from above (left) and below (right). . . . 147
C.13 Pathlines around the train (coloured by velocity magnitude) for the crosswind study at a yaw angle of 60°, viewed from the leeward side from above (left) and below (right). . . . 147
C.14 Pathlines around the train (coloured by velocity magnitude) for the crosswind study at a yaw angle of 70°, viewed from the leeward side from above (left) and below (right). . . . 147
C.15 Pathlines around the train (coloured by velocity magnitude) for the crosswind study at a yaw angle of 80°, viewed from the leeward side from above (left) and below (right). . . . 148
C.16 Pathlines around the train (coloured by velocity magnitude) for the crosswind study at a yaw angle of 90°, viewed from the leeward side from above (left) and below (right). . . . 148

D.1 Velocity magnitude contours around the train on a YZ cross-sectional plane for the crosswind study at a yaw angle of 0°. . . . 149
D.2 Velocity magnitude contours around the train on a YZ cross-sectional plane for the crosswind study at a yaw angle of 5°. . . . 150
D.3 Velocity magnitude contours around the train on a YZ cross-sectional plane for the crosswind study at a yaw angle of 10°. . . . 150
D.4 Velocity magnitude contours around the train on a YZ cross-sectional plane for the crosswind study at a yaw angle of 15°. . . . 150
D.5 Velocity magnitude contours around the train on a YZ cross-sectional plane for the crosswind study at a yaw angle of 20°. . . . 151
D.6 Velocity magnitude contours around the train on a YZ cross-sectional plane for the crosswind study at a yaw angle of 25°. . . . 151
D.7 Velocity magnitude contours around the train on a YZ cross-sectional plane for the crosswind study at a yaw angle of 30°. . . . 151
D.8 Velocity magnitude contours around the train on a YZ cross-sectional plane for the crosswind study at a yaw angle of 35°. . . . 152
D.9 Velocity magnitude contours around the train on a YZ cross-sectional plane for the crosswind study at a yaw angle of 40°. . . . 152
D.10 Velocity magnitude contours around the train on a YZ cross-sectional plane for the crosswind study at a yaw angle of 45°. . . . 152
D.11 Velocity magnitude contours around the train on a YZ cross-sectional plane for the crosswind study at a yaw angle of 50°. . . . 153
D.12 Velocity magnitude contours around the train on a YZ cross-sectional plane for the crosswind study at a yaw angle of 55°. . . . 153

D.13 Velocity magnitude contours around the train on a YZ cross-sectional plane for the crosswind study at a yaw angle of 60°. 153
D.14 Velocity magnitude contours around the train on a YZ cross-sectional plane for the crosswind study at a yaw angle of 70°. 154
D.15 Velocity magnitude contours around the train on a YZ cross-sectional plane for the crosswind study at a yaw angle of 80°. 154
D.16 Velocity magnitude contours around the train on a YZ cross-sectional plane for the crosswind study at a yaw angle of 90°. 154

E.1 Values of C_x over time for the main vehicle. 156
E.2 Values of C_x over time for the secondary vehicle. 157
E.3 Values of C_y over time for the main vehicle. 158
E.4 Values of C_y over time for the secondary vehicle. 159
E.5 Values of C_z over time for the main vehicle. 160
E.6 Values of C_z over time for the secondary vehicle. 161
E.7 Values of C_p over time for the midpoint of the intersection. 162

F.1 Velocity magnitude contour on the XZ plane at $t = 0.305$s. 163
F.2 Velocity magnitude contour on the XZ plane at $t = 0.395$s. 164
F.3 Velocity magnitude contour on the XZ plane at $t = 0.652$s. 164
F.4 Pathlines around the train at $t = 0.150$s. 165
F.5 Pathlines around the train at $t = 0.395$s (perspective view). 165
F.6 Pathlines around the train at $t = 0.395$s (viewed from above the vehicle). . . 166
F.7 Pathlines around the train at $t = 0.395$s (viewed from the vehicle's left side). 166
F.8 Pathlines around the train at $t = 0.395$s (viewed from below the vehicle). . . 167
F.9 Pathlines around the train at $t = 0.652$s. 167
F.10 Contour of absolute pressure on the XY plane at $t = 0.300$s. 168
F.11 Contour of absolute pressure on the XY plane at $t = 0.365$s - maximum value of C_p. 168
F.12 Contour of absolute pressure on the XY plane at $t = 0.395$s. 169
F.13 Contour of absolute pressure on the XY plane at $t = 0.435$s - minimum value of C_p. 169
F.14 Contour of absolute pressure on the XY plane at $t = 0.652$s. 170
F.15 Contour of absolute pressure on the XY plane at $t = 0.909$s. 170
F.16 Contour of absolute pressure on the XY plane at $t = 1.020$s. 171
F.17 Contour of absolute pressure around the vehicles at $t = 0$s. The unrealistic pressure distribution comes from the sudden movement initialization. 172
F.18 Contour of absolute pressure around the vehicles at $t = 0.255$s. 172
F.19 Contour of absolute pressure around the vehicles at $t = 0.375$s (perspective view). 173
F.20 Contour of absolute pressure around the vehicles at $t = 0.375$s (front view). 173
F.21 Contour of absolute pressure around the vehicles at $t = 0.420$s (perspective view). 174
F.22 Contour of absolute pressure around the vehicles at $t = 0.420$s (front view). 174
F.23 Contour of absolute pressure around the vehicles at $t = 0.500$s. 175
F.24 Contour of absolute pressure around the vehicles at $t = 0.595$s. 175
F.25 Contour of absolute pressure around the vehicles at $t = 0.652$s. 176
F.26 Contour of absolute pressure around the vehicles at $t = 0.652$s (closer view). 176
F.27 Contour of absolute pressure around the vehicles at $t = 0.909$s. 177

List of Tables

2.1 Overview of the contents of the EN 14067 series. 10

3.1 Dimensions of the domain. 40
3.2 Dimensions of the smaller volume of the domain. 41
3.3 Size parameters for the 5 different meshes. 43
3.4 Boundary conditions on the different surfaces of the domain. 46
3.5 Under-relaxation factors for all the simulations. 48
3.6 Values of C_x for the `S_1_O` configurations. 48
3.7 Values of C_x for the `S_2_O` configurations. 48
3.8 Values of C_x for the `S_1_E` configurations. 49
3.9 Values of C_x for the `S_2_E` configurations. 49
3.10 Dimensions of the domain for the ICE model. 53
3.11 Dimensions of the smaller volume of the domain for the ICE model. 54
3.12 Values of drag coefficient obtained for the 4 different configurations of the ICE model. 55

4.1 Dimensions of the domain for the crosswinds study. 58
4.2 Dimensions of the smaller volumes for the crosswinds study. 58
4.3 Cell size for the different volumes of the domain. 60
4.4 Quality parameters for the meshes. 61
4.5 Values of C_x, C_y and C_z for the ICE model (configuration with rails). 62
4.6 Values of C_x, C_y and C_z for the *TrainSolutions Portugal* model. 64
4.7 Values of C_x, C_y and C_z for the 0° transient simulation. 68

5.1 Dimensions of the domain volumes for the train passing simulations. 73
5.2 Dimensions of the train volume for the train passing simulations. 74
5.3 Mesh parameterization for domain. 76
5.4 Boundary conditions on the differente surfaces for the train passing simulations. 77
5.5 Dimensions of the domain volumes for the train passing simulations. 80
5.6 Mesh parameterization for domain. 82

6.1 Values of drag coefficient obtained for the 4 different configurations of the ICE model - sorted by how closer they got to the standard. 88
6.2 Average and maximum aspect ratio for the 5 meshes. 91

Acronyms

BoI Body of Influence

CFD Computational Fluid Dynamics

CP Comboios de Portugal

DES Detached Eddy Simulation

ELES Embedded Large Eddy Simulation

FEUP Faculdade de Engenharia da Universidade do Porto

FVM Finite Volume Method

FSA Fortified Solution Algorithm

ICE InterCity Express

INEGI INEGI - Instituto de Ciência e Inovação em Engenharia Mecânica e Engenharia Industrial

LES Large Eddy Simulation

PISO Pressure-Implicit with Splitting of Operators

PRR Plano de Recuperação e Resiliência

RANS Reynolds-Averaged Navier–Stokes

SAS Scale-Adaptive Simulation

TFC Total Final Consumption

UDF User-Defined Function

URANS Unsteady Reynolds-Averaged Navier–Stokes

Symbols List

A	Area	m^2
C_D	Drag coefficient	–
C_L	Lift coefficient	–
C_M	Moment coefficient	–
C_{Mx}	Moment coefficient x-direction	–
C_{Mx_lee}	Moment coefficient x-direction on the leeward side	–
C_{My}	Moment coefficient y-direction	–
C_{Mz}	Moment coefficient z-direction	–
Co	Courant Number	–
C_p	Pressure coefficient	–
C_x	Force coefficient in the x-direction	–
C_y	Force coefficient in the y-direction	–
C_Y	Lateral force coefficient	–
C_z	Force coefficient in the z-direction	–
F	Force	N
F_D	Drag force	N
F_L	Lift force	N
H	Height of the train	m
k	Turbulent kinetic energy	m^2/s^2
L	Length of the train	m
M	Moment	N . m
M_x	Moment in the x-direction	N . m
p	Pressure	Pa
p_∞	Freestream pressure	Pa
Re	Reynolds number	–
t	Time	s
u	Velocity in the flow direction	m/s
u_∞	Freestream velocity	m/s
v	Velocity	m/s
v_a	Apparent velocity	m/s
v_{tr}	Train velocity	m/s
v_w	Wind velocity	m/s
β	Yaw angle	$^\circ$
Δt	Time step	s
Δx	Characteristic length of a computational cell	m
ϵ	Turbulent dissipation rate	m^2/s^3
ω	Specific dissipation rate	s^{-1}
ρ	Density	kg/m^3

Chapter 1

Introduction

Being one of the two main means of land transportation, railroad has a crucial role in mobility all over the globe for economic, environmental and social reasons. It allows for a cheaper and less congested way of commuting for the masses while the better energetic efficiency gives a sustainable alternative to road transportation, which is a top priority among developed countries, in order to reduce GHG emissions [7].

Being responsible for about 8% of the world's passenger transportation and 7% of the world's freight transport, while accumulating only 2% of the total energy demand, gives a small idea about how much the global energy consumption can be decreased by diving massively into the railroad [7]. This is particularly important when we notice that transportation of people and goods is about 30% of the total final consumption of energy in 2025, as shown in figure 1.1 [1]. Not only that, but it allows for a convenient mean of transportation over medium to large distances for the vast majority of people. Moreover, considering there are those| (like children, elders and families with smaller incomes) who simply can not afford to commute by car daily, having a robust public transit infrastructure is mandatory in order to achieve a more just and well-rounded society.

In Portugal, investing in a solid train network to improve passenger and freight transportation, provides a competitive alternative to more nefarious means of transportation. At the same time, improving the existing technology (as in, new vehicles or infrastructure) gives room for better comfort and overall performance, attracting more attention to the railroad.

Nevertheless, this improvement not only demands a big financial investment in the railway framework as well as an effort in a wide range of areas of engineering (such as mechanical, materials and electrical). Currently, the time is for advancements rather than creating something, so developing teams are exploring new possibilities, like different materials and geometries.

So, in order to aspire to be a top-tier country in terms of social justice and energetic revolution, Portugal must commit to its railroad. For that to happen, capital and engineering know-how are obliged.

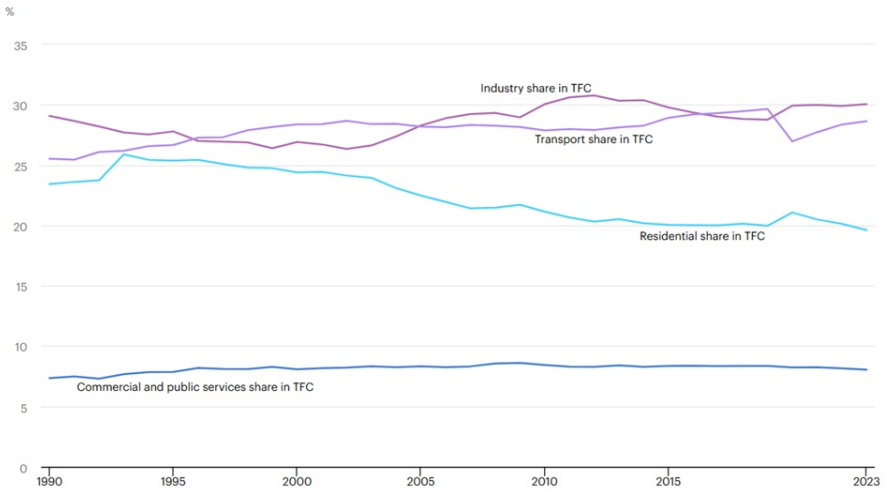


Figure 1.1: Share of TFC by sector over the years [1].

1.1 The Portuguese Railroad System

Portuguese railroad began in 1856, amidst the industrial revolution, with the first section of the line connecting Lisbon to Carregado, opening on the 28^{th} of October. Extending 37 kilometers, this marked the beginning of a new era in transportation [8].

At the time, transit was mostly done by boat or through scarce and poorly treated roads, with the help of animal traction. The train had the potential to complete the trips that previously took days or weeks in a matter of hours [9]. This meant that an immense leap could happen in economic growth; as transportation becomes easier new markets are available.

From the second half of the nineteenth century to the First World War, the railroad network only saw improvement, with new links being constructed, like connecting the 2 biggest cities (Porto and Lisbon) and international passages, to Spain. Since Portugal has a complicated topography, clearing some natural barriers (such as rivers and mountains) was no easy feat, but it was made possible due to engineering and political help [9]. Fontes Pereira de Melo was a major booster in the field, as he was a minister of public works who saw that betting on a good train infrastructure could lead to a great betterment in the economy and the quality of life [8]. At a slower pace than desirable, the railway system kept evolving, until the sixties where the electrification began.

Then, the carnation revolution, in 1974 changed the country. With the end of the dictatorship, a new leadership (more open to negotiations with Europe) began investing in forgotten sectors. As Portugal joined the CEE in 1986, european funds were pouring into the country to help its development, since the colonial war left behind severe damage. That investment went heavily into building roads and bridges, which skyrocketed the use of the automobile. Road transportation would see a massive increase in the next decades, until it becomes the norm, outclassing the poorly treated railroad [9][10].

This meant that public transit, in particular train usage, became less attractive. With the masses drifting away from it and successive governments making empty promises of growth, the railway system began shrinking since the seventies. In fact, as of 2026, Portugal has around the same length of railroad as it had by the time the monarchy ended; in 1910 [11]. In the last 50 years, around 40% of the links have been shut down. Not only that, there are fewer vehicles, worse frequencies, and the country is ever more separated from the rest of Europe [11].

The next figures show the precarity of the situation. Figure 1.2 shows the current railway system in Portugal; for its dimension, it is substantially small. Right now, the length of the Portuguese railway is around 2500 kilometers. It was nearly 3600 kilometers 5 decades ago.

As figures 1.3 and 1.4 demonstrate, the highways are clearly replacing the railways, a deliberate decision from the governments to invest more in such infrastructure.

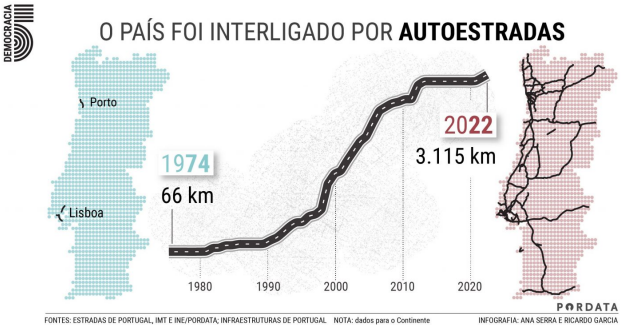


Figure 1.3: Evolution of the highway system in Portugal in the last 5 decades [2].

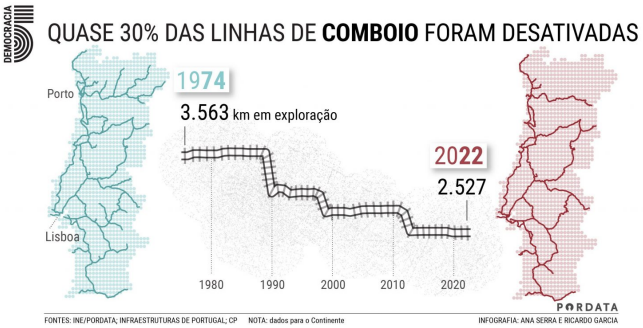


Figure 1.4: Evolution of the railway system in Portugal in the last 5 decades [2].

Luckily, in the last few years, some efforts are being conceived to change the situation. There has been some investment in light railway, with three existing metro systems in the country - Lisbon, Porto and MST (Metro Sul do Tejo) [12]. Train has also seen some prospects of improvement, with some new links and the possibility of high-speed,



Figure 1.2: Portuguese railway system as of 2020 [3].

connecting Porto and Lisbon to each other and some major Spanish cities (Vigo and Madrid, respectively), figure 1.5 [4].



Figure 1.5: High-speed projects in Portugal for the next years [4].

Nonetheless, Portugal is still far from being a country where railroad is a viable method of tranportation for a large fraction of its population. Truth is, when compared to most countries of similar size and HDI (Human Development Index), Portugal is in a terrible position, both in terms of miles covered by rail and number of passengers [13] - easily explained by the first.

It is important to notice that the data of this page neglects to use any parameter to adjust the rail mileage to the area of the country or population, as well as it compares data from different years. Even so, Portugal ranks 54^{th} in the ranking for longest railway system, a very low performance. So, from this, we can conclude that a lot of work needs to be put in the infrastructure to reinvent the Portuguese railroad, as well as better the technology to go along with it.

That is where the project *TrainSolutions Portugal* emerges from.

1.2 Framing of the Project

After the 2020 global pandemic and lockdown, world's economy took a major toll. As a country whose GDP relies heavily on exportations and tourism, Portugal's was no exception.

EU decided that in order to mitigate the social and economic impact of the crisis in the following years, it was necessary to create an instrument to cultivate investment in European countries to kick-start the businesses once more. So, a lot of money from European funds was poured into some nations, including Portugal [14].

So, Plano de Recuperação e Resiliência (PRR) (literally translated to Project of Recovery and Resilience) - was created, a national project to use the help from Brussels to its fullest. It is a strategic project whose main 3 goals are resilience and climatic and digital transition [14].

This way, a lot of projects related to public infrastructure came to light, as it would create value in fields requiring physical labour and technical expertise, such as engineering. This program was responsible for (partly) financing some projects like bridges and public transit foundation (for metro, train, BRT...). One of those programs was *TrainSolutions Portugal*.

TrainSolutions is a technological investment project financed by PRR with an overall cost of over 55 million euros. Formed by the cooperation of over a dozen companies (such as Comboios de Portugal (CP), SERMEC, Faculdade de Engenharia da Universidade do Porto (FEUP), INEGI - Instituto de Ciência e Inovação em Engenharia Mecânica e Engenharia Industrial (INEGI)...), its main purpouse was to create a new and in-demand "Portuguese train" [15][16]. With a refreshed look, higher energy-efficiency and more commodities for its passangers, this vehicle would hopefully contribute to the expanding the use of the train. An image of this model can be seen in figure 1.6.



Figure 1.6: First preview of the "portuguese train" [5].

Moreover, it is expected to have several inovations for the Portuguese paradigm, with the main focus going towards the *push-pull* mechanism; that is, the vehicle can circulate in both ways without the need for any bigger manoeuvres [15][16]. It has 3 types of passanger carriages and (with a renovation in the rails) it should circulate at higher speeds than those practiced currently, at around 200 kilometers per hour.

Highly invested in this project is FEUP, with a team of engineers conducting studies to many areas of interest, in order to ensure the Portuguese train is as good as expected. Naturally, in order to enhance fuel efficiency, it is mandatory to study the aerodynamic of the vehicle, to allow it to operate at higher velocities without too big of a cost. Not only that; executing aerodynamic studies is relevant to evaluate other parameters such as safety and stability of the trip and the level of noise and confort for the users.

In the light of these aerodynamic studies, this master's dissertation was proposed by Professors Abílio de Jesus and Delmar Jorge, as a new member joining the team allowed more possibilities to be explored. Being a student concluding a master's degree in mechanical engineering, specializing in fluids and energy, this is also the perfect oportunity to

gain some experience, while contributing significantly to a project of significant dimension.

1.3 Objective

The objective of this project was to study the aerodynamic of the new CP model train from the *TrainSolutions* program to evaluate its performance, safety and confort.

To do that, it is necessary to attain knowledge CFD simulation and testing and acquire a model of the train geometry. After that, running computer tests in order to analyse its aerodynamic coefficients (such as drag and lift) and the air flow in critical conditions; high-speed, crosswinds, crossing of vehicles, entrance of tunnels, the *push-pull* functionality... If possible, by the end of the work, it would be ideal to run small scale tests on a wind tunnel or maybe even real-size testing with a prototype.

Initially, since a lot of situations are to be tested, it was necessary to chose a few to be tackled in this thesis. So, considering the time window each task should take and the period for the realization of the work, it was decided to work on 3 different situations; headwinds at high-speed, crosswinds and crossing of trains. All of these would be tested in numerical simulation and the chosen CFD software for that was ANSYS Fluent.

At the end, for each case, the results are to be studied in order to take conclusions to validate or not this model for circulation. If possible, small tweaks could be done to the original geometry and some modifications could be suggested, if they happen to improve the overall performance.

1.4 Structure of the Dissertation

This dissertation is divided mainly in 6 chapters. This chapter is mostly the introduction and chapter 2 is the literature review on this topic. Then, the methodology is split between three chapters.

Chapter 3 describes the first work done related to the project. In the begining, simulations of headwinds were executed for the CP model, as well as the German ICE for benchmarking purpouses. Different mesh types, turbulence models and solution parameters were used, in order to evaluate its impact in the final results. This was important to choose the best configuration for further studies.

Chapter 4 focuses on the crosswinds studies. With a more precise goal in mind, different transit situations were considered and, with the same configuration, the main aerodynamic coefficients (drag and lift) were registered to analyse how they vary with the angle of the incident wind. Images of the airflow in critical geometries were also created to allow for a wider scope of discussion later. The benchmarking results from the ICE were used as much as possible here as well, to have a more solid ground for analysis.

Chapter 5 was dedicated to the passing of vehicles. This part of the project had to be under transient simulation, with the relative position of the trains changing. That was

the most challenging part, as expected. Once more, the simulations were run to get the aerodynamic coefficients and air flow on the surfaces to figure out whether the circulation is safe, stable and comfortable.

Chapter 6 is mostly the further analysis and discussion of the results obtained during the study. All the recommendations and final reparations belong here.

Chapter 7 is the conclusion of the thesis and contains a few reflections and suggestions for future works.

Chapter 2

Literature Review

This chapter contains the literature review for the relevant topics to the work performed regarding the aerodynamic study of the new Portuguese train. The main objetives of this section of the dissertation are to establish the theoretical and scientific framework that was necessary for the development of the present investigation, to report the main approaches to the preoblem inprevious research and to define a path to progressing in this study.

So, it is divided into three main sections. The first and second sections focus on the existing standards for the investigation of railway vehicles aerodynamics and the CFD fundamentals, respectively. These parts contain the common procedures and fluid mechanics theory that becomes the background for the final segment.

The third section is a conjugation of both, as addresses the existing research on the aerodynamic of trains using CFD. Various studies compose the compendium that is here presented, with studies focused on many different operating conditions and with different motivations mentioned; however, the focal point was in investigations regarding circulation under crosswinds and train passing manouevres, as this were the objects of this study.

Overall, this review provides the backbone and technical knowledge mandatory for progressing in this project.

2.1 Railway Aerodynamic Standards

The continuous increase in railway operating speeds over the last decades has increased the importance of considering aerodynamic phenomena in train design. While aerodynamic effects have always influenced railway operation, their impact becomes more notable as train speed exceeds 200 km/h. At these velocities, aerodynamic forces influence not just the energy consumption but also passenger comfort, safety, infrastructure loading and the interaction between trains and the surrounding environment. These phenomena include pressure waves generated during train passage, slipstreams, aerodynamic drag, crosswind effects, train-to-train interactions, and tunnel pressure transients. Consequently, railway administrations require standardized procedures capable of evaluating

these occurrences in a consistent and predictable way before a vehicle begins commercial service [17] [18].

To satisfy said requirements, the European Committee for Standardization developed the EN 14067 norm. This norm establishes methodologies, definitions, procedures and criteria for the behaviour of trains operating under a certain range of conditions. They provide a common structure that enables everyone involved in the process to evaluate aerodynamic performance using comparable methodologies [17] [19] [20].

Many numerical investigations validate CFD models by reproducing the testing conditions prescribed by the standard, which allows direct comparison between experimental measurements and computer simulations. As a result, EN14067 became one of the main references for railway aerodynamic studies worldwide [21].

The first version of the EN 14067 norm mainly established terminology and general procedures, while most recent revisions include updated assessment methods, improved requirements and extended guidelines regarding numerical simulations. These revisions come -among other reasons - as a result of the rapid growth of computational methods and the increasing reliance on CFD as a tool for experimental testing [22] [22].

Nowadays, the EN 14067 norm consists of six complementary documents (each addressing a separate aspect of train aerodynamics). Put together, they provide a comprehensive exoskeleton covering symbols and terminology, open-track and tunnel operation, crosswind stability and overall safety and stability. Table 2.1 summarizes the current structure of the norm [18] [19] [20].

Part	**Contents**
Part 1	Symbols and units used in railway aerodynamics.
Part 2	Aerodynamics on open track (withdrawn and incorporated into later revisions).
Part 3	Aerodynamics in tunnels.
Part 4	Requirements and assessment procedures for aerodynamics on open track.
Part 5	Requirements and assessment procedures for aerodynamics in tunnels.
Part 6	Requirements and test procedures for crosswind assessment.

Table 2.1: Overview of the contents of the EN 14067 series.

Among these parts, numbers 4, 5 and 6 are of greater relevance for modern railway engineering, since they establish systematic methodologies for testing the performance of vehicles under operating conditions. Part 4 focuses on open-track; this includes slipstream effects, pressure variations and other effects [23]. Then, part 5 addresses the circulation inside of tunnels, with phenomena such as pressure waves (generated during tunnel entry and exit) [19] [24]. Finally, part 6 defines the methodology used to evaluate the stability of vehicles subjected to crosswinds; this represents one of the most critical scenarios encountered during operation [6].

Furthermore, the increasing complexity in train design has also contributed to the adoption of numerical simulations during the development process. While full-scale experiments remain the reference for certification, CFD has become an indispensable tool, as it gives designers the opportunity to investigate various operating conditions at a significantly lower cost (and faster pacing) than larger experimental campaigns [25]. Newer versions of the EN 14067 recognise this change by providing specified guidance on the validation of numerical methods, alongside experimental measurements [26].

Nonetheless, this was not the only European Standard norm taken into consideration. When creating the 3D models for the simulations - in particular, the train passing ones - it was necessary to take into account the surrounding infrastructure. In this case, the most relevant is the space between the tracks. However, it is relevant to check what the padronized procedure is for situations like this and whether or not there are other issues to be addressed.

Then, the EN 15273-3 was also studied to better comprehend the predicament. The EN 15273-3 standard defines the methodology for determining the infrastructure gauge and the minimum clearances necessary to ensure safe operation of railway vehicles. It provides the formulas used to calculate infrastructure profiles, while considering factors like track geometry, suspension movements and construction clearances. Additionly, it establishes the procedures for determining the required distance between adjacent track centres (very important for this project) and platform clearances [27].

So, comprehending the objectives and requirements established in the normw is essential before discussing CFD methodologies. That being the case, the EN 14067 series was then carefully analyzed to find the most relevant parameters to this work.

2.1.1 Development of the EN 14067 Series

The continuous evolution of railway network and technology have naturally increased the importance of standardized aerodynamic assessment procedures. During the 1990s and early 2000s, the expansion of high-speed railway systems emphasized the need for common methodologies, capable of evaluating the performance under different operating conditions [18]. Before the publication of the EN 14067 series, these procedures varied largely between different operators and manufacturers, resulting in an awkward and complicated way to compare experimental results and establish common acceptance criteria [17] [22].

The primary objective of the series is to establish uniform requirements, symbols and terminology, procedures and methods for the behaviour of vehicles, ensuring consistency all over the European railway network and supporting the objectives defined by legislation [17].

The first editions of the EN 14067 standards mainly focused on defining terminology and introducing uniform experimental procedures for evaluating aerodynamics of railway vehicles. As research advanced, mostly due to the increasing use of high-speed trains (operating above 250 km/h), additional phenomena required standardized methodologies

[17] [18]. These included pressure variations generated during train passage, slipstream effects, tunnel aerodynamics, ballast projection... That called for an upgrade of the norm.

As railway technology kept advancing, the EN 14067 series underwent many updates to include new research findings and practical experience gained from both experimental campaigns and numerical simulations. Furthermore, it began acknowledging the role of CFD as a complementary engineering tool. Even though full-scale and wind tunnel experiments remain the reference methods for certification, validated numerical simulations are now widely employed during the design phase to investigate aerodynamics before experimental verification is performed [22] [17].

The continuous revision of the EN 14067 shows the development of train aerodynamics as part of engineering. By incorporating the both large-scale European projects and advances in numerical simulation techniques, it provides a scientifically robust framework for aerodynamic analysis while ensuring that certification procedures remain consistent with current practice. This has led the EN 14067 series to become the principal reference for railway aerodynamic investigations carried out in both industry and academia.

2.1.2 Overview of the EN 14067 - Parts 4 and 5

The EN 14067 series gives a uniform structure for the aerodynamic study of railway vehicles operating under a wide range of conditions. Rather than addressing train aerodynamics through a single document, the norm is divided into several complementary documents, with each one focusing on a specific matter. This structure allows manufacturers, railway operators and certification bodies to apply standardized methodologies according to the particular aerodynamic problem being investigated while ensuring consistency throughout the evaluation process [17].

As previously mentioned, the first part of the series, EN 14067-1, establishes the terminology, symbols and units used throughout the remaining documents. It defines the nomenclature adopted for aerodynamic forces, pressure coefficients, flow variables and characteristic dimensions, ensuring a common language for the whole process. Although it does not specify testing procedures, its role is fundamental in maintaining consistency across the complete work [17]. Most relevant for this dissertation are parts 4, 5 and 6.

EN 14067-4 focuses on the aerodynamic behaviour of railway vehicles operating on open track. This document specifies the requirements and assessment procedures for several phenomena, such as drag, pressure variations, slipstream effects and loads acting on nearby infrastructure and passengers. The standard defines measurement techniques, data processing procedures and acceptance criteria, allowing comparable results to be obtained from full-scale tests, reduced-scale experiments (such as wind tunnel) and validated numerical simulations, CFD. Since most trains spend the majority of their operational life on open track, this document represents one of the most used parts of the EN 14067 norm [23].

The fifth part of the standard, EN 14067-5, addresses the aerodynamic phenomena associated with train operation inside tunnels. When a high-speed train enters a tunnel, the surrounding air is rapidly compressed, generating pressure waves that propagate through the tunnel. These waves may affect passenger comfort, increase structural loading on both the vehicle and the tunnel infrastructure, and generate micro-pressure waves at tunnel exits. EN 14067-5 establishes standardized procedures for evaluating these effects, defining measurement methodologies and assessment criteria that contribute to the safe and efficient operation of railway systems in confined environments. As modern railway networks increasingly incorporate long tunnels to accommodate higher operating speeds and complex terrain, tunnel aerodynamics has become an essential aspect of railway vehicle design [24] [19]. This part of the study ended up not being included in this disseration, however it is an indispensable fragment of the certification.

Among the different parts of the norm, EN 14067-6 is particularly relevant to this work because it establishes the requirements for assessing railway vehicle stability under crosswinds. Crosswinds generate aerodynamic forces and overturning moments that may compromise stability, particularly for lightweight rolling stock and trains operating at high speeds. The standard specifies methodologies for determining the characteristic wind curves of railway vehicles through full-scale measurements, wind tunnel experiments and validated numerical approaches. These procedures provide a common framework for evaluating vehicle safety under crosswind conditions and have become an essential component of the aerodynamic certification process for modern railway vehicles [6] [28].

Although each document addresses a specific aerodynamic phenomenon, the different parts of the EN 14067 series are strongly interconnected. Open-track aerodynamics, tunnel pressure transients and crosswind stability are frequently analysed together during the aerodynamic design process to ensure that a railway vehicle satisfies all safety and performance requirements before entering commercial service. Consequently, manufacturers typically combine experimental testing with CFD simulations to evaluate vehicle performance throughout the complete operating envelope [23] [24] [6].

The next subsection is dedicated specifically to the part 6, as that is the one with the biggest revelance to this thesis.

2.1.3 Overview of the EN 14067 - Part 6

The increasing operating speeds of modern railway vehicles have significantly enhanced the importance of crosswind aerodynamics studies in railway engineering. Strong lateral winds can generate substantial aerodynamic forces and overturning moments, which compromise stability, comfort and safety. Consequently, crosswind assessment has become an essential aspect of railway vehicle design, particularly for high-speed trains operating in exposed environments such as embankments, bridges and open plains [6] [29] [28].

To address these issues, the EN 14067-6 norm establishes a uniform methodology for studying the behaviour of railway vehicles under crosswind conditions. The standard

specifies the procedures necessary to analyse the aerodynamic behaviour of rolling stock subjected to crosswind conditions, providing a common framework for manufacturers and operators across Europe [6].

Relevant points addresed is this norm are, for example, the conditions to which the vehicles must adhere to be subjected to this methodology (passenger vehicles with max speeds between 140 to 360 km/h and freight wagons from 80 to 160 km/h). It also calls 3 other standards that must be considered in the study, like the EN 14067-4. The other 2 are "EN 14363, Railway applications - Testing and Simulation for the acceptance of running characteristics of railway vehicles - Running Behaviour and stationary tests", as well as "EN 15663, Railway applications - Vehicle reference masses" [6]. Naturally, since one addresses testing parameters and the other the weight of the rolling stock, it only makes sense for both norms to be evoked.

Furthermore, it defines the conditions that must be met for the configuration to be valid. For example, that are a number of track + ballast configurations that can be validated, but they must obey the norm. It can even be omitted (a case of study in this thesis), but it must keep the distances required in the chapter 5, "Methods and requirements to assess cross wind stability of vehicles" [6].

Moreover, the norm defines a process based on the determination of aerodynamic coefficients acting on the vehicle under different yaw angles (β) and wind conditions. It extensively explains all the notions that must be taken into consideration to achieve a valid result, present how the methodology works and how both the yaw angle and the apparent wind velocity are calculated (as a function of the wind direction relative to the track and the train and wind speed, as shown in 2.1 and 2.2) [6].

$$v_{\mathrm{rel,a}}(t) = \sqrt{\left(v_{\mathrm{rel}} + v_w(t)\cos\beta_w\right)^2 + \left(v_w(t)\sin\beta_w\right)^2} \tag{2.1}$$

$$\beta(t) = \arctan\left(\frac{v_w(t)\sin\beta_w}{v_{\mathrm{rel}} + v_w(t)\cos\beta_w}\right) \tag{2.2}$$

Picture 2.1 shows a visual representation of this calculation.

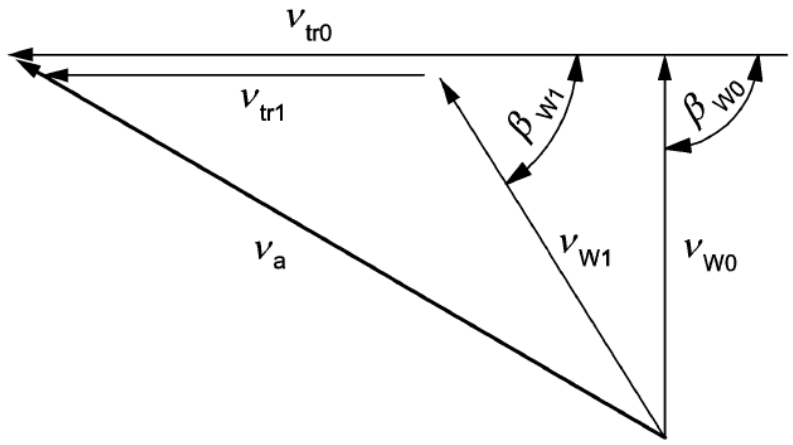


Figure 2.1: Visual representation of the apparent velocity [6].

Finally, it presents results from benchmark tests to allow comparison between those and the ones obtained by delevopers. Mostly, values of drag, lift and lateral force coefficient (C_x, C_z and C_y, respectively) are the main points of analysis and scrutiny in this work. These characterize the aerodynamics to which the train is subjected on different times and conditions.

These aerodynamic loads are subsequently combined with vehicle dynamic models to evaluate the risk of wheel unloading and overturning. Rather than considering aerodynamic forces in isolation, EN 14067-6 adopts an integrated approach in which both aerodynamic behaviour and vehicle dynamics contribute to the overall safety assessment. What this means is that, instead of isolating wind and train velocity, it considers the relative speed of the flow to encapsule the whole event. This methodology enables the determination of the characteristic wind curve, which presents the maximum crosswind velocity under which the railway vehicle can operate safely at a given running speed [6].

Several methods may be employed to determine the required aerodynamic coefficients. Full-scale testing provides the most representative measurements because the vehicle is evaluated under real operating conditions. However, such experiments are expensive, time-consuming and dependent heavily on environmental conditions. Reduced-scale wind tunnel testing therefore remains one of the most common experimental approaches, allowing highly controlled investigations of the aerodynamic forces generated under different wind angles and flow conditions [29].

In recent years, CFD has become an increasingly important complementary tool for crosswind investigations. Numerical simulations allow for detailed analysis of pressure distributions, flow separation and wake formation and aerodynamic loads on a wide range of conditions without requiring physical prototypes, a huge advantage. Although EN 14067-6 continues to regard experimental measurements as the primary reference for certification, validated CFD models are widely used during the design and optimisation stages to reduce

development costs and improve the understanding of complex aerodynamic phenomena [18].

Nevertheless, it makes it clear that, for a CFD study to be valid, it must be complemented with benchmark results, from tested models, such as the ones presented - like the ICE, TGV and ETR 500 it presents [6]. This is because the results from a numerical simulation can greatly vary with the defined geometry and mesh, as well as the selected setup parameters, like the turbulence models or convergence methods. So, to ensure the configuration is valid, this benchmark testing is fundamental [28].

The relevance of EN 14067-6 goes beyond crosswind assessment itself. It has promoted the uniformization of aerodynamic testing procedures across the European continent while encouraging the combined use of experimental techniques and numerical simulations. As computational methods continue to evolve, CFD is expected to play an increasingly significant role in supporting railway aerodynamic analyses, provided that appropriate verification and validation procedures are adopted [6].

2.1.4 Discussion and Relevance to the Present Work

The EN 14067 series has established itself as the principal regulation for the aerodynamic assessment of railway vehicles, providing harmonized procedures for evaluating aerodynamic phenomena that directly influence vehicle safety, passenger comfort and operational efficiency. By defining standardized testing methodologies and assessment criteria, the standard enables consistent comparison between experimental investigations and numerical simulations, ensuring that aerodynamic performance can be evaluated using reproducible and scientifically validated procedures [23] [24] [6].

The increasing complexity of railway vehicle design has also reinforced the importance of CFD. Advances in numerical methods, turbulence modelling and high-performance computing have enabled engineers to analyse highly transient and three-dimensional flow phenomena that would be difficult, expensive or even impossible to investigate exclusively through experimental testing. As a result, CFD has become an essential engineering tool during the early stages of railway vehicle development, allowing multiple design alternatives to be evaluated efficiently while reducing both development time and costs [25].

Although the EN 14067 standards continue to consider experimental measurements as the reference for certification, they acknowledge the increasing role of validated numerical simulations in aerodynamic investigations. Naturally, that becomes particularly interesting for a project such as this one, where it is not feasible - considering the means available - to conceive a large-scale model. CFD allows engineers to obtain detailed information regarding velocity fields, pressure distributions, turbulence structures and aerodynamic loads that cannot always be measured directly during experimental campaigns. When properly validated against experimental data, numerical simulations provide reliable predictions that support vehicle optimisation and improve the understanding of complex aerodynamic phenomena [23].

The *TrainSolutions Portugal* project is a large and important project for the future of public infrastructure in the country and as such, it needs validation in order to advance. The present dissertation focuses on the aerodynamic interaction between a train and strong winds, as well as two vehicles during a passing manoeuvre. Due to the complexity of the task and the limited time, it is not possible to conduct wind tunnels tests, let alone full-size studies. As such, it is imperative that CFD simulations are made in line with the norms, so they have meaning and can be analysed. In that case, the numerical methodology adopted in this work must be consistent with the engineering philosophy promoted by the EN 14067 series, allowing the next step to be performing experiments on prototypes, moving further the project.

The next part of this chapter presents the theoretical foundations of CFD, including the governing equations of fluid flow, turbulence models and numerical discretisation techniques that are the basis of the simulations performed in this work.

2.2 Computational Fluid Dynamics

2.2.1 Introduction to Computational Fluid Dynamics

CFD is a branch of fluid mechanics that employs numerical methods and computational algorithms to analyse and predict fluid flow phenomena. By solving the governing equations of fluid motion, CFD enables the simulation of complex flow fields that would otherwise require costly or impractical experimental investigations. Over the past few decades, significant advances in computational power and numerical algorithms have transformed CFD into one of the most important engineering tools for analysing fluid flow, heat transfer and other occurrences across a wide range of industrial applications [30] [31].

The development of CFD is closely tied to the growing availability of high-performance computers. Even though the governing equations describing fluid motion, namely the Navier-Stokes equations, have been known for over a century, obtaining analytical solutions is only possible for a limited number of simplified flow problems. Most engineering applications involve complex geometries, turbulent flows and transient phenomena, making analytical solutions impossible. Numerical methods overcome these limitations by discretising the governing equations over a finite computational domain, allowing approximate solutions to be obtained with a high degree of accuracy [31] [32].

A typical CFD analysis consists of three main stages: pre-processing, numerical solution and post-processing. During the pre-processing stage, the domain is created, the geometry is discretised into a finite number of control volumes or cells (elements), and the physical models, material properties and boundary conditions are defined. The solver then computes the variables throughout the domain by iteratively solving the discretised governing equations. Finally, the post-processing stage enables the visualisation and interpretation of the results; this includes velocity fields, pressure distributions, turbulence

quantities and forces, providing valuable knowledge about the physical behaviour of the flow [30].

One of the principal advantages of CFD is its ability to investigate operating conditions that are difficult or expensive to reproduce experimentally. Unlike physical testing, numerical simulations allow engineers to evaluate multiple design configurations and operating scenarios without the need to manufacture prototypes. In addition, CFD provides access to detailed flow information throughout the entire computational domain, including quantities that may be challenging or impossible to measure directly during experimental investigations - for example, different components of pressure. As a result, CFD has become an indispensable tool during the design and optimisation of engineering systems in sectors such as aerospace, automotive, marine and, like in this project, railway engineering [25].

Despite its capabilities, CFD remains an approximation of the physical problem. The accuracy of numerical predictions depends on several factors, including the quality of the computational mesh, the convergence method chosen, the selected turbulence model and the boundary conditions. Consequently, numerical simulations must be carefully verified and, whenever possible, validated against reliable experimental data before being used for engineering decision-making; like previously cited in the EN 14067-6 norm, the confrontation with benchmark models. International standards and best engineering practices therefore recommend combining numerical simulations with experimental investigations to ensure that the adopted computational methodology accurately represents the relevant flow phenomena [23].

Within railway engineering, CFD has become an essential tool for investigating aerodynamic events associated with high-speed train operation. Modern numerical techniques are capable of analysing aerodynamic drag, slipstream generation, tunnel pressure waves, crosswind stability and even train passing manoeuvres with increasing accuracy [33]. These capabilities have significantly reduced development time and cost while providing engineers with a deeper understanding of the complex flow structures surrounding railway vehicles. Consequently, CFD now plays a central role in the aerodynamic design and optimisation of modern railway systems and forms the numerical basis of the present dissertation.

2.2.2 Governing Equations of Fluid Flow

Numerical simulations of fluid flow are based on the fundamental conservation laws of physics (of mass, momentum and energy) within a liquid or a gas. These conservation principles are mathematically expressed through a system of partial differential equations, which are known as the Navier-Stokes equations. Put together, they form the theoretical basis of CFD, and enable the prediction of complex flow behaviour, often encountered in engineering applications [30] [31].

The first governing equation is the conservation of mass (often referred to as the continuity equation). This equation, shown in 2.3, ensures that mass is neither created

nor destroyed within the control volume - the computational domain, in CFD. For an incompressible fluid, where the density must remain constant, the continuity equation is expressed as in 2.4.

$$\frac{\partial \rho}{\partial t} + \nabla \cdot (\rho \mathbf{u}) = 0 \tag{2.3}$$

$$\nabla \cdot \mathbf{u} = 0, \tag{2.4}$$

Here, u is the velocity vector. This relationship states that the net mass flow ($\dot{m}$) entering any control volume must be equal to the mass flow leaving it, satisfying the principle of mass conservation [34].

Moreover, the conservation of momentum is described by the Navier-Stokes equations, that derive from Newton's 2^{nd} law. These equations relate the change of fluid momentum to the forces acting on the fluid; it includes pressure gradients, viscous stresses and external body forces. For an incompressible Newtonian fluid, the momentum equation can be written as represented in equation 2.5.

$$\rho \left(\frac{\partial \mathbf{u}}{\partial t} + (\mathbf{u} \cdot \nabla)\mathbf{u} \right) = -\nabla p + \mu \nabla^2 \mathbf{u} + \rho \mathbf{g} \tag{2.5}$$

In the Navier-Stokes equation, ρ is the fluid density, p is the pressure, μ is the dynamic viscosity and g represents the body force vector, typically associated with gravity. The equation describes how the fluid accelerates under the combined influence of pressure, viscous and external forces [34].

Finally, the conservation of energy is the last governing equation, describing the transport and transformation of energy across the control volume on a fluid mechanics problem. It is mostly relevant for heat transfer applications. In this dissertation, steady state was considered for most cases and, even in transient scenarios, no temperature variations where taken into account, as adding another variable would significantly increase the amount of possibilities to consider. So, that part is not as relevant for this project.

For lots of aerodynamic applications (particularly, those involving railway vehicles) the flow can be considered incompressible, as the operating velocities are well below the speed of sound. Under these conditions, density variations are small and thus have a negligible influence on the flow behaviour. Then, the incompressible form of the Navier-Stokes equations give an appropriate mathematical description for the numerical simulations conducted in the present dissertation.

Nonetheless, the analytical solution of the Navier-Stokes equations is only possible for a limited number of simplified problems, involving ideal geometries and boundary conditions. However, in practical engineering applications, the governing equations are almost always non-linear due to the convective acceleration terms and the complexity of the flow.

Railway problems involve additional challenges, like three-dimensional geometries, turbulent boundary layers, flow separation and transient wakes, making analytical solutions unthinkable [30].

To overcome these limitations, CFD employs numerical discretisation techniques to transform the governing differential equations into a system of equations which can be solved iteratively on a computational mesh. In the Finite Volume Method (FVM), which is adopted by the ANSYS Fluent software, the governing equations are integrated over a finite number of control volumes, ensuring the conservation of mass and momentum within each cell of the computational domain. This approach provides accurate and physically consistent solutions for complex engineering flows while maintaining the conservation properties of the original equations [32].

Even though the continuity and Navier-Stokes equations describe fluid motion completely, the numerical simulation of turbulent flows, present in most engineering applications nowadays, is extremelly challenging. Turbulence remais an enourmous unknown in fluid mechanincs, even today, and it becomes problematic to accuratelly represent it in numerical models [35].

That being the case, additional turbulence models are introduced to estimate the effects of turbulent fluctuations on the flow field, instead of predicting and representing every variation. These modelling approaches, particularly the RANS formulation, are discussed in the following subsection.

2.2.3 Turbulence Modelling

Most engineering problems include flows that are turbulent, characterised by irregular and three-dimensional velocity fluctuations that occur over a wide range of temporal and spatial scales. Compared with laminar flow, turbulence severely increases the transport of mass, momentum and energy, making it one of the most relevant phenomena affecting aerodynamic performance. In railway aerodynamics, turbulence plays a fundamental role in the development of boundary layers, flow separation, wake formation and the generation of unsteady aerodynamic forces acting on the vehicle [35] [30].

The most widely adopted approach in engineering applications is the RANS formulation. In this method, the instantaneous flow variables are decomposed into mean and fluctuating components, based on Reynolds decomposition. Applying this decomposition to the Navier-Stokes equations results in the RANS equations, in which additional terms (known as the Reynolds stresses) appear [36]. These stresses represent the momentum transfer caused by turbulent fluctuations and introduce the turbulence closure problem, requiring additional mathematical models to close the system of equations [30] [31].

Various turbulence models have been developed for RANS simulations, differing in complexity, computational cost and prediction accuracy. Among the most widely used are the k-ε model, the standard k-ω model and the Shear Stress Transport (SST) k-ω model.

The k-ε model provides robust and efficient predictions for fully developed turbulent flows and is widely applied in industrial CFD simulations. However, its performance might deteriorate in flows involving adverse pressure gradients, boundary layer separation or complex near-wall phenomena [35].

The standard k-ω model improves the prediction of near-wall flows by solving the specific dissipation rate instead of the turbulence dissipation rate. This characteristic makes it incredibly suitable for boundary layer calculations, even though its predictions are usually more sensitive to the specification turbulence conditions [35].

Then, to overcome the limitations of both models, the SST k-ω model was developed by Menter, in 1990s. It combines the advantages of the k-ω model (the near-wall accuracy) with the robustness of the k-ε model (in the free stream) using blending functions [37].

The SST k-ω model has become one of the most widely accepted turbulence models for aerodynamic simulations, because of its capability to predict flow separation, adverse pressure gradients and wake development with great accuracy, while maintaining a reasonable computational cost. Numerous studies have proved that it is suited for aerodynamic assessments, including the simulation of railway vehicles operating under crosswinds, tunnel entry conditions and train passing manoeuvres. Consequently, it is frequently recommended for rolling stock aerodynamic investigations and it has become a common choice for engineering analyses involving complex external flows [29].

Even so, alternative turbulence modelling approaches also exist. Large Eddy Simulation (LES) explicitly resolves the larger turbulent structures, while modelling just the smallest scales, providing significantly greater flow detail than RANS models. Hybrid methods, such as Detached Eddy Simulation (DES), combine RANS modelling near solid boundaries with LES in separated flow regions, offering improved predictions of highly unsteady flows. Nevertheless, both LES and DES require significantly greater computational resources than conventional RANS simulations, particularly for flows with high Reynolds number. For this reason, RANS-based turbulence models remain the preferred choice for most industrial railway aerodynamic studies [35].

In that case, using RANS-based turbulence models seemed to be the most logical decision for this work. Among the 3 models described, the k-ε and the SST k-ω would both be used in this project, to assess their differences in the attained results.

2.2.4 Numerical Methods and Mesh Generation

The governing equations of fluid flow cannot generally be solved analytically for practical engineering problems involving complex geometries and turbulent flows. Consequently, CFD relies on numerical methods to transform the partial differential equations into a system of algebraic equations that can be solved iteratively. The accuracy and stability of the numerical solution depend not only on the selected physical models but also on the numerical discretisation technique and the quality of the computational mesh [30] [32].

Among the various numerical methods available, the FVM is the most widely employed approach in commercial CFD software, including ANSYS Fluent. In this method, the computational domain is divided into a finite number of non-overlapping control volumes, and the governing equations are integrated over each individual cell. Therefore, the conservation of mass, momentum and energy is satisfied locally within every control volume, ensuring that the numerical solution preserves the physical laws throughout the domain. The flexibility of the FVM also allows it to be applied to complex 3 geometries commonly encountered in engineering applications [32] [30].

The discretisation of the governing equations requires the approximation of the convective and diffusive terms at the cell faces. Several discretisation schemes have been developed, differing mainly in their numerical accuracy and stability. On the one hand, first-order schemes provide robust solutions, but introduce relatively high numerical diffusion, which might "smooth" important flow structures. On the other hand, second-order schemes improve spatial accuracy and reduce numerical diffusion, allowing a more realistic representation of pressure gradients, boundary layers and wake development. The price to pay is a higher computational effort and a bigger sensitivity to mesh quality. Because of this, second-order discretisation schemes are widely employed in aerodynamic simulations where accurate prediction of complex phenomena is required [31] [38].

Moreover, an equally important aspect of CFD is the generation of an appropriate computational mesh. The mesh defines the spatial resolution of the numerical model and directly influences both the accuracy of the solution and the computational cost. Structured meshes provide high accuracy due to their regular build. Meanwhile, unstructured meshes offer greater flexibility for representing complex geometries. Hybrid meshes, combining different cell types, are frequently adopted to balance mesh quality and computational efficiency. In external aerodynamic simulations, like train aerodynamic assessments, additional refinement is commonly applied near solid surfaces and in regions where large velocity or pressure gradients are expected, ensuring that the relevant flow features are properly represented [30].

In a problem such as this one, regarding aerodynamic efficiency of a train, there are a couple of areas in the domain that should be properly analyzed when generating the mesh. Mainly, the areas around the train should have a finer mesh, not only because more elements usually translates to a better capture of the phenomena and thus better results, but also because using a coarse mesh around these complex geometries might cause a decrease in quality. The same can be said about surrounding areas with troublesome geometries, like the rails, ballasts or platforms. Performing mesh refinement operations is recommended and maintains a higher mesh quality, necessary for good convergence and precise results [28].

The quality of the mesh is a vital factor affecting convergence and the accuracy of the solution. Parameters such as aspect ratio, skewness and orthogonal quality are commonly evaluated to identify poorly shaped cells that may introduce numerical errors or

compromise solver stability.

The aspect ratio is the ratio between the longest and shortest characteristic dimensions of a cell. A lower aspect ratio (as close to 1 as possible) indicates more regular cells, which is desirable. A higher aspect ratio indicates more elongated cells, that can reduce accuracy of the solution [39].

The skewness measures how much a cell deviates from its ideal geometric shape (which can be a tetrahedron, hexahedron...) [40]. So, the skewness should be low, as a higher skewness indicates a distorted cell that can potentially lead to poorer convergence/accuracy [39].

Finally, the orthogonal quality measures how well the cell faces and connecting cell-centre vectors are aligned. Basically, a good orthogonal quality should be close to 1 and as closer as it gets to 0, the worse the mesh is. Low orthogonal quality might cause convergence problems [39].

Mesh independence studies are also performed to verify that further mesh refinement does not produce significant changes in the predicted aerodynamic quantities. Such analyses increase confidence that the numerical results are determined by the underlying physical model rather than by the discretisation of the computational domain [31].

For problems involving relative motion between bodies (like the problem of passing of trains), conventional mesh deformation techniques may lead to excessive cell distortion and deteriorate the quality of the computational mesh. To overcome this limitation, overset mesh methodologies have become increasingly popular. In this approach, independent meshes are generated for the stationary and moving domains and information is exchanged between them through interpolation at the overlapping interfaces. This technique preserves mesh quality during large relative displacements while allowing accurate simulation of transient problems involving moving vehicles, rotating machinery and other dynamic systems. Overset meshes are therefore particularly suitable for railway aerodynamic investigations involving train passing manoeuvres, where the relative motion between vehicles plays a fundamental role in the development of the flow field [41].

The numerical methodology adopted in the present thesis is based mainly on these principles. The governing equations are solved using the FVM implemented in ANSYS Fluent software. During most of the work, steady state was the norm. However, when transient was used and there was relative motion between the railway vehicles, an overset mesh approach was taken.

Combined with the turbulence modelling strategy addressed previously, these techniques give a well-rounded knowledge about the costs, efficiency and accuracy for the aerodynamic simulations to be performed in this work.

2.2.5 Advantages, Limitations and Relevance to Railway Aerodynamics

CFD has become one of the main tools for analysing fluid flow in modern engineering. Continuous developments in numerical methods and resources have allowed increasingly

complex aerodynamic phenomena to be studied with high levels of precision. When compared with experimental techniques, CFD offers immense flexibility, which permits multiple operating conditions and design configurations to be analysed without the need for physical prototypes. This capability has significantly decreased development costs and shortened product design cycles across a wide range of engineering disciplines, including aerospace, automotive and railway engineering [30] [31].

Within railway engineering, CFD has become an essential component of the aerodynamic design process. Numerical simulations are routinely employed to investigate aerodynamic drag and lift, pressure waves, slipstream generation, tunnel aerodynamics,crosswind stability and the transient interaction between passing trains and their surroundings. In addition to providing aerodynamic force coefficients, CFD enables visualisation of pressure and velocity distributions, as well as vortex structures and wake development, providing valuable insight that might be difficult to attain through experimental measurements [29].

One of the greatest advantages of CFD is the ability to analyse highly transient flow phenomena under controlled and repeatable conditions. Parameters like train speed and geometry and environmental conditions can be altered independently, allowing systematic investigations to be performed in a much easier fashion than full-scale tests. Furthermore, numerical simulations give access to the flow field across the computational domain, enabling the extraction of local variables at any time and position during the simulation [25].

In spite of these advantages, numerical simulations still carry several limitations. The accuracy of CFD simulations depends heavily on the quality of the computational mesh, the selection of appropriate turbulence models and discretisation methods and the adoption of realistic boundary for the solution process. Additionally, turbulence models involve assumptions that introduce a certain degree of approximation to the solution; at the same time, insufficient mesh resolution or inappropriate solver settings will lead to errors or convergence difficulties. Consequently, CFD results should always be interpreted having in ming the modelling assumptions employed and, whenever possible, validated against reliable experimental data [35] [30].

International standards and engineering best practices recognise the complementary nature of numerical and experimental approaches. Although experimental measurements remain the primary reference for certification, validated CFD models have become indispensable during the design and optimisation stages of railway vehicle development. Their ability to reduce development costs while providing detailed information regarding complex flow structures has made CFD a standard engineering tool in both industrial and academic research [23].

2.3 Computational Fluid Dynamics on Railway Aerodynamics

2.3.1 Development of CFD in Railway Aerodynamics

The application of CFD to railway engineering has increased considerably recently. The first investigations of railway aerodynamics relied almost exclusively on reduced-scale wind tunnel and full-scale experiments due to the limited computational resources available at the time. Although these experimental techniques provided valuable aerodynamic data, they were often expensive, time-consuming and restricted to a limited number of operating conditions. The continuous growth of computational power, together with significant advances in numerical algorithms and turbulence modelling, has enabled CFD to become a fundamental tool in the aerodynamic design and analysis of railway vehicles [22] [30].

Initially, numerical simulations were mainly employed to estimate global aerodynamic quantities such as drag and lift coefficients under steady operating conditions. Improvements in computational capabilities subsequently allowed increasingly sophisticated analyses involving transient flow phenomena, complex vehicle geometries and realistic operating scenarios. Modern CFD techniques are now routinely applied to investigate wake development, flow separation, pressure fluctuations, tunnel entry and exit, crosswind stability, slipstream generation and aerodynamic interactions between multiple railway vehicles [29].

One of the principal advantages of CFD in railway aerodynamics is the ability to obtain detailed information regarding the complete flow field surrounding the vehicle. Unlike experimental techniques, generally limited to measurements at specific locations, CFD simulations provide spatial and temporal distributions of velocity and pressure, as well as turbulence quantities, throughout the computational domain. This allows engineers to identify the mechanisms contributing to the aerodynamic loads and then proceed to evaluate design modifications before manufacturing physical prototypes [30].

Furthermore, the development of increasingly better and more robust turbulence models has naturally contributed to the adoption of CFD within the railway industry. RANS models, in particular, the SST k-ω turbulence model remain the most commonly used approach because they provide the best compromise between computational cost and prediction accuracy. They have demonstrated good performances for external aerodynamic applications involving flow separation, making them some of the most used models for train aerodynamic investigations [37].

Recent updates in numerical methodologies have expanded even further the capacities of CFD. Dynamic mesh techniques, sliding meshes and overset mesh methods now enable the accurate simulation of moving bodies and transient aerodynamic interactions, including train passing manoeuvres and overtaking events. These approaches overcome many of the limitations associated with stationary computational domains while maintaining

good mesh quality throughout the simulation. This has resulted in CFD becoming an indispensable tool for analysing complex railway aerodynamic events that would otherwise require extensive and expensive experimental testing [42].

Despite these advances, numerical simulations continue to require careful validation to ensure reliable predictions. International standards, namely the EN 14067 norm, recommend that CFD results should be validated against experimental measurements whenever possible before being employed for engineering design assessment. Consequently, modern railway aerodynamic investigations increasingly combine numerical simulations with wind tunnel experiments and full-scale testing to exploit the complementary advantages of each methodology [23].

Today, CFD represents one of the principal engineering tools for the aerodynamic analysis of railway vehicles. Its ability to investigate complex transient flows, evaluate multiple operating conditions and provide detailed flow visualisation has made it an essential component of modern railway vehicle development. The following subsections review the principal railway aerodynamic applications investigated using CFD, with particular emphasis on studies related to high-speed train aerodynamics and train passing manoeuvres.

2.3.2 Aerodynamic Flow Around Trains

Drag is the most significant resistive force acting on railway vehicles, particularly, at elevated velocities. While rolling resistance dominates at low speeds, the aerodynamic contribution increases (approximately) with the square of the train speed, which causes the power required for propulsion to rise substantially as circulation velocity increases. Consequently, aerodynamic optimisation has become an essential aspect of modern vehicle design, not just in railway, as it directly influences energy consumption and, as a result, operating costs and environmental sustainability [43] [44].

The flow around a railway vehicle is characterised by separated flow regions and large wakes. As the train moves through the air surrounding it, a stagnation region develops at the nose, producing high pressure at the leading edge. The flow then accelerates around the body, generating boundary layers that develop along the train length. Depending on the geometry and operating conditions, these layers may separate from the surface, resulting in vortexes that contribute to pressure drag and wake formation [22].

The aerodynamic performance of a vehicle is heavily impacted by its external geometry. The design of the nose, roof, underbody and tail sections plays a major role in determining the pressure distribution around the vehicle and the resulting aerodynamic forces. Streamlined nose geometries reduce the drag and flow separation; meanwhile, smooth transitions between vehicle components bring the generation of large-scale vortices to a minimum. In the same fashion, the optimisation of the train tail is essential for reducing wake size and improving pressure recovery, decreasing overall aerodynamic resistance [29].

The underbody region contributes largely to railway aerodynamics. Components such as bogies, wheelsets and other equipment mounted underneath the vehicle generate highly

turbulent flow structures that interact with the surrounding boundary layer. These interactions increase aerodynamic drag and influence the development of the train wake. Several papers, such as this one from Dong et al. [45], have studied the impact of the accuracy of the geometry representation in the attained aerodynamic results. They have shown that the inclusion of realistic underbody geometries can considerably impact the predicted coefficients, highlighting the importance of precise geometric representation in numerical simulations [29].

CFD is now an essential tool for analysing these aerodynamic phenomena. Modern CFD techniques enable engineers to evaluate pressure distributions, streamline patterns, velocity fields and turbulent wake structures with a level of detail that is difficult to obtain experimentally. Such information is particularly valuable during the design process, allowing multiple geometric configurations to be tested before prototype manufacturing. Consequently, CFD has become an integral part of railway vehicle development, complementing both wind tunnel experiments and full-scale testing [30].

Like previously mentioned,the accuracy of numerical predictions depends on several modelling choices, including the computational mesh, turbulence model and boundary conditions. Numerous studies have demonstrated that RANS simulations employing the SST k-ω turbulence model provide a satisfactory compromise between computational cost and prediction accuracy for external railway aerodynamics. Although higher credibility approaches such as LES are capable of resolving a greater range of turbulent structures, their computational requirements remain impeditive for many rolling stock engineering applications [37] [35].

Beyond reducing aerodynamic drag, the understanding of external flow around railway vehicles is fundamental for investigating more complex aerodynamic events. Pressure distributions generated along the vehicle surface directly influence crosswind stability and safe circulation; tunnel pressure waves and slipstream development are other interesting topics that can also be interpreted using CFD software such as ANSYS Fluent. Consequently, research on train aerodynamics has progressively evolved from the analysis of isolated vehicles towards the investigation of increasingly complex operational scenarios involving multiple interacting flow fields [29].

The present dissertation builds upon these developments by focusing on some of the most challenging aerodynamic problems in railway engineering: the circulation under the presence of strong headwinds, crosswind stability and the interaction between two passing vehicles. The knowledge gained from previous investigations on external train aerodynamics provides the theoretical foundation for understanding the pressure variations, boundary layer interactions and aerodynamic force fluctuations analysed in the following sections.

2.3.3 Crosswind Aerodynamics

Among the various aerodynamic phenomena that affect railway vehicles, crosswinds represent one of the biggest safety concerns, in particular for high-speed trains operating

on exposed sections of the track. Winds coming from the side generate aerodynamic lateral forces, lift forces and rolling moments that may reduce wheel-to-rail contact forces and, in extreme situations, cause the vehicle to overturn. As train operating speeds have continued to increase, crosswind stability has become a major consideration during both vehicle design and certification, motivating extensive experimental and numerical research over the years [29] [6].

The aerodynamic response of a train under crosswind conditions depends on several factors, including train geometry, wind and vehicle velocity, yaw angle and surrounding infrastructure. Flow separation occurring on the leeward (the side that faces away from the wind) side of the vehicle generates complex three-dimensional vortexes, producing highly asymmetric pressure distributions over the surface. These pressure variations are responsible for the aerodynamic loads acting on the vehicle and play a fundamental role in determining its stability [22] [28].

Nowadays, CFD is one of the most valuable tools for investigating said aerodynamic phenomena, enabling the analysis of a wide range of wind conditions and vehicle configurations, while providing detailed information regarding the flow impact on the vehicle. The successful application of numerical methods to solve this challenging problem in recent projects has boosted confidence in their use for investigating other aerodynamic problems. Consequently, crosswind assessments are playing a major role in establishing CFD as a reliable source of investigation for railway aerodynamic studies.

More often than not, CFD is used to perform aerodynamic tests in motorcycles and cars. There is not such a bigger literature concerning the use of numerical methods on trains, but it has been constatly updated, even though a lot of issues are still untouched [28].

The EN 14067-6 states some simulation requirements for crosswind studies. However, the methodology used is not imposed, and can greatly vary; for this reason, it relevant, in a study such as this one, to list the key parameters used during the numerical process to ensure a credible comparison and analysis of results [46] [28]. So, a good explanation on how the geometry and mesh were conceived, as well as a description of the simulation parameters like the turbulence models and discretisation methods is due. For most cases, to accommodate the whole set of yaw angles, the train is modeled and rotated inside the domain, to match the incidence of the wind.

According to some relevant researches on the topic, CFD is has a really great coverage of the aerodynamic phenomena and provides pretty accurate results; until yaw angles equal to 50°. As stated by Paradot et al. [47], who performed numerical simulations on the TGV Duplex, until that point, the simulations converged somewhat smoothly, and presented realistic and comparable results.

Then, at larger yaw angles, starting from around 60°, larger errors and convergence problems begin to happen. That is why several studies do not cover the whole spectrum

from 0 to 90 degrees. Looking at the work performed by Szudarek et al. [28] in said research, they looked at eleven crosswinds studies, from which only two covered the full range of angles, with some stopping at around 30° before moving to wind tunnel experiments like Gallagher et al. [48].

However, the investigation by Bocciolone et al. [49], showed maximum values of lateral forces being registered at around 70°, so that is still a relevant part of the spectrum. The instability of RANS turbulence models in this particular scenario is a handicap in CFD analysis. Even so, it is possible to conceive a study over the full set of angles; only with the acknowledgement that some values might need other sort of validation and scrutiny [28].

Several studies show the relevance of the mesh parameterization and quality to the final results [28] [50]. Not just the refinement and element sizing, but also the sharpening or smoothing of the edges and complex geometries can affect the results. Truth is that, the more realistic the geometry, the fairer the results will be. At the same time, it will mean a bigger computational effort, so it is mandatory to find the middle ground that allows for a valid solution with an affordable financial and time cost.

Some investigations, like Li et al. [51] studied the impact of the turbulence models on the crosswind assessment of railway vehicles. It kept the yaw angle stable at 30° and at a high Reynolds number and changed from several RANS turbulence models, testing on the inter-city express 2 (the ICE). In agreement with what had been previously found in general literature and order full-scale studies, SST $k-\omega$ was the best in terms of agreement and comparison with the validated results.

Others decided to flee from the common approach and try other turbulence models. Maleki et al. [52] compared RANS with other models (Unsteady Reynolds-Averaged Navier–Stokes (URANS), Embedded Large Eddy Simulation (ELES) and Scale-Adaptive Simulation (SAS)) to see what impact it had on the results. The main conclusions were that URANS was interesting for unsteady flows, SAS is good for flows with larger vortices or wakes and ELES (a hybrid between RANS and LES) is also a solid option for its combined qualities. Nevertheless, in the present disseration, RANS turbulence models had already a large enough room for investigation, and came with a much lighter computational effort.

There are still hundreds of papers that could be included in the present literature review; only the most relevant for this project were mentioned. From the catalogued ones, it can be concluded that there is still room for investigation in this topic.

Basically, this part presentes itself as a review on what considerations should be had, what troubles and findings other scientists/engineers had and what room for further investigation there is. This way, it was plausible to begin the crosswind study of the Portuguese train, knowing that analysing the difference the simulation parameters would produce in the results and how the crosswind characteristic curve would be are some of the most relevant outcomes of this work.

So, this dissertation can not only be an element of validation for the *TrainSolutions Portugal* train model as well as a contribution to the engineering discipline in the field of railway vehicles aerodynamics using CFD.

2.3.4 Train Passing Aerodynamics

The aerodynamic interaction between two passing trains is one of the most complex transient flow phenomena encountered in railway engineering. During a passing manoeuvre, the relative motion between the vehicles produces rapidly changing pressure fields, strong flow acceleration within the gap separating the trains, wake interactions and significant variations in the aerodynamic forces acting on each vehicle. These transient effects influence passenger comfort, structural loading and operational safety, particularly for high-speed trains operating with small lateral clearances. As railway operating speeds continue to increase, understanding the aerodynamic characteristics of train passing events has become an important research topic in both academia and industry [53].

The first investigations into train passing aerodynamics were primarily based on full-scale measurements. These studies demonstrated that the highest pressure values generally occur when the noses of the two trains meet [54]. The resulting pressure pulses propagate along the vehicle surfaces, producing transient aerodynamic loads that differ significantly from those observed during steady operation. Experimental campaigns also showed that the magnitude of these loads depends on the train geometry, operating speed, lateral separation distance and surrounding infrastructure [53] [23].

Although experimental methods remain essential for validation and certification, they present several practical limitations. Full-scale testing requires dedicated railway infrastructure and favourable environmental conditions (besides being costly and time consuming), while wind tunnel experiments remain incredibly difficult to perform (due to the movement relative to the ground) and often require geometrical simplifications and scaling procedures [53]. These constraints have motivated the increasing use of CFD as a complementary tool capable of reproducing train passing manoeuvres under controlled numerical conditions [29].

The first CFD investigations on the topic were limited to simplified 2D geometries and steady-state simulations due to the restricted computational resources available back then. As computational capabilities grew more advanced, researchers began employing 3D transient simulations capable of solving the highly unsteady flow structures generated during these events. These studies demonstrated that numerical methods could successfully reproduce the principal aerodynamic phenomena observed experimentally, including pressure fluctuations, wake interactions and transient force histories [29].

The paper published by Fujii and Ogawa in 1995 [53] was among the earliest CFD investigations of train passing manoeuvres that remains relevant today. They tested two vehicles crossing inside a tunnel at a velocity of 270 km/h. In this study, a Fortified

Solution Algorithm (FSA) interface scheme is employed to handle the moving bodies in the domain and so the mesh is divided into four separate zones.

Furthermore, the evolution of the force coefficients under the x, y and z axis were also monitorized over the whole event. They are a representation of drag (C_D) or lift (C_L) coefficients over said directions, which are the dimensionless measures of drag (aerodynamic resistive force acting parallel and opposite to the direction of motion) and lift (aerodynamic force acting perpendicular to the direction of motion) forces.

Mathematically, drag and lift coefficients are calculated as shown in 2.6 and 2.7, respectively [34].

$$C_D = \frac{F_D}{\frac{1}{2}\rho V^2 A} \tag{2.6}$$

$$C_L = \frac{F_L}{\frac{1}{2}\rho V^2 A} \tag{2.7}$$

C_x corresponds to the drag coefficient, C_z to the lift coefficient and C_y (although, techically, it is also a lift coefficient for being in a direction perpendicular to the flow) is the lateral force coefficient.

Another important topic that it introduces is the fact that the dimensions of the vehicles must be normalized in order to permit a valid comparison and analysis of results. ANSYS Fluent software already possesses a feature that does that calculation automatically.

To this day, this work is still cited in the literature review of many CFD studies of railway vehicles, demonstrating that it kept its relevance, and the results attained are corroborated by newer investigations with more robust computational methods.

The effects of the passage of a train are felt not just in the passing of two vehicles. As reported by Rocchi et al. [55], it produces an air flow that pushes both people and objects nearby which can be studied in order to optimise the desing of both the vehicle and the infrastructure. These "wind loads" are the result of masses of air being dragged by the train. This work emphasizes the importance of paying attention to this kind of details by mentioning some accidents (such as windows breaking and track damage) caused by the wind loads associated with train passage.

This particular article foccused on studying the effects of the passage of one train in open air on its surroundings, not a passing of two vehicles. Nonetheless, it is still worth mentioning, as it gave predicitons about the slipstreams and wake created that can be extrapolated for other cases. Not only that, it also mentions the existence of three zones in the fluid flow (an inviscid zone around the nose, turbulent and unsteady along the train profile and a large turbulent wake behind its rear). When two vehicles pass by each other, what happens is an overlap of these profiles that will produce pressure distributions which will produce aerodynamic forces on the bodies [55].

While most CFD studies use the SST or the standard $k-\omega$ turbulence model, Li et al. [56] instead went for the RNG $k-\epsilon$. Their study considered a passing manoeuvre of two trains moving at 350 km/h in a shield tunnel. A small-scale experiment, comparable to a wind tunnel was conceived using a dynamic model. This allowed for a comparison between this model and the numerical method and there was a big correlation between the data.

Both curves of pressure coefficients (a dimensionless measure of local pressure, calculated as in 2.8, where p is the local static pressure and the other variables are the pressure, density and velocity of the stream) presented a zone of high pressure as the trains came closer, followed by a suction zone (negative pressures pushing the trains appart) and finally the pressure rises again and stabilizes as the trains move away from one another. There was a big overlap of the attained results, particularly during the first half of the manoeuvre. Other investigations showed similar characteristic curves, both for the pass-by of a singular train [55] and two trains passing each other [53].

$$C_p = \frac{p - p_\infty}{\frac{1}{2}\rho_\infty V_\infty^2} \tag{2.8}$$

Hu et al. [57] also made remarkable progress in the field. This work analyzed the passing manoeuvre under the effect of crosswinds, and even performed simulations under different yaw angles. It produced results with good repeatability and proved that the train on the windward side shielded the one on the leeward side from the crosswinds. Some patterns previously encountered were met here as well.

There are more interesting works, Duan et al. [58] studied the influence that, not just of speed, but line spacing as well, had on the train passage. This is relevant for the *TrainSolutions Portugal* project as the track distance, defined by the norm, will be input in the simulations and, according to said work, the smaller the gap, the bigger the aerodynamic effects. That can decide whether the existing infrastructure is suited or not for a new model in circulation.

Other interesting article was written by Kwon et al. [59]. It tests the passing of vehicles and different conditions and mentions the importance of validation of the solution. As results, it presents the values of pressure coefficients and pressure distributions on the bodies durint the passing manoeuvre, in order to conclude where and when the maximum lateral forces would be, in order to assess stability.

This study discretizes the values of time step and mesh element size to mention the importance of keeping the Courant number below 1 in the simulation. The Courant number (Co) or CFL (Courant–Friedrichs–Lewy) number is a dimensionless parameter used in numerical fluid dynamics that correlates the flow velocity, time step size and mesh cell size. It is calculated according to 2.9 (u being the fluid velocity, Δt the time step and Δx the mesh element size) and it should always be lower than the unity; a Courant number bigger than 1 means the fluid travels more than one cell per time step, causing

instability in the solving process [60].

$$Co = \frac{u\Delta t}{\Delta x} \tag{2.9}$$

So, this parameter is something that must be taken into consideration when conceiving the configuration for the transient simulations.

In summary, one of the principal challenges associated with train passing CFD simulations is the representation of the relative motion between the vehicles. Several numerical approaches have been proposed to address this problem. Sliding mesh techniques divide the computational domain into moving and stationary regions separated by interfaces through which flow information is exchanged. Although this methodology has proven effective for many engineering applications, it may become less efficient when large relative displacements are involved. More recently, overset mesh techniques have gained increasing popularity because they allow independent meshes to move relative to one another while maintaining high mesh quality throughout the simulation. Information is exchanged between overlapping mesh regions through interpolation, making overset methodologies particularly suitable for modelling train passing manoeuvres involving long travel distances.

The choice of turbulence model also plays a significant role in the prediction of train passing aerodynamics. RANS simulations remain the most widely employed approach because they provide satisfactory predictions of the global aerodynamic loads while maintaining reasonable computational costs. In particular, the SST k-ω turbulence model has demonstrated good performance in capturing boundary layer development, flow separation and wake evolution around railway vehicles. Higher accuracy methods such as LES provide more detailed representations of transient vortex structures but require substantially greater computational resources, limiting their routine application to full-scale engineering analyses.

Several recent numerical investigations have demonstrated the capability of CFD to predict the transient pressure histories generated during train passing events with good agreement when compared with experimental measurements. These studies have analysed the influence of train speed, lateral spacing, vehicle geometry and operating conditions on the resulting aerodynamic loads. In general, increasing the relative speed between the trains leads to larger pressure fluctuations and greater transient aerodynamic forces, while increasing the lateral separation distance reduces the intensity of the aerodynamic interaction. The optimisation of train nose geometry has also been shown to reduce pressure peaks generated during passing manoeuvres, contributing to improved passenger comfort and reduced structural loading.

Despite the considerable progress achieved in recent years, train passing aerodynamics remains an active area of research. The continuous increase in railway operating speeds, together with the development of new vehicle configurations and aerodynamic optimi-

sation strategies, requires increasingly more accurate numerical methodologies capable of reproducing complex transient flow phenomena. Furthermore, relatively few studies have investigated aerodynamic interactions involving modern railway vehicles using overset mesh techniques under realistic operating conditions. Continued research is therefore essential to improve the understanding of these highly transient aerodynamic processes and to support the development of safer and more energy-efficient railway transportation systems.

2.3.5 Summary and Research Gap

The literature reviewed in this chapter demonstrates that railway aerodynamics has become an increasingly important research field as train operating speeds continue to rise. Together, experimental testing and numerical simulation have become complementary tools for the aerodynamic assessment and optimisation of modern railway vehicles [48].

This revision of CFD fundamentals highlights the capacity of modern numerical methods to predict the flow behaviour around railway vehicles with a satisfactory relation between computational cost and accuracy. In particular, RANS simulations with the SST k-ω turbulence model remain the preferable approach for many industrial applications as well as academia, offering reliable predictions of aerodynamic forces and pressure gradients [52] [51].

The literature has also shown that CFD has been successfully applied to a variety of train aerodynamic problems, including circulation under crosswinds and train crossing manoeuvres. Improvements in numerical methodologies, in particular moving mesh techniques such as sliding and overset meshes, have enhanced the ability of CFD to reproduce transient aerodynamic phenomena involving relative motion between vehicles and their surroundings. Moreover, various certified studies have demonstrated solid correlation between numerical predictions and experimental measurements, further increasing confidence in the application of CFD as a design tool for engineering in the railway field [42] [48].

Despite these advances, several challenges remain. The transient nature of train passing manoeuvres generates complex three-dimensional flow structures, rapidly varying pressure fields and strong wake interactions that are still difficult to capture accurately. The selection of appropriate turbulence models, mesh resolution and numerical methodologies continues to influence the quality of the predicted aerodynamic loads, while the computational cost associated with credible simulations remains a significant limitation. Consequently, further research is required to improve both the efficiency and accuracy of numerical approaches for transient aerodynamic analyses.

Although numerous studies have investigated the aerodynamics of high-speed trains using CFD, considerably fewer have focused on this topic (due to its complexity), in particular using overset mesh methodologies under realistic operating conditions. Moreover, much of the existing literature is based on generic train geometries or internationally

recognised high-speed train models, whereas limited information is available regarding the aerodynamic behaviour of newer designs. This highlights the need for additional numerical investigations capable of supporting the development of future railway vehicles and complementing present experimental knowledge. So, having a completely new desgin, it is really interesting to test it and confront it with previous research.

Motivated by these observations, the present dissertation investigates some of the most important and complex aerodynamic phenomena in the *TrainSolutions Portugal* model resorting to CFD simulations performed in ANSYS Fluent, an area with still much room to grow in the field.

The study aims to analyse the evolution of pressure distributions, wake structures and aerodynamic forces during strong headwinds and crosswinds, and then assess the stability during train passing manouvers, in order to have a first certification study of the Portuguese train. Other than that, there is hope to increase the understanding of transient railway aerodynamics and provide additional insight into the application of CFD for the analysis of modern railway vehicles.

Chapter 3

Headwinds and Model Testing

The first weeks of the work were dedicated to fully grasping the problem and understanding what needed to be done. So, after learning the basic concepts of ANSYS Fluent software, completing the literature review on the topic and being assigned the first tasks of the project, it was time to get a geometry of the CP model train and begin preparing the first simulations.

As mentioned earlier in chapter 1, there are many situations that must be investigated before a railway vehicle can initiate commercial activities.

Furthermore, the results attained need validation. Usually, developers take previous tests or simulations on the same model or similar ones [46] [61]. However, in this case, there was no such thing, as this project is recent and there were no other similar results from which it would be reasonable to extrapolate and compare with the ones from this thesis.

Then, it was decided to run CFD simulations of the simpler event that is still relevant to an aerodynamic assessment - circulation under strong headwinds - and compare the results with benchmark experiments presented in the standards.

In that case, after an initial phase of experimenting different testing configurations for the *TrainSolutions* model, these were replicated to the ICE model, whose results are present in the EN 14067-6 norm [6]. Then, it would be possible to get different results from different configurations for the CP model and, by seeing which configuration performed better in reaching similar results to those in the norm for the ICE model, assume that these results are somewhat closer to reality and more trustworthy.

3.1 Train Geometry

The train will have 3 different types of passangers carriages. However, for this study, only the first will be considered, as that makes it easier in terms of computational effort while maintaining most of the interest in terms of data analysis - since the first carriage is the most critical in terms of aerodynamics.

CP's new train is set to circulate at speeds up to 200 km/h. In most cases, that is the velocity which shall be tested, since it is likely that if any troubles where to occur it would be at higher speed transit. Figure 3.1 shows this model once more.



Figure 3.1: First preview of the "portuguese train" [5].

Its first carriage has a length of approximately 25.7 meters and a height of 4.3 meters. It is 3 meters wide and its front area is around 11.8 m^2. Figures 3.3 and 3.2 show the dimensions of the model. For the headwind simulations, the train was modeled with the wheels and bogies, and the rail and ballast were also represented.

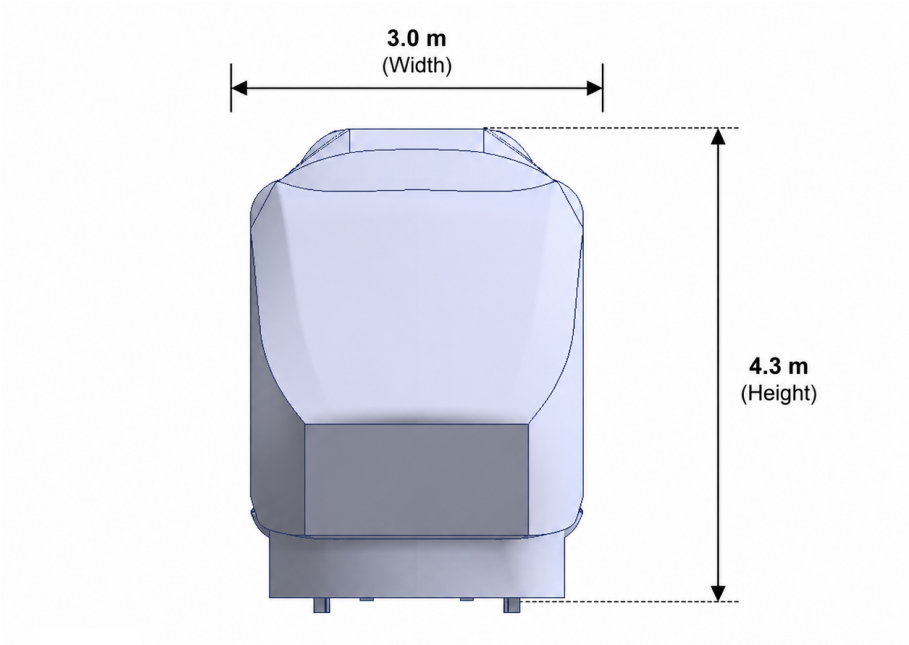


Figure 3.2: Front view of the first carriage of *TrainSolutions*'s model.

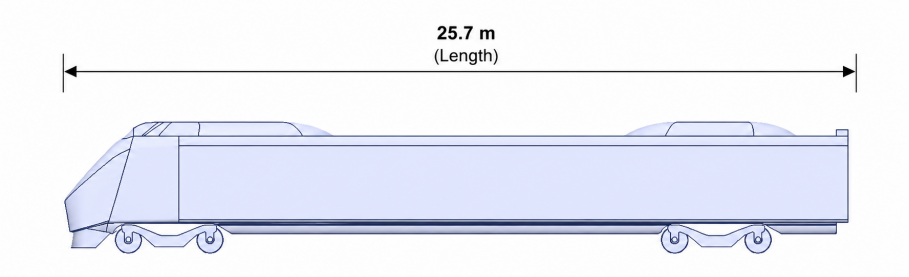


Figure 3.3: Side view of the first carriage of *TrainSolutions*'s model.

A quick look at the geometry shows it is nothing out of the ordinary. The mais points of interest (in terms of numerical simulations) might be the wheels and the bogies - where it could be hard to generate consist elements - and the features on the front and rear which should heavily influence drag and lift forces.

3.2 Headwind Simulations

This study was conducted for yaw angles (β) of 0° - headwind - and a relative velocity of 80 m/s. This speed, although higher than usual for similar studies, was chosen for 2 main reasons.

Firstly, it is the one used in the EN 14067-6 norm for the ICE. So, in order to have a better mean of comparison, it was decided to keep the same wind speed, to have one less variable affecting the results. Second, the relative velocity is the sum of the moving vehicle speed plus the wind speed (since the angle is 0°). The maximum speed of the Portuguese train is around 200 km/h (55.5 m/s) and, assuming a wind speed of around 90 km/h (24.5 m/s), we obtain the 80 m/s. These values of wind velocity are much higher than regular for Portugal and circulation usually ceases (or happens under controled conditions) for such stormy weather; however, it is better to validate the solution for a more extreme scenario and, for the sake of simplicity, the 80 m/s were selected.

Furthermore, the fluid flow happens at an elevated velocity so the Reynolds number is very high (larger than 10^5); meaning that dynamic changes have little impact in the aerodynamic coefficients [62], so it can be manipulated to facilitate the calculations. This also indicates that the 80 m/s can be used to correlate with the benchmark results and no significant fluctuations will be noted.

Finally, it was important to create the domain for the numerical simulation. Taking advantage of the simulation of the flow (since it is a 0° angle), it was possible to halve the volume (with a symmetry along the length of the train) to allow for a finer mesh with the same computational effort.

The domain consists of a rectangular prism, with each dimension being determined by the height of the vehicle. Literature states the distance from the front of the domain to the tip of the train should be at least 10 times the height, to allow for the flow to fully

develop; that same measurement should be applied to the height of the domain, from the floor to the "roof" of the prism. The width of the domain should be 20 times the height, so, in this case, 10 times, since a longitudinal symmetry is applied. Finally, behind the rear of the vehicle, at least 30 times the height should be left just for the wake to develop completely, so it is certain that the flow is fully captured [63].

Table 3.1 and the figures 3.4 and 3.5 present the dimensions of the domain. This volume is not too small that it would not represent important characteristics of the flow while not being unnecessarily big that it ends up taking too much of a computational effort to solve.

	Front	Rear	Height	Width
Relation to the Heigth	10H	30H	10H	10H
Length	43m	129m	43m	43m

Table 3.1: Dimensions of the domain.

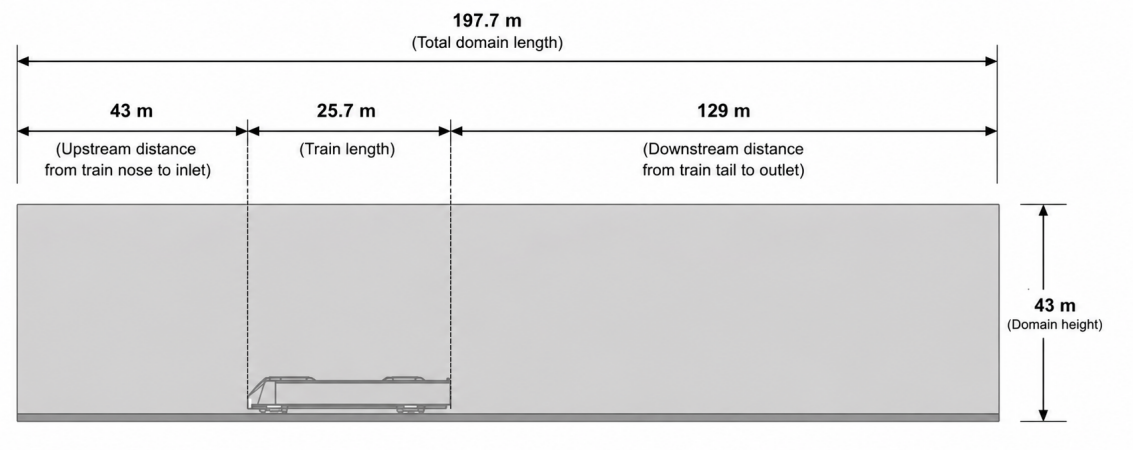


Figure 3.4: Side view of the computational domain.

The axis system of the simulations is presented in figure 3.6. The x axis follows the length of the train (meaning C_x is the drag coefficient).



Figure 3.6: Axis system.

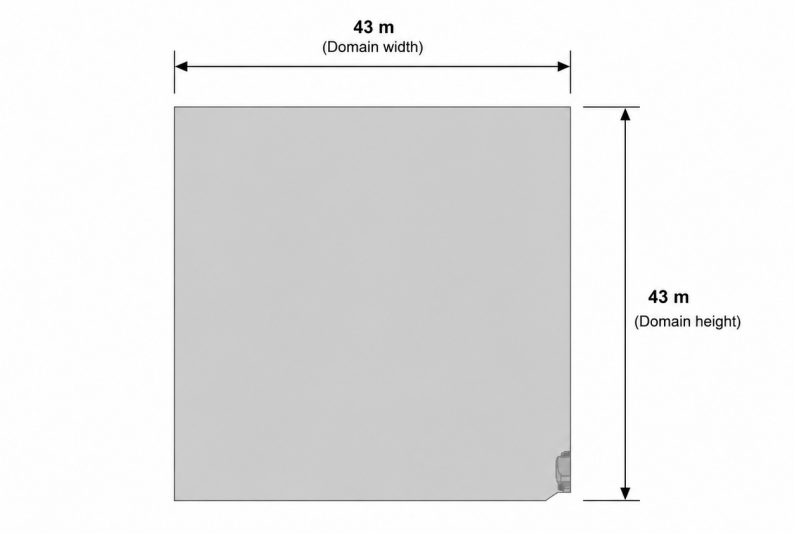


Figure 3.5: Front view of the computational domain.

3.2.1 Mesh Generation

Then, it was time to proceed to the mesh generation. This is a delicate and time consuming task of the project.

The domain is immense; nevertheless, it is necessary in order to fully capture the air flow. In these circumstances, it is not plausible to have the same element size across the whole domain. So, a smaller volume was created, for a finer mesh to exist (naturally, closer to the train) whereas the rest of the domain keeps a coarser mesh, since it is only to allow the flow to develop and no significant changes are expected [61] [63]. Consulting other similar works, and taking into account the singularities of this one, the dimensions of the smaller volume were decided and are presented in table 3.2 while figures 3.7 and 3.8 show the size of the second volume.

Moreover, with these 2 different volumes and with the diverse functionalities of ANSYS Meshing, it was possible to create a large number of mesh configurations by experimenting distinct parameter combinations.

So, to test how much the mesh refinement would impact the results, 5 separate meshes were conceived. They were all created in the same logic, just with different element sizes and element growth rates.

First, the element size (Δx) for the main volume was selected. It decreased with each new mesh. Then, a body sizing by Body of Influence (BoI) was created (in the smaller

	Front	Rear	Height	Width
Relation to the Heigth	4H	12H	1.75H	1.25H
Length	17.5m	52m	7.6m	5.4m

Table 3.2: Dimensions of the smaller volume of the domain.

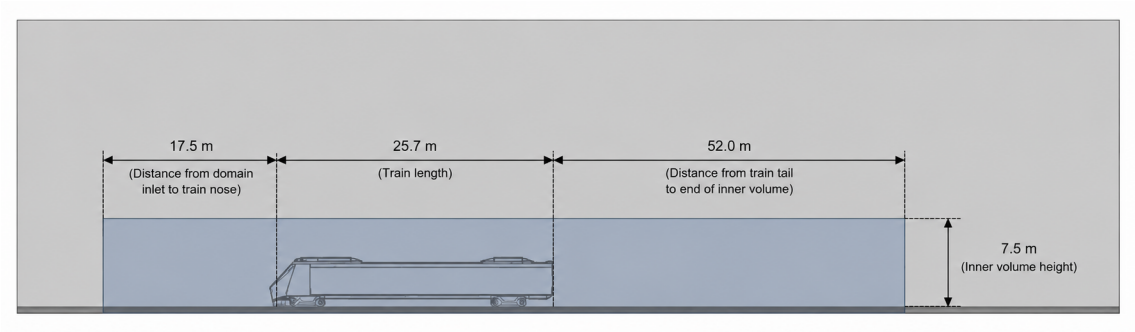


Figure 3.7: Side view of the smaller volume of the domain.

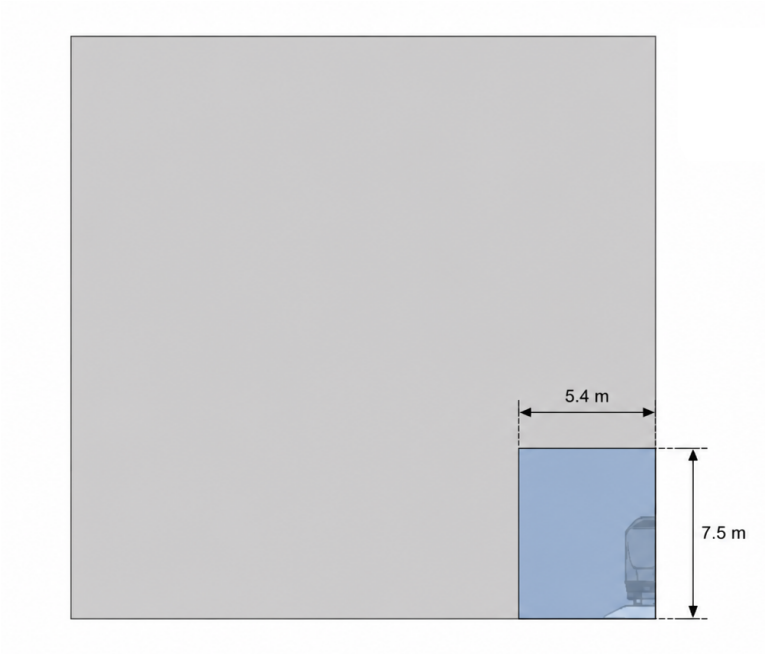


Figure 3.8: Front view of the smaller volume of the domain.

domain) where the element size is reduced, to have better accuracy closer to the train. Once more, all meshes have a different element size for the BoI and they may also vary in terms of growth rate - a parameter which defines how quickly the size of adjacent cells increases as you move away from regions of refinement. Furthermore, a face sizing was created near the rail surface, to ensure smaller elements in that region; for having a complex region (and being near the bogies and wheels) a coarse mesh could lead to bad aspect ratio and complicate convergence.

Table 3.3 shows the values used for each individual mesh and how many elements compose them. It varies from around 2 to 8 million elements.

Mesh	Δx	Δx **(BoI and face sizing)**	**Growth Rate**	**Number of Elements**
Mesh 1	1.8m	0.5m	1.2	2 146 814
Mesh 2	1.5m	0.4m	1.2	2 878 081
Mesh 3	1.4m	0.4m	1.14	4 379 833
Mesh 4	1.35m	0.4m	1.1	6 844 063
Mesh 5	1.2m	0.35m	1.1	8 398 967

Table 3.3: Size parameters for the 5 different meshes.

Naturally, it is expected that the finer meshes will provide better and more accurate results. The goal is to evaluate how much better these results are, compared to how much is the increase in the necessary computational effort. With this investigation, it is possible to find a "sweet spot" where a reasonable computational cost is met with an accurate solution.

Moreover, some other tweaks were tested, but all were abandoned, as they did not improve the overall performance of the simulation. First, a third layer between the existing two was tested, to allow for a smoother transition, but it spiked the element number so much that the simulation took too long to converge, and it had a similar effect to decreasing the growth rate. Next, a refinement near the rails (instead of face sizing) was experimented, but it made some cells near it have terrible values of aspect ratio, which affected the values of pressure near the train, disrupting the results. Finally, all of these meshes are tetrahedral; polyhedral meshes were considered but abandoned because of the complexity associated with it for such an early stage of the work.

Figures 3.9, 3.10 and 3.11 show mesh number 5 (the one with the smaller element size) from the symmetry plan with different proximities; first, the whole mesh, then a zoom-in to see the separation zone and finally a closer look at the cells around the train. Figures 3.12 and 3.13 illustrate the mesh from a section plane.

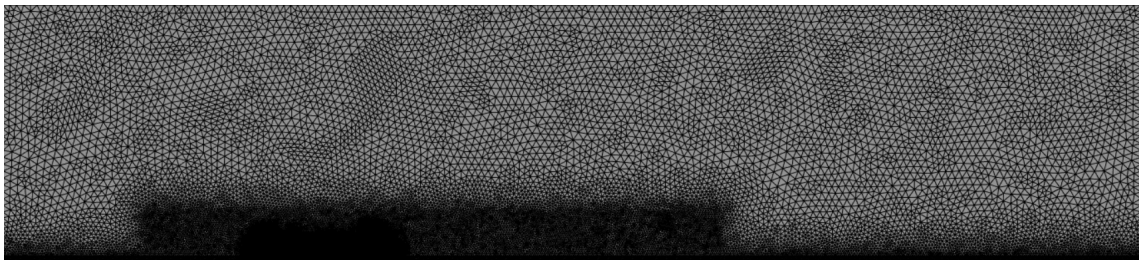


Figure 3.9: View of the finest mesh from the symmetry plan.

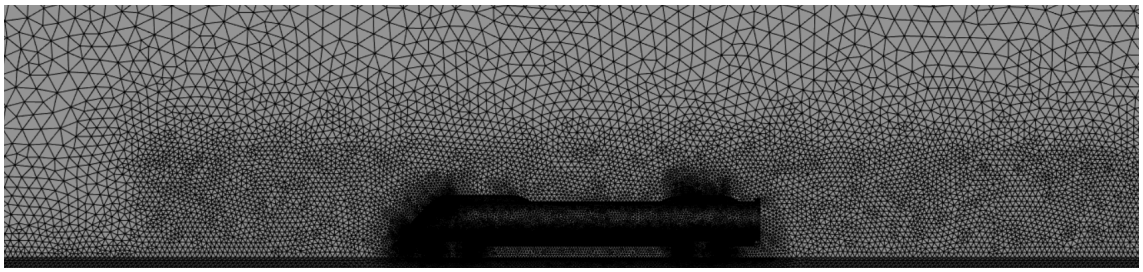


Figure 3.10: Closer view of the finest mesh from the symmetry plan, focusing on the separation zone.

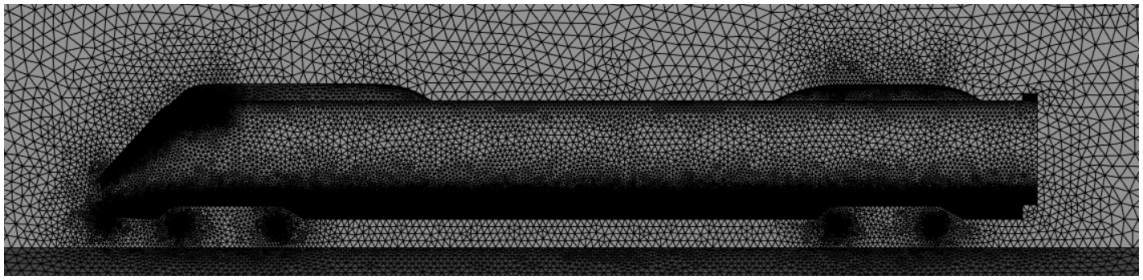


Figure 3.11: Closer view of the finest mesh from the symmetry plan, focusing on the train.

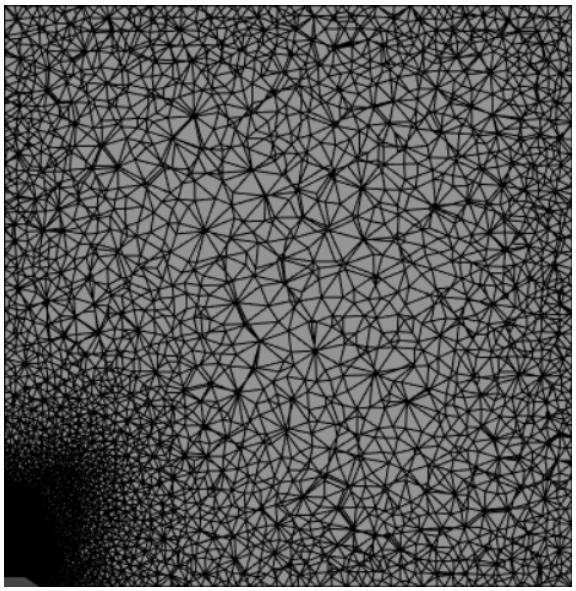


Figure 3.12: View of the mesh from a section plane.

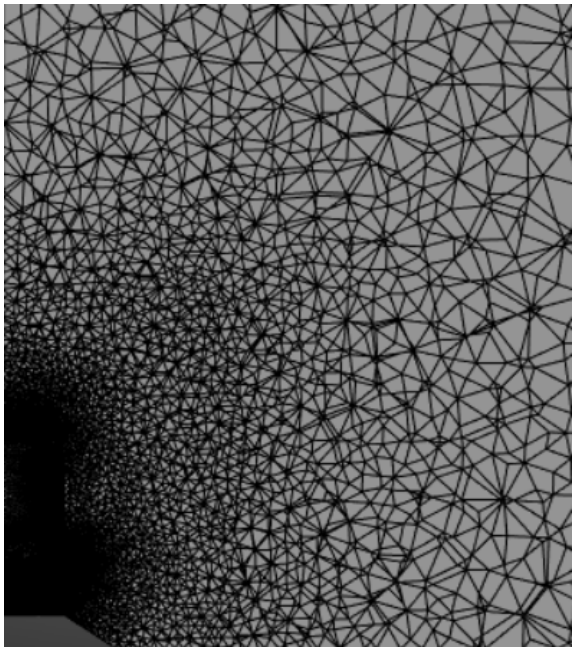


Figure 3.13: Closer view of the mesh from a section plane.

It is important to note that the preparation of the domain geometry, the mesh generation and the ANSYS Fluent simulations was not always a linear process, as it involved travelling back and forth in order to achieve the most satisfactory configuration. The geometry suffered some minor tweaks to get a better mesh and the mesh parameters were changed sometimes to match the necessities of the numerical simulations.

3.2.2 ANSYS Fluent Parameterization

Then, it was time to prepare the setup for the simulations. It is important to understand why numerical solutions are often the way to go for types of problems.

Basically, as explained in 2.2.2, the motion of fluids is governed by the Navier–Stokes equations, that describe the conservation of mass and momentum. These equations describe fluid motion completely; however,obtaining an analytical solution is extremely difficult for most practical engineering problems, since the Navier-Stokes equations are nonlinear partial differential equations [64]. So, in complex scenarios, it is not ideal to use this method to reach a solution.

Such is the case for this project, where the air flow around a train is a really complicated problem of fluid mechanics. Being a 3D problem, with turbulence and accounting the existence of flow separation (near the nose and rear of the vehicle) plus other unpredictable variables, makes this a problem impossible to solve through the analytical method.

In that case, numerical solutions are adopted. ANSYS Fluent is a modern and user-friendly CFD software which solves complex engineering problems by solving the RANS equations. After creating the geometry and generating the mesh (explained previously) and defining a few simulation parameters, ANSYS Fluent employs the FVM to discretize and solve the governing equations of mass and momentum over the computational domain. Finally, turbulence effects are modelled with RANS equations coupled with a turbulence model, chosen for the specific problem [65].

3.2.2.1 Boundary Counditions

Assessing boundary counditions to the model is essential, as it is what allows the software to produce an unique solution; other way, only a general solution would be attainable. That being said, the boundary conditions used where as shown in table 3.4.

Surface	**Boundary Condition**	**Observations**
Frontal surface	Velocity inlet, v = 80m/s	TI = 1% TVR = 10
Rear surface	Pressure outlet (gauge), p = 0Pa	TI = 10% TVR = 100
Train's surface	Wall (no-slip)	\
Lower surface	Wall (slip)	\
Upper and side surfaces	Symmetry plane[1]	\
Symmetry	Symmetry plane	\

Table 3.4: Boundary conditions on the different surfaces of the domain.

[1]Not a symmetry plane, but can be defined as such for simplicity

Here, *TI* stands for Turbulence Intensity (a parameter which describes how strong the velocity fluctuations are relative to the mean flow) and *TVR* for Turbulent Viscosity Ratio (the ratio between turbulent and dynamic viscosity). The "roof" and "walls" of the domain (upper and side surfaces) are technically not symmetry planes, but they can be defined as such, as they are far enough from the flow not to affect it.

3.2.2.2 Numerical Configurations and Results

When running simulations for the portuguese model, it was decided that it could be interesting to test diferent numerical configurations (besides the different meshes) to see how a change in some parameters would impact the results. This allows for a more profound study (and, subsquentially, better understanding of the ANSYS Fluent software before advancing to the more complex problems) and to get results in different quadrants, since using a single configuration could end up leading to convergence far away from the "real" solution. Furthermore, this makes it possible to try and understand the effect that each change had in the results and what that might say about the problem and the configuration.

So, besides the refinement of the mesh, two other parameters were changed and introducing a third change was studied; however, it was abandoned, for not matching the complexity of the problem. The main differences were whether to use $k-\epsilon$ or SST $k-\omega$ for the turbulence model and to use 1^{st} or 2^{nd} order of convective scheme for the solution. The other alteration that was to run simulations on a steady and transient regime. At this stage, everything was simulated on a steady regime, as transient would be too complex for such an early phase of the project.

Each simulation was named accordingly, depending on these mentioned parameters that make each configuration unique. So, the first character indicates whether it is steady (S) or transient (T) - although they are all steady - the second character defines whether it is a first (1) or second (2) order convective scheme, the third character determines if it uses a $k-\epsilon$ (E) or $k-\omega$ (O) turbulence model and, finally, the last one is the number of the mesh (from 1 to 5). As an example, configuration `S_1_O_4` means that this simulation happens on a steady regime, with $k-\omega$ turbulence model and first order convective scheme, and it is the forth mesh.

Then, the rest of the input data were kept the same to stabilize the results. The reference values were kept as indicated in the norm, area of 10 m^2, length of 3m and the velocity equal to that of the fluid flow (80 m/s). Simulations with 1^{st} order convective schemes had a hybrid initialization (with the wind speed at 80m/s) and the ones with 2^{nd} order convective schemes were initialized after its respective 1^{st} order configuration; this is because 2^{nd} order convective configurations are more prone to diverge or take longer to reach convergence when the initialization is not appropriate [66].

Additionally, the solver is pressure based and the under-relaxation factors (used to monitor how much a variable updates between consecutive iterations) are as shown in

Pressure	**Density**
0.3	**1**
Body Forces	**Momentum**
1	**0.7**
Turbulent Kinetic Energy	**Specific Dissipation Rate**
0.8	**0.8**

Table 3.5: Under-relaxation factors for all the simulations.

table 3.5. Convergence is reached when residuals drop below 1×10^{-4} (ideally, even lower) and the controlled variables stabilize (less than 1% change over 200 iterations).

Finally, the setup is completely ready and it is possible to start running the simulations. For all simulations, the values of drag, lateral force and lift coefficients - the force coefficients over the x, y and z axis (C_x, C_y and C_z) - were monitorized. However, since the domain has a symmetry over the y axis, its values are most likely not going to be reliable. The values of C_z were also not considered as relevant for this study, so only the value of drag (C_D or C_x) was studied.

So, for all configurations, the fluid flow of air around the moving train was simulated until convergence was reached. The results are shown in tables 3.6, 3.7, 3.8 and 3.9.

Configuration	C_x
S_1_O_1	-0.312
S_1_O_2	-0.304
S_1_O_3	-0.292
S_1_O_4	-0.279
S_1_O_5	-0.280

Table 3.6: Values of C_x for the `S_1_O` configurations.

Configuration	C_x
S_2_O_1	-0.231
S_2_O_2	-0.229
S_2_O_3	-0.228
S_2_O_4	-0.225
S_2_O_5	-0.225

Table 3.7: Values of C_x for the `S_2_O` configurations.

For both the $k-\omega$ and $k-\epsilon$ turbulence model, the 2^{nd} order of convective scheme alternative was initiated after its 1^{st} order counterpart. One of its disadvantages is that

it diverges easily; so, after around 1000 iterations with the 1^{st} order configuration, it is switched to 2^{nd} order to ensure correct convergence.

Configuration	C_x
S_1_E_1	-0.312
S_1_E_2	-0.305
S_1_E_3	-0.292
S_1_E_4	-0.279
S_1_E_5	-0.278

Table 3.8: Values of C_x for the `S_1_E` configurations.

Configuration	C_x
S_2_E_1	-0.231
S_2_E_2	-0.232
S_2_E_3	-0.230
S_2_E_4	-0.224
S_2_E_5	-0.225

Table 3.9: Values of C_x for the `S_2_E` configurations.

With these results, it is hard to start immediatly taking conclusions, but there are some interesting points to be made. First, by comparing the configurations that differ only in the turbulence model, from $k-\epsilon$ to $k-\omega$, it is visible that the changes are often neglegible. Comparing the 2 models, for external fluid flows (such as the aerodynamic of a train), $k-\epsilon$ is usually a more robust and stable model, with low computational effort, quick convergence and overall good performance across the whole domain. Meanwhile, the $k-\omega$ model is much more sensitive to the mesh, meaning its results are way more dependable on the quality of the configuration; however, for a better setup (higher quality mesh and high computational capacity available) the $k-\omega$ performs the best, with the most accurate results, mainly due to its great near-wall accuracy [67].

Looking at tables 3.6 and 3.8 again, we notice that the values for the same mesh never change more than 0.002; a really small difference. So, most of these meshes are not refined enough to take advantage of the higher near-wall accuracy of $k-\omega$. Nevertheless, there is another significant difference between these models;the residuals and convergence. Comparing the same two setups again, but, this time, looking at the iterations for convergence, the $k-\epsilon$ models converge (on average) 200 iterations sooner, and the residuals often hit lower values.

Figures 3.14, 3.15, 3.16 and 3.17 show in a graphic the values of drag for each configuration as the mesh gets progressively more refined. It usually tends to a lower value as

the number of elements increases and its fluctuations are smaller, meaning it is converging somewhere closer to the last values.

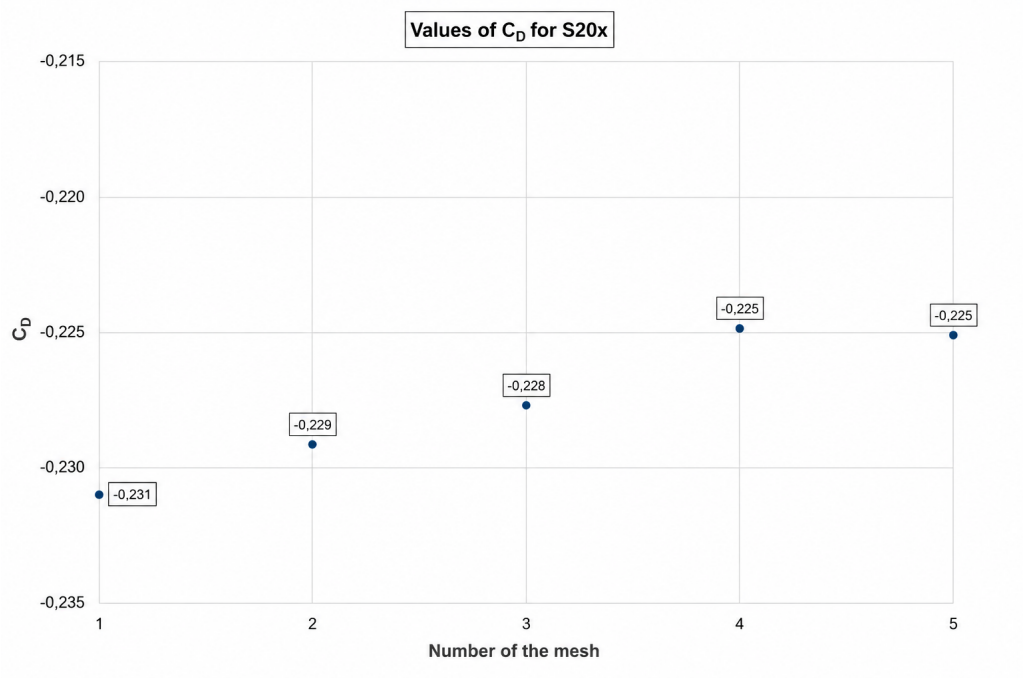


Figure 3.14: Evolution of drag coefficient for the different meshes for the `S_1_0` configurations.



Figure 3.15: Evolution of drag coefficient for the different meshes for the `S_2_0` configurations.

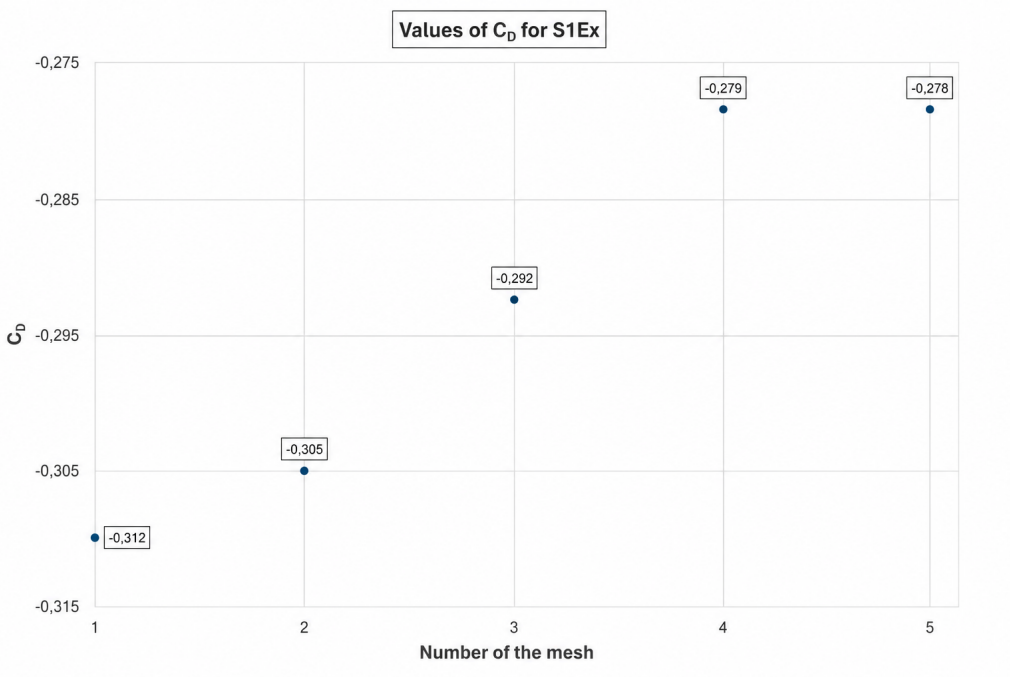


Figure 3.16: Evolution of drag coefficient for the different meshes for the `S_1_E` configurations.

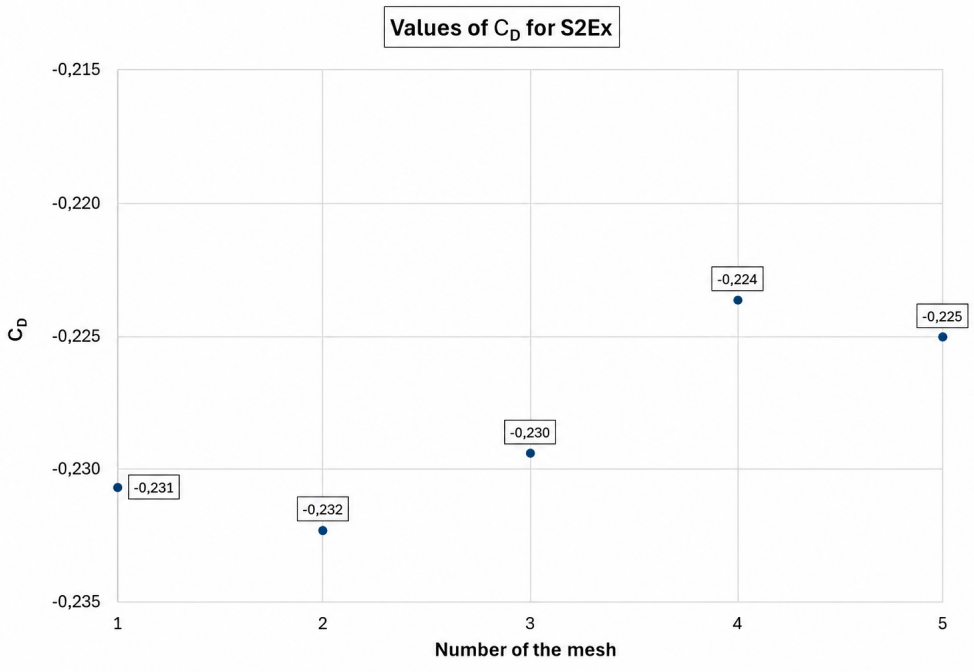


Figure 3.17: Evolution of drag coefficient for the different meshes for the `S_2_E` configurations.

With the help of these graphs, matching the simulations that vary from first to second convective scheme, there are some noticeable distinctions as well. This time, the results

did not match at all, as shown in figure 3.18. Configurations using the second order convective scheme present lower values of drag, which are also closer to one another (less discrepancy between the results from different meshes). Analyzing the main focal points of these parameters, first order is usually more simple and stable; it is good for more basic problems or for initializing a solution to be then taken over by a second order convective scheme. Second order is much more sensitive to the setup, and a poor configuration can lead to non-convergence. However, its results are often more reliable [66].

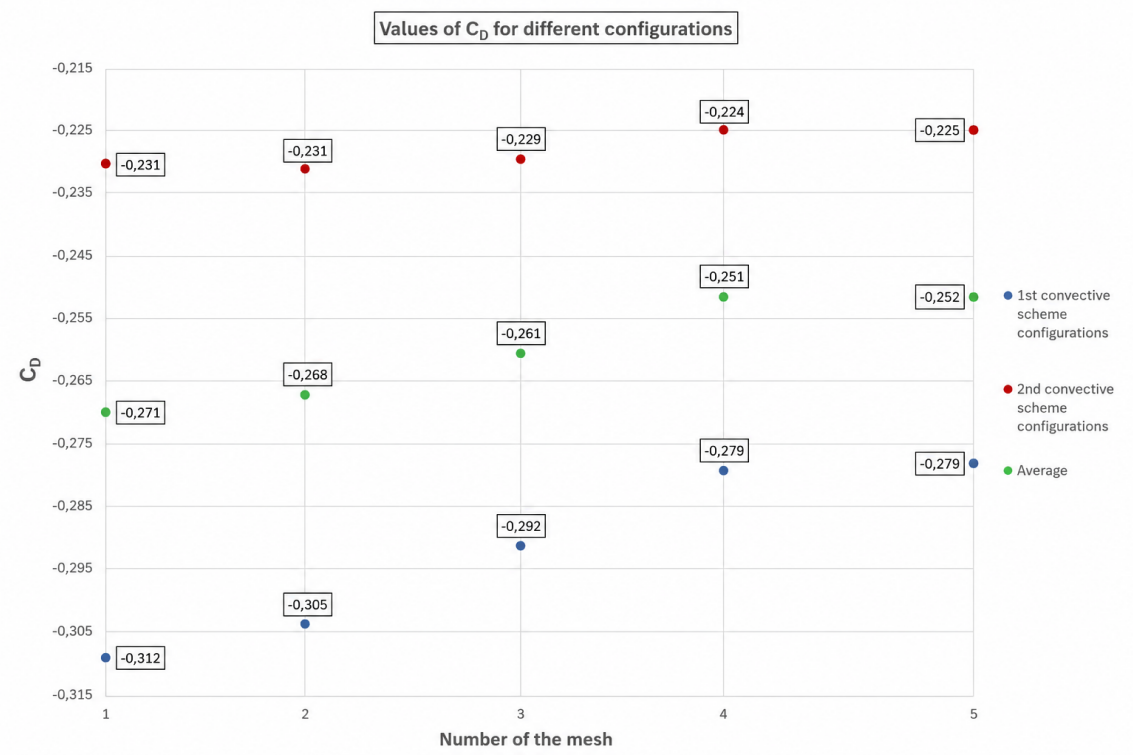


Figure 3.18: Drag coefficients for different meshes and convective schemes.

Naturally, these are all predictions based on the literature, and they must all be confirmed with the benchmark results.

3.3 ICE - Benchmark Testing

In works such as this, it is the norm to verify the results obtained by comparing them to those of previous (and similar) studies [46] [61]. However, there was nothing like that in this particular case, since it is a brand new train from a developing project.

Then, the solution was to subject a comparable vehicle with standardized results to a simulation with the same configuration as the Portuguese train and compare those results to the existing ones. That allows for a comprehensive analysis where it can be assessed which simulations got closer values to reality. This was done recurring to the german ICE from the EN 14067-6 norm [6].

Simply put, this part of the project was basically a repetition of what was done with the *TrainSolutions* model, just to the ICE train. Its geometry and dimensions are as shown in figures 3.19 and 3.20. It has a length of 37.5 meters and a heigth of around 3.625 meters, with a frontal area of around 8.75m^2. The domain had the same relative dimensions as the previous model, so, adjusting to the height of the ICE it translates to the values shown in table 3.10. The symmetry along the length was also kept.

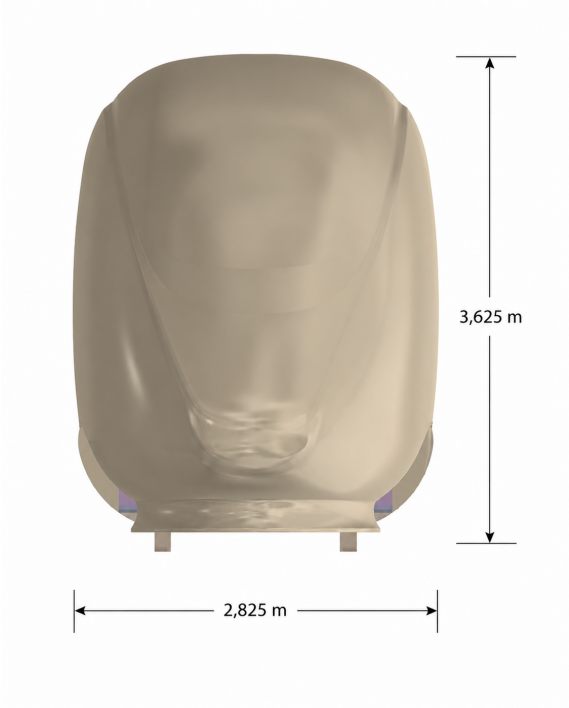


Figure 3.19: Front view of the carriage of ICE's model.

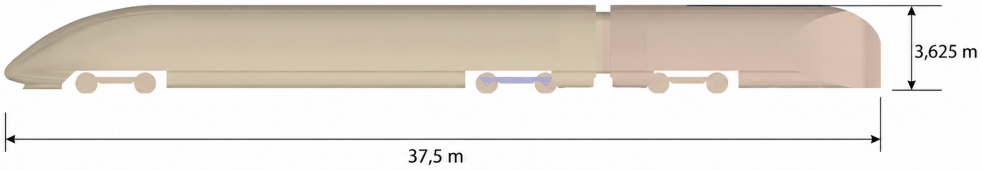


Figure 3.20: Side view of the carriage of ICE's model.

	Front	Rear	Height	Width
Length	36.25m	108.75m	36.25m	36.25m

Table 3.10: Dimensions of the domain for the ICE model.

The geometry presented in this report is not 100% loyal to that obtained with the norm, as it had too many tiny and complicated features which the ANSYS Meshing software was incapable of representing. As they were mostly small interior cavities, they were surpressed, in order to have a configuration with the same aerodynamic that could be incorporated into the CFD program.

There was a big difference between the geometry of the Portuguese train and the ICE; this one did not have the rail and ballast represented. This made some modifications to the domain necessary, and changed the target values of the aerodynamic coefficients to be attained. With this new configuration, an "air gap" of 235 milimeters between the wheels of the train and the floor of the domain was created, to conform with the standard representation.

To generate the mesh, a smaller volume was created, following the same relative dimensions as those used before, for the *TrainSolutions* train. The absolute dimensions are presented in table 3.11.

	Front	Rear	Height	Width
Length	14.5m	43.5m	6.3m	4.5m

Table 3.11: Dimensions of the smaller volume of the domain for the ICE model.

This time, when generating the mesh, 2 separate bodies were created, with different element sizes (1 meter for the outer body and 0.3 meters for the inner body, closer to the vehicle).

It created a mesh with 5 475 263 elements. Here, only this mesh was used, as there was no interest in comparing the effect of the mesh refinement.

The mesh (specifically, the transition between the different cell-sized volumes) is shown in figures 3.21 and 3.22, from the symmetry plane and a cut section along the train's width. The first noticeable difference is that there is a harsher transition from one element size to another; the BoI creates a smooth transition that usually allows for better continuity inside the domain.

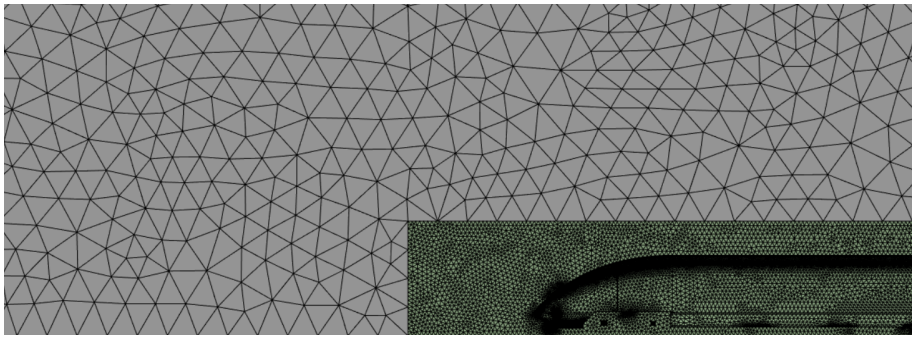


Figure 3.21: Close view of the mesh of ICE's model from the symmetry plane.

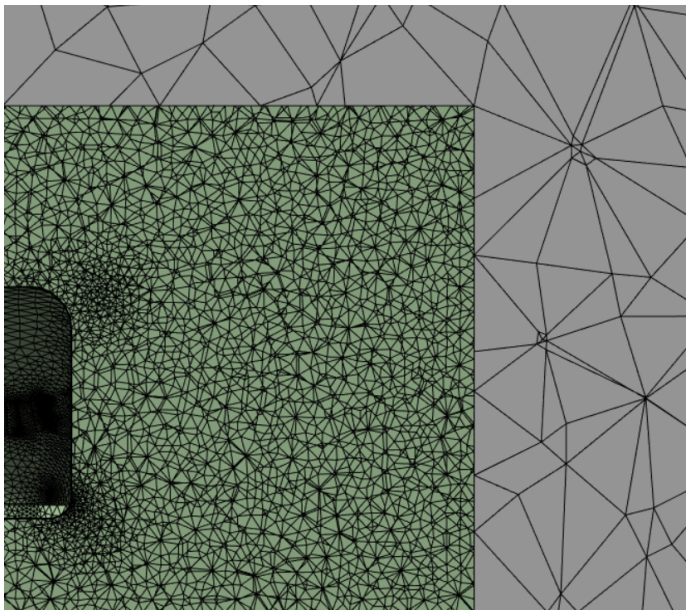


Figure 3.22: Close view of the mesh of ICE's model from a section plane along the width of the train.

3.3.1 Benchmark Results

Finally, in the ANSYS Fluent software, all parameters were kept the same (boundary conditions, initialization method, under-relaxation factors...) as well as the criteria for convergence.

So, four different simulations were run with the same mesh, changing between first and second order convective scheme and $k-\epsilon$ and $k-\omega$ turbulence model. The results of drag coefficient for each configuration is shown in table 3.12.

	S__1__O	**S__2__O**	**S__1__E**	**S__2__E**
C_x	-0.156	-0.138	-0.173	-0.154

Table 3.12: Values of drag coefficient obtained for the 4 different configurations of the ICE model.

According to the EN 14067-6 norm, for the ICE train carriage circulating through a 0° headwind, the value of C_x should be -0.12 [6]. In that case, the `S_2_O` configuration got the closest to the standardized results.

Then, some solid conclusions could be taken and some patterns from before could be confirmed; others, not so much.

First, just as with the Portuguese train model, using second order convective schemes gave smaller values of drag, that, in this instance, we can confirm were closer to reality. Once more, it was sloppier in terms of convergence, taking more iterations and requiring to be started as first order but, in the end, the results were better.

Second, using SST $k-\omega$ instead of $k-\epsilon$ as the turbulence model translated to a significant difference in the drag coefficient, something that was not happening previously. This could likely be explained by a higher mesh quality; even though it has less elements, it has a simpler geometry (the edges were simplified and it does not have the rail and ballast represented) which allowed for better mesh quality parameters, which relates to a more precise representation. And, as expected, a higher mesh quality provided the necessary conditions for $k-\omega$ to have more robust results.

So, the SST $k-\omega$ turbulence model and the second order convective scheme gave the best results; however, these configurations (`S_2_O`) were also the most troublesome in terms of convergence. On the other side of the spectrum, `S_1_E` was the best for convergence, but it did get the furthest results.

To conclude, the `S_2_O` configuration was the one that provided the most confidence in achieving the best results for the upcoming analysis, so it was adopted for the next investigations in this thesis (starting with the crosswinds assessment). In this study, it became clear why it is the norm to adopt this parameters for studying the aerodynamic performance of railway vehicles. At the same time, the fact that it was the toughest configuration to stabilize, indicated that, in the next steps, the ANSYS Fluent setup must be carefully prepared, in order to create the necessary conditions to attain desirable and reliable results.

A more profound analysis of these results shall be performed later in this disseration; however, at the time it was done, this was sufficient, as the main goal was to define the best parameterization in order to move forward in the project's goals.

Chapter 4

Crosswinds

So, after testing the new model for headwinds, it was important to run simulations to assess its behaviour when exposed to crosswinds.

Crosswind study on a train is necessary as its poses a big risk of derailment. Moreover, it also compromises the stability and confort of the trip for the passengers, which is undesirable. This threat happens not only at high wind speeds, but also at sudden strong currents or particular circumstances, such as tunnel exit [28].

In that case, the *TrainSolutions* train had to had crosswind resistance tests realized before advancing to commercial service. Naturally, as explained during the literature review (2), experimental tests on full-scale models are ideal and, almost always, mandatory. However, they were too expensive and time-consuming for this dissertation and for the early stage of the project so, since CFD is being more and more credited in the field, the goal became to run numerical simulations of the problem. This way, it would be expected to attain solid numerical results that could serve as foundation for future tests on wind tunnels and large-scale prototypes.

Obviously, this had to be conceived with all due respect to the standards, methodology and patterns defined on the EN 14067 norm. For this particular stage, the 6^{th} part was the most relevant. It is solelly dedicated to the assessment of crosswinds in railway vehicles, and has various models (with different configurations) for comparison [6].

This chapter was dedicated to explaining how these CFD simulations were planned and how the crosswinds study was done. Most of the methodology is described swiftly, since it is an extension of the methodology adopted for the headwind study.

During this part of the project, the most coherent configuration (according to the benchmark tests performed) was adopted to the selected operating conditions. The steps to create the ANSYS Fluent setup are presented and the primary results are displayed, for future analysis.

4.1 Geometry and Mesh

In accordance to the work realized in chapter 3, the train geometry (3.2 and 3.3) was "subtracted" from a prismatic domain to create a volume of air that flows around the vehicle. For this case study, the relative velocity of 80 m/s was kept, for the reasons previously exposed.

In preparation for creating a layered mesh (with different sized elements, allowing for a finer mesh near the train), the geometry of the domain consisted of three rectangular prims - not just two, like previously. This makes it possible to create an intermediate mesh, making the transition smoother (which translates to better mesh quality). The overall dimensions, of the outer prism, are presented in table 4.1 and are relative to the height of the train, same as before.

	Front	**Rear**	**Height**	**Width**
Relation to the Heigth	10H	30H	10H	20H
Length	43m	129m	43m	86m

Table 4.1: Dimensions of the domain for the crosswinds study.

The dimensions of the smaller volumes are in table 4.2. Those ones were chosen somewhat arbitrarily, in an iterative process in order to find the combination that produced the most satisfactory mesh quality parameters while keeping the computational cost at a minimum.

Volume	**Front**	**Rear**	**Height**	**Width**
2^{nd} volume	17 m	27.5 m	17.5 m	30 m
3^{rd} volume	2.5 m	3.8 m	6.5 m	5.8 m

Table 4.2: Dimensions of the smaller volumes for the crosswinds study.

Figure 4.1 illustrates the geometry from a front and side view. The 2^{nd} volume has a considerable size while the inner one is as close to the train as possible, in order to create a region where the element size could be really small, to attain a high-quality mesh and a loyal representation of the fluid flow.

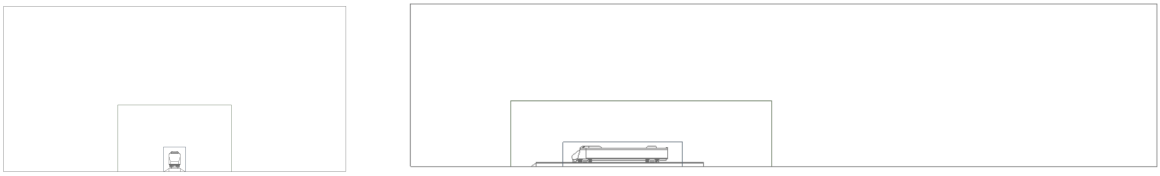


Figure 4.1: Front and side view of the geometry of the domain for the crosswinds study at 0°.

This geometry was used for the simulations at 0°. Starting from this one, all others were created, by simply rotating the outer volume (where the inlet and outlet boundary conditions are defined) to match the desired yaw angle. It is essential that the axis system (same as previously, 3.6) accompanies the vehicle as the yaw angles changes, so that the aerodynamic coefficients calculated by ANSYS Fluent stay coherent.

The EN 14067 norm, for the ICE train model, experiments for crosswinds for yaw angles of every multiple of 5 from 0° to 90°. Since, in this dissertation, CFD is being used to run these tests, and expecting issues with convergence for the larger angles as veryfied in other researches (2.3.3), the simulations were realized at intervals of 5° until 60° and then 10° until the end of the spectrum.

Initially, the plan was to have the whole range covered (in particular, since it is something most similar investigations failed to accomplish), but as the troubles with reaching convergence emerged, this alteration had to be made, to not halt the progress of the project in a seemingly endless struggle. It is unfortunate - as it would have created a characteristic curve that would be easier to read and compare with the one from the standard - but necessary.

Figures 4.2 and 4.3 show the isometric views of the volumes for 0° and 90° and then 30° and 45°, to allow for a perception at different significant angles.



Figure 4.2: Isometric view of the domain at 0° and 90°.

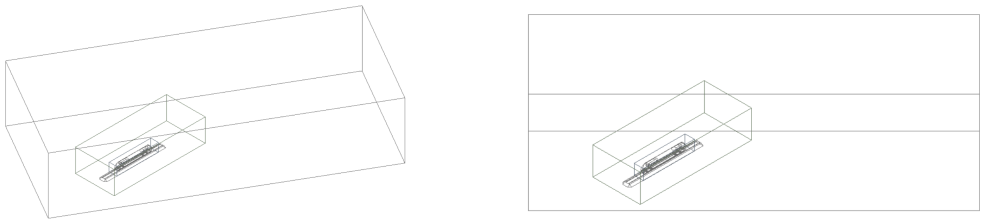


Figure 4.3: Isometric view of the domain at 30° and 45°.

With that cleared, the next step was the mesh generation.

As stated, the conception of the inner volumes was heavily connected to the defining parameters of the mesh. So, the final combination is the one presented in table 4.3. The overall mesh had an element size of 2.2 meters, with two BoI with 0.8m and 0.2m sized cells. This small length was to represent the train's features with a high accuracy. The mesh was once more tetrahedral across the whole domain.

Volume	Size
Outer Volume	2.2m
Intermediate	0.8m
Inner Volume	0.2m

Table 4.3: Cell size for the different volumes of the domain.

Figures 4.4 and 4.5 show the default mesh (for a 0° yaw angle) used for this study, from the side and front, respectively. With these, it is possible to see the transition in the size of the cells. It helps understand the necessity of the intermediate mesh, since, without it, the mesh surrounding the train would be 10 times smaller than the outer mesh.

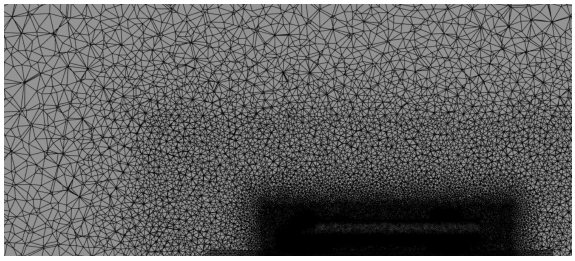


Figure 4.4: Close-up side view of the mesh for crosswinds with a 0° yaw angle.

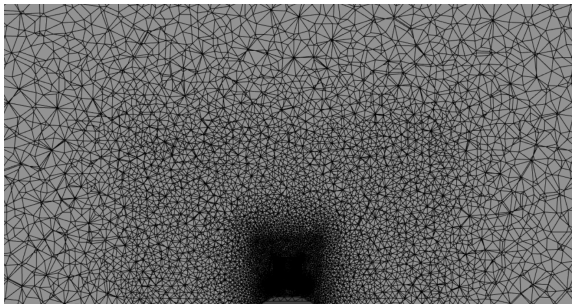


Figure 4.5: Close-up front view of the mesh for crosswinds with a 0° yaw angle.

Nevertheless, as the mesh generation comes after the processing of the geometry, every time the geometry suffered an alteration (in this case, every 5° to adjust the yaw angle) the mesh had to be created again. That being the case, it was impossible to exactly replicate the same mesh every single time. Even so, with no changes in the parameterization, the meshes were akin to the original one; all had a number of elements between 8.3 and 8.5 million.

The quality parameters - namely, the aspect ratio, the skewness and the orthogonal quality - where monitorized to guarantee the similarity between them. The window for the average values for each of those is shown in table 4.4.

Quality Parameter	Average
Aspect Ratio	1.80 to 1.82
Skewness	0.21 to 0.22
Orthogonal Quality	0.77 to 0.79

Table 4.4: Quality parameters for the meshes.

Comparing to the reference values mentioned in the literature, all were fit. Still, not only the average, but also the worst cells were controlled. The generation was repeated until no cell had an aspect ratio worse than 100; even if the average was acceptable, poor quality cells spread across the domain could cause divergence or lead to a wrong solution.

Then, with the geometry prepared and the meshes created for each case, it was time to advance and define the ANSYS Fluent setup.

4.2 ANSYS Fluent Parameterization

The ANSYS Fluent setup was much similar to the one adopted for the headwinds study.

All simulations were under steady regime and the boundary conditions were the same as previously. The solver is still pressure-based and the under-relaxation factors were kept as in table 3.5. The principal condition for convergence was maintained as the residuals dropping below 10^{-4}.

This time, the geometry was more realistic (without the symmetry to lower computational effort); so, the values of all the coefficients, drag, lateral force and lift, were taken as outputs. From this point forward, they will mainly be refered to as C_x, C_y and C_z, respectively. Since, even when convergence is reached, these values oscilate slighty, to have the most precise results, the result was considered as the arithmetic average of the past 200 iterations.

Finally, the configuration was to be the one that performed the best according to the benchmark results, shown in section 3.3.1, so, 2^{nd} order convective scheme with SST $k-\omega$ turbulence model.

To avoid causing divergence in the first hundred iterations, and since the 1^{st} order convective scheme proved to be more reliable in terms of initialization the solution, the method used then was repeated in this stage of the project. All simulations for each yaw angle were launched with a hybrid initialization and, for the first 1000 iterations, it was run with a SST $k-\omega$ and 1^{st} order configuration. Only after that time, if the residuals seemed stable, would be made the change to the `S_2_0` configuration, relying on the fact that, according to both the literature and the earlier investigation, it was the most accurate setup.

In the end, it was possible to get a good read on the behaviour under crosswinds of the *TrainSolution Portugal* model, with some notorious complications explained in the next part.

4.3 Results

While the simulations were running, it was possible to use that time for other tasks; for example, finding a solid basis for comparison.

So, to keep the consistency with the analysis for headwinds, and since it is a model already brought up in the project, the ICE model present in the EN 14067 is the most logical choice. The norm presents (as annexes) tables of values for C_x, C_y and C_z for different configurations of different models. It also presents the coefficients associated with the torque (not just the forces) which were not considered for this study, since introducing to many variables would complicate the evaluation of the results.

Yaw Angle	C_x	C_y	C_z
0º	-0.162	-0.026	0.037
5º	-0.203	0.496	-0.151
10º	-0.232	1.072	-0.775
15º	-0.261	1.736	-1.662
20º	-0.257	2.543	-2.631
25º	-0.189	3.432	-3.7
30º	-0.101	4.455	-4.702
35º	0.025	5.616	-5.638
40º	0.2	6.806	-6.368
45º	0.58	8.085	-6.979
50º	0.954	8.655	-7.158
55º	0.976	8.802	-6.543
60º	1.041	8.511	-5.9
65º	0.815	7.629	-5.27
70º	0.6	7.346	-5.057
75º	0.576	7.214	-5.008
80º	0.542	7.011	-4.685
85º	0.47	6.869	-3.799
90º	0.399	6.687	-3.794

Table 4.5: Values of C_x, C_y and C_z for the ICE model (configuration with rails).

To compare with the values from the *TrainSolutions* model, since its geometry includes the rails and ballast, the values to be extracted from the standards must be the ones with

the same configuration. The results from the experiments performed in the ICE, which were used as a reference to the results in this study are those in table 4.5.

It is important to note that, these comparison is not 100% accurate. It is not guaranteed, in any way, that the values (or the shape of the curve) will match this one. Nevertheless, being both railway vehicles, with the same representation, with similar body shapes, and under the same conditions (even though one's values are from CFD, the other from experiments), there must be some correlation between the results, which facilitates the later analysis and serves as a point of critique to the new model.

Moreover, even if the results are close and can be extrapolated, this does not eliminate the necessity for small-scale or full-scale crosswinds tests with the CP model. Validation still requires a prototype, this only serves the purpose of enriching the analysis produced in this dissertation.

The ANSYS Fluent simulations for the TrainSolutions model were starting to converge and output results. For the smallest yaw angles, convergence was smooth and the simulation ended shortly after switching to the 2^{nd} order convective scheme. As the yaw angles increased, it was taking progressively longer to reach the convergence condition, but a trend was becoming visible for all three coefficients under the scope of this study.

Eventually, the residuals were not dropping below the minimum for convergence, and the configuration for 60° was the last one to stop automatically. That is why, from that point onward, until 90°, the simulations were performed at intervals of 10° of yaw angles, instead of 5°. Even so, none of them reached convergence; calculations were stopped manually, when the values of C_x, C_y and C_z started settling around a value, and it was considered that the solution it had converged to that point.

That being the case, those values are not as reliable as all the other ones.

Table 4.6 presents the results extracted directly from ANSYS Fluent, for all the simulations concluded. It also shows the number of iterations to reach convergence, a value that was gathered as well during these stage of the work. As mentioned, this number keeps increasing until eventually, the residuals simply do not descend below 10^{-4}; after 2000 iterations, if the value is not close to that, it might never fully reach convergence.

An important note to make is that, by remembering the axis system once more (3.6), a negative value of drag (C_x) indicates that the resistive force in the direction of the train's movement is positive; the minus sign comes from the fact the axis is aligned with the vehicle's movement. The same is true for the lift coefficient; negative value of C_z indicates a vertical ascending force.

However, with this table alone, it is hard to come to any sort of understanding. So, figures 4.6, 4.7 and 4.8 display the values in a graphic way. In the x axis, the yaw angle increases and in the y axis, the coefficients, C_x, C_y and C_z, respectively.

Yaw Angle	**Iterations**	C_x	C_y	C_z
0º	1200	-0.532	0.000	0.245
5º	1200	-0.618	-0.642	0.187
10º	1200	-0.662	-1.319	-0.149
15º	1200	-0.663	-2.082	-0.775
20º	1200	-0.609	-2.941	-1.482
25º	1400	-0.499	-3.852	-2.331
30º	1400	-0.333	-4.871	-3.111
35º	1800	-0.200	-5.702	-3.985
40º	1800	-0.028	-6.735	-4.671
45º	2000	0.143	-7.321	-5.744
50º	2000	0.254	-8.541	-6.301
55º	2400	0.355	-9.854	-4.906
60º	2400	0.429	-9.972	-3.396
70º	\	0.538	-9.010	-3.019
80º	\	0.598	-8.974	-2.937
90º	\	0.490	-9.549	-2.380

Table 4.6: Values of C_x, C_y and C_z for the *TrainSolutions Portugal* model.

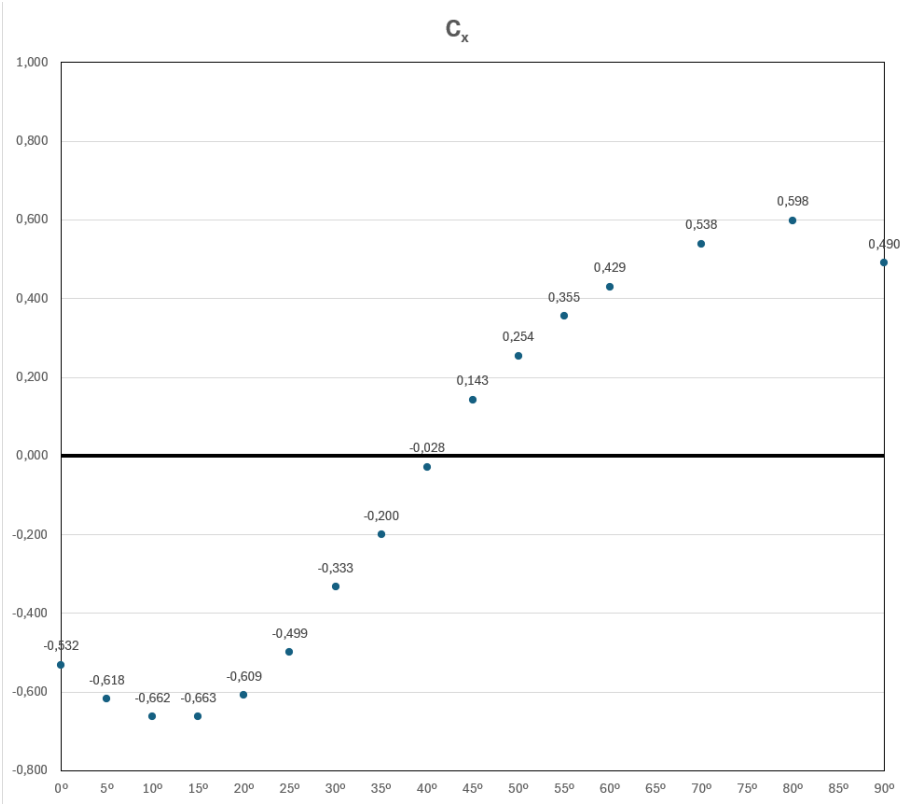


Figure 4.6: Graphic of C_x for corresponding yaw angle.

The analysis of these results is a topic further dealt with in chapter 6. Even so, for now, some conclusions are easy to make.

All 3 graphs present a certain tendency. The cleanest one is the graphic of C_x, figure 4.6, with 2 clear points where drag coefficient hits a maximum and minimum value (and a somewhat clear inflexion point). The resistive force keeps increasing until around 20°, then decreases until 80° (inside the area where the conditions for convergence were not entirely met).

The values of drag coefficients is not the most interesting one for this analysis in particular, as drag is a resistive force to the movement of the locomotive inside the fluid. It largely affects fuel consumption and energy efficiency; however, C_Y and C_L are more relevant when considering the safety and stability of circulation under strong crosswinds.

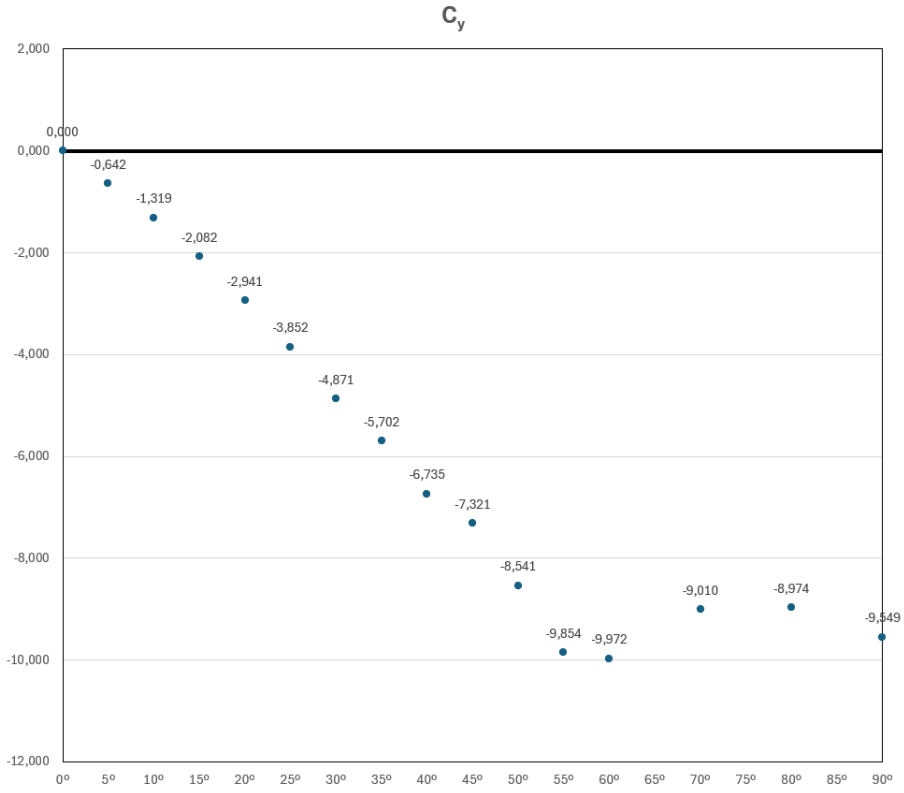


Figure 4.7: Graphic of C_y for corresponding yaw angle.

Meanwhile, the graphic of C_y, figure 4.7, also has a distinct pattern until around the beggining of the "gray area" of the spectrum where most CFD studies of the sort have trouble getting realistic solutions. The lateral force coefficient is constantly increasing (at an almost linear rate) until 60°, meaning that, as expected, as the wind strikes the vehicle from a more tilted position, the force pushing the train away from the track grows, meaning a bigger risk of derailment.

Nevertheless, the values from the end of the range can not be trusted 100%, due to the aforementioned issues. Those might also explain the seemingly random pattern.

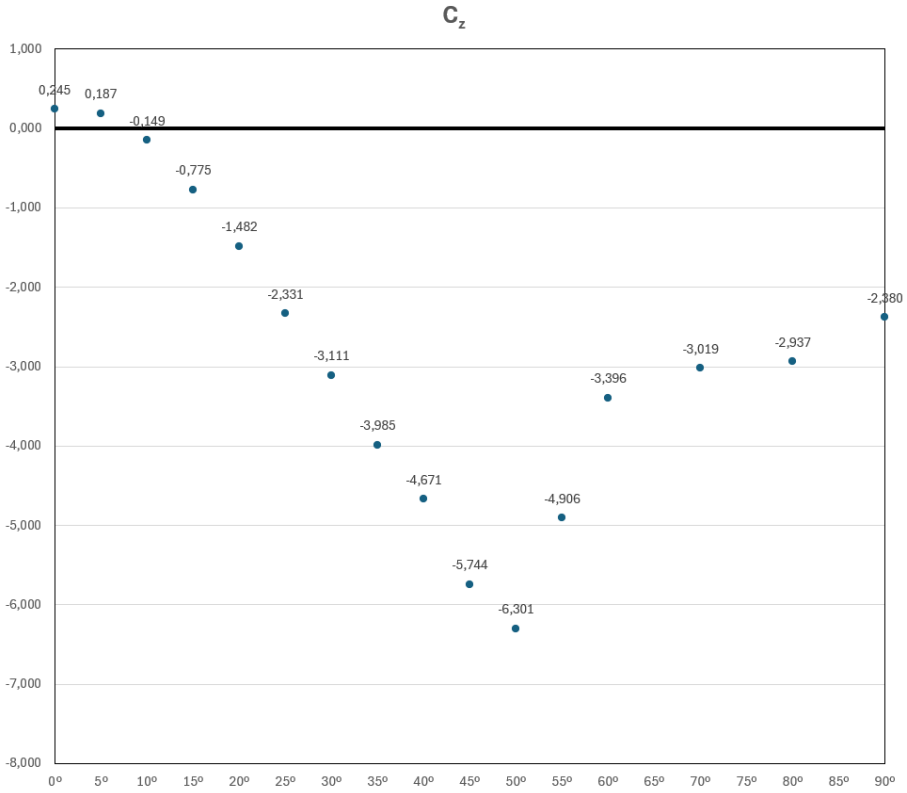


Figure 4.8: Graphic of C_z for corresponding yaw angle.

Finally, a quick look at the graph of C_z, figure 4.8, is enough to recognise a distinct pattern for most of the range of angles. The lift is increasing until around 50°. If this force is too high, it can destabilize and overturn the vehicle. That angle seems to be the critical one for this quantity, as it decreases from that point forward. Still, after the 60° mark, once more, the tendency becomes blurrier.

This is the simplest analysis performed at the data attained from the ANSYS Fluent calculator. The extended analysis is not until further in the dissertation.

Nonetheless, before moving up to the next operating condition to be studied (passing manoeuver) - and since that needed to be done using a transient configuration - a separate test was conducted in order to have at least one unsteady simulation for the crosswinds study. That also allowed to gain some experience with this type of CFD simulations while progressing with the project.

4.3.1 Transient Simulation

Since it was only a preliminary experiment, the only unsteady case studied was for a yaw angle of 0°. The geometry and the mesh were exactly the same used for the steady procedure, same with the ANSYS Fluent parameterization; the sole difference was from a steady to an unsteady regime.

The boundary conditions were the same for the whole crosswinds investigation and it was still the 2^{nd} order convective scheme with SST $k-\omega$ turbulence model. The pressure-velocity coupling scheme could be either Pressure-Implicit with Splitting of Operators (PISO) or *Coupled*. *Coupled* was chosen; despite the bigger computational cost, it is usually more stable [68].

Despite it being a transient setup, no dynamic mesh was employed for this case. The simulation was run until a maximum of 100 time steps of 0.01 seconds was reached or the residuals dropped below 10^{-4}. The solver is set to perform 20 iterations per timestep.

Convergence was reached in the 82^{nd} timestep. The values of C_x, C_y and C_z are displayed in table 4.7.

Yaw Angle	C_x	C_y	C_z
0º	-0.619	0.003	0.302

Table 4.7: Values of C_x, C_y and C_z for the 0° transient simulation.

Since this was the only unsteady configuration, there is no complex analysis that can be done. It is only relevant to compare with the respective value from the steady setup (table 4.6). The lateral force coefficient is once more almost null; which is coherent, considering the wind is frontal.

The values of drag and lift coefficients are somewhat close to the previous ones. A plausible explanation for the fact that both are larger than in the steady layout is that the transient simulation might have managed to capture flow recirculation, wake development and/or vortices around the train better than a steady configuration. This made for a more accurate representation of the fluid motion (representing phenomena that would be ignored otherwise) and that contributed to increasing the pressure gradient in certain areas, therefore increasing C_x and C_z.

Nevertheless, this research is not particularly important for the overall progress of the work. Consequently, no further analysis was performed for this case study.

The main point of interest was to have at least one unsteady setup to see how large the difference would be to the existing ones and start interacting with the interface in preparation for the next step.

With that cleared, it was proceeded to the most complex and intriguing part of the project; the CFD investigation of the passing manoeuver of 2 trains.

Chapter 5

Passing of Vehicles

The passing manoeuvre between 2 high-speed trains is characterized by highly unsteady aerodynamic phenomena. The interaction of the flow fields moving in opposite directions is unpredictable and the effects suffered by the vehicles change rapidly, as the whole event lasts only a fraction of a second. Significant variations in pressure and aerodynamic forces occur in both bodies as a result of said interaction.

Along with circulation under crosswinds, this presents one of the most critical operating conditions for railway vehicles. Not only that, it is also one of the toughest to investigate. As mentioned in chapter 2, it is not convenient to study the passing manoeuvre in a wind tunnel, since the relative motion can not be simulated with the trains standing still. This point in particular makes CFD studies really interesting for this matter.

This chapter presents the numerical investigation of this manoeuvre performed using the ANSYS Fluent software. Its main focus is describing the setup used for the simulations performed to allow for a better perception of the results to be later presented. The relative motion of the two trains is reproduced using the overset mesh approach.

Furthermore, since this was a significant part of the project (both in terms of time spent on the task and in relevance for the final product) more than one configuration was tested. Various different options were used, until a balance between accuracy and applicability was found. So, in order to show the progress made towards finding the final transient configuration, the previous and simpler ones are first described. Then, some ideas for more advanced configurations are also shown; they were not completed due to the inability to finish them in time for the end of the work.

Even so, this part of the project was the pinacle of the CFD research performed to the Portuguese train in this dissertation, so its purpose is to give a full disclosure of the work done in order to understand how the results came to be, to facilitate the analysis of results and the conclusions that followed.

5.1 Preliminary Test Configurations

Transient simulations in CFD are a tricky subject. They are inherently more complex than steady state ones, since the flow field must be resolved as it evolves over time.

So, instead of obtaining a single converged solution, the governing equations are solved sequentially at every single time step, with the solution from one influencing the next. The selection of an appropriate size for the time step and the number of iterations for each one, how much time should be given for the whole phenomenon to be accurately represented and so on. All these matters are exclusive to this regime, and they are particularly important to accurately capture the flow while keeping numerical stability and computational costs at a reasonable point.

Even with the sole simulation performed for the crosswinds study (mentioned in 4.3.1), there was still much to understand. That is because there was no relative movement of the objects in that configuration; the mesh was stationary. In this case, the use of a dynamic mesh was mandatory.

There are some approaches regularly used for solving this issue in numerical investigations.

Smoothing technic is particularly interesting when the deformation is small. It moves or rearranges the existing mesh without changing the connectivity. It is ideal when there is a small and gradual deformation and no large displacements [69]. In that case, that was not a suitable option for the passing manoeuvre.

There is also a remeshing feature, which can be combined with smoothing. Remeshing reconstructes some cells when smoothing alone would have created poor-quality ones. Even so, despite it handling somewhat larger deformations, the moving boundaries should still be close to their original position [69]. Once more, not ideal for this problem.

For some time, while doing the theoretical research and primary tests on ANSYS Fluent, this second approach was the one being considered. Then, upon learning about the existence of overset meshes, that changed the direction of the work.

The overset approach is generally the most suited for bodies moving independently or undergoing large displacements. Its way of reconnecting the background and component meshes (as the meshes for the domain and moving part are commonly called) allows the first to avoid deformation. All of these characteristics make it the perfect match for the investigation of the train passing manoeuvre.

First, the domain, the large volume of air around the train's path, is created, and it shall be the background mesh. In this case, it does not have the "negative" of the vehicle, it is just a rectangular prism. Then, a smaller volume of air closer to the train - now subtracting it - is created to be the background mesh.

This approach, not only is the best fit for this operating condition for the reasons mentioned above, but it is also great for the project, as it gives room for versatility; part of the reason why more than one configurations were designed.

As long as ANSYS Fluent is able to overlap the background and component meshes correctly, both can be independently changed to produce several different setups. So, in order to quickly experiment with different parameters without compromising much time, some simple geometries where created to perform transient simulations of train passing manoeuvres.

While thinking about the best way to represent the whole event, it was noted that a good start could be simulating only the movement of one train (or rather, one train's mesh). If the relative velocity between all objects is kept the same as in the real event and boundary conditions are adjusted, it is plausible to have only the mesh of one vehicle moving, while the other is stationary with the rest of the domain.

To test this hypothesis, the first geometry for the dynamic mesh assessment of this thesis was created. The component mesh was a small rectangular prism around the train, with only a few meters of air in each direction. However, the background mesh contained not only the large volume of air which is the whole domain, but also a small extraction in the form of a block. This block was a simple representation of the second train, moving in an opposite direction. Naturally, no significant results were produced, and this was just to get used to the transient possibilities of the software.

After that, more realism was put into this configuration. The block was replaced by the geometry of the *TrainSolutions* model. Now, there were 2 trains on separate tracks.

It was necessary to adjust the boundary conditions to this nuance. So, the train in the component mesh needed to be put at twice its velocity (to compensate the fact that the other one is still) and the floor, as well as the air inside the domain had to move at the train's speed - all of this is necessary to keep the relative movements loyal to the actual flow.

These configurations were conceived in the earliest stage of the train passing investigation. Because of that, all of them failed to output revelant data that could be used for aerodynamic performance analysis. What they provided instead was the knowledge of the most critical requirements for this project; the ones that were compromising the convergence or the precision of the experiment.

On the one hand, it is regretful that there are no results to analyse these configurations. On the other hand, they saved a lot of time in the project when using the more accurate ones.

When advancing through the difference stages of the CFD arrangement, a few problems emerged, which were promptly studied and solved, to not be repeated when facing the more complex (that are more costly and time consuming) setups. The 2 most notable were related to the Courant number (an essential factor in transient simulations, explained in 2) and the existence of orphan cells in the overset interface.

The Courant number is a delicate matter concerning the unsteady simulations. It represents how far the fluid travels during one time step relative to the size of a mesh cell. It should always be lower than the unit, to ensure the continuity of the flow. A large

Courant number means that relevant changes in the flow can occur in consecutive time steps, resulting in instability and loss of accuracy.

To ensure this does not happen, the inequality in equation 5.1 must be verified.

$$\frac{u\Delta t}{\Delta x} < 1 \tag{5.1}$$

The velocity (u) is already defined, 55 m/s. Then, the time step (Δt) and the characteristic cell size (Δx) can be conjugated to secure this condition. Since the characteristic cell size can be defined in ANSYS Meshing, it appears to be only a matter of choosing a solid value that accuratly represents the geometry, then solving for the time step and everything is correctly defined.

In spite of that, some issues were emerging, concerning the continuity of the simulation. Contrary to what it seemed, it is not that simple. The value input to the Meshing software defines the value of the "regular" elements of the domain. When getting closer to the vehicle (or any other complicated shape) it has to create smaller cells to better represent its form. With that happening, some cells have lower Δx which, for the same time step, means the Courant number grows larger than 1.

The other main problem was, as stated, regarding orphan cells. They are a complication in the overset mesh approach, and are usually a result of insufficient overlap between the component and background meshes.

Simply put, in an overset mesh, the information is transferred between the overlapping meshes through donor and receptor cells, in the background and component meshes, respectively. A receptor cell receives interpolated flow variables from one or more valid donor cells. During the overset connectivity process, ANSYS Fluent searches for suitable donor cells for every receptor; when it can not do that, that cell is marked as a orphan cell. So, an orphan cell is a receptor for which the software could not find at least one valid donor cell. This translates to a loss of information [70].

Orphan cells contribute to solution inaccuracies and divergence. This software has the capacity to solve through it; however, if the number of orphan cells is too high (and their location is critical) they compromise the results. Therefore, they should be eliminated.

Most of the times, they are caused by insufficient overlap between the meshes, poor positioning and large differences in mesh resolutions (the size of the elements). From these, the most likely to be actively increasing the number of orphan cells is the later.

So, from the early testing phase, the main conclusion was that, in order to have a robust transient simulation for the train passing manoeuvre, the mesh generation was a vital step. Controlling the cell size would be fundamental to keep the Courant number small and create a good overlap between the background and component mesh, to reduce the number of existing orphan cells.

With that in mind, the first topic to note was that, as expected, the element size was much smaller in the volume around the train than in the complete domain. Adjusting

the element size to be closer to one another is essential to solve this problems. In that case, one solution that comes to mind is manually changing the cell size parameter in the Meshing software.

Nevertheless, since that does not control the size of all elements, the problem would most likely remain. Either that or, to solve this issue, both meshes are refined to a point where the computational effort skyrockets and the simulations become too costly and prolonged. However, there was another solution.

The regions of the geometry where most elements (of reduced size and irregular shape) are generated is usually next to the more complex parts of the vehicle. So, as an initial fix for these issues, removing or not reproducing some components of the train would help to uniformize the cell size across the separate meshes and increase the overlap, partially solving the orphan cell problem, while also reducing the number of elements where the Courant number exceeds the unity. For that, a simplified train geometry without the wheels and bogies was created.

For the purpose of uncomplicating the geometry, the rails are also not represented. The air gap configuration was chosen, respecting the demands of the standard.

After the initial testing phase, it was concluded that having one of the vehicles stationary with the domain barely simplifies anything, but it does complicate a few steps of the parameterization like the boundary conditions. In that case, this time, the geometry is divided in 3; the domain and the 2 trains running in opposite directions. This does not compromise the overset mesh approach, as the only difference is that the component now consists of the parts.

This configuration was the first to produce relevant and coherent results. Therefore, the setup is presented in the dissertation, as it was mostly retained for the final simulations.

The domain had a length of 200 meters. It was divided into 3 different volumes, to allow for different element sizes in the mesh, with their widths and heigths shown in table 5.1.

Volume	**Width**	**Heigth**
Outer Volume	60m	30m
Intermediate	35m	18m
Inner Volume	18m	10m

Table 5.1: Dimensions of the domain volumes for the train passing simulations.

Figure 5.1 shows the separate volumes. Here, it is important to note that the smaller volumes are centered around one of the tracks (for the train following the x axis as previously), not the domain itself. The axis system is once more the same as in figure 3.6.

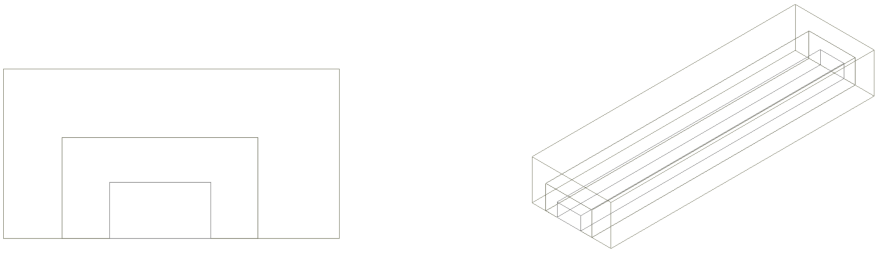


Figure 5.1: Front and isometric view of the geometry of the domain for the train passing study.

For the trains, it was only a matter of creating the geometry once, then mirroring it and placing on the correct coordinates to be on the opposite track. The dimensions are those in table 5.2 and the volume can be seen in figure 5.2. The length of the volume is 28 meters, with the train being placed 1 meter from the front. On the same note, the width is 8 meters, and it is 1 meter from the side which is adjacent to the other track. More space could be allowed on the other flank to allow for a better representation of the fluid flow; however, in the middle, it is crucial to make sure the volumes do not overlap.

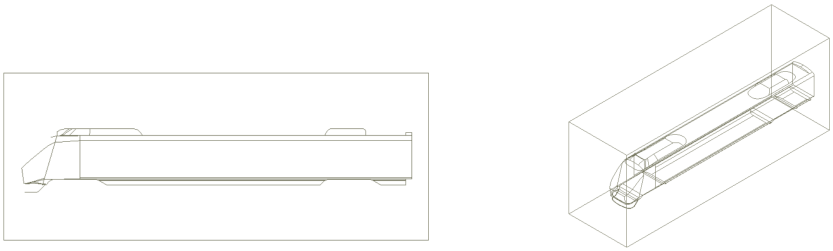


Figure 5.2: Front and isometric view of the geometry around the vehicles for the train passing study.

	Length	**Width**	**Heigth**
Train Volume	28m	8m	8m

Table 5.2: Dimensions of the train volume for the train passing simulations.

Moreover, according to the standard EN 15273-3, for the maximum velocity at which this model is to circulate, the distance between the tracks should be 4 meters (from the middle). Then, it is imperative to not extend the volume much further, to not cause interference and issues with the interaction of the train's fluid flow.

Finally, concerning the height, from those 8 meters, the air gap was the same 235 milimeters to conform to the standard. It was left a pocket of 3 meters below the bottom of the vehicle to facilitate the mesh generation and analysis, and to ease future alterations. These cells are not a problem for the overset approach; since this region does not exist in the background (it is below the "floor") these elements are called "dead cells" and they

simply do not count for the transient flow solution. Without the air pocket, the geometry would look like figure 5.3.



Figure 5.3: Side view of the train volume without the air pocket.

With both geometries created, the only thing missing was to adjust the coordinates of each of the trains to place them where desired. Naturally, they were facing opposite directions, on the different tracks separated by 4 meters. Both vehicles were placed with its rear approximately 40 meters from the extremity of the domain. That made it so that they were initially - at $t = 0$s - separated by 68,6 meters.

Figure 5.4 is from the ANSYS Fluent software and shows the initial relative position of the trains.

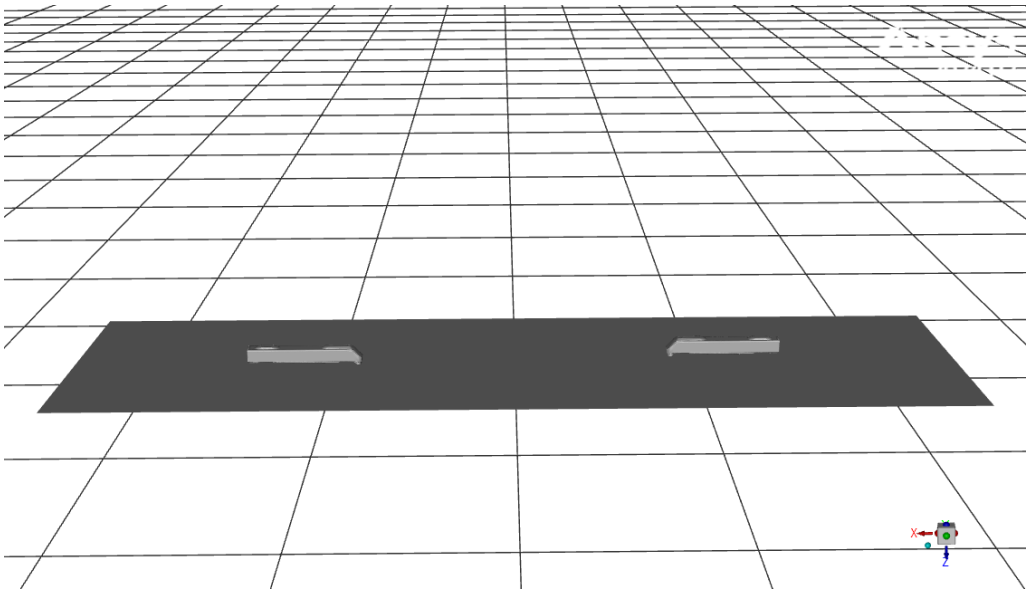


Figure 5.4: Perspective view of the 2 vehicles and their initial positions in the domain (only the floor is represented).

Afterwards, it was proceeded to the mesh generation. The outer volume had an element size of 4 meters - quite large, but enough for the distance to the vehicles. Then, 2 BoI's were conceived, with the one on the intermediate volume having a cell size of 2 meters and on the inner volume 1 meter. A face sizing was created on the "floor" of the domain

(element size of 0,5 meters) to improve the mesh quality and overlap nears the bottom of the trains. The growth rate was always 1.1. These data are synthesized in table 5.3.

Volume/Surface	**Element Size**	**Growth Rate**
Outer Volume	4m	\
BoI (Intermidiate)	2m	1.1
BoI (Inner Volume)	1m	1.1
Face Sizing (Floor)	0.5m	1.1

Table 5.3: Mesh parameterization for domain.

The mesh had 2 454 823 elements. The average aspect ratio was 1.85 and the maximum (on the worst cells) was 8.02; both were adequate to the project. It can be seen in figure 5.5.

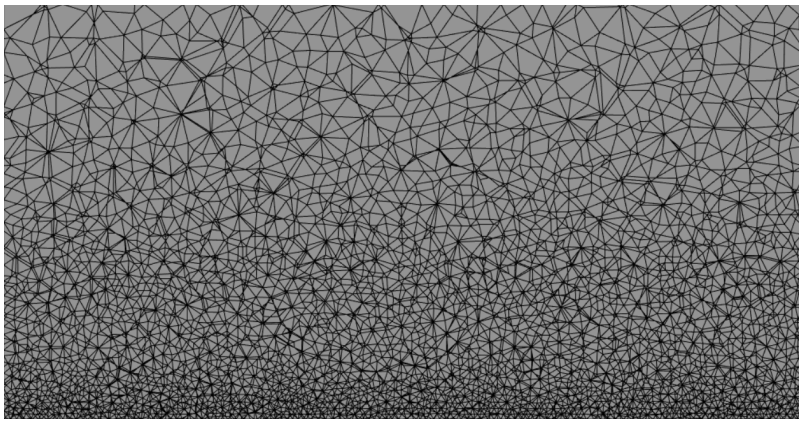


Figure 5.5: Close side view of the mesh of the domain, allowing to distinguish the different layers of element sizes.

For the train, an element size of 1 meter was set, with a growth rate of 1.1. It generated around 2.1 million elements (it varies between the vehicles) and the aspect ratio was around 1.81 on average and 8.13 maximum. The mesh is shown in figure 5.6.

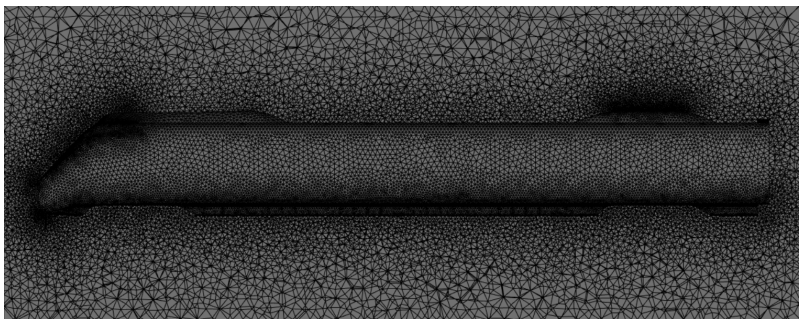


Figure 5.6: Side view of the mesh of train volume.

Therefore, in total, the whole configuration had around 7.5 million elements.

It was now possible to create the transient ANSYS Fluent setup. Once more, the turbulence model was SST $k-\omega$; however, to guarantee stability with less iterations and regardless of the time step initialization, it was decided to use a 1^{st} order convective scheme. The pressure-velocity coupling algorithm chosen was PISO to lower the computational effort.

The boundary conditions are those in table 5.4. The most significant changes are the fact that all the "walls" of the domain are set to pressure outlet and that the turbulence intensity was decreased to reduce the chance of instability in the first time steps. After inputting the reference values for calculating the aerodynamic coefficients, the solution was initialized (with a standard initialization) with the values of $0.375\text{m}^2/\text{s}^2$ for the turbulent kinetic energy (k) and 7.3s^{-1} for the specific dissipation rate (ω).

Surface	**Boundary Condition**	**Observations**
Frontal, rear, side and upper surfaces	Pressure outlet (gauge), p = 0Pa	TI = 1% TVR = 10
Train's and lower surfaces	Wall (no-slip)	\
Overset (limits)	Overset	\

Table 5.4: Boundary conditions on the differente surfaces for the train passing simulations.

Then, the overset interface entitled "moving_train" was created, with the fluid cell zone of the domain being the background mesh and the trains as the component zones. To create the dynamic mesh, an UDF was imported and compiled into ANSYS Fluent to define the motion of the moving trains. It was a few simple lines of code in the C programming language, defining the x velocity to 50m/s (instead of 55, for simplification). There were actually 2 UDF files, where the only difference is the minus sign in the velocity, to make sure the "secondary" train is moving in the opposite direction as the "primary" one. Both files are attached as appendices, in A.

The only things left to input were the variables associated with time and convergence. The condition for convergence inside a time step were the same as previously, residuals dropping below 10^{-4}. For each time step, 15 iterations were run; this number usually changes from 15 to 20, sometimes more, sometimes less. However, for this case, this should suffice.

To define the time step, the inequality in 5.1 was looked into once again. Solving for Δt and updating it with the values of u and Δx, it looks as in equation 5.2.

$$\Delta t < \frac{\Delta x}{u} \iff \Delta t < \frac{0.5}{50}\text{s} \tag{5.2}$$

Which translates to equation 5.3, so the time step must be smaller than 0.01 seconds.

$$\Delta t < 0.01\text{s} \tag{5.3}$$

To allow smoother transition of information and cover the tiny elements around the more complicated protrusions of the vehicle, a time step of 0.001 seconds was selected, which signifies a Courant number of 0.1 along the majority of the domain. This is good enough to guarantee continuity between consecutive time steps and accurate results.

Hence, the problem of low Courant number is solved. All that remains is to evaluate the number of orphan cells. ANSYS Fluent has a functionality for that, which immediately informs about the number of orphan cells in the overset interface. It also allows the user to input a command to identify where they are.

In the previous configurations, there were around 3 000 to 8 000 orphan cells, in a mesh with no more than 10 million elements. The number itself is not that high; however, since they were concentrated in the same places (close to the train's critical zones) this became an issue.

Then, in this case, at $t = 0$s, there were 146 orphan cells, a considerate improvement. This number changed at every time step (as the overlap is rebuilt) but it never left the gap from 100 to 400 orphan cells - this decline was likely due to the modifications in the geometries and numerical meshes. So, this issue was also resolved. This setup has been redesigned to not have convergence or accuracy issues.

The number of time steps to be covered by the simulation is the only thing left to decide. That is a function of the time step value and the total time of the event. The total time to include the whole passing manoeuvre is given by equation 5.4.

$$t_{total} = \frac{2L}{u} \tag{5.4}$$

Where L is the characteristic length of the train and u is the characteristic velocity of the flow. Solving for the values of 25.7m and 100m/s, we get equation 5.5, and a total time of approximately 0.5s.

$$t_{total} = \frac{2 \times 25.7}{100} = \frac{51.4}{100} = 0.514s \approx 0.5s \tag{5.5}$$

This implies that 500 time steps is enough to cover the whole phenomenon.

Nevertheless, at the initial distance the vehicles are stationed at, more than that is necessary. To cover the initial distance between them (68.6m, which will take them 0.686s to travel) and give some margin after they pass each other, where their wakes are still interacting, the total time was set to $1.3s$.

This can always be adjusted by simply running the simulation for consequent timesteps after finishing. Still, at the moment, the setup was for 1300 timesteps.

Finally, it was possible to start running the simulations. For the first time in the passing manoeuvre investigation, everything was progressing smoothly; it was headed to convergence and the values of the aerodynamic coefficients, as well as the pressure gradients along the bodies looked regular.

Nonetheless, there was an anomally in the beginning of the simulation; something that was expected to happen and, because of that, accounted for. At the end of the first time step ($t = 0.001$s), there was a sort of shock wave, as the vehicles who were completely stationary started travelling at a high speed; that caused great pressure variations which disrupted the whole control volume for a fraction of a second.

So, the values of aerodynamic and pressure coefficients in the start are not accurate. The drag coefficients was the most affected. That is the main reason why the vehicles are so far apart at $t = 0$s; to give them time and space to stabilize and develop the actual slipstream before. The effect of the shock wave at the start of the movement was irrelevant at $t = 0.3$s, after 300 timesteps; that was when all the coefficients, as well as pressure gradients and velocity fields all over the domain become stable and coherent.

Another point of interest of this configuration, something to learn from in order to optimize the next one was how close to each other were the trains when their boundary layer's began interacting. Judging by the patterns of the aerodynamic coefficients, as well as the pressure gradients along the bodies during different points in time, it was deducted that the vehicles' started perceiving the effect of the passing manoeuvre when they were at around 8m of distance (in the x direction). At that point, interference and variations in performance parameters was significant and could only be justified by the change in flow field caused by the passage of the other train.

For this simulation, a lot of time was spent simply waiting for the vehicles to get closer. The almost 70m of distance separating them initially was a huge overshoot. So, for the next case, it would be possible to reduce that distance, based on the experience gained from this test. In the 0.3s it takes the trains to stabilize, at 50m/s, they each travel 15m. Considering all these values, the distance could be reduced significantly, to around 38m $(15 + 15 + 8)$.

This saves computational cost and human effort that can be transfered to other tasks.

Overall, this configuration was really interesting, as it was the first to be completed and achieve solid results. Nonetheless, by the time the manoeuvre was completed (in ANSYS Fluent), the final setup was ready, with better accuracy and more refined output data.

Even so, it was from this one that the final setup was created; so, in the next section - where it is described - most of the (repeated) parameters are either omitted or just addressed as a redundancy of these. The importance of all these arrangements, in particular, the last one, is that they helped understand how the *TrainSolutions* model behaves with unsteady CFD simulations. That contributed to establishing the highest-performing settings and apply them for the next stage of the work, in a continuous improvement methodology.

The final transient configuration largely replicates the best simulation conditions of the whole project, with a few adjustments introduced to enhance numerical stability and further refine the results.

5.2 Final Transient Configuration

While the preliminary simulation just described was running, the final transient configuration was being created. It is an improvement upon it.

As mentioned, the setup extensively detailed during the last section of this dissertation was the first unsteady one to converge and produce coherent results.

Nevertheless, these results are not as precise as desired, since it was necessary to remove the wheels and bogies from the geometry of the train. So, this configuration was created, with the same air gap (without the rails and ballast) but representing the wheels and bogies of the train, for a more accurate solution.

The goal of this part of the project was to end up with a setup as close to reality as possible; since the CFD investigation allow for many experiments to occur in a short period of time, it would be interesting to take advantage of that. As the work moves forward and mistakes get corrected, the setup gets progressively better. This configuration is the "final" one, as it was the more realistic and with the more sophisticated output data to be completed in time.

Then, its development occured as follows.

The geometry suffered few alterations. The domain is similar to the one used previously. The outer volume has the same dimensions; however, the other 2 have progressively smaller lengths, focusing the refinement closer to the trains.

Not only that, a lower volume - neighbouring the floor of the computational region - was created (comparable in size to the inner volume) to further refine the mesh in the area around the wheels of the vehicles, since that area has complicated edges and tiny geometries.

Table 5.5 displays the dimensions of the domain.

Volume	**Length**	**Width**	**Heigth**
Outer Volume	200m	60m	30m
Intermediate	160m	35m	18m
Inner Volume	120m	18m	10m
Lower Volume	120m	10m	0.9m[1]

Table 5.5: Dimensions of the domain volumes for the train passing simulations.

Figure 5.7 illustrates the domain from two different angles.

[1] Below the train, so -0.9m in the z direction

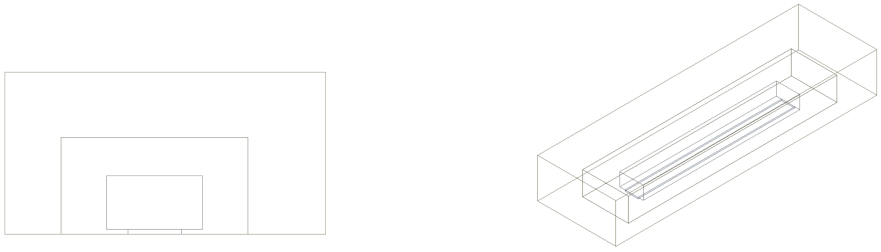


Figure 5.7: Front and isometric view of the geometry of the domain for the final configuration of the train passing study.

Afterwards, the geometry of the train was altered. Most notably, the wheels and bogies were introduced in this configuration, as that was the main path towards improving precision. The space left below the train (containing air that does is not accounted for during the transient simulations) was reduced to 1 meter. The reason behind it was reducing the total element number, to decrese the computational effort, since 3 meters was a margin bigger than necessary.

Other than that, everything dimension was preserved. Figure 5.8 shows the new geometry.

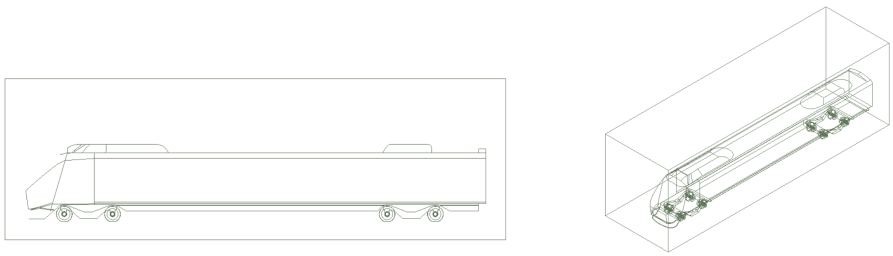


Figure 5.8: Front and isometric view of the geometry around the vehicles for the final configuration of the train passing study.

Figure 5.9 shows the train volume without the margin (how the solver treats it).



Figure 5.9: Side view of the train volume without the air pocket.

As stated in the end of the last section, the initial distance between the 2 vehicles was greater than it needed to be. So, based on the previous data, this time, the trains were stationed approximately 55m from each extremity of the domain, standing at 38.6m from one another at $t = 0$s.

Figure 5.10 depicts the new initial separation between the trains.

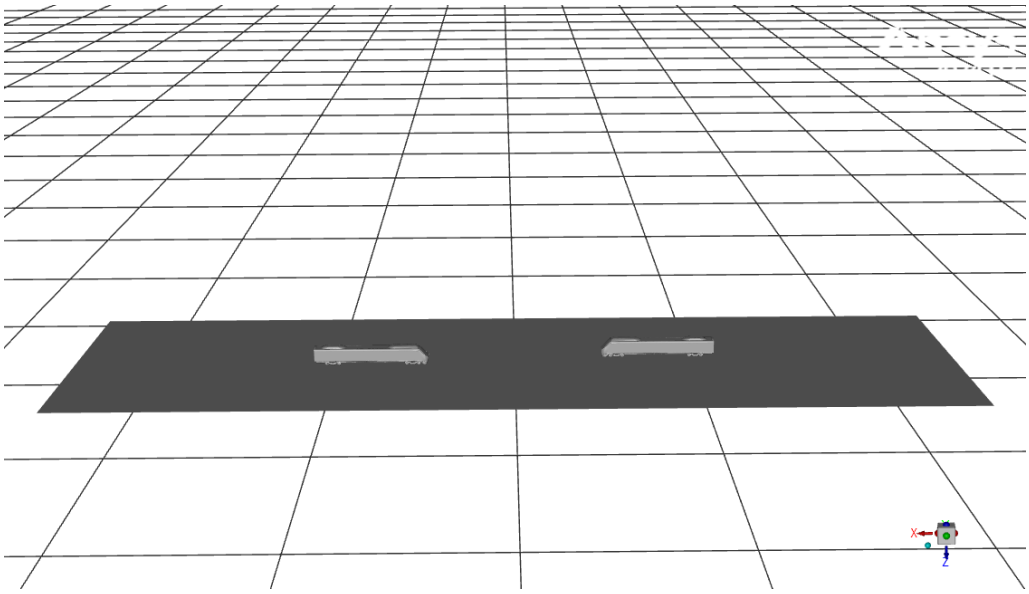


Figure 5.10: Perspective view of the 2 vehicles and their initial positions in the domain.

Then, the next step was to generate the background and component meshes. For the domain, the same logic was applied, with smaller cell sizes and one change. For the three existing volumes, the element size was reduced. The goal was to reduce it in the innermost region; however, to prevent poor information passage due to an exaggerated discrepancy between consecutive layers, all the element sizes were reduced, to protect continuity inside the whole volume.

The other variation was replacing the face sizing on the "floor" of the domain for another BoI body sizing in the lower volume. It had the lowest element size in this configuration (0.25m) to feature the best overlap with the component zone (the wheels and bogies on the train volumes). Table 5.6 presents the values selected.

Volume	**Element Size**	**Growth Rate**
Outer Volume	3m	\
BoI (Intermidiate)	1.5m	1.1
BoI (Inner Volume)	0.5m	1.1
BoI (Lower Volume)	0.25m	1.1

Table 5.6: Mesh parameterization for domain.

The domain's mesh had 4 010 429 elements. This time, the average aspect ratio was 1.81 and the maximum was 8.35, comparable to the previous one, so no issues here. Figure 5.11 shows the numerical grid from a section plane through the its length, from a closer point of view, to note the discrimination of the different cell sizes.

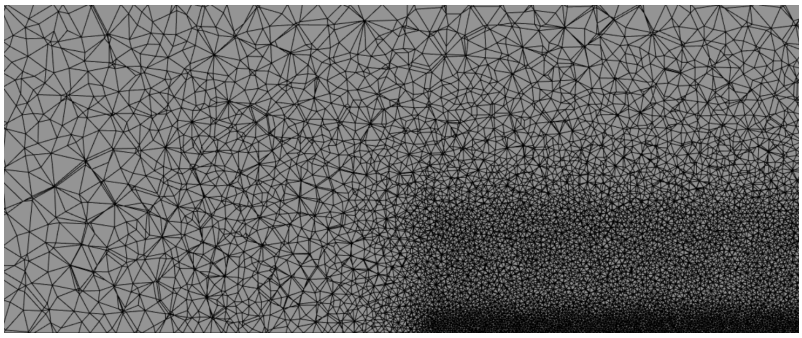


Figure 5.11: Close side view of the mesh of the domain for the final configuration.

For the trains' meshes, for this configuration, the element size was reduced to 0.5m. Since the wheels and bogies are complicated parts of the geometry, they are bound to induce problems in the mesh generation process. This is because the Meshing software is forced to generate tiny elements to represent the curvature and edges of these components. The sudden decrease in element size might produce issues like elements with high Courant number, large size discrepancy in consecutive layers and an elevated number of orphan cells in the overset interface.

High mesh quality is mandatory for this research. Therefore, to ensure that the software does not develop a numerical grid with poor quality and miniscule elements near these critical regions, the minimum defeature size was altered. Minimum defeature size is, by definition, the smallest geometric feature size that the Meshing is allowed to suppress from the geometry during defeaturing. By default (in ANSYS Meshing) this value is equal to 0.005m (5×10^{-3}m). This indicates that features smaller than 5 millimiters (such as small gaps or bulges) get removed from the train's geometry.

Then, for this study, that value was increased to 5×10^{-2}m or 5 centimeters. It was chosen to guarantee that all cells verify the condition $Co \leq 1$, equation 5.6.

$$Co \leq \frac{50 \times 0.001}{5 \times 10^{-2}} \iff Co \leq 1 \tag{5.6}$$

That was a significant increase; however, it was necessary. It made it possible to create a mesh with higher quality, despite the curves in the wheels and bogies (as well as the rest of the vehicle) not being depicted as accurately as if the parameter was not changed. This change meant the geometry was slightly less precise.

Nonetheless, it promoted an homogenization of the element size, as the difference between the average and smaller cells was reduced, which significantly improved continuity and overlap between component and background zones. This also lowered the computational cost (less elements) and improved convergence and the reliability of the results. A slighty less faithful geometrical representation of the train is rectified by an excellent numerical mesh.

Each one generated nearly 2.6 million elements with aspect ratios of around 1.81 on average and 8.41 maximum. The mesh is shown in figure 5.12.

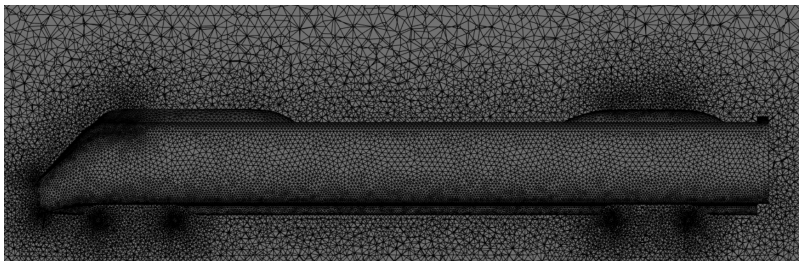


Figure 5.12: Side view of the mesh of train volume.

The whole arrangement had a total of 9 125 478 elements.

The ANSYS Fluent parameterization was unaltered. Same turbulence model, pressure-velocity coupling algorithm, boundary conditions and so on.

Here, as a result of the carefully selected mesh parameterization, the presence of orphan cells was even lower. At $t = 0$s, there were only 36 orphan cells in the whole overset interface. This number swayed during the manoeuvre, from around 20 to 80; so, the overlap between background and component zones is almost perfect, which is outstanding.

In order to get significant output data out of this simulation, the quantities and graphics for analysis had to be previously selected, for ANSYS Fluent to register them during the whole event. The aerodynamic coefficients were monitored along the 3 axis for both vehicles (C_x, C_y and C_z). The value of pressure coefficient (C_p) in the midpoint of their intersection was also deemed interesting for this case.

Moreover, to have some images of the fluid flow, animations were created; they are a compilation of the same graphic result at every time step. They allow the perception of how certain values evolved, both in time and in space, during the passing manoeuvre. For this simulation, 4 animations were designed.

There is an animation displaying the absolute pressure around both trains during the manoeuvre, as well as one displaying the absolute pressure on a longitudinal xy plane (top view), to better understand their interaction. An animation to show the pathlines around one of the vehicles was created to see where the air flows to when they pass by each other. Finally, another one was created on a longitudinal xz plane (side view) to perceive the wake formation and perturbation in the manoeuvre, by creating a velocity contour on said plane.

All these results are to be presented and analyzed further ahead in chapter 6.

To ensure stability, the number of iterations per time step was boosted to 20. This increase, conjugated with the higher number of mesh elements and the existence of more animations and force reports (more data to be written at the end of every time step) rose the computational cost; previously, it took ANSYS Fluent around two and a half minutes to run each time step, now, it takes four minutes per time step. That is why it is essential to take into consideration computational effort when setting up the configuration, particularly for broad projects with sensitive time windows such as this one.

All that was left was to define the total time of the simulation. Given that each train moves at 50m/s in opposite directions, the relative velocity is 100m/s. The system has to move 38.6m for the vehicles to reach the midpoint, then 50.4m (combined length of the 2) to complete the passing manoeuvre. Then, leaving the simulation running for a few more time steps to see wake interaction and allow other phenomena to develop fully might be wise. So, in the end, the total time was set to be 1 second (in reality, it was extended to 1.02s); after that, the flow becomes predictable, and it is not reasonable to continue an expensive CFD experiment to see the trains fully leaving the other's wake.

This simulation took a few days to be ready. The results were satisfactory and they contributed significantly to characterizing the Portuguese train's aerodynamic performance. Even so, in the pursuit of a more profound knowledge, an attempt to create a brand new configuration was made, to increase the accuracy of the results even further. The objective was to solidy to a greater extent the numerical research before moving to the field experiments.

5.3 Advanced Configurations and Further Developments

From a similar perspective to the last section, while the simulation for the new configuration with the wheels and bogies was running, another one was being developed.

Despite already having the "exact" representation of the train for the CFD analysis, it neglects all of the surroundings. It would be interesting to have results from a geometry including the rails and ballast below the vehicles. So, that was the main focus while waiting for the earlier-mentioned results.

Changing from the "air gap" approach to the one with rails represented would improve precision and reliability of the results before proceeding to full-scale experiments.

Nevertheless, this proved to be an insurmountable challenge. Despite applying the best-performing techniques used across the whole project, some problems persisted. Even after successive attempts to alter the geometry to make a more fitting mesh, and combining that with the different Meshing possibilities (like increasing the minimum defeature size) the overset interface still included thousands of orphan cells.

Several different techniques were employed to try to solve this issue; even experimenting with a different turbulence model ($k-\epsilon$, usually better to ensure convergence) but to no avail, as the simulation kept diverging in the first few time steps. Since the project is extremely time sensitive, the idea to go forward with this advanced configuration was abandoned for this dissertation.

Nonetheless, that is still a relevant analysis to be performed in the context of studying the *TrainSolutions Portugal* model. So, it might be carried on as an extension of this project, hence it being mentioned ahead in this report, in the future works section, 7.3.

The discretization of the methodology adopted in this project ends here, after these 3 past chapters outlining 3 different studies. Naturally, there was much more that could

be done; however, the experiments performed up until this point turned out to be useful for characterizing the aerodynamic performance and solid enough to develop a noteworthy thesis.

The next chapter covers the detailed analysis of the results found during the study of the 3 different operating conditions. The results already presented, combined with new output data extracted from ANSYS Fluent, are examined to produce a concrete assessment of the Portuguese train's aerodynamics, in a technical report seeking to verify its safety and stability, while depicting strategies to improve its energy efficiency and reliability.

Chapter 6

Results and Analysis

After the previous chapters - divided as the 3 main tasks of the project - described the methodology adopted during this investigation, this one is dedicated to fully dissecting the results attained from the CFD aerodynamic study of the Portuguese train.

In the same logic, this chapter is also split in 3 sections, each focusing on one of the operating conditions whose simulations were carefully explained in chapters 3, 4 and 5. It is intended to provide a deeper understanding and interpretation of some of the data that was previously presented, while introducing other output information as they become relevant for the analysis.

While some analysis was performed in said chapters, that only happened as it was necessary for enabling the progression of the work. For example, that was the case for the headwinds simulation, when comparing the results obtained for the Portuguese model with the benchmark ones from the ICE allowed to assess the validity of the numerical model and verify if the project was in the right track.

That being said, in this part of the report, the assessment of the results is for the main purpose of reviewing the aerodynamic performance of this model, understanding the behaviour in different situations and verifying its stability and by analysing the key flow regions, predict and suggest changes to the geometry.

6.1 Headwinds Simulations

A project of this dimension requires a substantial amount of operating conditions to be investigated. Naturally, some are more complicated than others.

Having little experience with any CFD software prior to the realization of this thesis, it would be unthinkable to begin the aerodynamic assessment of the *TrainSolutions Portugal* train model with the unsteady passing manoeuver, which requires a lot of skill in handling all the steps of the process. Part of the reason for beggining this study with the headwinds case was to progress in the work while conducting a simpler research, which allowed to get used to ANSYS Fluent. Several months were necessary to complete this task, even though

it was the simplest one. Nevertheless, that time was not lost, as it was fundamental to begin with an easier situation to learn the basics of the software (geometry modelling, mesh generation, parameterization, post-processing...) before proceeding to the more sophisticated simulations.

Furthermore, that was a good opportunity to learn the specifics of this project. Getting to know the phisical model of the train being studied, as well as the conditions under which it shall operate is essential. Not only that, but some conclusions drawn from this assessment Being able to do that while producing results worth analysing was a plus for the dissertation.

With the decisions made in preparation for the headwinds study, the results obtained for both the aerodynamic coefficients and the airflow around the vehicle ended up not being the main point of interest. Instead, comparing the different configurations and addressing what changes were provoked by each modification has the potential to improve the following experiments in this work.

In chapter 3, it was concluded that the using the configuration with SST $k-\omega$ turbulence model and 2^{nd} order convective scheme would be the best for attaining the most accurate results.

Comparing the 1^{st} and 2^{nd} order convective schemes, it was easy to notice some differences. In fact, both had their strengths and weaknesses, which made them equally relevant for this project. When comparing the values of C_x obtained from the study realized to the ICE model with the ones stated in the standard, it was clear that the configurations using 2^{nd} order got closer to reality, as seen in table 6.1.

	S_1_E	**S_1_O**	**S_2_E**	**S_2_O**	**Standard**
C_x	-0.173	-0.156	-0.154	-0.138	-0.12

Table 6.1: Values of drag coefficient obtained for the 4 different configurations of the ICE model - sorted by how closer they got to the standard.

Nevertheless, throughout most of the project, everytime a 2^{nd} order configuration was adopted, it had to be initialized as a 1^{st} until reaching a certain degree of stability; this was particularly important during the crosswinds study. Starting immediately with 2^{nd} order led to divergence more often than not. So, it is possible to conclude that, even though using 2^{nd} order helps getting the more exact results, this configuration is riskier - more influenced by the mesh quality and other setup parameters - meaning it is wise to switch between the two considering the ocasion.

1^{st} order convective scheme is more stable, while 2^{nd} order convective scheme gets the more reliable results.

Then, it was also concluded that SST $k-\omega$ produced better results compared to $k-\epsilon$, once more, corroborated by the data in table 6.1. This was expected, as the literature states that the SST $k-\omega$ turbulence model performs better in train aerodynamic works.

The other difference already stated between these 2 turbulence models was the fact that configurations using $k-\epsilon$ usually converge much faster. However, in this case, this advantage was not interesting for the project, as the $k-\epsilon$ model was never used.

All of these deductions had already been stated; they were fundamental in allowing the work to progress.

So, the most interesting remarks regarding the benchmark tests left for this chapter are concerning the mesh generation. Creating the mesh for a specific ANSYS Fluent simulation takes time and often requires some iteration to get the parameterization right, in order to get the best numerical grid for that specific case. In that regard, having some notions about what values or features are appropriate for each situation is incredibly helpful.

First of all, it was important to study the impact that the difference in the number of elements created. Looking at the different values of C_x for the different meshes of the best-performing configuration, we can see how much the coefficient changes with the number of elements, in figure 6.1.

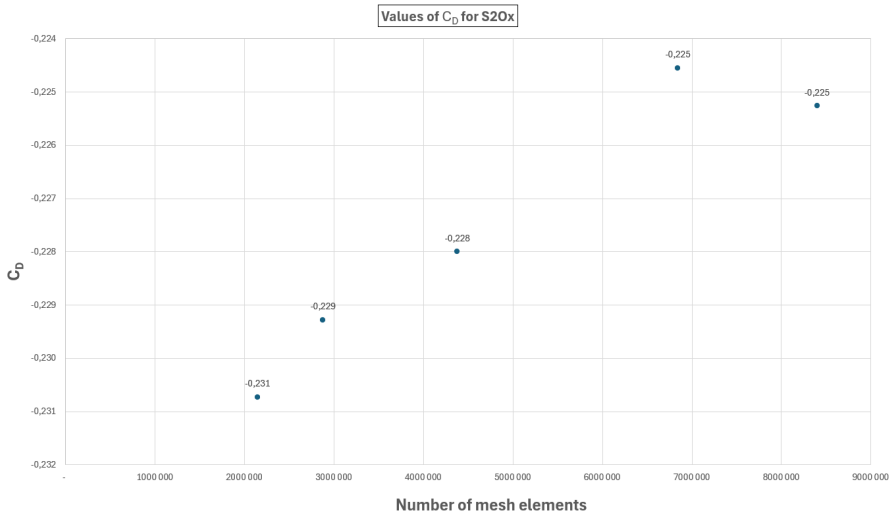


Figure 6.1: Values of C_x plotted with number of elements in each mesh.

The number of elements varies from slightly over 2.1 million to almost 8.4 million. Even so, by analysing the pattern in the data of 6.1, it is noticeable that the biggest changes in the value of C_x happen between the first 3 meshes; the 2 best ones have a high difference in the number of elements, while getting really close results. This is particularly important to understand, because even though increasing the number of elements is almost guaranteed to improve the quality of the solution, it also increases the computational effort associated with the simulation.

Until around 6 million elements, all simulations had a low computational cost. That started to be an issue for the last configurations, with these taking longer per time step to run. So, since the results were getting to a point where increasing the mesh quality

did not translate to a significant rise in the accuracy of the results, while it is making the simulation much more demanding, it was deduced that, for this particular case, it was reaching a point where it does not make sense to keep refining the mesh.

Hence, most simulations performed that ended up producing significant results in this dissertation, had a number of cells between 6 and 9 million. This was found to be the region where the computational cost is manageable and the results are satisfactory, and generating a mesh with more elements intensifies the first but not necessarily the second.

Naturally, this varies with other parameters (the dimensions of the domain, the operating conditions being studied, if the regime is steady or transient...) but this is a solid base to work on.

Moreover, looking at the C_x values produced while testing the ICE model, there were clear discrepancies between using the SST $k-\omega$ and the $k-\epsilon$ turbulence models; however, that was not verified for the Portuguese train. The likely justification for that is the fact that $k-\omega$ performs better than $k-\epsilon$ only if the mesh quality allows it.

Therefore, the best mesh for this model was not good enough for what was intended in this study. That is not exactly a problem caused by the number of elements, since the ICE mesh had fewer elements; it possibly relates to whether or not they are correctly positioned.

Figure 6.2 illustrates the mesh used for the ICE and the best one for the Portuguese train besides one another, from a side view. It is clear that for the ICE the inner volume is much closer to the vehicle than for the other model. This allowed a smaller cell size (0.3m compared to 0.4m) which ended up creating a more coherent numerical grid, that allowed the SST $k-\omega$ model to provide more accurate results.

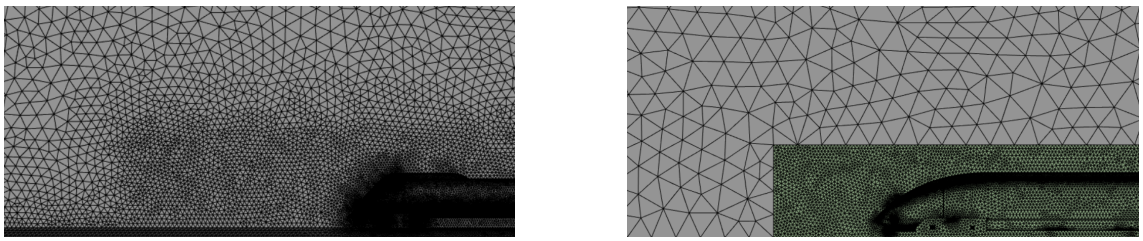


Figure 6.2: Close side view of the meshes used for both models in this experiment, to verify the volume of the region near the train.

This encouraged the creation of intermediate volumes in future studies, to have smooth transitions between element sizes, allowing for a coarse mesh to coexist in the majority of the domain with a much finer mesh near the trains. This way, the domain can remain extensive to show the whole fluid flow, while having a significantly small cell size in the region bordering the train, to replicate the great results obtained in the benchmark tests, getting a robust solution at the minimum computational cost possible.

So, for the following parts of this aerodynamic assessment, not only was the best numerical configuration chosen, the importance of selecting an appropriate division of the domain - combined with the mesh generation process - was considered as well.

Finally, regarding the mesh generation process, it is important to take into account its quality parameters, in particular, the aspect ratio. The average and maximum aspect ratio for the 5 meshes used for the *TrainSolutions Portugal* model was compared; these values correspond to those in table 6.2.

Mesh	Average Aspect Ratio	Maximum Aspect Ratio
Mesh 1	1.87	24.3
Mesh 2	1.87	12.3
Mesh 3	1.84	35.4
Mesh 4	1.82	14.5
Mesh 5	1.82	9.98

Table 6.2: Average and maximum aspect ratio for the 5 meshes.

The average kept declining (which means, improving) as the refining progressed; however, that was not true for the maximum value. It is important to note that, without the face sizing applied to the rails, these values were all in the hundreds, as the Meshing software was generating elements of irregular shapes to patch the track with its surroundings. Having a mesh containing cells with terrible quality (even if its only the worst 1%) will decrease the of the solution - even so, all of these cases are acceptable. Nevertheless, these variations likely stem from the discrepancy in size between consecutive layers, as well as the growth rate chosen.

So, after creating the mesh, analysing the quality parameters to ensure that there is no region of poor quality is essential.

This concludes the analysis of the results obtained for the headwinds experiments and benchmark model testing. The main finding was that the best configuration to use for the next studies is the one using SST $k-\omega$ turbulence model and 2^{nd} order convective scheme. Furthermore, considerable knowledge regarding CFD investigation of railway vehicles aerodynamics was acquired. That was useful for the rest of the project; in particular, the proficiency in developing a high quality mesh proved to be incredibly helpful, as that is a time consuming task whose quality impacts the whole research.

6.2 Crosswinds Simulations

The study of the aerodynamic response of the *TrainSolutions Portugal* model when operating under crosswinds produced valuable results, namely, the values of C_x, C_y and C_z for each yaw angle, which were exposed in 4.

The output data from the ANSYS Fluent simulations are divided into 2 main categories; the aerodynamic coefficients and the graphic representation of pressure and velocity around the train's body.

6.2.1 Aerodynamic Coefficients

In this part, the values of force coefficients felt by the vehicle are to be further analysed.

Previously, the curves of C_x, C_y and C_z were presented and analyzed. Now, overlapping these values with the ones for the ICE (from the standard) it is possible to have a more thorough understanding of the Portuguese train's aerodynamic performance.

Figure 6.3 shows, in the same graphic, the values of C_x for both models.

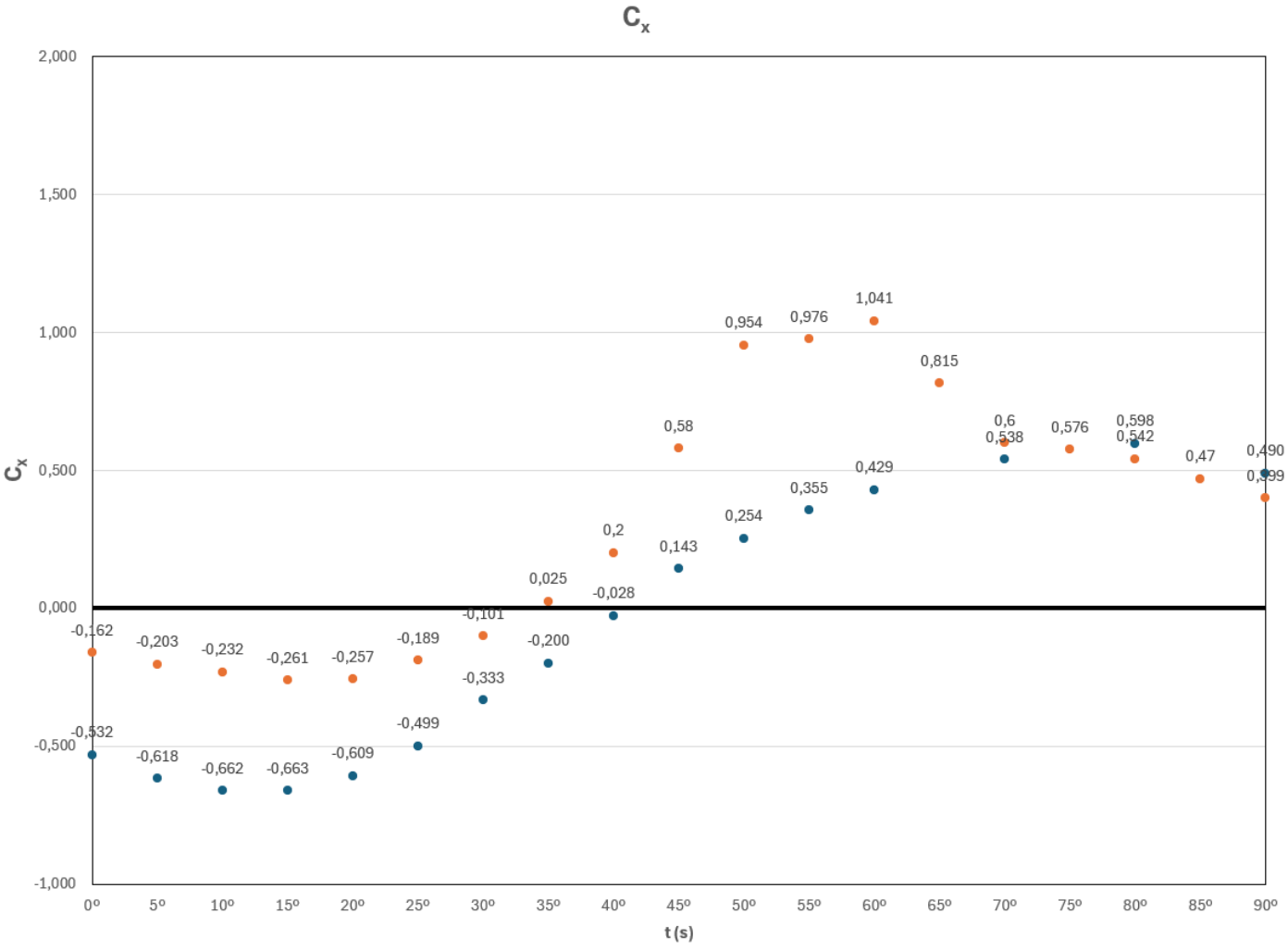


Figure 6.3: Graphic of C_x for both models for each yaw angle.

The first feature to notice is that the shape of the characteristic curves is similar. The minimum (highest value of drag coefficient) happens at almost the same exact point of the spectrum. After that, the evolution of the force coefficient in the x direction follows a

similar path for both models. However, it is important to note that the C_x always has a lower value for the *TrainSolutions* model, which indicates that the drag is higher. In fact, that happens for most yaw angles. This indicates that this train is likely to have a lower energy efficiency than the ICE, since the resistive force (felt by the vehicle) is higher.

The curves follow a resembling trajectory until around 60° (the point at which convergence issues began) where the values of C_x for the Portuguese train keep increasing (at a slower pace) while for the ICE a maximum is reached at that yaw angle. For the last yaw angles (70°, 80° and 90°) the results are close, but the trajectory is different. Even though the force in the x direction is not necessarily the most relevant for this case study, some conclusions can still be drawn - like the probable lower energy efficiency.

In the end, the overall aspect of the curves was comparable, which likely indicates that the study was performed correctly and that the behaviour of the Portuguese train under crosswinds circulation is as expected. Other than that, analysing the other aerodynamic coefficients is useful for affering the stability and comparing to the benchmark results.

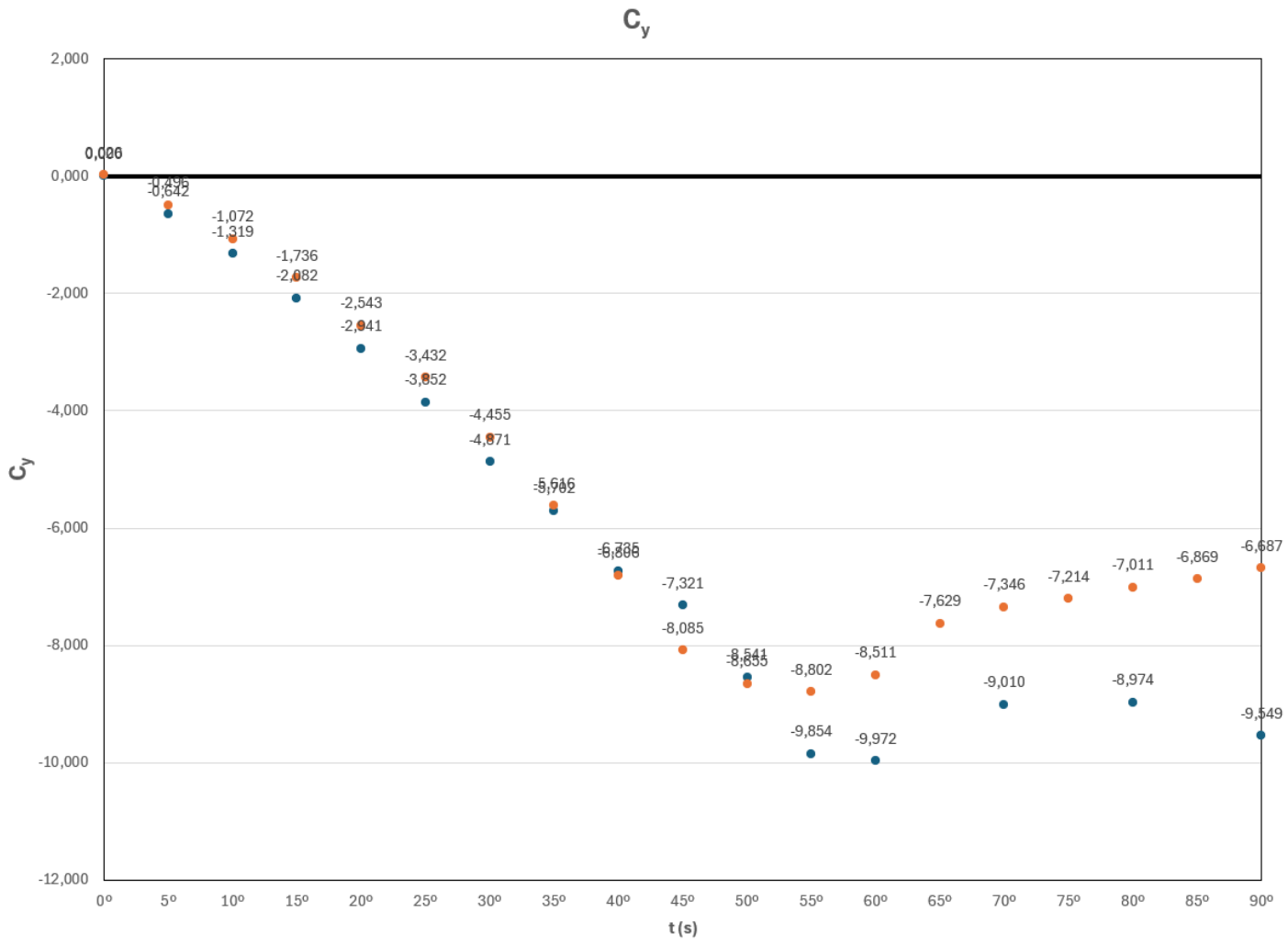


Figure 6.4: Graphic of C_y for both models for each yaw angle.

Figure 6.4 illustrates the same curve, now for C_y.

This is possibly the most important quantity when analysing the stability under cross-wind, since C_y is equivalent to the lateral force coefficient C_Y, the force in the direction perpendicular to the movement and aligned with the lateral wind. It indicates how strong is that force pushing the vehicle away from the track, posing the risk of derailment.

This time, the overlap between the 2 curves is almost perfect until 40°, which is remarkable. C_y is practically null for 0°, and then it is slightly higher (more negative) for the Portuguese train for almost every yaw angle. For both models, the maximum value is registered between 50° and 60°, showing once more that the correlation is elevated.

After that, ICE's curve follows a clear ascending trajectory, while the other model does not, once more, possibly due to the convergence issues in that part of the range. Even so, the curve for the tested model is surprisingly close to that of an approved vehicle, with the same pathway and similar values of C_y for the most relevant angles of incidence.

Hence, the project was starting to gain shape. The aerodynamic performance of the *TrainSolutions Portugal* train under crosswinds is a bit worse than the german model, but still heavily predictable which is great for confirming its stability and safety during circulation.

When analysing the pressure gradients and velocity graphics ahead in this chapter, it might be interesting to see why the maximum values of C_y do not happen for the highest yaw angles; since that is when the incidence of the wind in the y direction of the train is at its peak, that would be the most logical conclusion.

Finally, figure 6.5 displays the results of C_z.

C_z is the lift coefficient. Since the z axis is downwards, negative values of C_z correspond to positive values of C_L.

Once again, the curves have the same trajectory. Between 0° and 10°, C_z is positive, meaning that the vehicles feel a force pulling to the ground. After that, it keeps decreasing, meaning that there is a lift force pushing the train upwards, which can destabilize it and cause it to derail.

The values of C_z keep descending until around 50°, where it hits a minimum for both vehicles. After that, the lift force reduces, with a clearer trajectory for the ICE, which might also be explained by the fact that the increment was altered to 10° insted of 5° in the end of the spectrum for the Portuguese model.

This time, this model actually performs better, as it always has a higher value of C_z, meaning less C_L and more stability. This can be explained by the fact that is has a more robust body geometry. While the ICE looks design to cut the energy consumption by being as aerodynamic as posible, the *TrainSolutions* model is bulkier, which reduces the energy efficiency but improves stability. That is proven here.

Even so, the values of C_z still follow a similar characteristic curve, meaning this study has succeeded in replicate real test aerodynamic coefficients.



Figure 6.5: Graphic of C_z for both models for each yaw angle.

In chapter 4, the analysis of the moment coefficients was discarded. However, in order to have a more in-depth analysis of the stability and the risk of derailment, that decision was reverted.

Just like the force coefficients, they are adimensional quantities, which can be calculated for all 3 axis. In this case, the most relevant one is C_{Mx}, since that is the direction of the movement. This provides information regarding the overturning loads to which the vehicle is subjected.

ANSYS Fluent software calculates this by itself, using the equation in 6.1.

$$C_{Mx} = \frac{M_x}{\frac{1}{2}\rho v^2 AL} \tag{6.1}$$

Even so, for this study, the value of C_{Mx} was calculated in a specific point, to allow a particular comparison with a value from the standard. In the same table where the values

of C_x, C_y and C_z where extracted from, there is a column for C_{Mx}, C_{My} and C_{Mz}; and another one for a quantity entitled C_{Mx_lee}.

C_{Mx} is a dimensionless measure of the aerodynamic rolling moment acting on the train around the longitudinal x-axis C_{Mx_lee} is the moment coefficient in the x-axis evaluated for the leeward side - the side facing away from the wind.

For this study, C_{Mx_lee} was analysed for a point in the train near the leeward rail. In ANSYS Fluent, it can be calculated by creating a report for keeping track of a moment coefficient in the train, in a point in the aforementioned rail, along the x-direction.

Due to geometry, that is often one of the most critical points to be studied; the value of C_{Mx} usually peaks there, and it is a great way to analyse the risk of overturning (since a high moment in this point may cause the wheel to lose contact with the track). So, the value of C_{Mx_lee} for every yaw angle was then acquired from the CFD software and plotted along the values in the standard for the ICE model.

That curve is presented in figure 6.6.

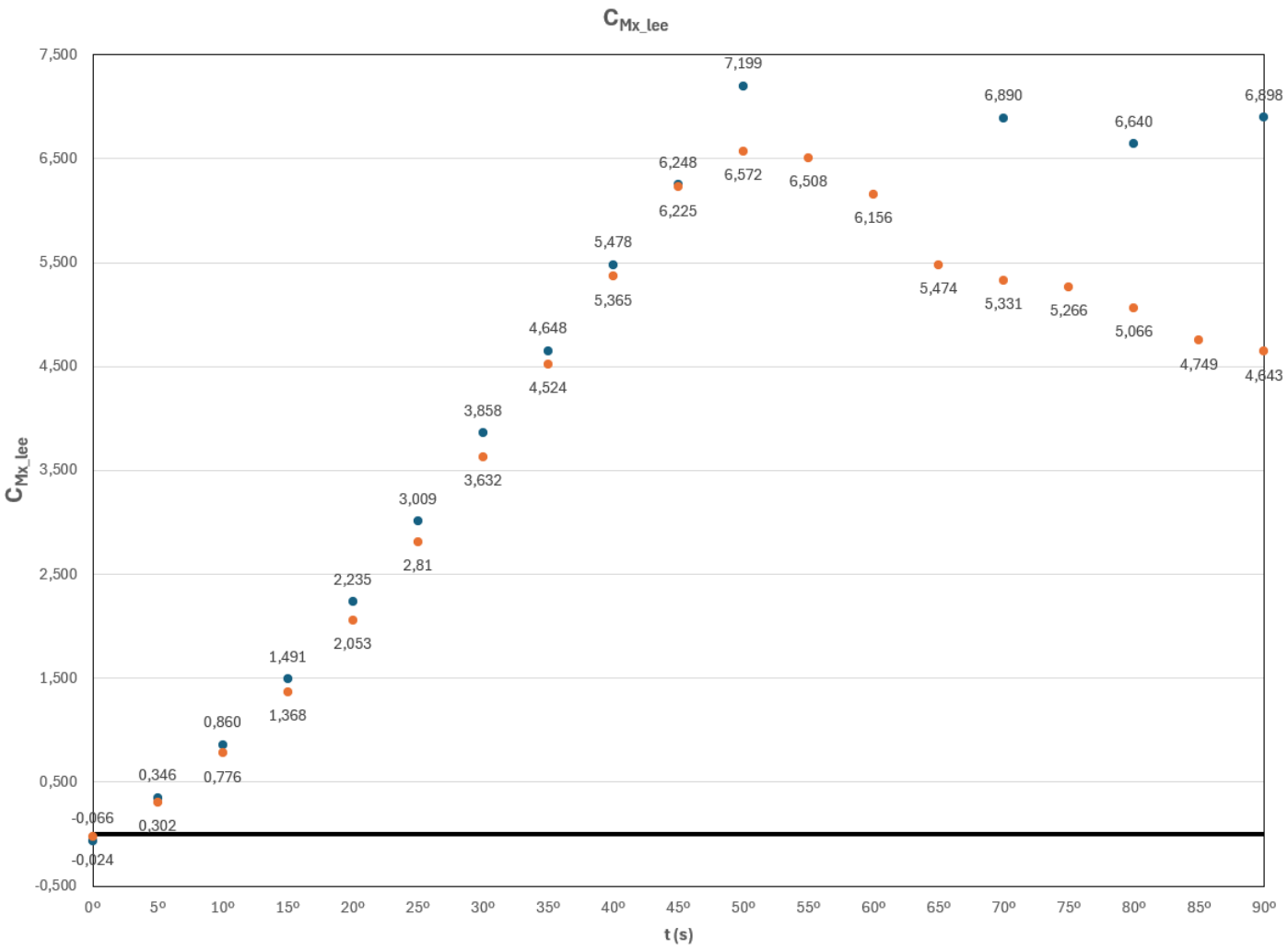


Figure 6.6: Graphic of C_{Mx_lee} for both models for each yaw angle.

Once more, the overall shape of the 2 curves is the same. Until 45° there is a big overlap of the values of C_{Mx_lee}, with the Portuguese train performing slightly worse. After that, the convergence issues began and some yaw angles even failed to produce significant results, just like mentioned previously.

Both curves have a maximum between 50° and 60°. This corroborates the data attained from the C_y analysis (6.4); these 2 quantities are the principal force and moment being exerted in the wind direction, responsible for destabilizing the train's movement and, in the worst case scenario, derailring it. It proves that this is, in fact, the most critical region.

After 45°, the values of C_{Mx_lee} for the model being studied are relativelt high compared to the ICE. This is not ideal; even so, those are not worrying loads, strong enough to pose a significant threat to regular operation. It just shows that, in this matter, this train performed worse than the benchmark model present in the norm.

To further defend this model, it would be interesting to replicate this testing conditions in a small-scale or full-scale experiment, instead of CFD simulations.

To close this section, after analysing all the aerodynamic coefficients for both models, the Portuguese train is likely to have a worse energy efficiency and have a similar sensibility to strong crosswinds, with bigger loads pushing it out of the track, but more vertical stability. These data should be complemented with experimental validation. This model performed as expected and this research indicates that it is safe and reliable.

The next part, focuses on analysing the fluid flow with graphical support.

6.2.2 Pressure and Velocity Distributions

In this section, the graphical results obtained are presented. Three sorts of graphics were created to assess the aerodynamic performance.

They were contours of absolute pressure around the train, pathlines around the vehicle (coloured by velocity magnitude) and velocity magnitude contours around the train's cross section. The full results are presented in appendices B, C and D, respectively.

There, the images of these graphics are presented for every yaw angle; in this chapter, to avoid pointless repetition, only the more relevant ones are presented.

So, the first ones to be analyzed were the pressure contours. They show the train geometry with different colours, representing the absolute pressure in each region. Hot colours represent high pressure and cold ones low pressure zones.

In the beggining of the study, 0°, the pressure distribution is simetrical (as expected) and the areas of high and low pressure can be predicted easily. This is seen in figure 6.7.

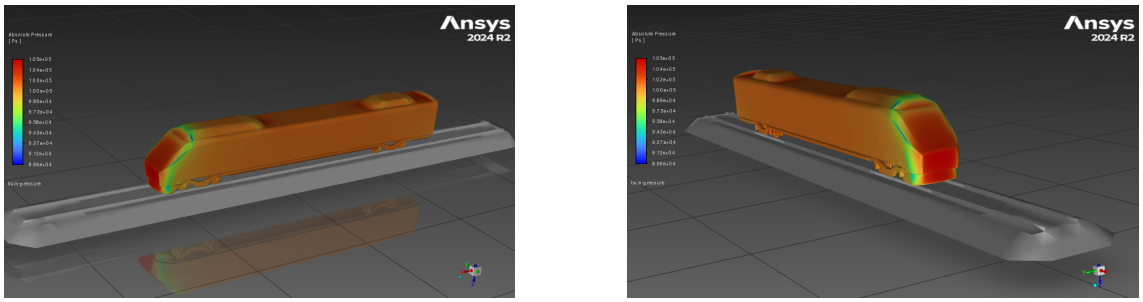


Figure 6.7: Contours of absolute pressure around the train for the crosswind study at a yaw angle of 0°, viewed from the leeward (left) and windward (right) sides.

There is a region of high pressure around the train nose, since it is facing directly the wind, followed by a few lighter colours, which indicate an area of low pressure near the edge. The rest of the train has the same shade of orange, so the rest of the body has the same absolute pressure, being subjected to viscous drag forces.

There is no clear distinction between the windward and the leeward side. For reference, the y-axis is positive from right to left in these images; so, the picture on the left shows leeward side, while on the right it is the windward side.

As the yaw angle increases, some changes start to appear. On the windward side, the absolute pressure increases (as it is being hit directly by the air flow). On the leeward side, the pressure does not necessarily decrease, but it is lower, hence the increase in C_y, the train feels a lateral force caused by the wind. This can be clearly seen already at 30°, in figure 6.8.

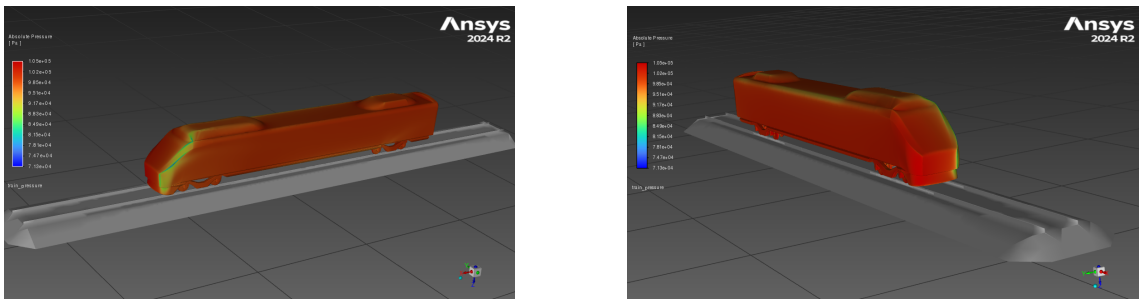


Figure 6.8: Contours of absolute pressure around the train for the crosswind study at a yaw angle of 30°, viewed from the leeward (left) and windward (right) sides.

Another difference to notice is that, the low pressure area that circled the train's frontal area is now an oblique line starting in the front at the leeward side, extending to the windward side, where it follows the horizontal edge until its rear.

This phenomena becomes clearer on larger yaw angles, such as 45°, as shown in figure 6.9.

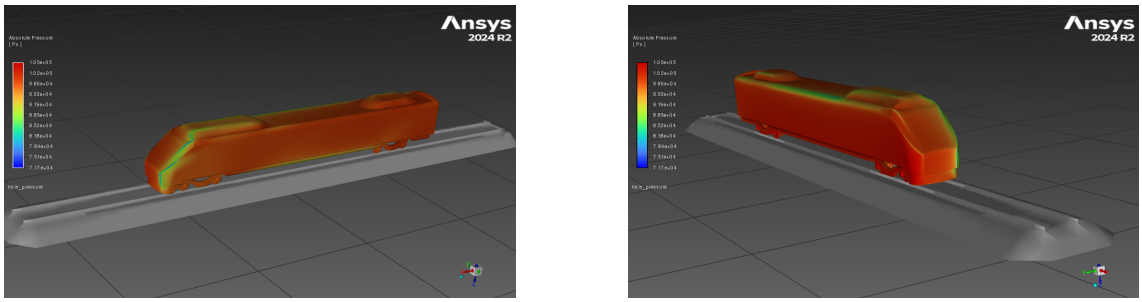


Figure 6.9: Contours of absolute pressure around the train for the crosswind study at a yaw angle of 45°, viewed from the leeward (left) and windward (right) sides.

Here, there is a distinct yellow line along the edge on the windward side, indicating low absolute pressure (below atmospheric) on that region.

For the points of higher C_y and C_{Mx_lee}, around 60°, the contour looks nothing like in the beggining, figure 6.10.

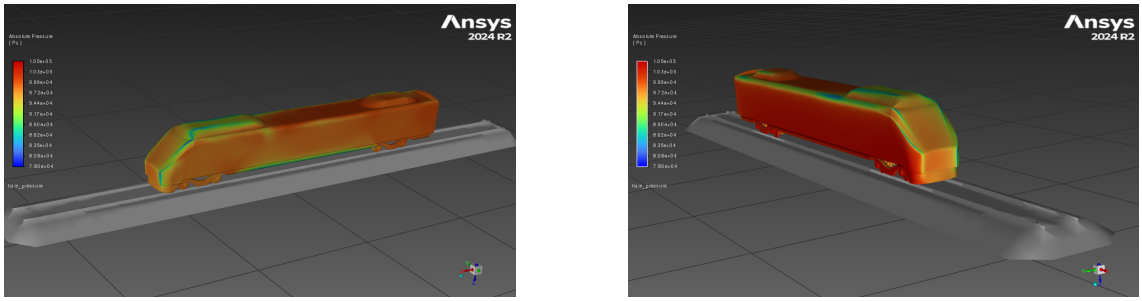


Figure 6.10: Contours of absolute pressure around the train for the crosswind study at a yaw angle of 60°, viewed from the leeward (left) and windward (right) sides.

For this yaw angle, there is a clearly higher pressure gradient between the windward and leeward side. The reddish colour on the right shows that the incidence of the crosswinds is increasing the pressure on that side; then, the vehicle's body is shielding the other one, making it less exposed and thus having a lower pressure.

This is responsible for such an elevated value of lateral force coefficient which, in critical cases, could lead to derailment. However, for this model, that is likely not the case, as neither the C_y curve neither this images show a potential threat to the train's safety.

Towards the end of the range, there was a weird phenomenon happening; the value of C_y and C_{Mx_lee} started decreasing, even though the yaw angle was higher, so the wind impact was more direct. Figure 6.11 might help explain that.

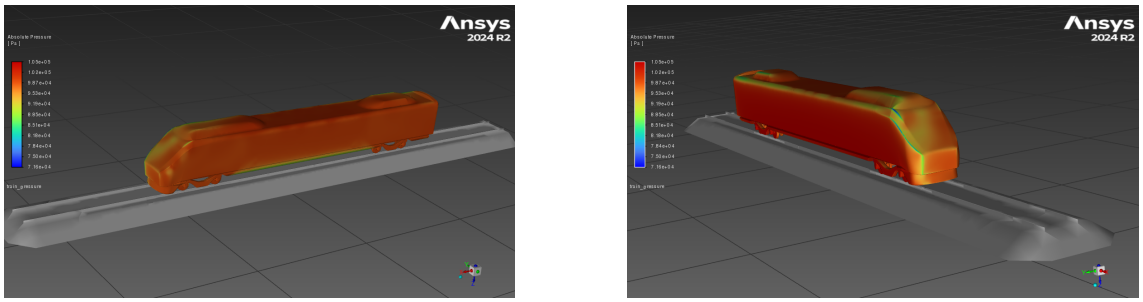


Figure 6.11: Contours of absolute pressure around the train for the crosswind study at a yaw angle of 90°, viewed from the leeward (left) and windward (right) sides.

It is visible that, contrary to the tendency, the gradient of absolute pressure started decreasing. The pressure on the windward side is still higher; however, on the leeward side, the pressure is moderate, compared to previous values. So, since the differential was a lot less, the force being felt by the vehicle is not as significant, and the lateral force and overturning moment coefficients decline.

Another difference is that, at 90°, the region of low pressure around the frontal area that was drifting to the side is now fully developed around the side facing the wind, which is expected, considering the evolution of the flow's direction along the experiment.

Still, these images does not explicity demonstrate why that occurs. What is causing the rise in pressure on the side shielded from the wind, which consequentially decreases pressure gradient?

The next graphical analysis was performed to the pathlines around the train. For each yaw angle, a set of pathlines, describing the direction of the air flow around the vehicle was created. It is coloured by velocity magnitude, so it indicates 2 different aspects at once.

For 0°, the result is shown in figure 6.12.

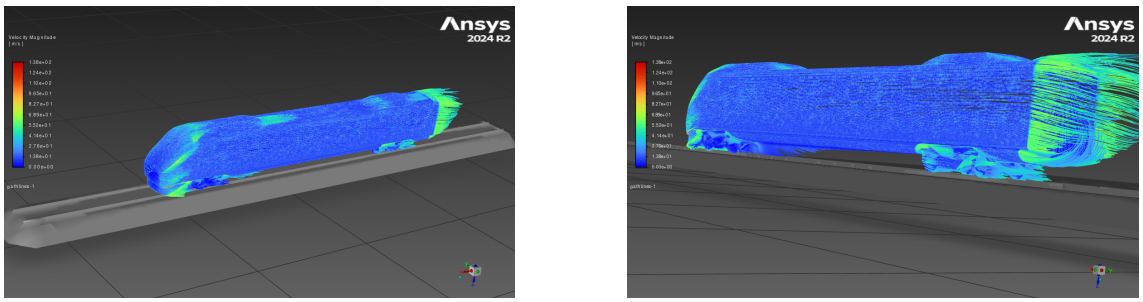


Figure 6.12: Pathlines around the train (coloured by velocity magnitude) for the crosswind study at a yaw angle of 0°, viewed from the leeward side from above (left) and below (right).

At this point, there is not much to be seen; however this an is interesting point for comparison. The only real thing to notice is the colour spread, to see the values of velocity expected during the fluid flow and that the only detectable air current is behind the body, the slipstream created by the moving train.

Then, moving up a few steps, for a yaw angle of 30°, the results are shown in figure 6.13.

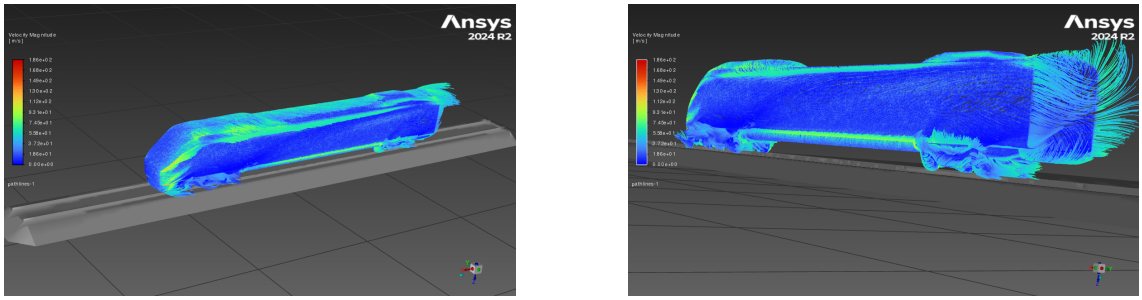


Figure 6.13: Pathlines around the train (coloured by velocity magnitude) for the crosswind study at a yaw angle of 30°, viewed from the leeward side from above (left) and below (right).

At this point, there is a distinct air flow moving from the windward to the leeward side, mainly visible on the extremities. Since the yaw angle is still moderate, this effect is controled; for larger β, this becomes more pronounced.

The next yaw angle analysed was at 45°, in figure 6.14.

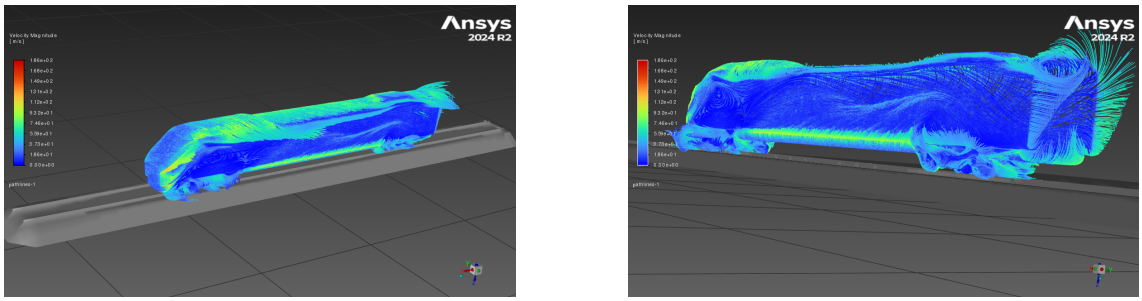


Figure 6.14: Pathlines around the train (coloured by velocity magnitude) for the crosswind study at a yaw angle of 45°, viewed from the leeward side from above (left) and below (right).

Here, there are some clear turbulent effects happening around the vehicle that can not be ignored. There are small vortexes being formed close to the rear, as well as around the wheels. The boundary layer is starting to detach from the body in the top, near the bulges. This separated air flows certainly impact the aerodynamic coefficients.

Next is figure 6.15, for a 60° yaw angle.

For this incidence angle, there is already a huge detachment of the boundary layer on the bulges on top of the train. The eddies in near the back are growing in size and some are starting to form in the front. At this point, the slipstream is heavily affected by the crosswinds.

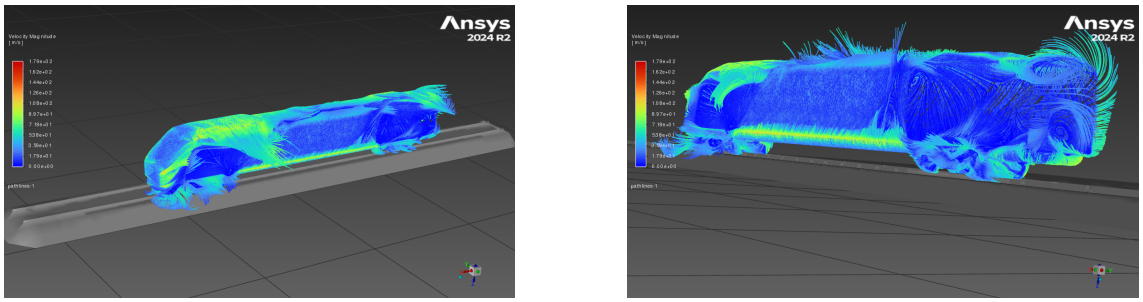


Figure 6.15: Pathlines around the train (coloured by velocity magnitude) for the crosswind study at a yaw angle of 60°, viewed from the leeward side from above (left) and below (right).

Looking not only at the direction, but also the colours of the pathlines, it is now clear that near some of the sharp edges in the geometry the air velocity is much higher.

Finally, figure 6.16 depicts the results obtained for 90°.

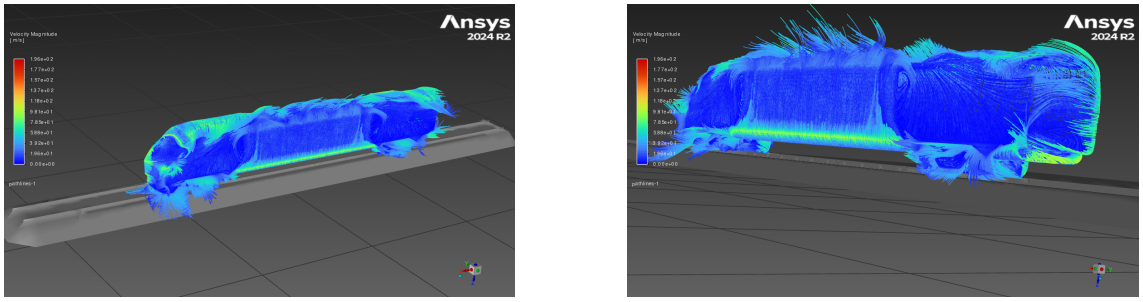


Figure 6.16: Pathlines around the train (coloured by velocity magnitude) for the crosswind study at a yaw angle of 90°, viewed from the leeward side from above (left) and below (right).

By this point, the vortexes generated due to turbulent effects have a considerable size. There are now 2 clear regions where these effects are more noticeable, one immeadiately after the train's nose and another in the rear. In the middle of the body, there is a shielded region with a much smooth air flow. The detachment of the fluid in the top of the train is even more irregular and disrupts the flow across the whole train's length.

Basically, as the yaw angle increased, there begins to appear some vortices in the more complicated geometries, caused by turbulent effects inside the fluid's boundary layer. These effects grow exponentially, to the point where the eddies extend across almost the whole body and start to interact creating unpredictable scenarios.

Even so, the evolution was somewhat linear, with a clear path being followed, which indicates that the results are coherent and can be trusted. By examing some more data, it might be possible to get a full grasp at what is really happening and explain these phenomena, in order to evaluate the model's stability.

Analysing these data gives a new perspective to this investigation. After looking at the velocity contours around the vehicle's cross section, the understanding about its aerodynamic performance becomes much easier and broader.

For the final part of this segment, velocity magnitude contours here created in a longitudinal YZ cross-sectional plane (orthogonal to the direction of the movement, x). Figure 6.17 shows precisely that for a 0° yaw angle.

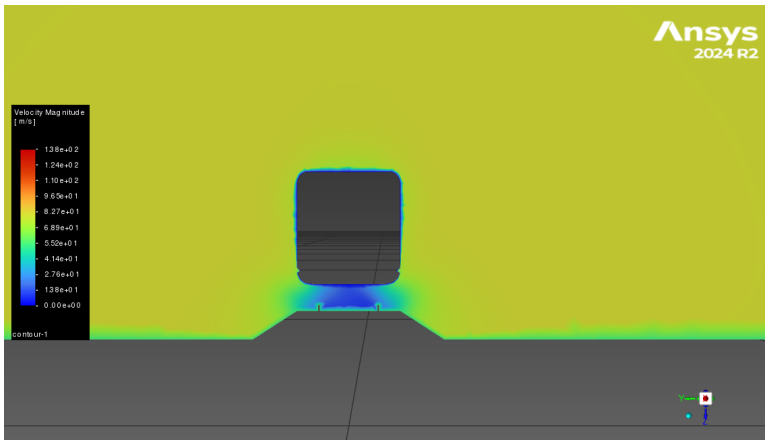


Figure 6.17: Velocity magnitude contours around the train on a YZ cross-sectional plane for the crosswind study at a yaw angle of 0°.

Similar to with the other data, at 0° there is not much to be seen. The wind is in the direction opposed to the movement (orthogonal to the cross-sectional plan). The whole area is at approximately the same velocity, with a region of lower velocity near every surface (due to viscous effects slowing down the fluid) and a blue-coloured region below the train's body, as the air slows down when deflected to pass through that space.

The next one is figure 6.18 for 10°.

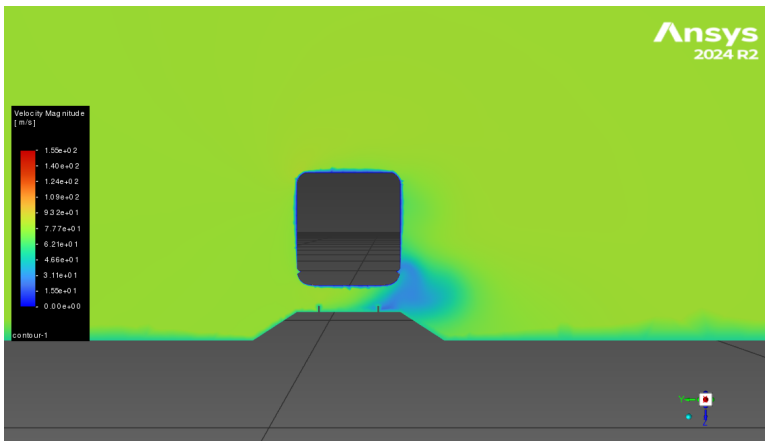


Figure 6.18: Velocity magnitude contours around the train on a YZ cross-sectional plane for the crosswind study at a yaw angle of 10°.

For now, that is onyl a few differences. It is already possible to separate the windward (left) from the leeward (right) sides. The blue area of low-velocity is drifting to the leeward side, still at a low elevation, caused by the passage of air below the train.

Then, at 30°, it looks like what is presented in figure 6.19.

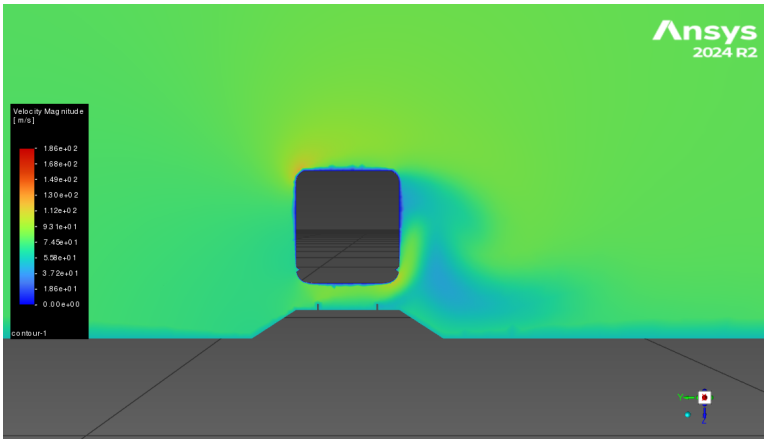


Figure 6.19: Velocity magnitude contours around the train on a YZ cross-sectional plane for the crosswind study at a yaw angle of 30°.

The low-velocity region keeps changing its shape. On the leeward side, that area is propagating from the bottom of the train to the top, with a new shade of orange near the edge indicating high velocity.

The crosswinds are leaving a wake-like region in the y direction. There are now some clear distinctions from the 2 sides of the train.

At 45°, it is as shown in figure 6.20.

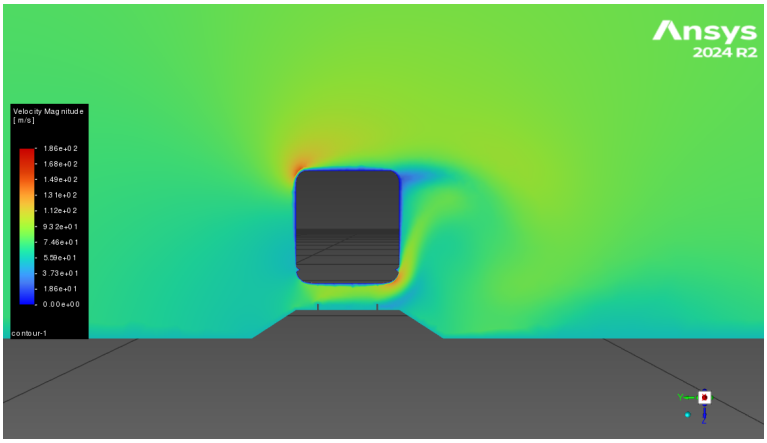


Figure 6.20: Velocity magnitude contours around the train on a YZ cross-sectional plane for the crosswind study at a yaw angle of 45°.

At this point, the upper edge on the windward side and the lower edge on the windward side have a much larger speed than the rest of the geometry. These are the same points

that, as seen in the pressure contours around the train, had a lower pressure, as the yaw angle increased.

The low-velocity region keeps developing at the vehicle's wake, and its interaction with the areas of high velocity is starting to form small whirls. These are the vortexes depicted through the pathlines. As the incidence of the crosswinds becomes more direct, this effect only grows in size and impact.

That can be seen clearly at 60°, in figure 6.21.

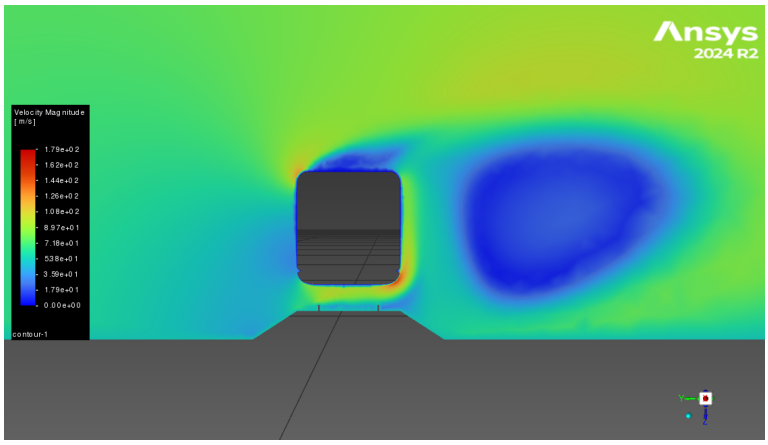


Figure 6.21: Velocity magnitude contours around the train on a YZ cross-sectional plane for the crosswind study at a yaw angle of 60°.

The edges mentioned now are a clear point of deflection, which is reflected by the high-velocity regions marked as orange/red. The air flow gets detached from the train, creating areas of low velocity in its leeward side. When the separated air flows meet again, complicated turbulent effects happen, and they create a recirculation in the wake which creates a massive vortex, like reported previously.

That large blue area is the center of the eddy, and the recirculation of flow at high speeds creates a zone of higher pressure on the side of the train shielded from the wind, which exerts a force that counteracts the force from the crosswinds. At 60°, this is the first time that this phenomenon happens with a clear presence and strong infuence.

So, this explains why that is the point of maximum C_y and C_{Mx_lee}. As the yaw angle increases, the crosswinds more direct incidence on the windward side progressively increases the absolute pressure on that side, putting up a strong push force. However, at a certain angle, the air flow that is redirected and detached from the vehicle on the edges start to create a reflux on the leeward side, with massive turbulent effects, which end up producing massive vortexes (low velocity in the center surrounded by strong gusts of high velocity) that act on that side of the vehicle. The pressure rises, creating a force to balance the other one, hence the fact that the lateral force coefficient starts to decline.

Finally, analysing the contour for 90° (figure 6.22) helps to fully comprehend these unsettling results.

The eddy on the leeward side increases in size. The velocity near the train's body caused by the recirculation also grows. This explains the fact that the pressure gradient was smaller for the larger angles than for 60°.

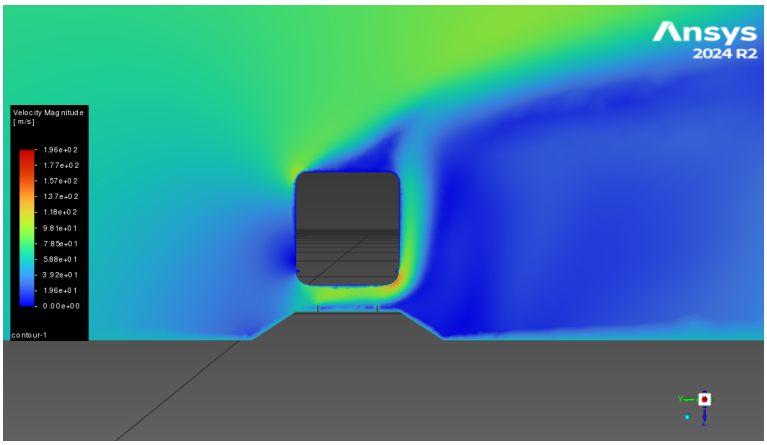


Figure 6.22: Velocity magnitude contours around the train on a YZ cross-sectional plane for the crosswind study at a yaw angle of 90°.

So, the combined analysis of the aerodynamic coefficients and the graphical results was successful in creating a solid understanding of the aerodynamic performance of the Portuguese train.

First of all, it is important to recon that, unfortunately, it was not possible to conceive a complete crosswinds study to the full range of yaw angles with a high level of accuracy, as intended. Nevertheless, the assessment is still complete and well-rounded.

In this research, the aerodynamic coefficients relevant for affering the stability and efficiency of the model were obtained. That allowed an immersive process of examining the vehicle's performance. Moreover, graphical results (generated in ANSYS Fluent) were a great help in comprehending the phenomena and justifying the decision and conclusions drawn.

The *TrainSolutions Portugal* model has a decent energy efficiency, likely worse than the ICE used for comparison, judging by the C_x values attained. However, its stability in operation during crosswinds is very close to that of the ICE, as confirmed by the curves of C_y, C_z and C_{Mx_lee} where, for the most significant yaw angles, there was a near perfect overlap of results (with the Portuguese train even outperforming its german counterpart in some ways).

These results were incredibly satisfactory towards the objective of validating this model. The CFD analysis provided solid evidence to prove its reliability.

Then, the graphics became the backbone to support the mathematical data.

The contour of absolute pressure was essential to justify the values of the aerodynamic loads felt by the vehicle, since these were mainly caused by pressure gradients along its body. The pathlines image was important to have visual confirmation of the aerodynamic

phenomena that was happening (in particular, the vortexes) and which regions were causing them. Finally, the last pressure contour on the cross section helped comprehend how these phenomena were occuring, at what yaw angles were they occuring and, once more, identifying critical parts of the geometry.

These provided a new lens to the flow analysis and solidified the aerodynamic assessment.

In the end, it was not possible to test geometry modifications, due to the time limit for this thesis. Nevertheless, it is possible to address some changes that could be tested as future works (7.3).

Firstly, changing the frontal area of the train would naturally impact the resistive forces its subject to (C_D); it would be interesting to find a point of better energy efficiency without compromising the stability and robustness of the model. Next, addressing some areas that were causing turbulence could change the behaviour under crosswinds for the best, such as the bulges on top of the vehicle. Also, reshaping the sharp edges along its body could also contribute to improve its performance.

It is important to leave the disclaimer that these are just hypothesis based on the results obtained, and none of them were tested. Testing them, particularly in CFD, would be intriguing, both for optimization purposes and for enlarging the knowledge in the area. Even so, this geometry is highly promising.

Then, running experiments on prototypes of the model would provide the validation it needs to start commercial operation.

This concludes the analysis of results for the crosswinds study, leaving only the train passing manoeuvre to be covered.

6.3 Train Passing Simulations

Simulating the train passing manoeuvre in CFD was the most complicated part of the project. When the simulation was finished, the results were extracted from ANSYS Fluent and it was possible to start analysing them.

Due to all the peculiarities of this operating condition (having more than one vehicle involved, the unsteady regime...) the aerodynamic assessment was more challenging than for the other cases. Even so, to maintain the logic of the crosswinds study, in this section, the results were also divided in two parts, one to analyse the aerodynamic coefficients and another for the graphical results.

6.3.1 Aerodynamic Coefficients

For the passing manoeuvre, the force coefficients in the 3 directions for both trains were used as part of the analysis (C_x, C_y and C_z), same as previously. To complement the understanding of the aerodynamic phenomena happening between the vehicles, a pressure coefficient (C_p) was measured at the midpoint of the intersection.

Before presenting and examining these values, it is important to mark the most relevant points of the simulation, to aid in comprehending the important variations in the characteristic curves.

First of all, a small correction was made to adjust the initial position of the vehicles; instead of 38.6m apart from each other, their initial distance was 39.5m (at $t = 0$s). So, at a combined speed of 100m/s, the trains take 0.395s to "meet" - that is to say, their noses reaching the same point in the x-axis. Then, their fronts pass by the rear of the other vehicle at $t = 0.652$s and they complete the passing manoeuvre (their rears pass by each other) at $t = 0.909$s. The simulation ends at $t = 1.020$s.

So, the setup was prepared for ANSYS Fluent to register the values of C_x, C_y, C_z and C_p at every Δt. When the simulation ceased, the software plotted a curve for each variable. However, it was not easy to discern the information with all the fluctuations happening between time steps. So, the data was exported and the curve was plotted manually, with only value for every ten time steps (that being the average). This way, there is a much smaller number of points in the graphic, and the tiny variations are removed, facilitating the review of the results.

Each of these 7 curves is presented exactly as it was made in E; for this chapter, only the 3 curves of the aerodynamic coefficients for the main vehicle and the one for the pressure coefficient are analysed. More so, each of these images was modified to identify the vital points of the curve and the passing manoeuvre; the graphs are more clustered with information (regarding the time of the simulation) in order to help explaining the flow development, which might make them harder to read. So, in appendix, the curves are presented with no additional information to simplify the reading of the data.

That being said, the analysis of each parameter can begin.

First of all, figure 6.23 illustrates the evolution of the force coefficient on the x-direction over time for the main vehicle.

The 3 red lines running down the whole graph mark the 3 key points of the passing manoeuvre (when they start passing by each other, when their front passes the other's rear and when the manoeuvre is complete).

The first thing to notice is that, as mentioned during chapter 5, in the first few time steps, the value of some aerodynamic coefficients was heavily disrupted by the sudden acceleration of the vehicles. So, the C_x here presented for the first fractions of a second are completely irrelevant, as they are only the simulation trying to stabilize from the initialization.

After a few points of an unrealistic value of drag coefficient, it seems to be converging towards a value. At $t = 0.255$s, the value of C_x seems to be stable and it is considered that the simulation has evolved past the initial shockwave. Then, it starts to increase (or decrease, in modulus) at around $t = 0.375$s, just before the trains meet.

The likely explanation for this is that, the effect of the passing manoeuvre is already happening and the C_D is being affected; the slipstream created by one of the vehicles is

clearing the air particles in front of the other, reducing the resistive force to the movement. Then, the value of C_x becomes somewhat constant for a fraction a second until around $t = 0.585$s, where it increases again, slightly. After a few more time steps, just before the train's front passes the rear of the other, C_x decreases quickly.

After that, it stabilizes once more until almost the end of the simulation, where a few time steps with convergence issues disrupted the values across the whole domain. From $t = 0.909$s onwards, the results are not so reliable.

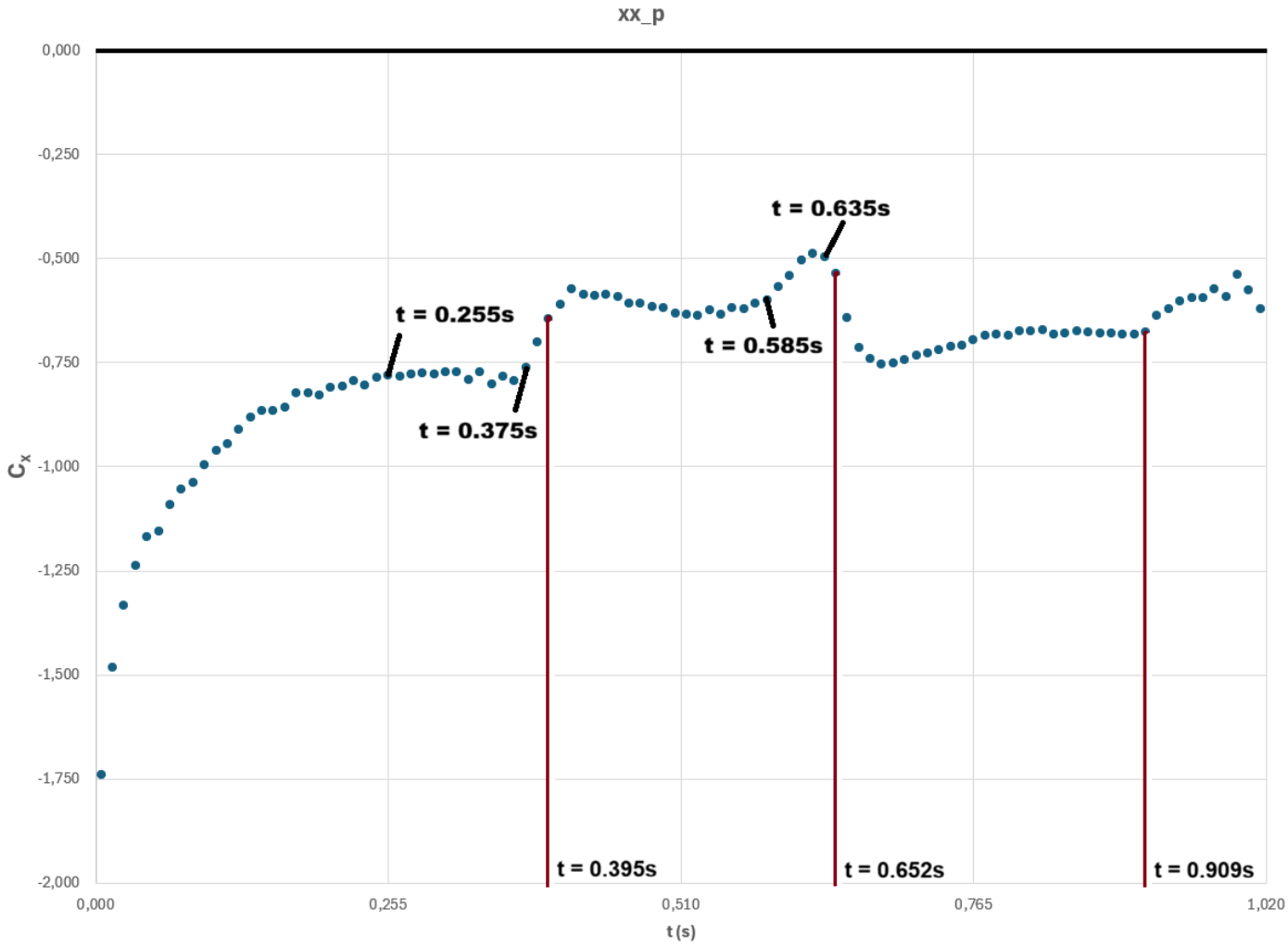


Figure 6.23: Values of C_x over time for the main vehicle.

So, the C_x is a good barometer of the influence that the trains have on each other. It is possible to detect when their slipstreams start to interact and how they evolve over time and space. These effects were predictable, which is a great indicator towards considering its behaviour during the passing manoeuvre as safe and secure.

Nevertheless, this only helps inferring the points of interest during their passage. C_y, for instance, gives a much broader impression about what is actually happening. This

curve is presented in figure 6.24.

When the simulation starts, C_y is close to 0 (for both vehicles) as there is no crosswinds and their interaction is yet to start, so there is no pressure gradient between its sides. At around $t = 0.285$s (around the time their slipstreams started affecting C_x), it starts to rise exponentially, reaching the maximum value of approximately 0.750 at $t = 0.395$s; when their fronts pass by each other.

After that, it drops immediately, even reaching negative values. It stabilizes at $t = 0.505$s, and keeps increasing slightly for a fraction of a second. Then, when $t = 0.585$s, it drops again; C_y reaches a global minimum of -0.750 at $t = 0.652$s - the moment when the nose of one vehicle crosses the other's rear.

From that point onwards, it increases once more, with a few fluctuations. C_y reaches positive values and hits a local maximum almost at the time when the train's rear pass by one another, and the manouevre is complete, $t = 0.909$s.

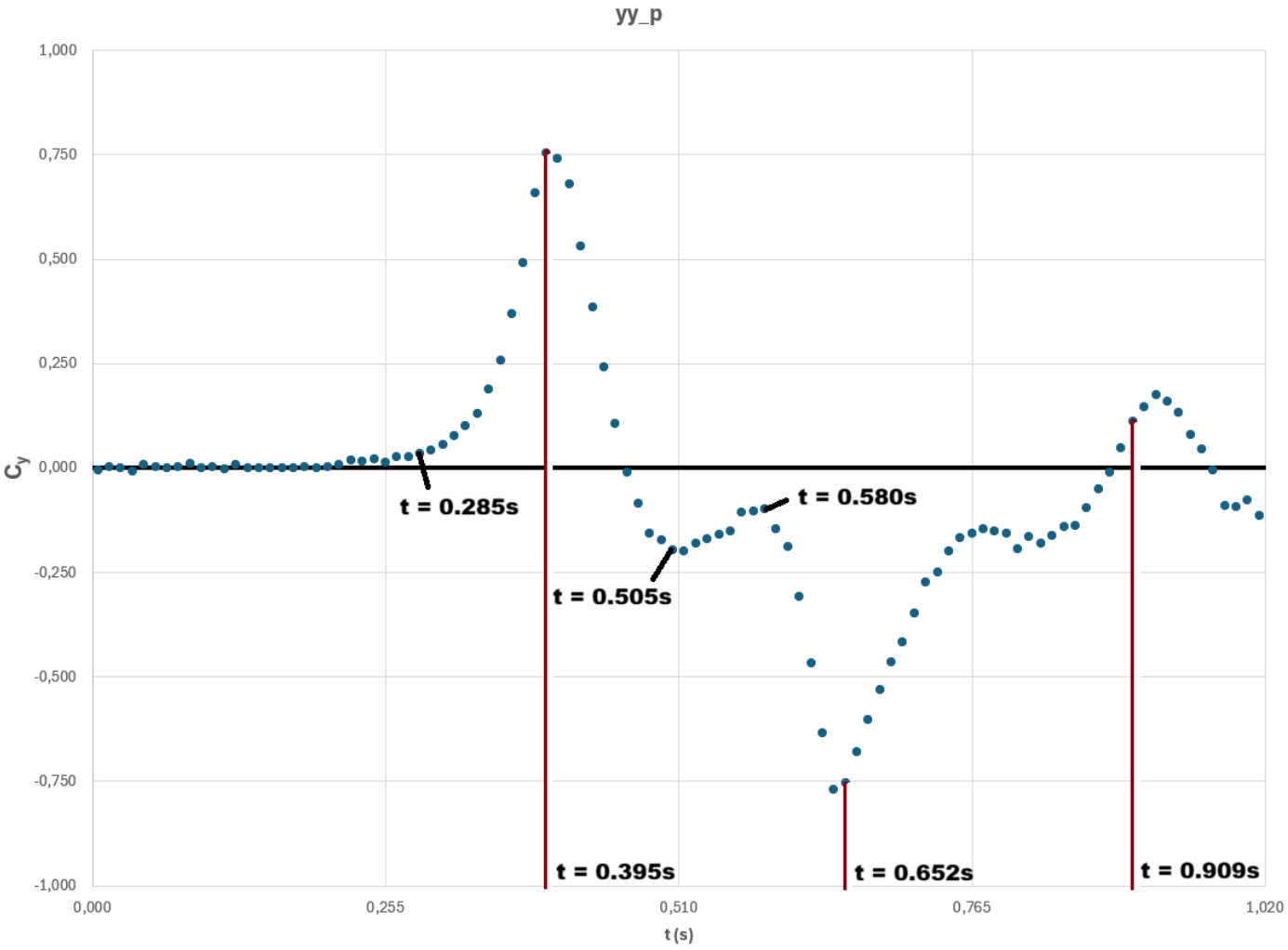


Figure 6.24: Values of C_y over time for the main vehicle.

As mentioned, the simulation was halted before the trains distanced themselves enough for their interference to end. Nevertheless, in the final moments, the lateral force coefficient just suffers some small variations before inevitably becoming null once more, when the main vehicle is sufficiently far from the secondary one.

The development of this quantity is really interesting and opens the possibility to comment on what might be happening in the region in the middle of the intersection.

When the C_y increases at that rhythm, it is deduced that the absolute pressure on the left of the main vehicle (the side closer to the other train) is greater than on the right side. This indicates a pressure increase in the middle, as the air is compressed between the 2 metal bodies as pushes them outwards.

Likewise, when C_y suddenly decreases, it points to a low-pressure zone in the middle of the vehicles, often described as "suction zone"; both trains feel pulled to the center, as the pressure in that zone is below atmospheric, creating a heavy pressure gradient.

Then, the unsteadiness and turbulence caused by the interaction of the train with the other's wake and slipstream causes fluctuations in the value of C_y. Along its body, in the left side, there are regions of higher pressure (caused by the compression between the vehicles) and lower pressure (when the air particles are dispersed from the interaction of aforementioned aerodynamic phenomena) which keep developing as the passing manoeuvre continues.

These are the most notorious conclusions drawn from the analysis of this curve. They would later be confirmed when analysing C_p evolution over time. Before that, the graphic of C_z is presented in figure 6.25.

Here, the curve is not so distinct, as the fluctuations were greater than for the previous quantities. C_z keeps decreasing for a few hundreds of time steps, before stabilizing (for a short time period) at $t = 0.305$s. After that, its value drops significantly and reaches a global minimum when the two trains meet ($t = 0.395$s).

Then, when the lift coefficient is almost 0, it rises rapidly and the stabilizes just below $C_z = 0.5$, at $t = 0.535$s. It stays somewhat constant until $t = 0.595$s, where it rises again and its a maximum of 0.625, when the front of the main vehicle crosses the other's back. Then, C_z declines until $t = 0.755$s.

Always with small fluctuations, this quantity stays unchanged until just before the passing manoeuvre is concluded, at $t = 0.909$s, when it decreases again.

Near the end of the simulation, the value of C_z diverges heavily, even seen in this graph by a few points completely out of the characteristic curve that was being plotted. It is hard to take conclusions from this point on, so its development is only analysed where it was stable and predictable.

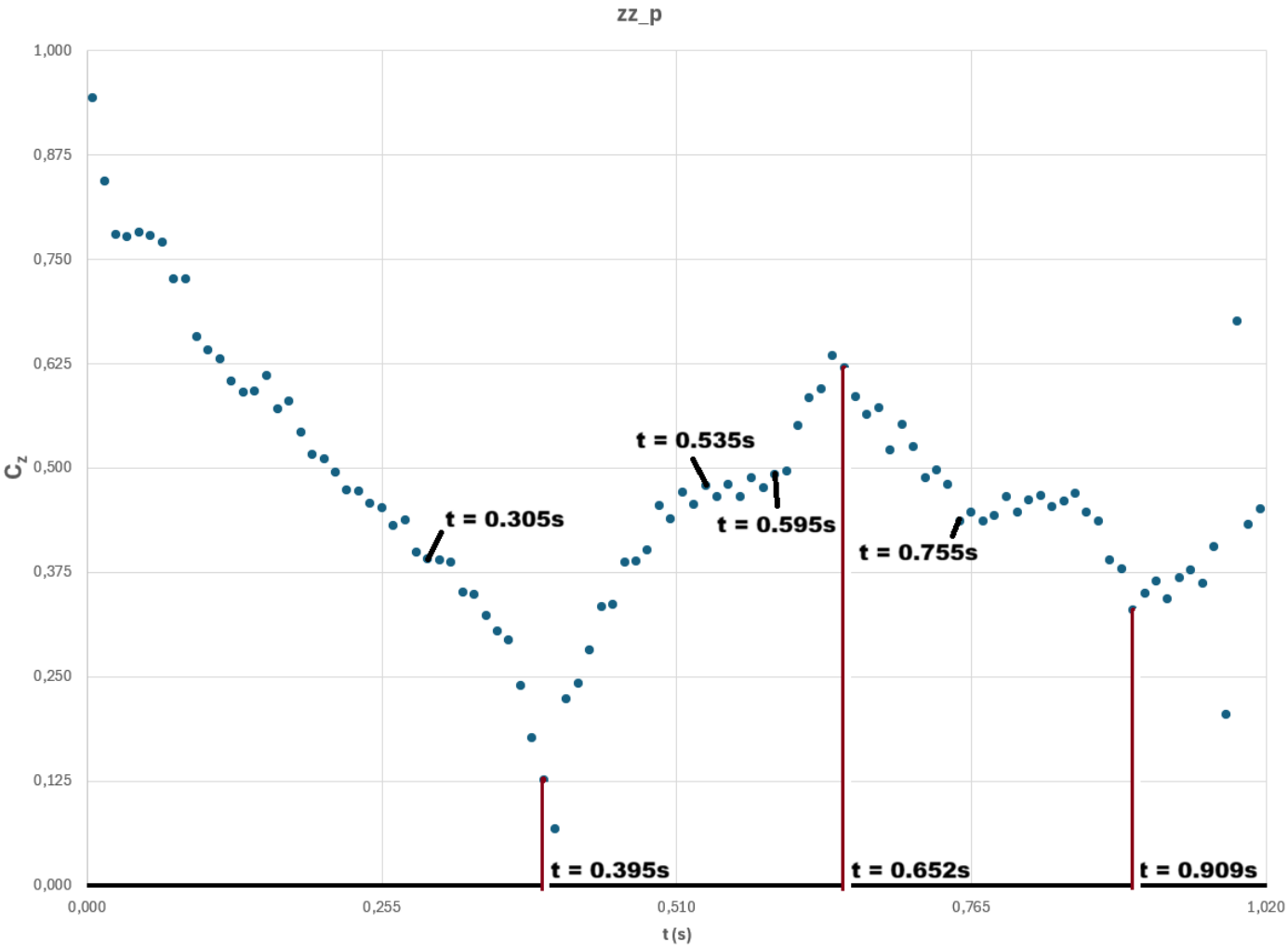


Figure 6.25: Values of C_z over time for the main vehicle.

So, by the changes in the lift coefficient caused by the passing manoeuvre, it is possible to try and learn how the air flew when the slipstreams interacted.

The reduction in C_z when their fronts meet at the midpoint of the intersection (from a positive value to almost 0), indicates a lower vertical pressure gradient, likely caused by a stronger absolute pressure below the train's body. Considering the axis system used, there was a downwards force being exerted (higher pressure above the vehicle) whose effect was counteracted.

The most plausible explanation was that the fluid slipped below the train to escape the high-pressure zone formed in the middle of the vehicles, which increased the pressure below their bodies, reducing the lift force.

For the rest of the simulation, it is hard to predict how the fluid flow developed around the vertical direction of the train, without the confirmation of visual representations of pressure and velocity fields. Throughout the manoeuvre, the air was pushed from the re-

gion of elevated absolute pressure in the middle to the train's geometry, exerting ascending and descending forces along its body. This resulted in constant changes to C_z over time.

That being the case, some parts of the analysis are dependent on graphical output data from ANSYS Fluent.

For the second train, the curves of these 3 aerodynamic coefficients were almost similar, but simetrical for the x and y directions, since those are inverted in the referential adopted.

Then, the only quantity left to analyse is C_p, whose curve is presented in figure 6.26.

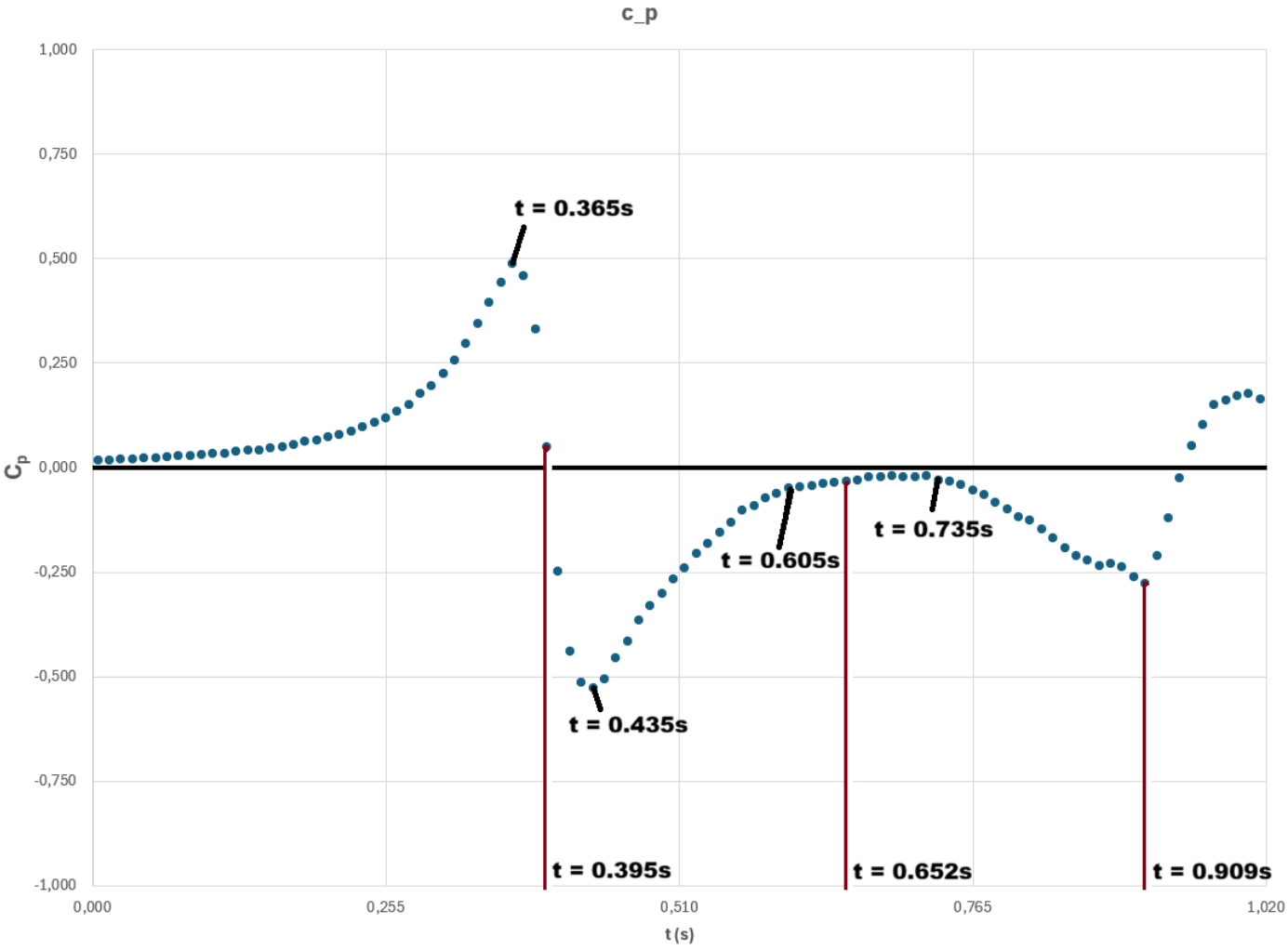


Figure 6.26: Values of C_p over time for the midpoint of the intersection.

The first thing to notice is that it has a great resemblance to the C_y curve.

From the beggining of the simulation, C_p is already increasing, at an incredibly slow pace, as the trains are still far apart. As they get closer, C_p increases at a faster rhythm, until reaching a maximum value of around 0.5, when $t = 0.365$s, just before their fronts meet.

After reaching a peak, it drops rapidly, and at the time the intersection begins ($t = 0.395$s) it is almost 0. The pressure coefficient reaches a global minimum of around -0.5 at $t = 0.435$s.

Then, it rises again until around $t = 0.652$s; between 0.605 and 0.735s it is almost constant and close to being null. At that time step, it declines again until a new local minimum at $t = 0.909$s, when the passing manoeuvre is complete, where $C_p \approx -0.250$.

Towards the end of the simulation, as verified in similar studies, the value of pressure coefficient spikes again and keeps fluctuating until eventually becoming null, when the midpoint where this quantity was measured leaves the vehicle's wakes.

Analyzing the graphic of C_p as a whole, there are some features that help understanding the previous curves. As predicted during the study of the lateral force coefficient, the pressure in the region between the trains rises in a fraction of a second as they get close to it, with the slipstreams colliding and compressing the air. This results in a positive force in the y-direction (for the main train, negative for the secondary one), pushing the vehicles outwards, with the risk of derailment in the worst case scenario.

Then, the absolute pressure drops to values below the atmospheric, as the vehicles are passing each other; as the air gets pushed out of that area due to their movement, the two large bodies form the "suction zone" aforementioned. Therefore, the pressure gradient is pulling the trains towards the middle, which is corroborated by the negative value of C_y for the main vehicle.

During the manoeuvre, the pressure coefficient keeps changing due to the relative position of the 2 trains influencing the fluid flow around them. After $t = 0.909$s, where the trains have bot completely passed the midpoint of the intersection, the pressure in that point (and, consequently, its C_p) is only altered due to their wakes' presence. This causes the fluctuations in the end until it inevitably reaches 0.

From the evaluation of the aerodynamic and pressure coefficients, it can be deduced that the behaviour of the Portuguese train during the passing manoeuvre is consistent with the expectations. This is a solid indicator towards verifying its stability.

However, the final remarks regarding the aerodynamic performance were preceded by the presentation of the graphical results extracted from the recorded animations.

6.3.2 Pressure and Velocity Distributions

For the study of the passing manoeuvre, to make good use of the CFD capabilities, 4 different animations were created to have different perspectives of the aerodynamic phenomena.

Each of those was set up to display a separate feature, in order to improve the knowledge of the fluid flow development. Since the graphical results for this investigation are videos, it is not possible to fully present them in this report. Instead, frames of some keypoints were saved and presented in this dissertation.

Therefore, the most relevant to analyse in order to get a full comprehension of the flow are present in this chapter. In appendix F, more images are displayed to show different angles or moments of these quantities, to increment the flow's characterisation.

The first animation to be analyzed was the velocity magnitude contour on a XZ plane created along the main vehicle's length. Figure 6.27 depicts this contour at $t = 0.305$s.

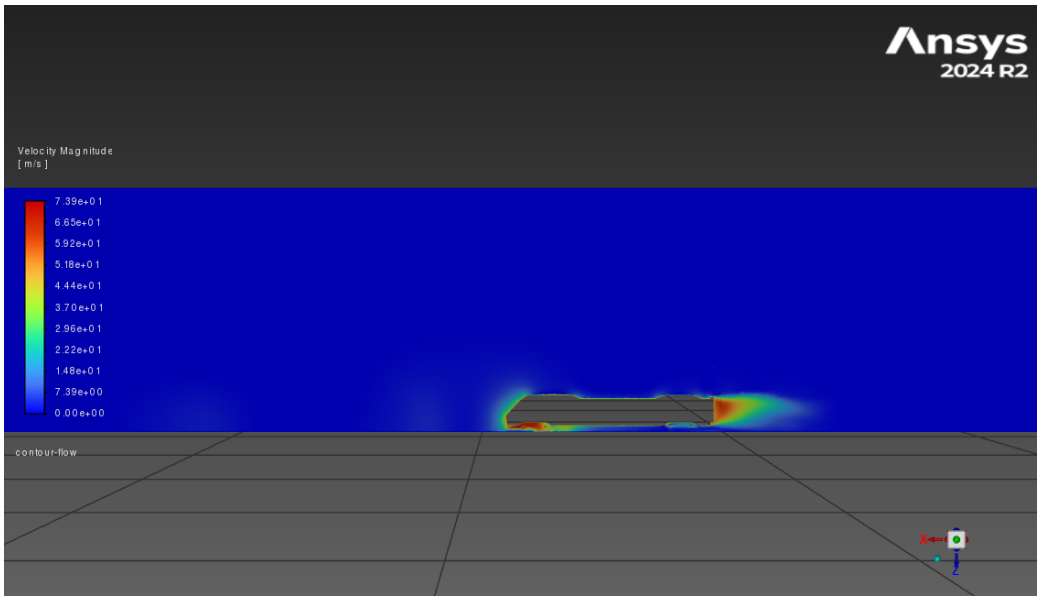


Figure 6.27: Velocity magnitude contour on the XZ plane at $t = 0.305$s.

This animation was conceived in order to see the development of the train's wake and slipstream - easily identified by the different colours. Even so, it ended up revealing something of greater interest.

Below the vehicle's body, in the front (near the wheels), there is a region of high velocity. This region is likely at a different pressure than the rest of the area surrounding the train; in this case, the pressure should be lower than everywhere else.

Then, figure 6.28 shows the same contour at $t = 0.652$s (when this vehicle's front crosses the other's rear).

Here, the high-velocity area below the body has expanded until close to its rear. Considering that this strongly suggest a lower pressure, this explains the variations of C_z over time.

C_z is positive and nearly constant at $t = 0.305$s; the pressure gradient here causes the train to feel a vertical and descendant force, indicating that the area-weighted pressure is larger above than below the body. As time progresses, due to the passing manoeuvre, the air fleeing from the middle of the vehicles escapes to the area below them, changing the absolute pressure. This counteracts the pressure above the train, altering the value of C_z.

As C_z has a higher value at $t = 0.652$s than at $t = 0.305$s, that would make sense. In different moments during the passage, the air flow would cause distinct pressure gradients, mainly below the train, which make the lift force fluctuate.

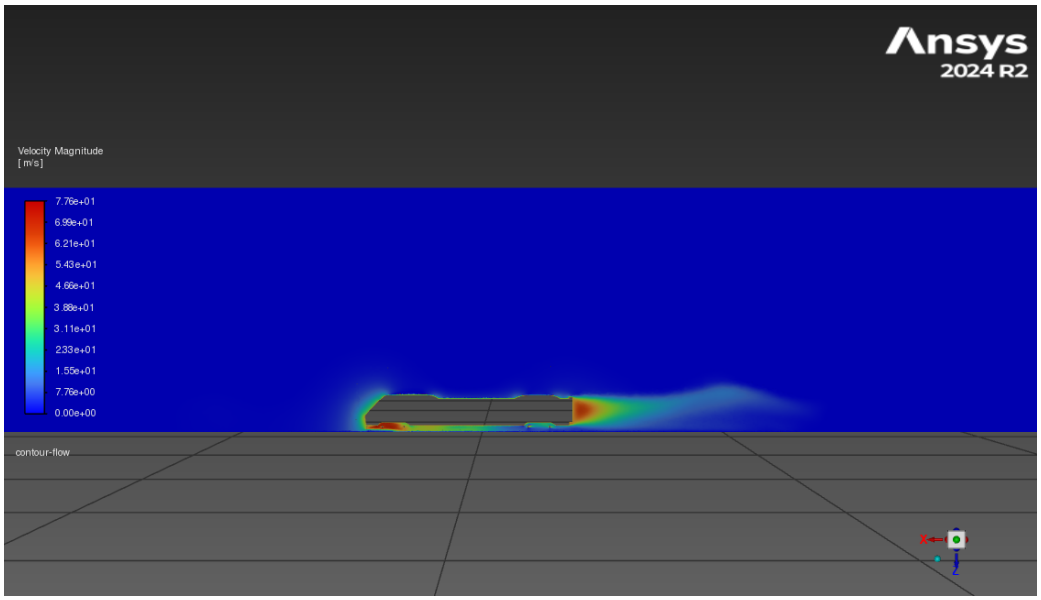


Figure 6.28: Velocity magnitude contour on the XZ plane at $t = 0.652$s.

In appendix, more images are presented to show that this process is gradual.

That was an intriguing realization about the evolution of C_z over time and what might be causing it. Following this was the analysis of the pathlines around the train at different points in time.

Figure 6.29 shows the pathlines at $t = 0.150$s.

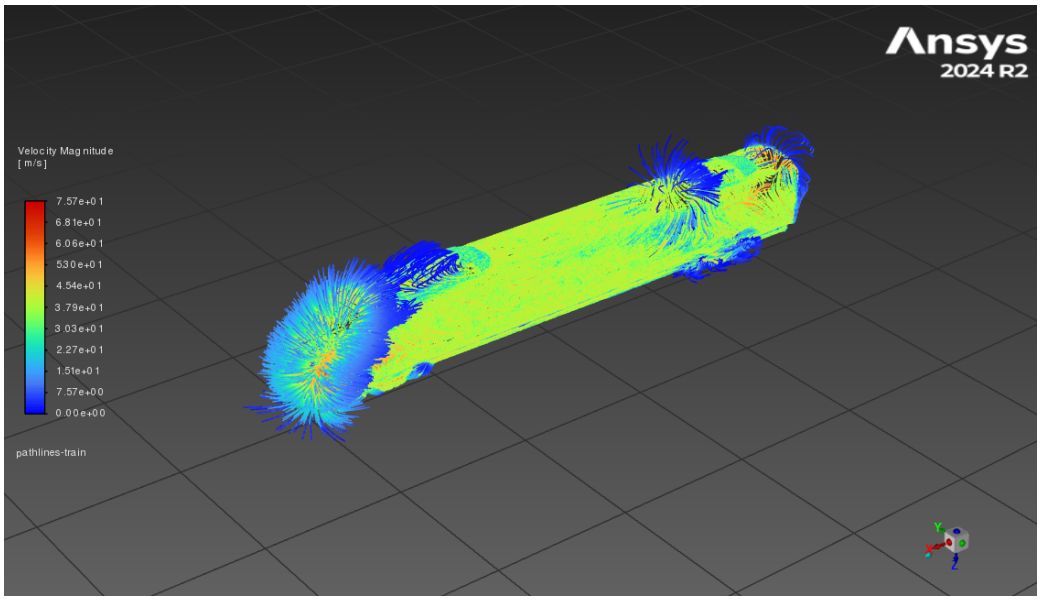


Figure 6.29: Pathlines around the train at $t = 0.150$s.

The pathlines are coloured by velocity magnitude, same as in the crosswinds study.

In this time step, there is little interference caused by the other train, as they are still outside the other's slipstream. As a result, the pathlines mainly flow in the x-direction (the direction of movement).

However, that is not the case in $t = 0.395$s (when the passage initiates), shown in figure 6.30.

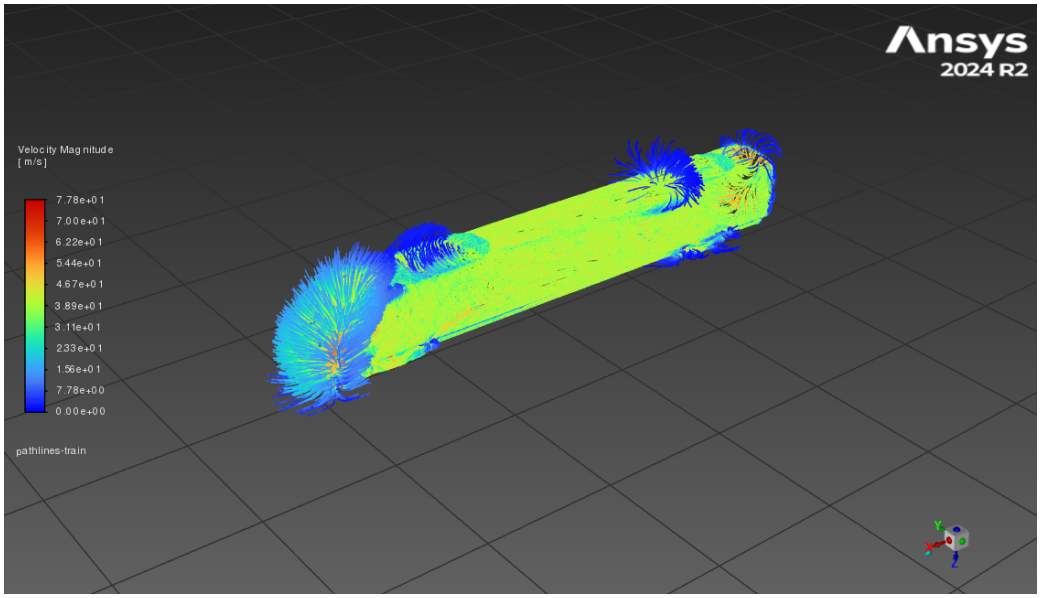


Figure 6.30: Pathlines around the train at $t = 0.395$s.

Here, the pathlines are clearly starting to drift in the y-direction, pointing outwards, as the air particles in the middle are being pushed away. They are flowing around the body and are visible mainly in the front and rear, as well as the protrusions on top.

Moreover, there is a clear flux below the train, close to the wheels, in the region identified by the analysis of the velocity contour on the XZ plane, reinforcing the hyphothesis that this is what is causing the lift coefficient to drift.

The objective of this animation was precisely to capture where the air was flowing to as the trains move past each other, to help understand the aerodynamic coefficients (mainly, C_y and C_z) and possibly find unique aerodynamic phenomena.

Pictures from this animation at different timesteps and from other angles (for better visualisation) are in appendix F; they were excluded from this chapter to avoid redundancy.

Next, was one of the most interesting animations to be created; a contour of absolute pressure on an XY plane created at mid-height of the trains. The goal was to support the curve of C_p and reveal how and why it reaches its minimum and maximum values.

Figure 6.31 shows this contour at $t = 0.365$s; when C_p hits a global maximum.

As expected, in front of the vehicles the pressure is elevated, due to their slipstreams.

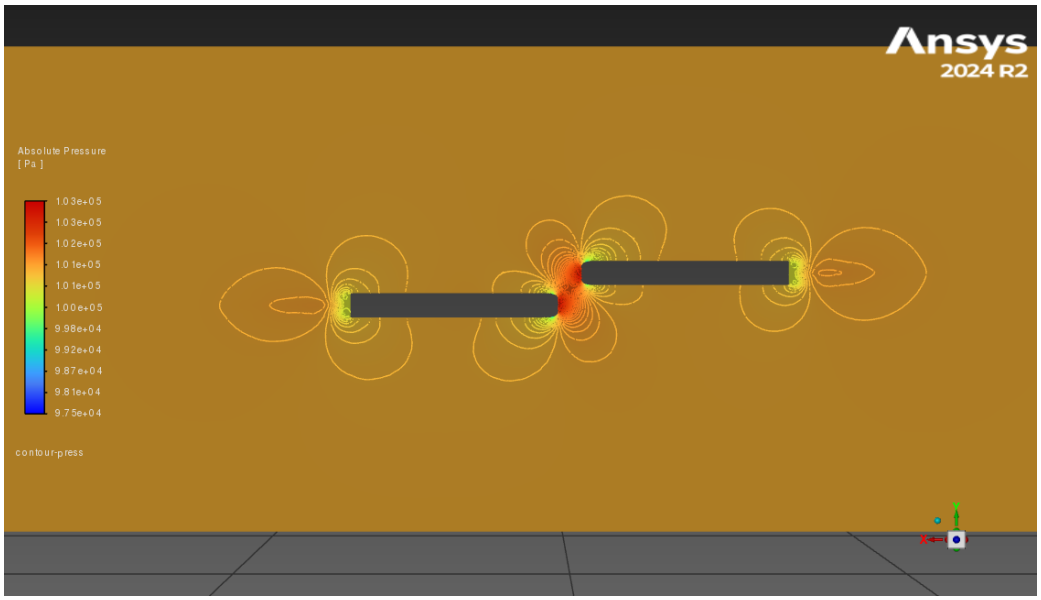


Figure 6.31: Contour of absolute pressure on the XY plane at $t = 0.365$s.

As the slipstreams collide, they compress the air in the midpoint of their intersection, to a pressure much higher than atmospheric, hence, the value of $C_p = 0.5$. After that time, the pressure in that point begins to decrease rapidly.

Figure 6.32 illustrates just that. At $t = 0.435$s, C_p hits a global minimum of around -0.5.

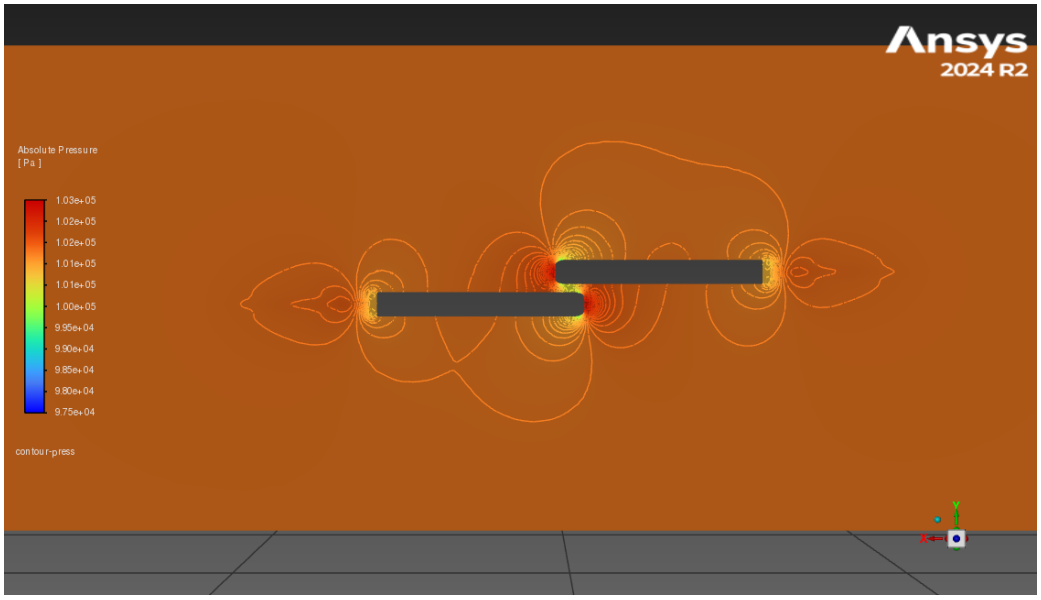


Figure 6.32: Contour of absolute pressure on the XY plane at $t = 0.435$s.

Immediately after the high-pressure region in front of the train, that is a low-pressure region. When they meet, they form the "suction zone" in the middle of the vehicles. This

area of reduced absolute pressure (almost always lower than atmospheric) propagates throughout the train's length during a good part of the manoeuvre.

In annex are frames of more timesteps to support this claim.

In figure 6.33, this contour is presented for $t = 0.909$s.

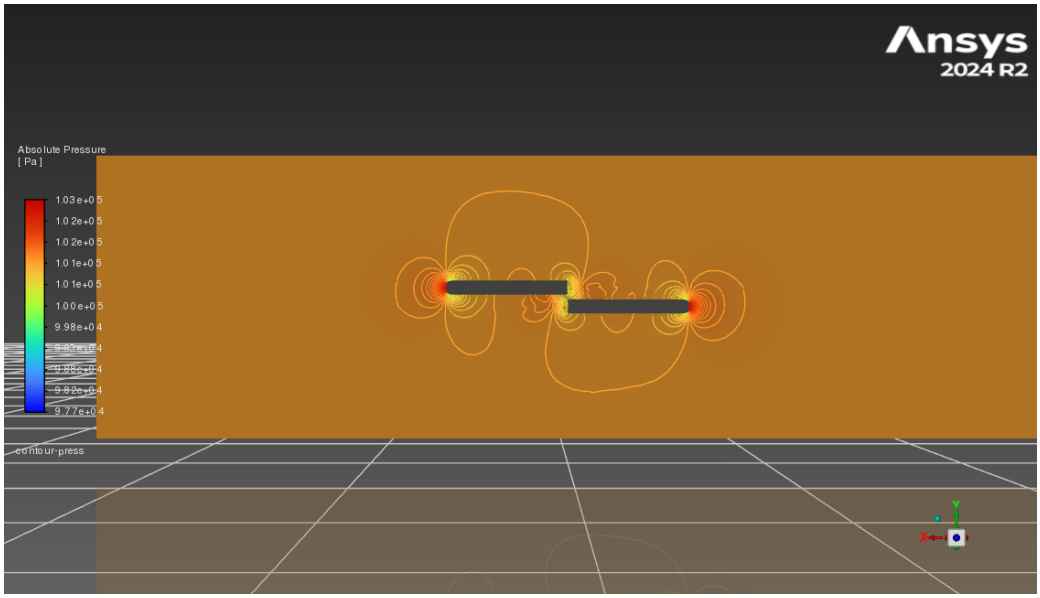


Figure 6.33: Contour of absolute pressure on the XY plane at $t = 0.909$s.

The low-pressure in the wakes causes the pressure coefficient to decline once more to its second minimum verified in its curve.

This animation was extremely helpful in conforming the reliability of the analysis, by explaining the evolution of the C_p. Consequently, this also justifies the development of C_y, as they are strongly correlated (the pressure in the middle influences the loads felt by the vehicles).

Finally, the last graphical results come from an animation of a contour of absolute pressure around the vehicles.

Figure 6.34 shows this contour at $t = 0.255$s. This is around the time when the value of C_x stabilized completely, before the interaction began affecting the aerodynamic coefficients. This pressure distribution is for a train circulating under headwinds (hence its similarity to the 0° yaw angle image in the crosswinds study).

It mainly contributes to showing the "default" pressure field before the trains intersect each other and start creating different pressure gradients.

This image is from a perspective view, just like most of the ones included in this report (both in this chapter and in appendix). However, there are a few images from different angles, to give a better depiction of some phenomena.

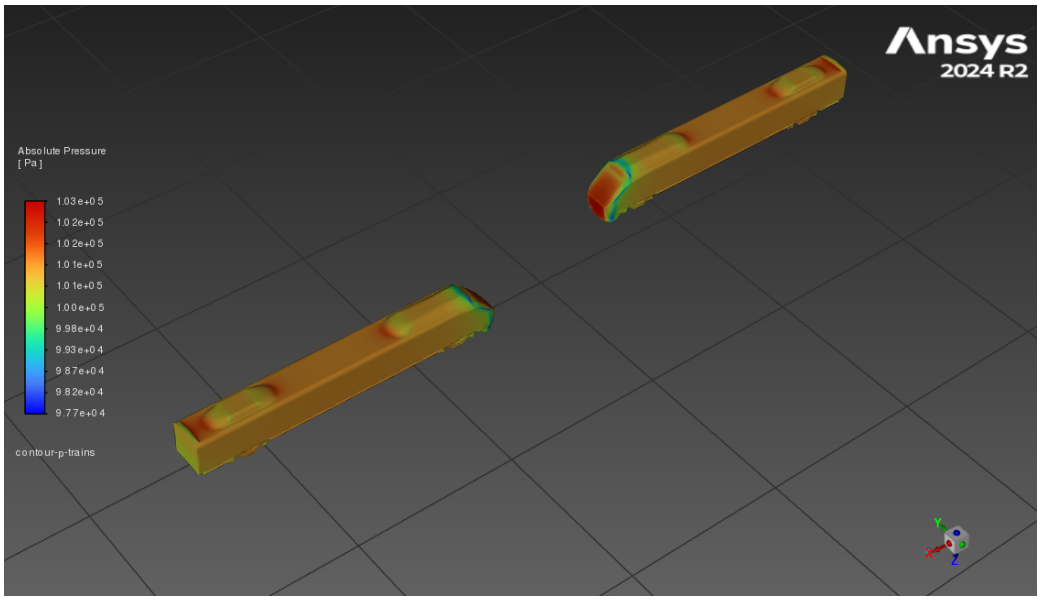


Figure 6.34: Contour of absolute pressure around the vehicles at $t = 0.255$s.

An example of this is figure 6.35, where the contour is shown from a frontal view, at $t = 0.420$s.

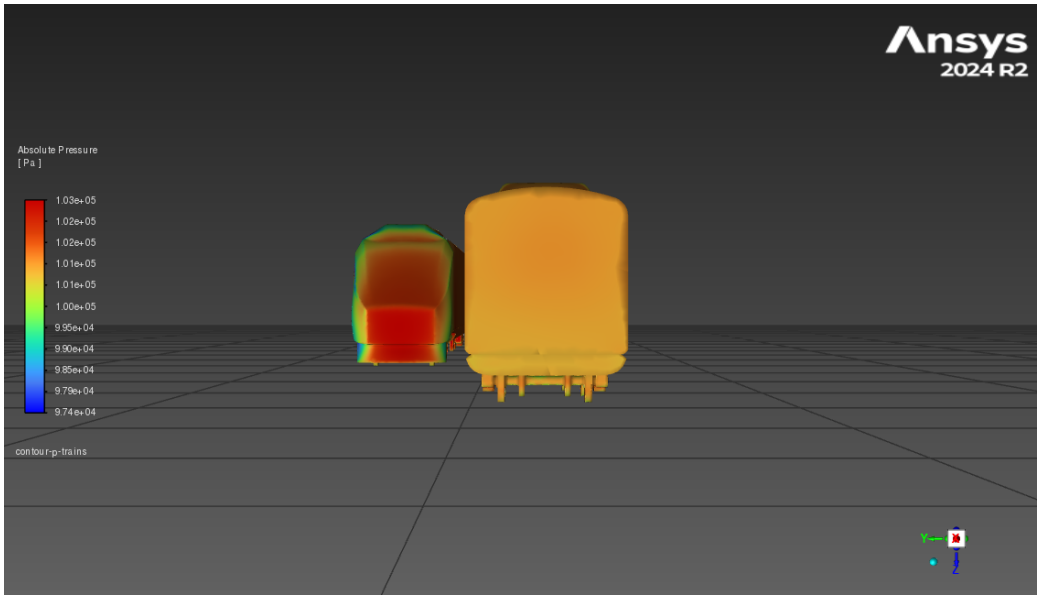


Figure 6.35: Contour of absolute pressure around the vehicles at $t = 0.420$s (front view).

Here, the passing is already underway and the pressure in the middle has already been affected by the collision of their slipstreams.

This frame shows how the pressure distribution in the frontal area is no longer symmetrical, as there is a clear shift; on the right side (close to the other vehicle) there are higher absolute pressures than on the left side (which is less disturbed by the second train).

Just like the pressure contour on the XY plane confirmed, as time advances, the fluid flow keeps changing as the train's slipstreams interact and evolve. The pressure felt the bodies changes not only with time, but also with space, as confirmed by figure 6.36, for $t = 0.500$s.

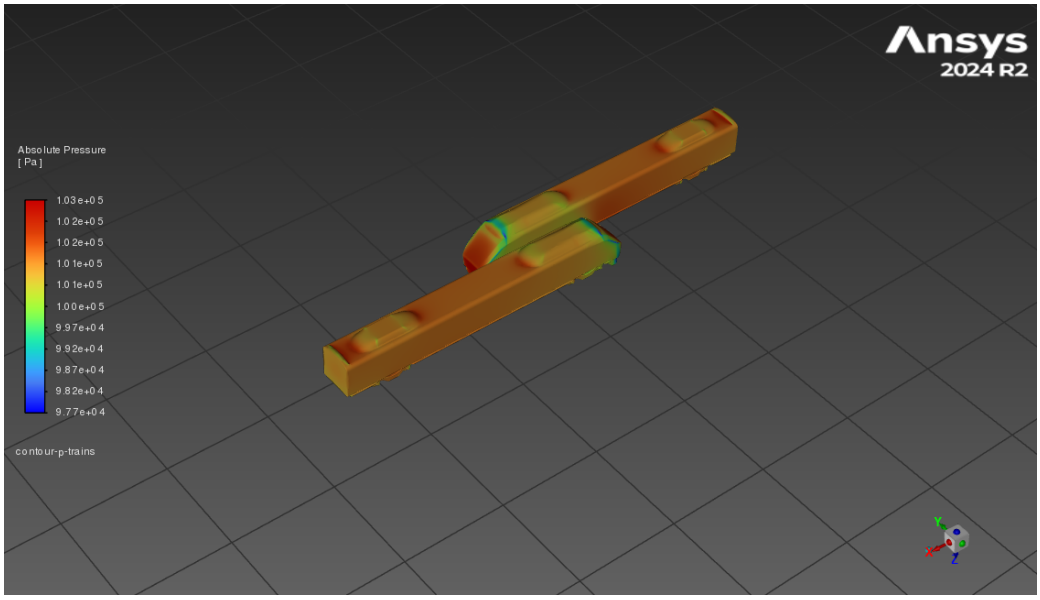


Figure 6.36: Contour of absolute pressure around the vehicles at $t = 0.500$s.

In this image, it is clear that the main vehicle has a lower pressure in the area which is already "in contact" with the other's boundary layer. This is due to all the phenomena previously described; after the high-pressure region near the tip of the slipstream is passed, a low-pressure one follows.

This creates that strange phenomena where the train being observed has a higher pressure where the other train is yet to cross it, which decreases after immediately after. Even so, this analysis reinforces the propositions made during the analysis of the characteristic curves, mainly the lateral force coefficient and the pressure coefficient.

More frames from this animation are presented in appendix F; although they were not essential for this analysis, they still complement it and help understanding the flow.

The graphical results, attained from singling out chosen frames from the animations recorded, heavily corroborate the data and assumptions made during the past section. In that case, it can be deduced that the results from that study were reliable. The coefficiets (in particular, C_y) did not show any worrying values.

Therefore, the critical moments of the manoeuvre happen at a reduced magnitude, so the risk of derailment or any incident is minimal.

So, after this extensive assessment, it is possible to judge the aerodynamic performance of the Portuguese train during the passing manoeuvre.

Just like in the crosswinds study, the data suggested a predictable behaviour of the model during the whole experiment, which increases the reliability in this CFD experiment. Unfortunately, there is not a clear case to compare the model to.

Nevertheless, the development of pressure and velocity fields, as well as the aerodynamic coefficients monitored over time, suggest a solid stability of the model in this operating condition. The critical values were all within reasonable limits. Not only that, they were easily justified by the evolution of the fluid flow depicted in the animations created.

Therefore, it is concluded that, according to the CFD data, the *TrainSolutions Portugal* model is highly stable during the passing manoeuvre. It should proceed to physical experiments in order to be certified.

In this case, no geometry modifications are suggested, as no significant regions were found to be creating particularly troublesome turbulent effects. On a more general note, since crosswinds and passage of trains were studied separately, it would have been interesting to conceive a combined experiment to see how the model behaves.

To conclude the analysis of results, the Portuguese train model presented is robust and stable. After finding the best configuration to study it, numerical experiments were performed to assess its aerodynamic performance in circulation under crosswinds and during a passing manoeuvre. The results proved that the model is reliable, and a few optimizations to the geometry were postulated as possible means to improve its energy efficiency and safety even further.

Chapter 7

Conclusions

This chapter contains the conclusions drawn from the work developed throughout the length of this project. The main aspects of the study are briefly revisited, followed by a discussion of the principal findings obtained from the CFD aerodynamic investigation of several manoeuvers for the Portuguese train.

The results attained and their relevance is addressed, as well as the extent to which the objectives established in the beginning were achieved. A quick look at the limitations and difficulties met in this assignment is also present.

Finally, the dissertation ends with some sugestions of future projects to complement this one and a personal reflection on the work carried out throughout the thesis.

7.1 Summary of the Thesis

In summary, this thesis investigated the aerodynamic behaviour of a new Portuguese high-speed train model under some of the most critical operating conditions using the CFD named ANSYS Fluent. The study focused mainly on circulation under crosswinds and the interaction between 2 vehicles travelling in opposite directions. Particular emphasis was given to the unsteady aerodynamic phenomena generated in the train passing manoeuvre, due to its complexity.

So, 3D computational models were developed to reproduce these events in order to evaluate the resulting flow field and aerodynamic loads. To provide validation, in a first stage, the CFD setup and the numerical mesh were tested (with benchmark results from the European standards), to obtain the most solid configuration for analysing the results, while keeping the computational cost manageable. In that sense, the SST $k-\omega$ turbulence model was chosen for getting the closest to the standard results in the benchmark tests that were performed to assess the robustness of the layout. To represent the transient case, an overset mesh approach was adopted.

Then, for one case study at a time, a complete reseach was carried out, always keeping in mind the end goal. Different approaches were included, since the train model was new

and there is still much to learn in the field of numerical validation for railway vehicle aerodynamics. The complete range of crosswinds was studied and the passing manoeuvre was represented with a reasonable amount of realism. The whole procedure was laid out so the results can be reproduced in subsequent studies.

Naturally, the interpretation of the results followed. The simulations were conceived to allow for the best possible way to analyse some traits of the complex fluid flow associated with the train circulation. The values of force coefficients and visual confirmation of the induced aerodynamic phenomena provided an insight into the intricate world of unsteady airflow around moving vehicles and, regarding this project in particular, the behaviour of the *TrainSolutions Portugal* model.

Finally, conclusions were drawn to provide an overall assessment of the work.

7.2 Conclusions

7.2.1 Importance of the Results

This section evaluates the practical and scientific relevance of the main findings obtained in this work.

Chapter 6 analyzed the results from the CFD simulations performed during this research, providing key insights for the assessment and geometric optimization of the *TrainSolutions Portugal* vehicle.

Given the ongoing challenges and unknowns in the numerical aerodynamic assessment of railway systems, this study addresses critical operating conditions while offering practical guidelines for the application of ANSYS Fluent in train aerodynamics. These insights contribute to advancing a domain that is essential for the energy transition in transportation.

Regarding the primary objective of this study - the assessment of the Portuguese train model - the numerical results were fundamental in characterizing its aerodynamic behavior under the two critical scenarios investigated.

In the crosswinds analysis, the primary aerodynamic coefficients (C_x, C_y, C_z and C_{Mx_lee}) were evaluated across yaw angles ranging from 0° to 90°. This allowed the characterization of the force and moment evolution as a function of wind incidence. Furthermore, comparing these curves with the benchmark ICE model enabled the validation of the characteristic trends against an established reference platform.

The evolution of these variables with the yaw angle exhibited a predictable trend, consistent with the behaviors documented in the literature and normative standards. Graphical outputs, including absolute pressure contours and flow pathlines, provided visual evidence of the flow field, enabling the identification and tracking of turbulent structures such as vortex formations. The overall assessment indicates that the vehicle complies with

the stability and safety requirements for commercial operation. Additionally, specific regions (such as sharp edges and geometric protrusions) were identified as candidates for aerodynamic shape optimization to further enhance energy efficiency.

Regarding the train passing manoeuvre, unsteady CFD simulations spanning over 1000 time steps ($\Delta t = 0.001$s) enabled a detailed transient tracking of the aerodynamic coefficients (C_x, C_y, C_z) for both vehicles, as well as the pressure coefficient (C_p) at the intersection midpoint. The analysis confirmed that the localized pressure gradients generated during the passage induce transient push-pull forces on the vehicle structures.

Flow animations and time-history plots allowed for the identification of critical transient phases and geometric interactions. The data demonstrate that the *TrainSolutions Portugal* model maintains structural and aerodynamic stability throughout the manoeuvre, with all monitored variables remaining within safe operational limits.

While the identified geometric disturbance regions are not critical under isolated conditions, their influence could be amplified during combined scenarios (e.g., passing manoeuvres under severe crosswinds). Addressing these regions through minor geometric refinements can prevent localized flow instabilities and avoid the need for operational speed restrictions.

In conclusion, the CFD framework implemented in this study provides a reliable performance assessment of the new Portuguese train model, confirming its aerodynamic efficiency and safety while outlining clear paths for geometric optimization. These results establish a consistent baseline for future full-scale experimental testing and the formal certification of the TrainSolutions Portugal project.

7.2.2 Challenges and Limitations

This section addresses the primary technical challenges encountered during the research and outlines the inherent limitations of the implemented methodology.

Regarding the operational and computational challenges, the high computational cost associated with the simulations - particularly the unsteady CFD models for the train passing manoeuvre - represented a significant constraint, requiring strict optimization of mesh size and time step selection within the available timeframe. Additionally, mastering the complex setup and convergence parameters in ANSYS Fluent for high-Reynolds transient flows required an extensive preliminary calibration phase.

Concerning the methodological limitations, the primary constraint lies in the simplification of the computational domain and boundary conditions. The physical environment was modeled with idealized surrounding geometry, excluding real-world features such as ground ballast roughness, surrounding terrain topography, and atmospheric boundary layer crosswind profiles. Furthermore, due to resource and infrastructure constraints, direct experimental validation (e.g., wind tunnel testing or full-scale field measurements) was not performed; consequently, model validation was carried out against benchmark data from the literature and established numerical references (ICE model).

7.3 Future Works

This dissertation covered the work accomplished over a period of almost seven months. During this period, significant resources were devoted to investigating several operating conditions of the Portuguese train in order to assess its aerodynamic performance. It was possible to study several events; however, various other aspects could be addressed in order to provide a more comprehensive understanding of the vehicle. Furthermore, this work contributes to compiling additional information on CFD studies of train aerodynamics, thereby contributing to the existing literature and further expanding the knowledge in an engineering field that still offers considerable scope for research.

Regarding the first stage of the project, comparing different testing conditions to evaluate the effect of each on the results provided an effective means of validating the subsequent work, while also allowing different setup parameters to be tested and their accuracy assessed. Nevertheless, given the nature and scope of the project, only a limited number of variables could be modified. It was useful and pertinent to compare simulations performed using the SST $k-\omega$ and $k-\epsilon$ turbulence models, as well as the 1^{st} and 2^{nd} order convective schemes and different mesh refinements. Nonetheless, there is a much wider range of numerical approaches that could have been incorporated into the testing process in order to investigate their influence on the results. As mentioned in chapter 2, there is value in comparing different RANS turbulence models; additionally, exploring other modelling approaches, such as LES, DES and, in particular, URANS for the transient simulations, would further broaden the scope of the analysis. Each of these approaches has its own particularities, making them suitable for specific applications that may also be relevant to the present study.

Moreover, although separate meshes were created to investigate their influence on the results, this aspect remained relatively unexplored during the initial assessment, as the only modifications introduced concerned the element size, growth rate, and manner in which the finer mesh was integrated into the domain. Some of this potential was explored again in the crosswind and train passing studies; however, it would be interesting to investigate more extensively the various features available in ANSYS Meshing. For instance, experimenting with different element shapes, such as hexahedra or polyhedra, would provide greater depth to the analysis.

Regarding the crosswind study, there are also several aspects that could be investigated further. First of all, performing the simulations under transient conditions would be of interest. In addition, in light of the considerations previously discussed regarding the testing of different configurations, developing alternative setups to better represent the aerodynamic phenomena around the vehicle could be pursued in future work, thereby extending the scope of the analysis. This is particularly relevant in the present case, since convergence issues were observed for the largest yaw angles, a behaviour that has also been reported in numerous studies in the literature. Therefore, identifying a reliable

numerical configuration capable of consistently providing credible results for crosswind train assessments across the full range of yaw angles would be particularly valuable.

With regard to the passing of vehicles, there are also several interesting possibilities for future work. First of all, the use of different geometries, with varying levels of complexity, showed that geometry affects the way ANSYS Fluent represents the aerodynamic phenomena around the trains, consequently influencing the results and the conclusions drawn from them. It would therefore be interesting to investigate other carriage configurations or to incorporate additional elements of the surrounding environment, such as the rails and ballast, as intended in 5.3, in order to assess their influence on the results. Furthermore, some recent studies, such as those cited in chapter 2, have investigated the combined aerodynamic effects of multiple events occurring simultaneously, such as the passing of vehicles under strong crosswind conditions. Investigating such combined scenarios for the present model would therefore be a worthwhile extension of the work.

Considering the *TrainSolutions Portugal* project as a whole, there were other operating conditions that needed to be investigated before the train could enter commercial service. In particular, investigating the *push-pull* mechanism and simulating the entrance into and exit from tunnels are essential to ensure the safety and comfort of passengers.

Finally, it would be particularly valuable to compare the CFD results obtained in the present work with experimental results. Future work involving experimental validation, either through wind-tunnel testing or full-scale experiments, would substantially increase the value of the investigation performed. As stated throughout the earlier chapters, numerical simulations provide an effective starting point for assessing the aerodynamic performance of a railway vehicle; however, certification still relies heavily on experimental measurements. Such experimental data would not only contribute to the comprehensive validation of the Portuguese train, but would also provide an important basis for assessing the accuracy of the numerical models and for further improving the CFD methodology.

References

[1] International Energy Agency. Energy statistics data browser, 2025.

[2] Welectric. 1974–25 de abril: Como Éramos e como somos, April 2024.

[3] Infraestruturas de Portugal. Ferrovia 2020, 2026.

[4] Infraestruturas de Portugal. Projeto de alta velocidade, 2025.

[5] Nomad Tech. R&d projects, 2026.

[6] Railway applications – aerodynamics – part 6: Requirements and test procedures for cross wind assessment, 2022.

[7] International Energy Agency. The future of rail: Opportunities for energy and the environment. Technical report, International Energy Agency, 2019.

[8] Rádio e Televisão de Portugal. História dos comboios em portugal, 2024.

[9] Infraestruturas de Portugal. Caminho de ferro: 168 anos de história e compromisso com o futuro, 2024.

[10] Raquel Abecasis. Adesão à CEE. um tratado que mudou radicalmente Portugal, June 2025.

[11] Inês Teotónio Pereira. Comboios. quase metade das linhas férreas foram encerradas depois do 25 de abril, June 2024.

[12] Autoridade da Mobilidade e dos Transportes. Relatório dos sistemas de metro em Portugal (2018–2020). Technical report, Autoridade da Mobilidade e dos Transportes, December 2021.

[13] World Population Review. Railroads by country, 2026.

[14] Recuperar Portugal. Plano de recuperação e resiliência (prr), 2026. Portal oficial do Plano de Recuperação e Resiliência de Portugal.

[15] TrainSolutions Portugal. Trainsolutions Portugal, 2026.

[16] Centro de Competências Ferroviário. Trainsolutions Portugal, 2026.

[17] Railway applications – aerodynamics – part 1: Symbols and units, April 2003.

[18] International Union of Railways (UIC). *High-Speed Rail: Fast Track to Sustainable Mobility*. International Union of Railways (UIC), Paris, France, 2015.

[19] Railway News. Why europe's en 14067-5 is key to high-speed rail safety, December 2024.

[20] Joseph A. Schetz, editor. *Aerodynamics of High-Speed Trains*. Von Karman Institute for Fluid Dynamics, 2001.

[21] Aerotrain: Aerodynamics: Total regulatory acceptance for the interoperable network. Final project report, European Commission, Sixth Framework Programme (FP6), 2009.

[22] Christopher J. Baker. A review of train aerodynamics part 1: Fundamentals. *The Aeronautical Journal*, 118(1202):201–232, 2014.

[23] Railway applications – aerodynamics – part 4: Requirements and assessment procedures for aerodynamics on open track, 2024.

[24] Railway applications – aerodynamics – part 5: Requirements and assessment procedures for aerodynamics in tunnels, 2024.

[25] Duarte Cachulo. Numerical simulation: Faster and more efficient production with fewer resources, February 2025.

[26] High-speed rail aerodynamic assessment and mitigation. Technical report, Federal Railroad Administration, 2015.

[27] Railway applications – gauges – part 3: Infrastructure, 2025.

[28] Maciej Szudarek, Adam Piechna, Piotr Prusiński, and Leszek Rudniak. Cfd study of high-speed train in crosswinds for large yaw angles with rans-based turbulence models including geko tuning approach. *Energies*, 15(18):6549, 2022.

[29] Christopher J. Baker. A review of train aerodynamics part 2: Applications. *The Aeronautical Journal*, 118(1202):345–382, 2014.

[30] H. K. Versteeg and W. Malalasekera. *An Introduction to Computational Fluid Dynamics: The Finite Volume Method*. Pearson Education, Harlow, United Kingdom, 2 edition, 2007.

[31] John D. Anderson Jr. *Computational Fluid Dynamics: The Basics with Applications*. McGraw-Hill, New York, NY, USA, 1995.

[32] Suhas V. Patankar. *Numerical Heat Transfer and Fluid Flow*. Hemisphere Publishing Corporation, Washington, DC, USA, 1980.

[33] Mark Sterling. Slipstreams and wakes generated by trains. Master's thesis, University of Birmingham, 2003.

[34] Frank M. White and Henry Xue. *Fluid Mechanics*. McGraw-Hill Education, New York, NY, 9 edition, 2021.

[35] David C. Wilcox. *Turbulence Modeling for CFD*. DCW Industries, La Cañada, California, USA, 3 edition, 2006.

[36] ScienceDirect Topics. Reynolds-averaged navier-stokes, n.d.

[37] F. R. Menter. Two-equation eddy-viscosity turbulence models for engineering applications. *AIAA Journal*, 32(8):1598–1605, August 1994.

[38] Tian Li, Hassan Hemida, Mohammad Mehdi Rashidi, and Weihua Zhang. The effect of numerical divergence schemes on the flow around trains. *Fluid Dynamics Research*, 52(2):025509, 2020.

[39] Aravind Seeni, Parvathy Rajendran, Mamat Hussin, and Farzad Ismail. Errors and uncertainties in simulation of steady, viscous flow past a circular cylinder at Re = 20 using a systematic approach. *INCAS Bulletin*, 12(3):203–217, 2020.

[40] Zhuming Bi. *Finite Element Analysis Applications: A Systematic and Practical Approach*. Academic Press, 1 edition, 2018.

[41] William M. Chan. Overset grid technology development at nasa ames research center. *Computers & Fluids*, 38(3):496–503, 2009.

[42] G. Chesshire and W. D. Henshaw. Composite overlapping meshes for the solution of partial differential equations. *Journal of Computational Physics*, 90(1):1–64, September 1990.

[43] Piotr Łukaszewicz. *Energy Consumption and Running Time for Trains: Modelling of Running Resistance and Driver Behaviour Based on Full Scale Testing*. Doctoral thesis, Royal Institute of Technology (KTH), Stockholm, Sweden, 2001.

[44] P. Fernández, I. Villalba Sanchis, V. Yepes, and I. Ruiz Fernández. A review of modelling and optimisation methods applied to railway energy consumption. *Journal of Cleaner Production*, 222:153–168, 2019.

[45] Tianyun Dong, Xifeng Liang, Sinisa Krajnović, Xiaohui Xiong, and Wei Zhou. Effects of simplifying train bogies on surrounding flow and aerodynamic forces. *Journal of Wind Engineering and Industrial Aerodynamics*, 191:170–182, 2019.

[46] João Ricardo Coroado Pedro. Controlo aerodinâmico ativo de um comboio de alta-velocidade. Master's thesis, Instituto Superior Técnico, 2016.

[47] Nicolas Paradot, B. Angel, Pierre-Etienne Gautier, and Louis-Marie Cléon. Numerical simulation and experimental investigation of the side loading on a high speed train. In *Engineering Turbulence Modelling and Experiments 6*, pages 657–666. Elsevier, 2005.

[48] Martin Gallagher, Justin Morden, Christopher Baker, David Soper, Andrew Quinn, Hassan Hemida, and Mark Sterling. Trains in crosswinds – comparison of full-scale on-train measurements, physical model tests and cfd calculations. *Journal of Wind Engineering and Industrial Aerodynamics*, 175:428–444, 2018.

[49] Marco Bocciolone, Federico Cheli, Roberto Corradi, Sara Muggiasca, and Gisella Tomasini. Crosswind action on rail vehicles: Wind tunnel experimental analyses. *Journal of Wind Engineering and Industrial Aerodynamics*, 96(5):584–610, 2008.

[50] Zijian Guo, Tanghong Liu, Miao Yu, Zhengwei Chen, Wenhui Li, Xiaoshuai Huo, and Hongkang Liu. Numerical study for the aerodynamic performance of double unit train under crosswind. *Journal of Wind Engineering and Industrial Aerodynamics*, 191:203–214, 2019.

[51] Tao Li, Zhen Dai, and Wei Zhang. Effect of rans model on the aerodynamic characteristics of a train in crosswinds using ddes. *Computer Modeling in Engineering & Sciences*, 122(2):555–570, 2020.

[52] Siavash Maleki, David Burton, and Mark C. Thompson. Assessment of various turbulence models (eles, sas, urans and rans) for predicting the aerodynamics of freight train container wagons. *Journal of Wind Engineering and Industrial Aerodynamics*, 170:68–80, 2017.

[53] Kozo Fujii and Takanobu Ogawa. Aerodynamics of high speed trains passing by each other. *Computers & Fluids*, 24(8):897–908, 1995.

[54] Harvey Shui-Hong Lee. The aerodynamic effects of passing trains to surrounding objects and people. Technical Report DOT/FRA/ORD-09/07, U.S. Department of Transportation, Federal Railroad Administration, 2009.

[55] Daniele Rocchi, Gisella Tomasini, Paolo Schito, and Claudio Somaschini. Wind effects induced by high speed train pass-by in open air. *Journal of Wind Engineering and Industrial Aerodynamics*, 173:279–288, 2018.

[56] Feilong Li, Jianjun Luo, Dengke Wang, and Lei Wang. Aerodynamic characteristics when trains pass each other in high-speed railway shield tunnel. *Applied Sciences*, 12(12):6244, 2022.

[57] Hao Hu, Huo-yue Xiang, Ke-hong Liu, Jin Zhu, and Yong-le Li. Aerodynamic characteristics of moving vehicles of two trains passing each other on bridge under crosswinds. *Journal of Central South University*, 29(8):2558–2573, 2022.

[58] Xiuping Duan, Yuangui Mei, Xiao Hu, and Changbao Qi. Influence of speed and line spacing on aerodynamic forces in high speed train passing in tunnels. *Scientific Reports*, 14:26814, 2024.

[59] Hyeokbin Kwon, Beomsu Kim, Woonghee Lee, and Junsun Ahn. Aerodynamic forces and moments on high-speed trains passing by each other. *Journal of Mechanical Science and Technology*, 38(12):6645–6656, 2024.

[60] Jiri Blazek. *Computational Fluid Dynamics: Principles and Applications*. Butterworth-Heinemann, 3 edition, 2015.

[61] Carlos Alberto Fernandes Izidoro. Desafios aerodinâmicos de um comboio ligeiro de alta-velocidade. Master's thesis, Instituto Superior Técnico, 2019.

[62] H. C. Lim, I. P. Castro, and R. P. Hoxey. Bluff bodies in deep turbulent boundary layers: Reynolds-number issues. *Journal of Fluid Mechanics*, 571:97–129, 2007.

[63] B. Xu, T. Liu, Y. Xia, W. Li, X. Huo, H. Gao, Z. Chen, and H. Liu. Computational fluid dynamics prediction of the aerodynamic difference between stationary and moving trains. *Alexandria Engineering Journal*, 70:685–699, 2023.

[64] NASA Glenn Research Center. Navier-stokes equations, 2025.

[65] Oregon State University. Intermediate fluid mechanics: Cfd basics, 2024.

[66] CFDLand. Discretization of equations in cfd solver: A detailed guide to first order, second order, quick, and muscl schemes, 2025.

[67] Engineering Downloads. K-epsilon vs k-omega sst: Choosing your cfd turbulence model, April 2026.

[68] Kiarash Kord. Pressure-velocity coupling: Simple vs simplec vs piso vs coupled, 2024.

[69] ANSYS, Inc. *ANSYS Fluent User's Guide: Dynamic Mesh and Fluid-Structure Interaction*. ANSYS, Inc., 2024. Release 2024 R2.

[70] ANSYS, Inc. *ANSYS Fluent User's Guide*. ANSYS, Inc., 2024. Release 2024 R2.

Appendix A

UDF for the Transient Simulations

A.1 UDF File "prime" for the Movement of the Main Vehicle (Along the x-Direction)

```
#include "udf.h"

/* Translational motion of the overset zone */
DEFINE_CG_MOTION(moving_train, dt, vel, omega, time, dtime)
{
    /* Translational velocity */
    vel[0] = 50.0;              /* x-direction */
    vel[1] = 0.0;               /* y-direction */
    vel[2] = 0.0;               /* z-direction */

    /* No rotation */
    omega[0] = 0.0;
    omega[1] = 0.0;
    omega[2] = 0.0;
}
```

A.2 UDF File "secondary" for the Movement of the Second Vehicle (Opposite to the x-Direction)

```
#include "udf.h"

/* Translational motion of the overset zone */
DEFINE_CG_MOTION(moving_train, dt, vel, omega, time, dtime)
{
    /* Translational velocity */
    vel[0] = -50.0;            /* x-direction */
    vel[1] = 0.0;              /* y-direction */
    vel[2] = 0.0;              /* z-direction */

    /* No rotation */
    omega[0] = 0.0;
    omega[1] = 0.0;
    omega[2] = 0.0;
}
```

Appendix B

Contours of Absolute Pressure Around the Train (Crosswinds Study)

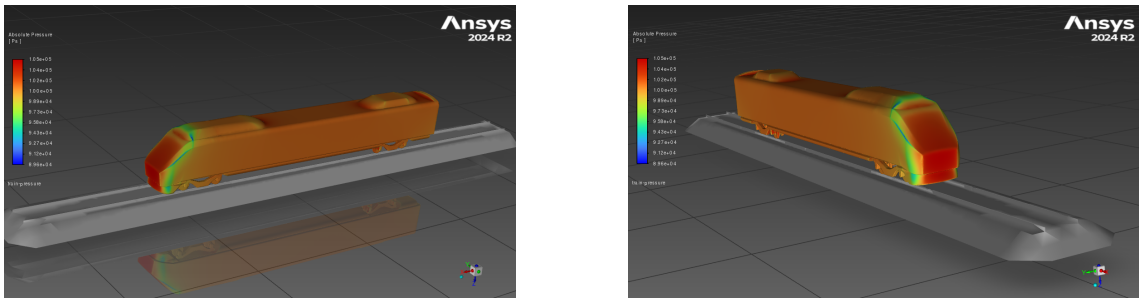


Figure B.1: Contours of absolute pressure around the train for the crosswind study at a yaw angle of 0°, viewed from the leeward (left) and windward (right) sides.

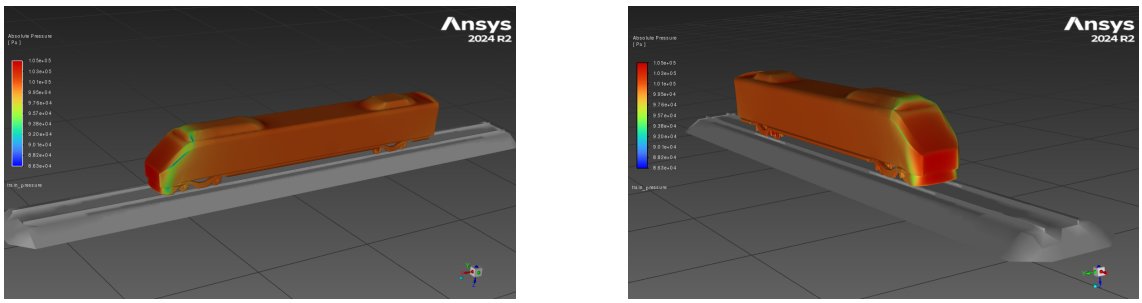


Figure B.2: Contours of absolute pressure around the train for the crosswind study at a yaw angle of 5°, viewed from the leeward (left) and windward (right) sides.

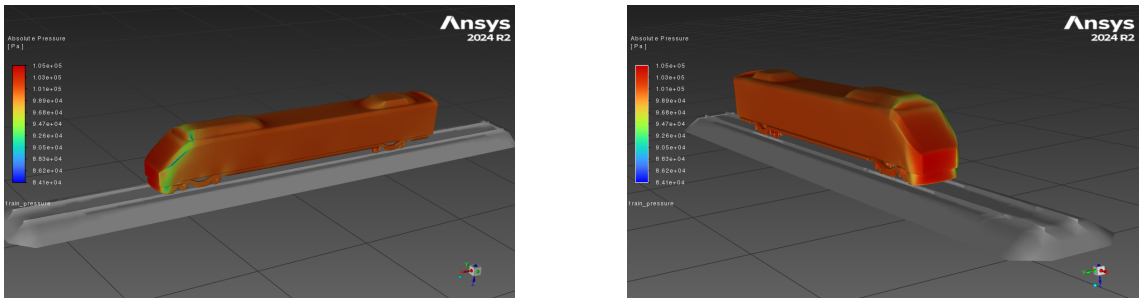


Figure B.3: Contours of absolute pressure around the train for the crosswind study at a yaw angle of 10°, viewed from the leeward (left) and windward (right) sides.

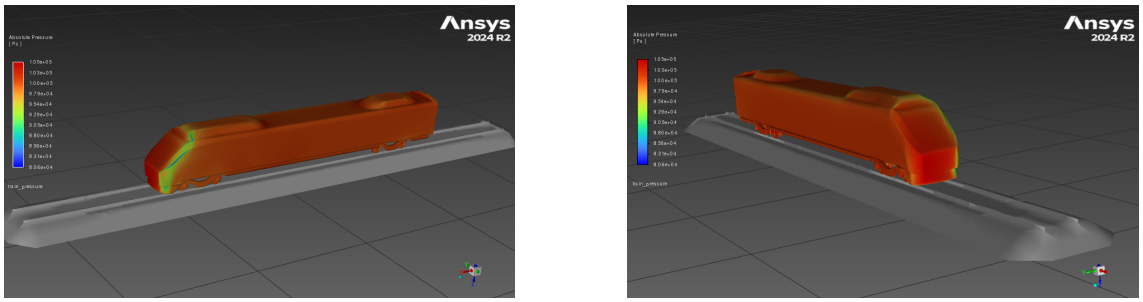


Figure B.4: Contours of absolute pressure around the train for the crosswind study at a yaw angle of 15°, viewed from the leeward (left) and windward (right) sides.

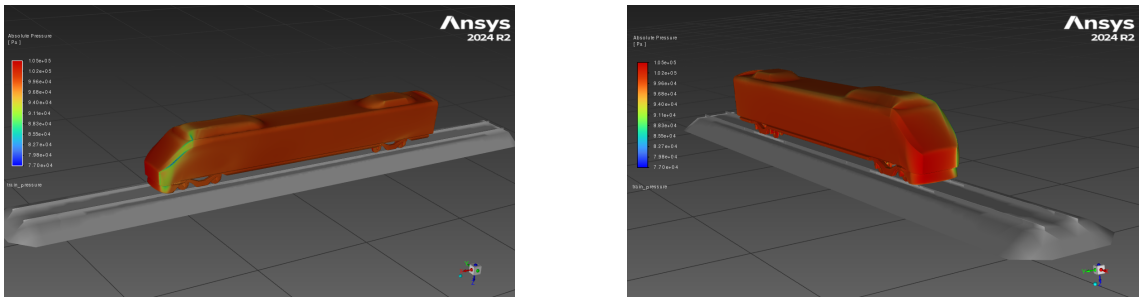


Figure B.5: Contours of absolute pressure around the train for the crosswind study at a yaw angle of 20°, viewed from the leeward (left) and windward (right) sides.

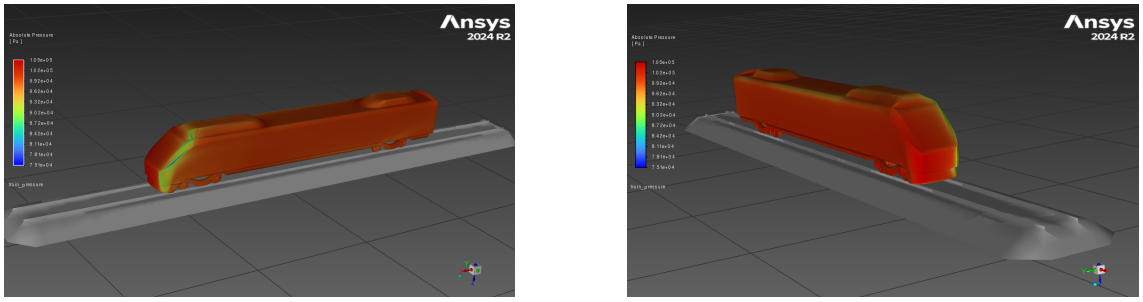


Figure B.6: Contours of absolute pressure around the train for the crosswind study at a yaw angle of 25°, viewed from the leeward (left) and windward (right) sides.

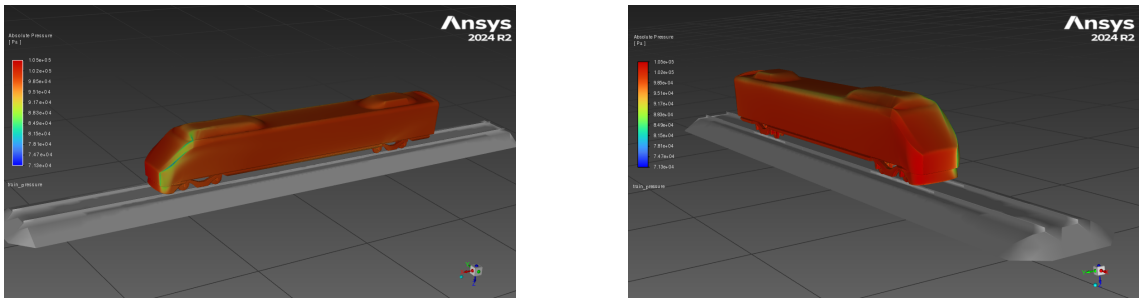


Figure B.7: Contours of absolute pressure around the train for the crosswind study at a yaw angle of 30°, viewed from the leeward (left) and windward (right) sides.

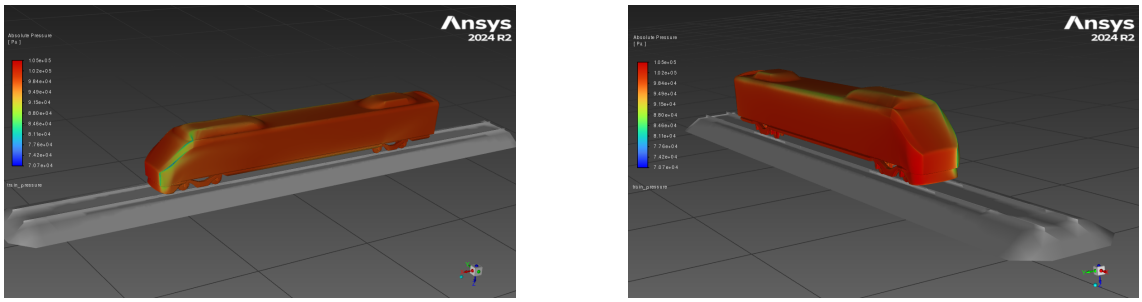


Figure B.8: Contours of absolute pressure around the train for the crosswind study at a yaw angle of 35°, viewed from the leeward (left) and windward (right) sides.

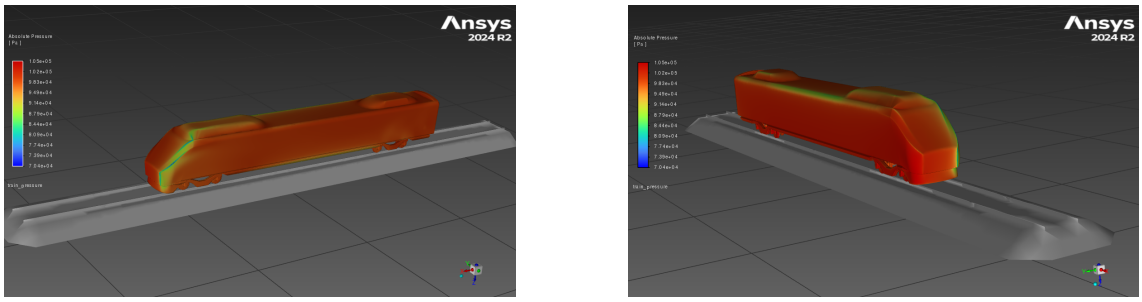


Figure B.9: Contours of absolute pressure around the train for the crosswind study at a yaw angle of 40°, viewed from the leeward (left) and windward (right) sides.

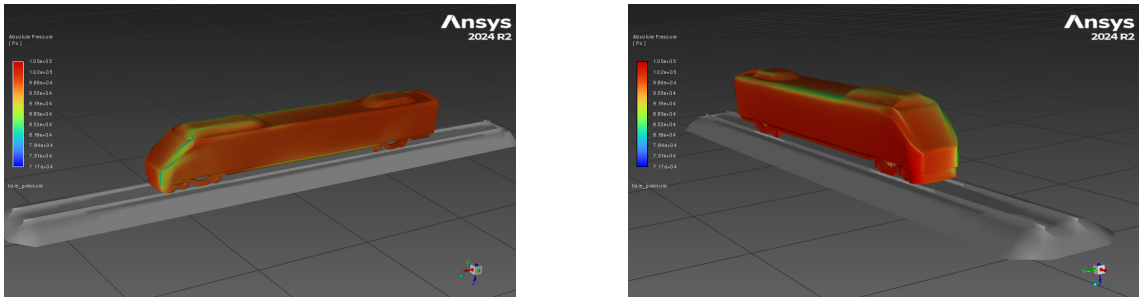


Figure B.10: Contours of absolute pressure around the train for the crosswind study at a yaw angle of 45°, viewed from the leeward (left) and windward (right) sides.

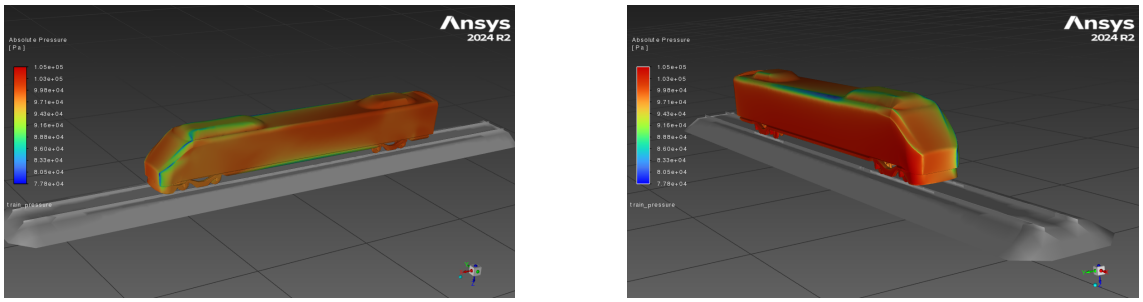


Figure B.11: Contours of absolute pressure around the train for the crosswind study at a yaw angle of 50°, viewed from the leeward (left) and windward (right) sides.

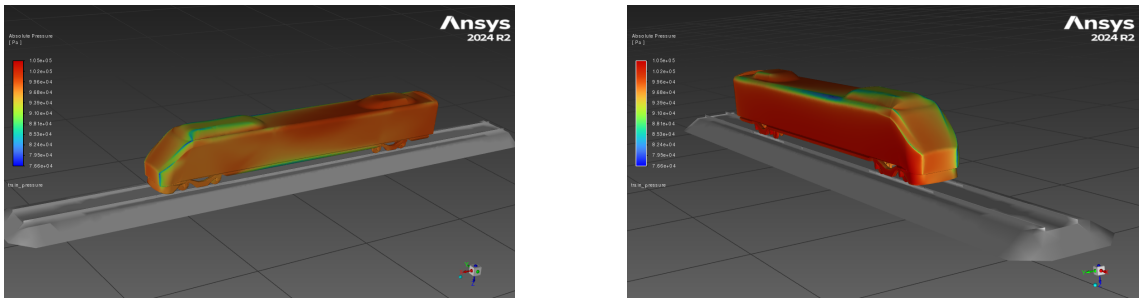


Figure B.12: Contours of absolute pressure around the train for the crosswind study at a yaw angle of 55°, viewed from the leeward (left) and windward (right) sides.

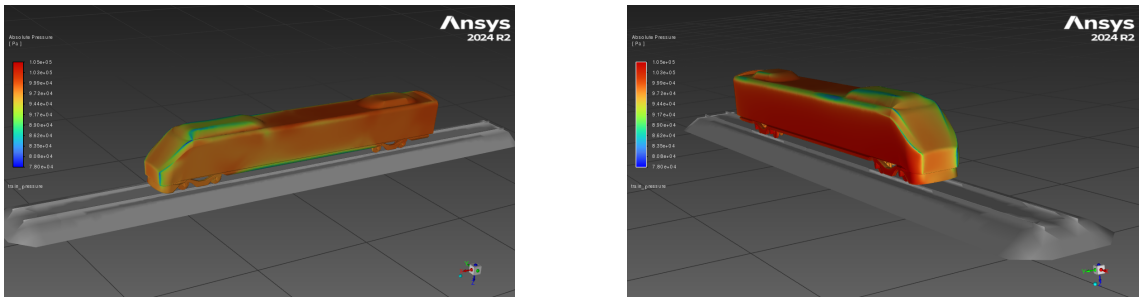


Figure B.13: Contours of absolute pressure around the train for the crosswind study at a yaw angle of 60°, viewed from the leeward (left) and windward (right) sides.

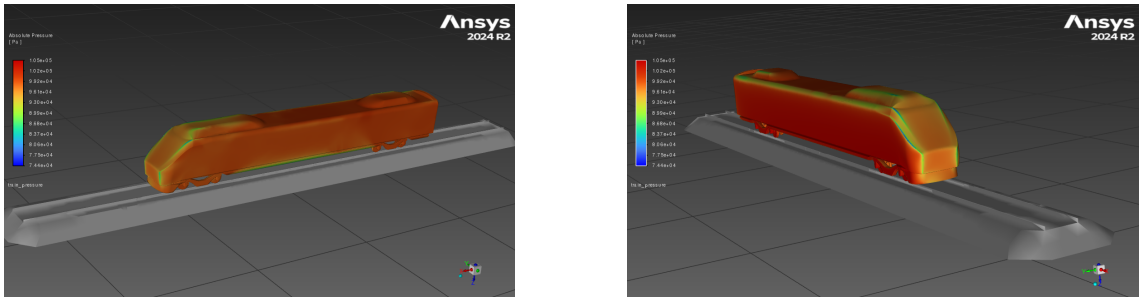


Figure B.14: Contours of absolute pressure around the train for the crosswind study at a yaw angle of 70°, viewed from the leeward (left) and windward (right) sides.

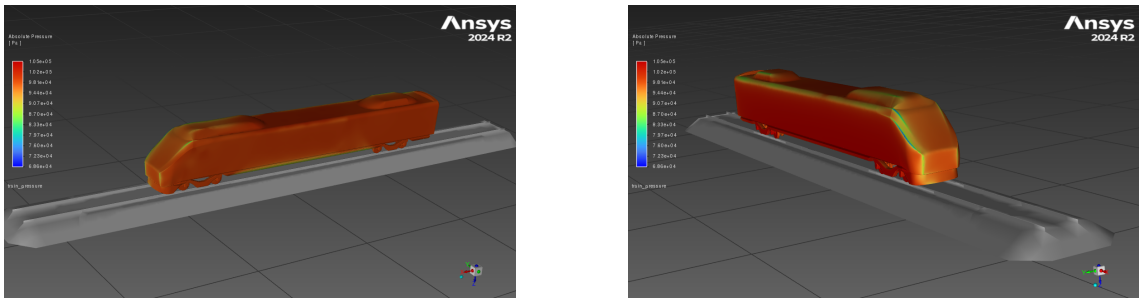


Figure B.15: Contours of absolute pressure around the train for the crosswind study at a yaw angle of 80°, viewed from the leeward (left) and windward (right) sides.

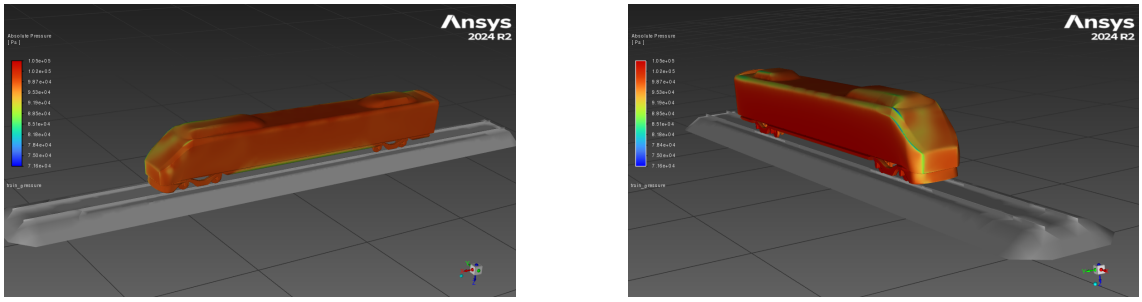


Figure B.16: Contours of absolute pressure around the train for the crosswind study at a yaw angle of 90°, viewed from the leeward (left) and windward (right) sides.

Appendix C

Pathlines Around the Train (Crosswind Study)

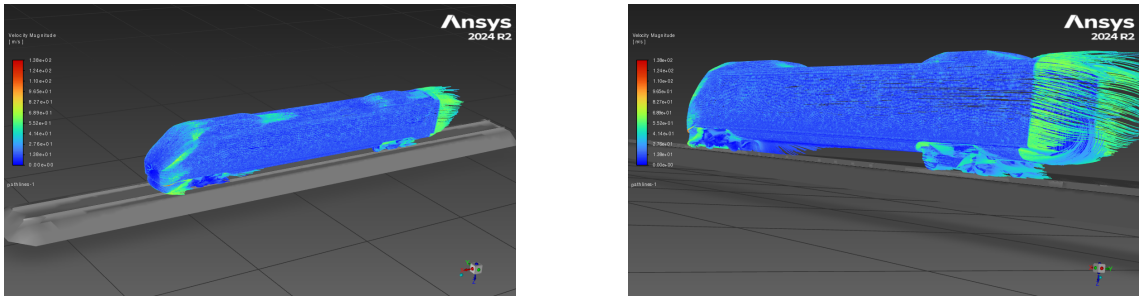


Figure C.1: Pathlines around the train (coloured by velocity magnitude) for the crosswind study at a yaw angle of 0°, viewed from the leeward side from above (left) and below (right).

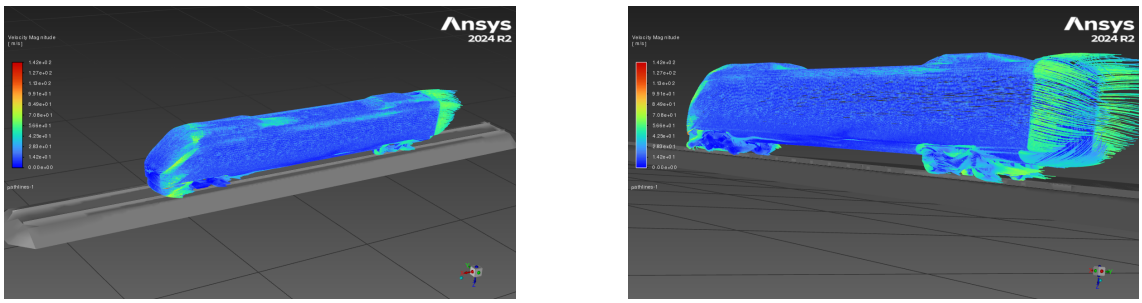


Figure C.2: Pathlines around the train (coloured by velocity magnitude) for the crosswind study at a yaw angle of 5°, viewed from the leeward side from above (left) and below (right).

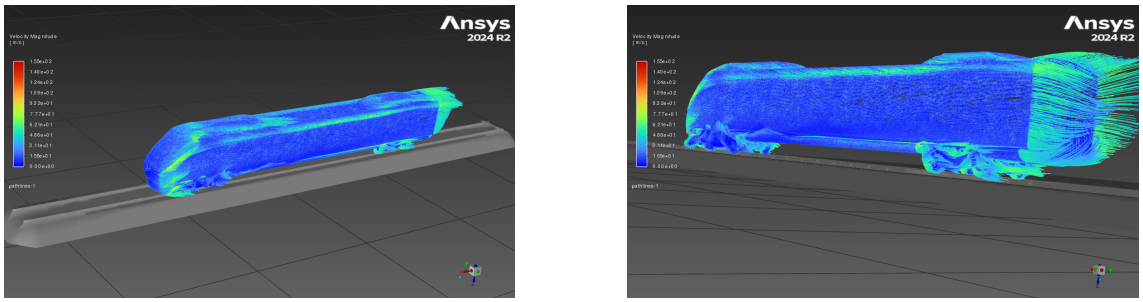


Figure C.3: Pathlines around the train (coloured by velocity magnitude) for the crosswind study at a yaw angle of 10°, viewed from the leeward side from above (left) and below (right).

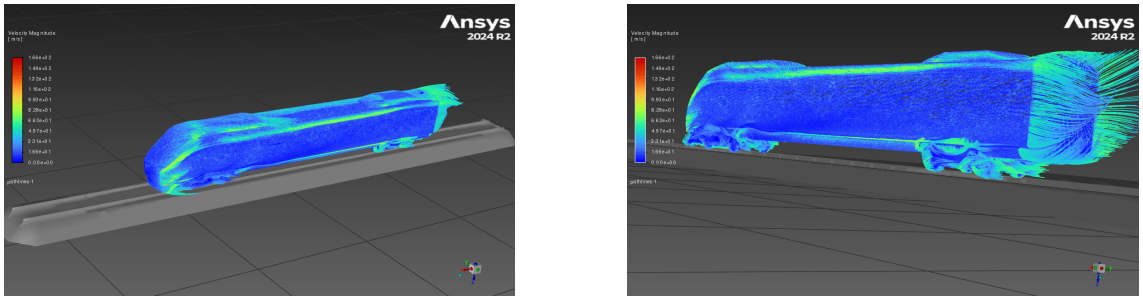


Figure C.4: Pathlines around the train (coloured by velocity magnitude) for the crosswind study at a yaw angle of 15°, viewed from the leeward side from above (left) and below (right).

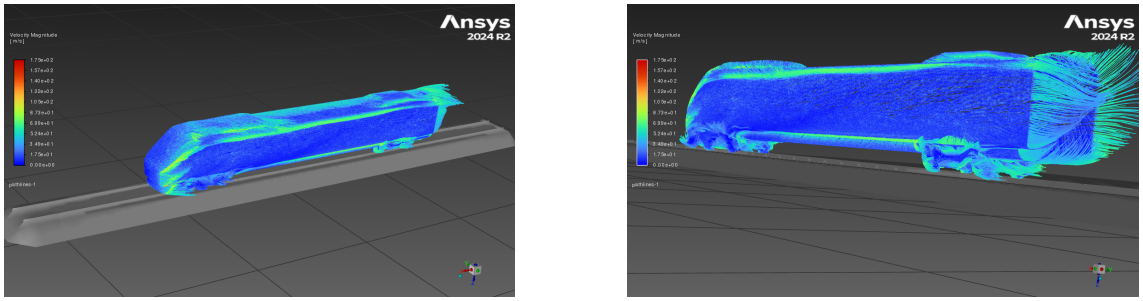


Figure C.5: Pathlines around the train (coloured by velocity magnitude) for the crosswind study at a yaw angle of 20°, viewed from the leeward side from above (left) and below (right).

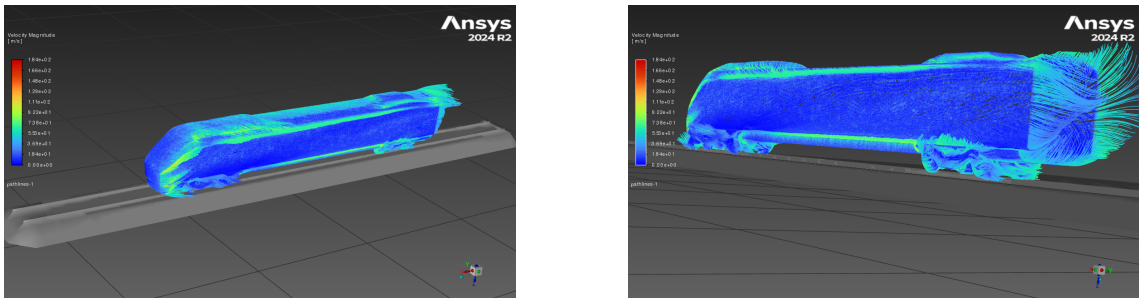


Figure C.6: Pathlines around the train (coloured by velocity magnitude) for the crosswind study at a yaw angle of 25°, viewed from the leeward side from above (left) and below (right).

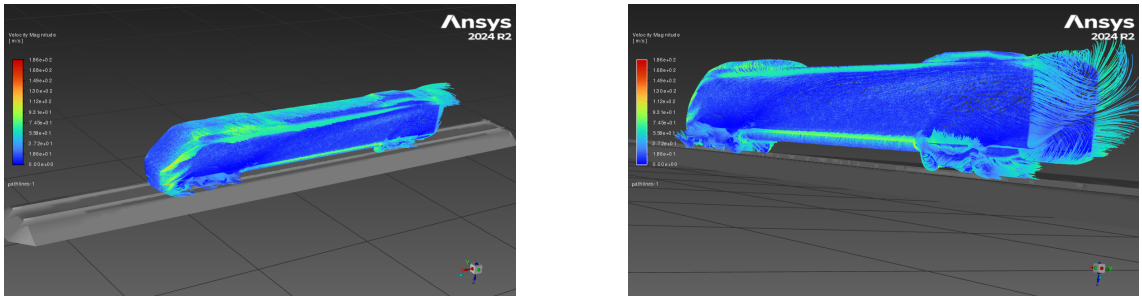


Figure C.7: Pathlines around the train (coloured by velocity magnitude) for the crosswind study at a yaw angle of 30°, viewed from the leeward side from above (left) and below (right).

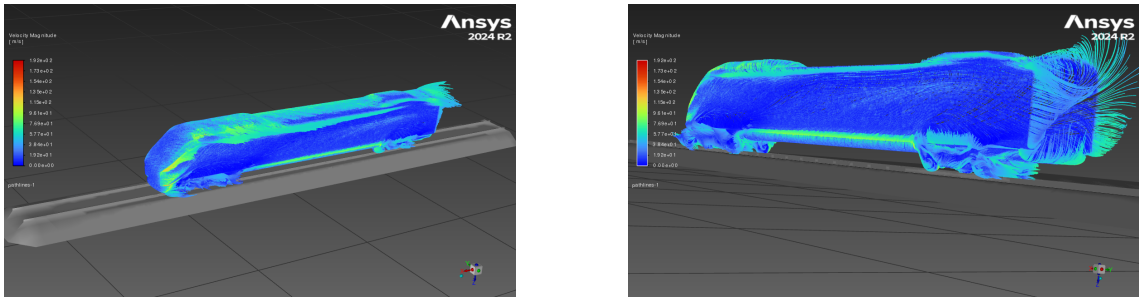


Figure C.8: Pathlines around the train (coloured by velocity magnitude) for the crosswind study at a yaw angle of 35°, viewed from the leeward side from above (left) and below (right).

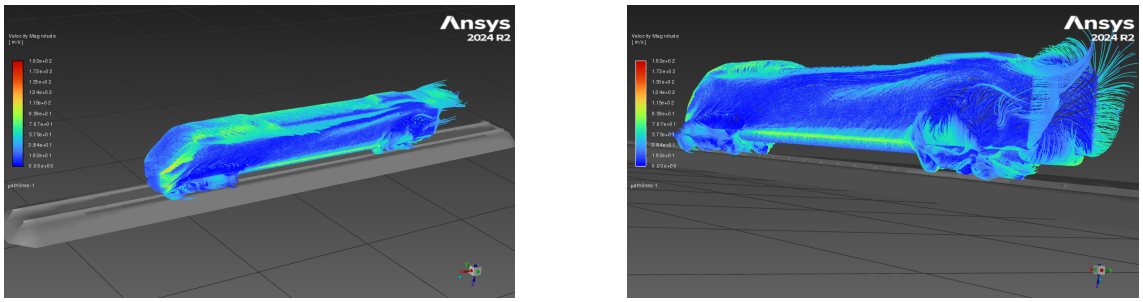


Figure C.9: Pathlines around the train (coloured by velocity magnitude) for the crosswind study at a yaw angle of 40°, viewed from the leeward side from above (left) and below (right).

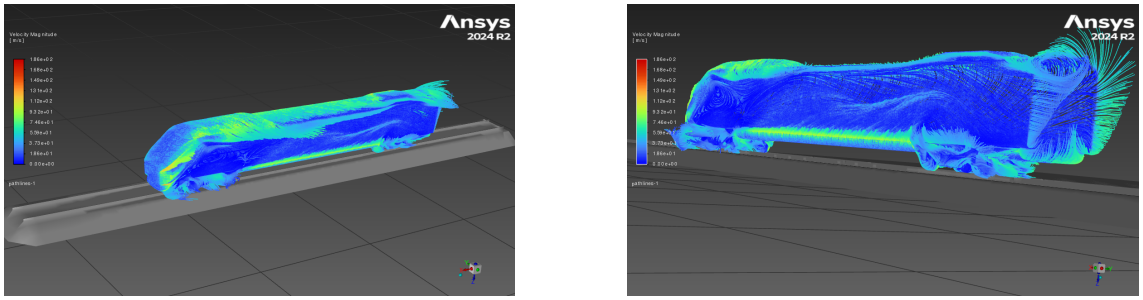


Figure C.10: Pathlines around the train (coloured by velocity magnitude) for the crosswind study at a yaw angle of 45°, viewed from the leeward side from above (left) and below (right).

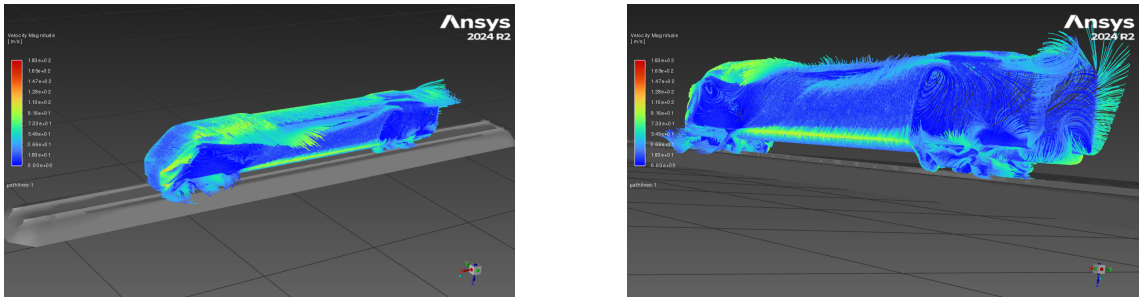


Figure C.11: Pathlines around the train (coloured by velocity magnitude) for the crosswind study at a yaw angle of 50°, viewed from the leeward side from above (left) and below (right).

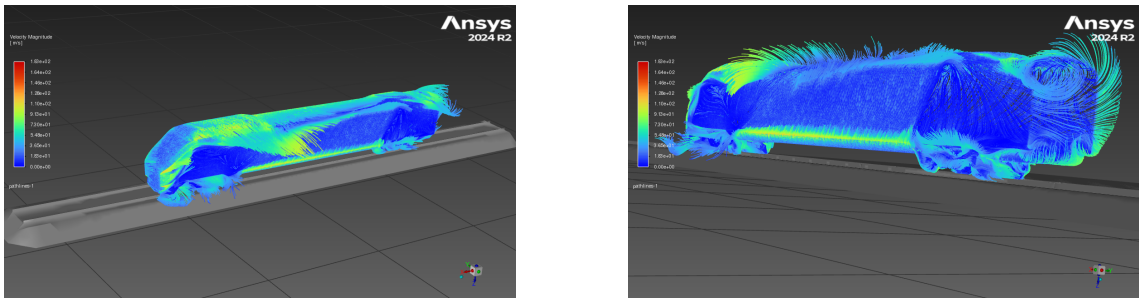


Figure C.12: Pathlines around the train (coloured by velocity magnitude) for the crosswind study at a yaw angle of 55°, viewed from the leeward side from above (left) and below (right).

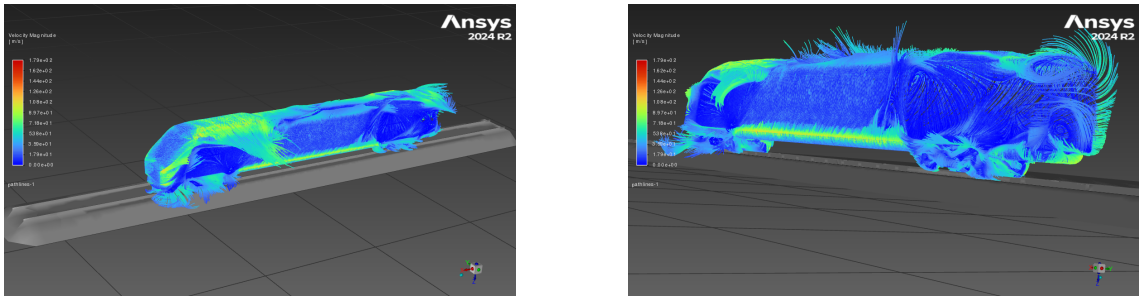


Figure C.13: Pathlines around the train (coloured by velocity magnitude) for the crosswind study at a yaw angle of 60°, viewed from the leeward side from above (left) and below (right).

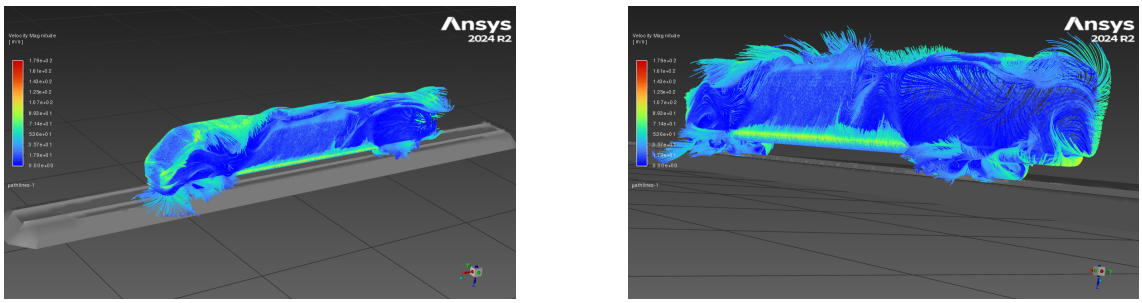


Figure C.14: Pathlines around the train (coloured by velocity magnitude) for the crosswind study at a yaw angle of 70°, viewed from the leeward side from above (left) and below (right).

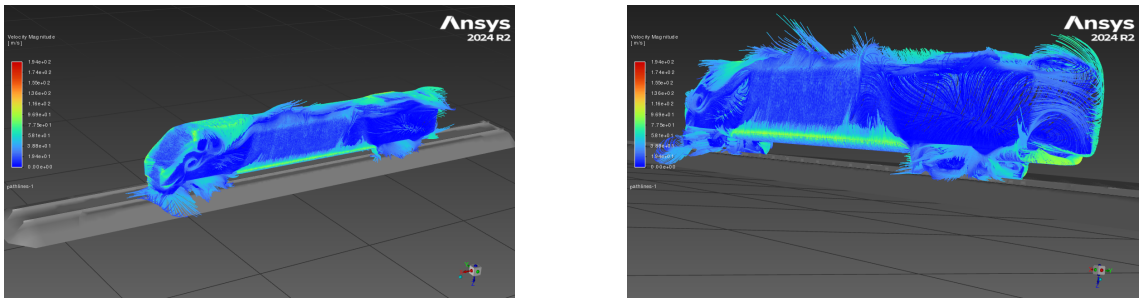


Figure C.15: Pathlines around the train (coloured by velocity magnitude) for the crosswind study at a yaw angle of 80°, viewed from the leeward side from above (left) and below (right).

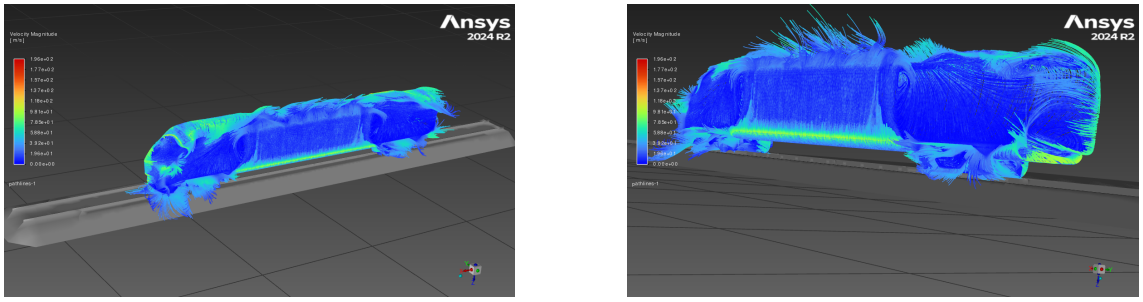


Figure C.16: Pathlines around the train (coloured by velocity magnitude) for the crosswind study at a yaw angle of 90°, viewed from the leeward side from above (left) and below (right).

Appendix D

Velocity Magnitude Contours Around the Train's Cross-Section (Crosswind Study)

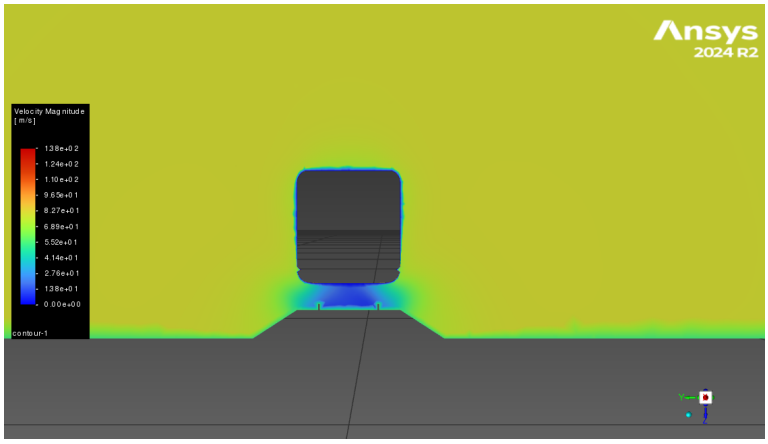


Figure D.1: Velocity magnitude contours around the train on a YZ cross-sectional plane for the crosswind study at a yaw angle of 0°.

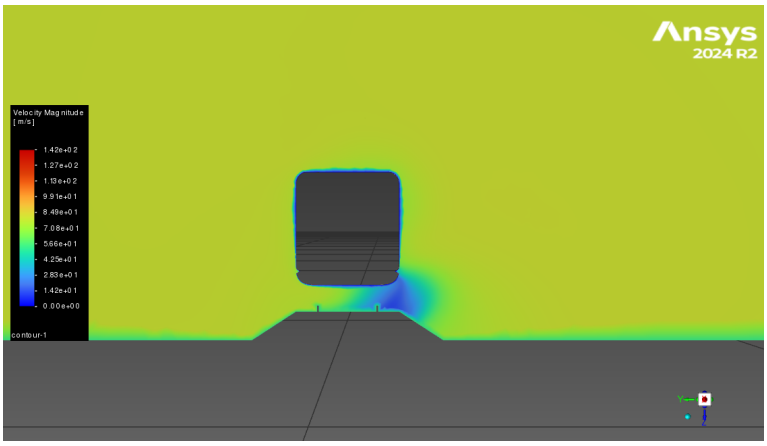


Figure D.2: Velocity magnitude contours around the train on a YZ cross-sectional plane for the crosswind study at a yaw angle of 5°.

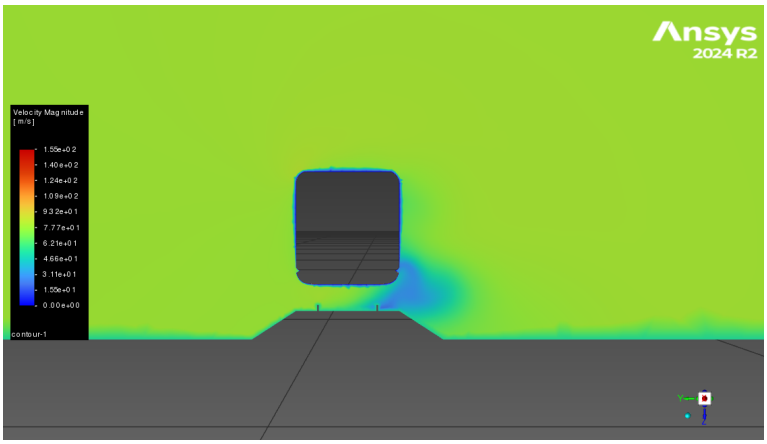


Figure D.3: Velocity magnitude contours around the train on a YZ cross-sectional plane for the crosswind study at a yaw angle of 10°.

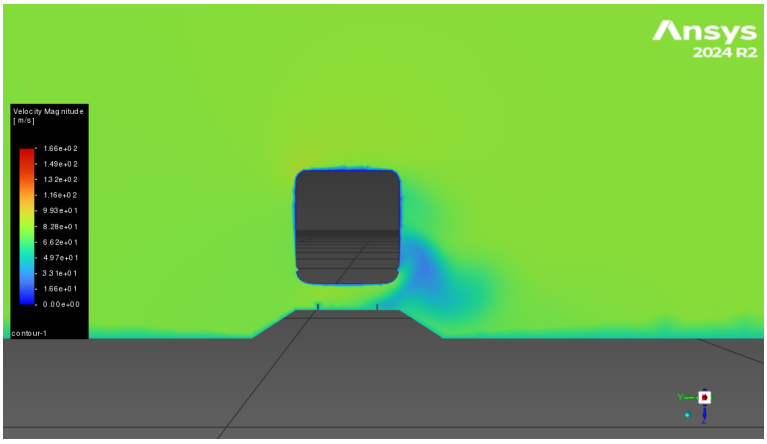


Figure D.4: Velocity magnitude contours around the train on a YZ cross-sectional plane for the crosswind study at a yaw angle of 15°.

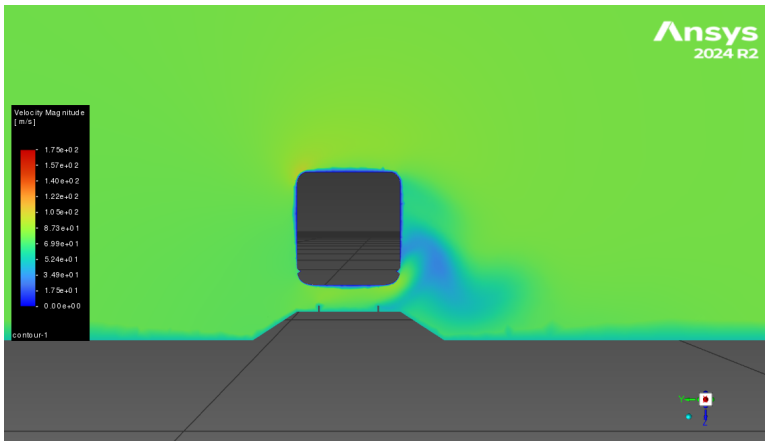


Figure D.5: Velocity magnitude contours around the train on a YZ cross-sectional plane for the crosswind study at a yaw angle of 20°.

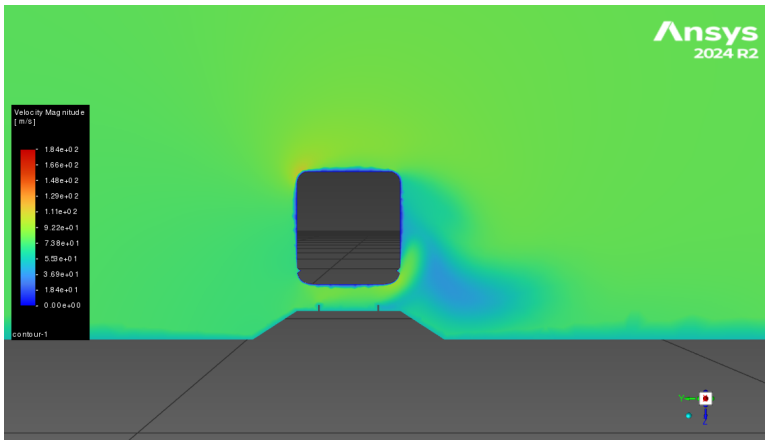


Figure D.6: Velocity magnitude contours around the train on a YZ cross-sectional plane for the crosswind study at a yaw angle of 25°.

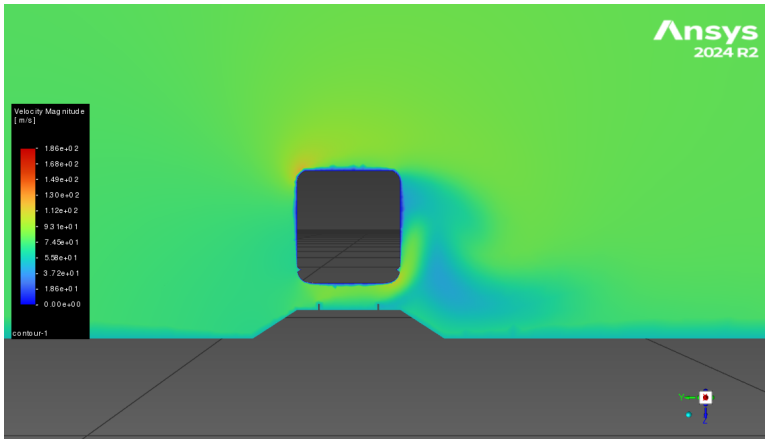


Figure D.7: Velocity magnitude contours around the train on a YZ cross-sectional plane for the crosswind study at a yaw angle of 30°.

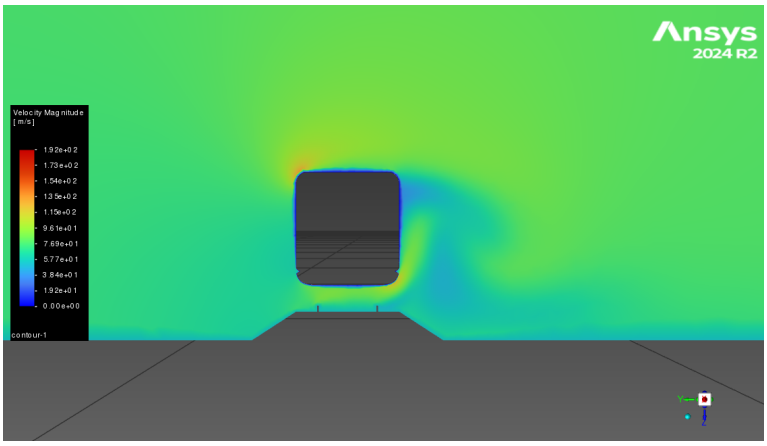


Figure D.8: Velocity magnitude contours around the train on a YZ cross-sectional plane for the crosswind study at a yaw angle of 35°.

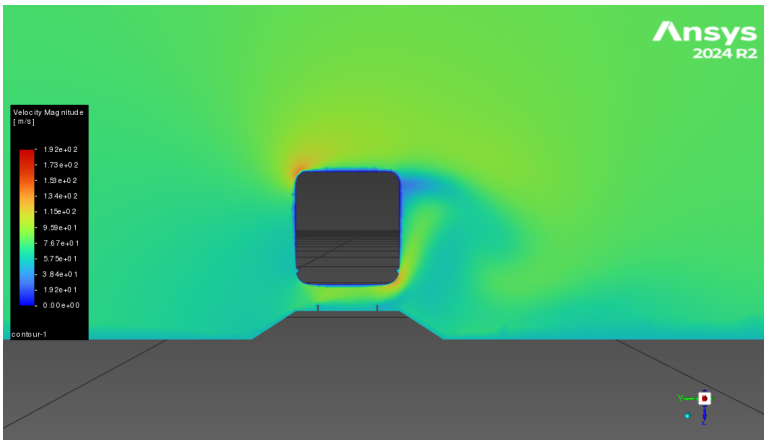


Figure D.9: Velocity magnitude contours around the train on a YZ cross-sectional plane for the crosswind study at a yaw angle of 40°.

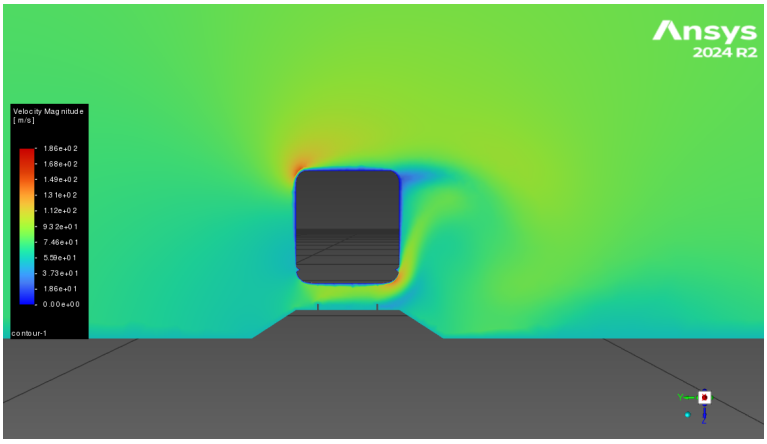


Figure D.10: Velocity magnitude contours around the train on a YZ cross-sectional plane for the crosswind study at a yaw angle of 45°.

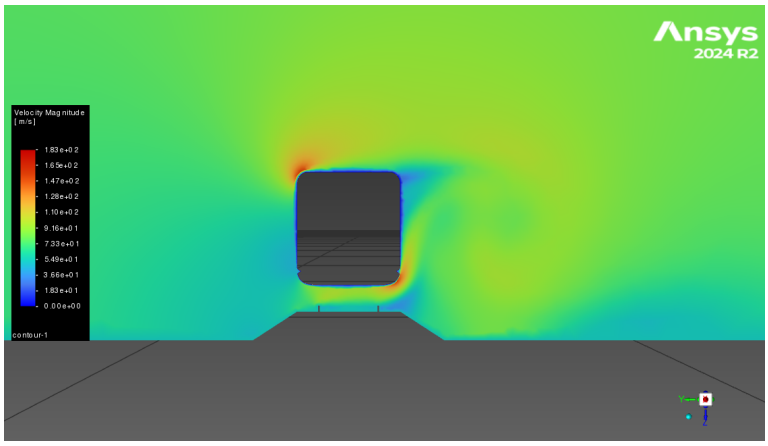


Figure D.11: Velocity magnitude contours around the train on a YZ cross-sectional plane for the crosswind study at a yaw angle of 50°.

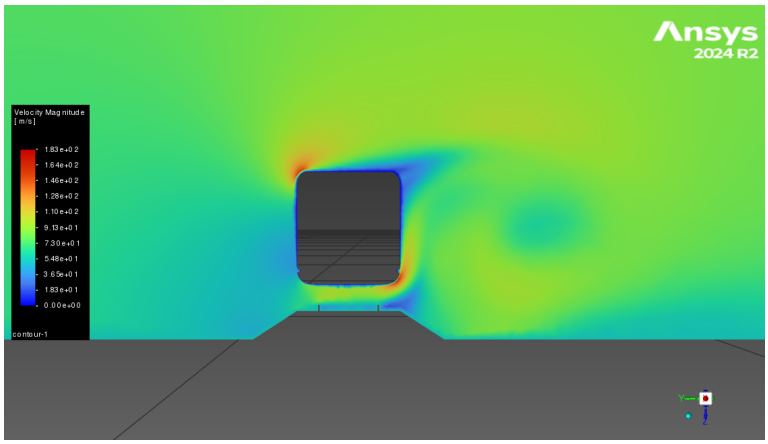


Figure D.12: Velocity magnitude contours around the train on a YZ cross-sectional plane for the crosswind study at a yaw angle of 55°.

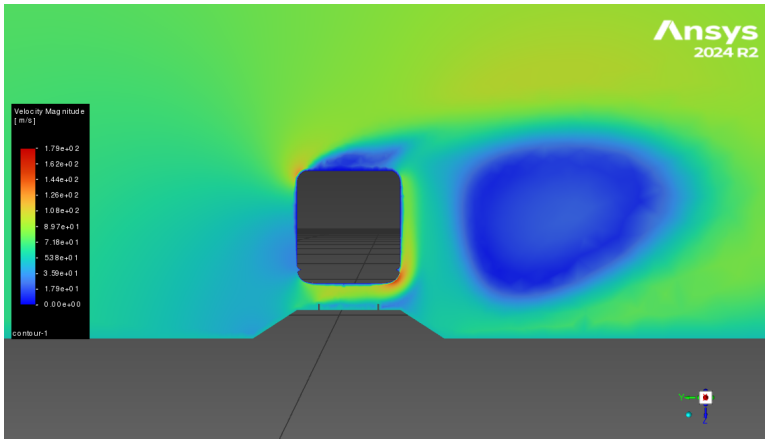


Figure D.13: Velocity magnitude contours around the train on a YZ cross-sectional plane for the crosswind study at a yaw angle of 60°.

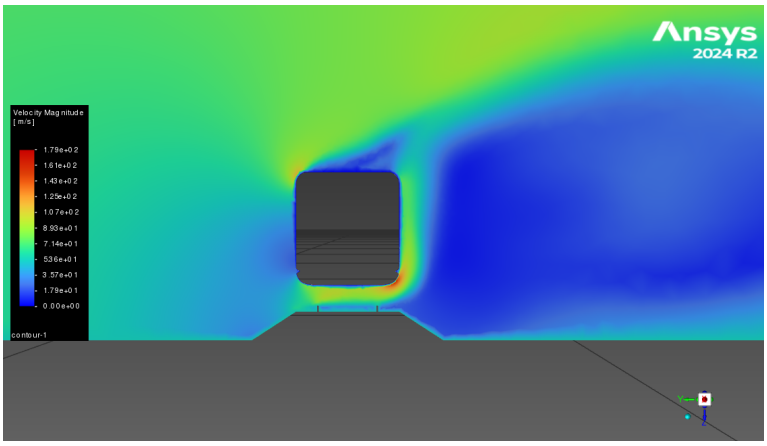


Figure D.14: Velocity magnitude contours around the train on a YZ cross-sectional plane for the crosswind study at a yaw angle of 70°.

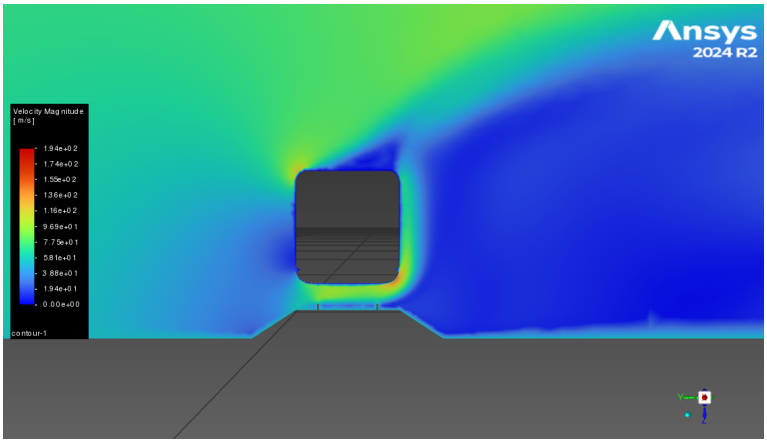


Figure D.15: Velocity magnitude contours around the train on a YZ cross-sectional plane for the crosswind study at a yaw angle of 80°.

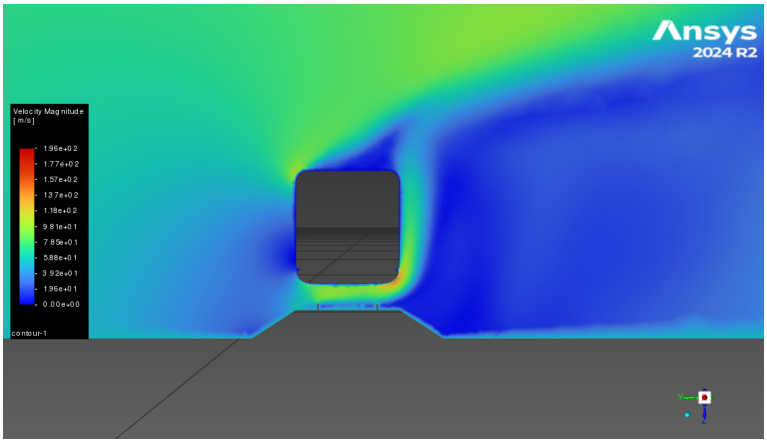


Figure D.16: Velocity magnitude contours around the train on a YZ cross-sectional plane for the crosswind study at a yaw angle of 90°.

Appendix E

Aerodynamic and Pressure Coefficients over Time during the Passing Manoeuvre

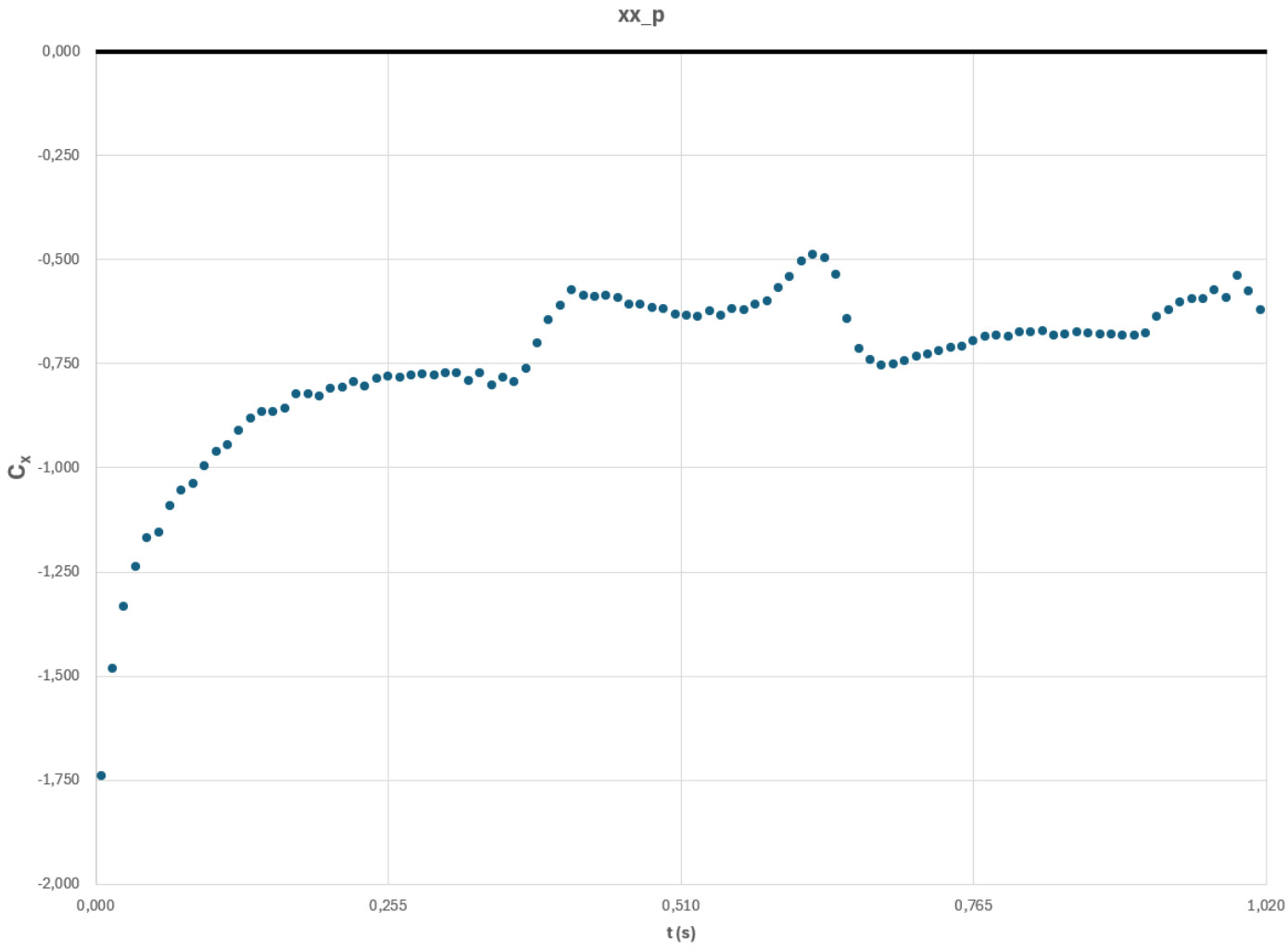


Figure E.1: Values of C_x over time for the main vehicle.

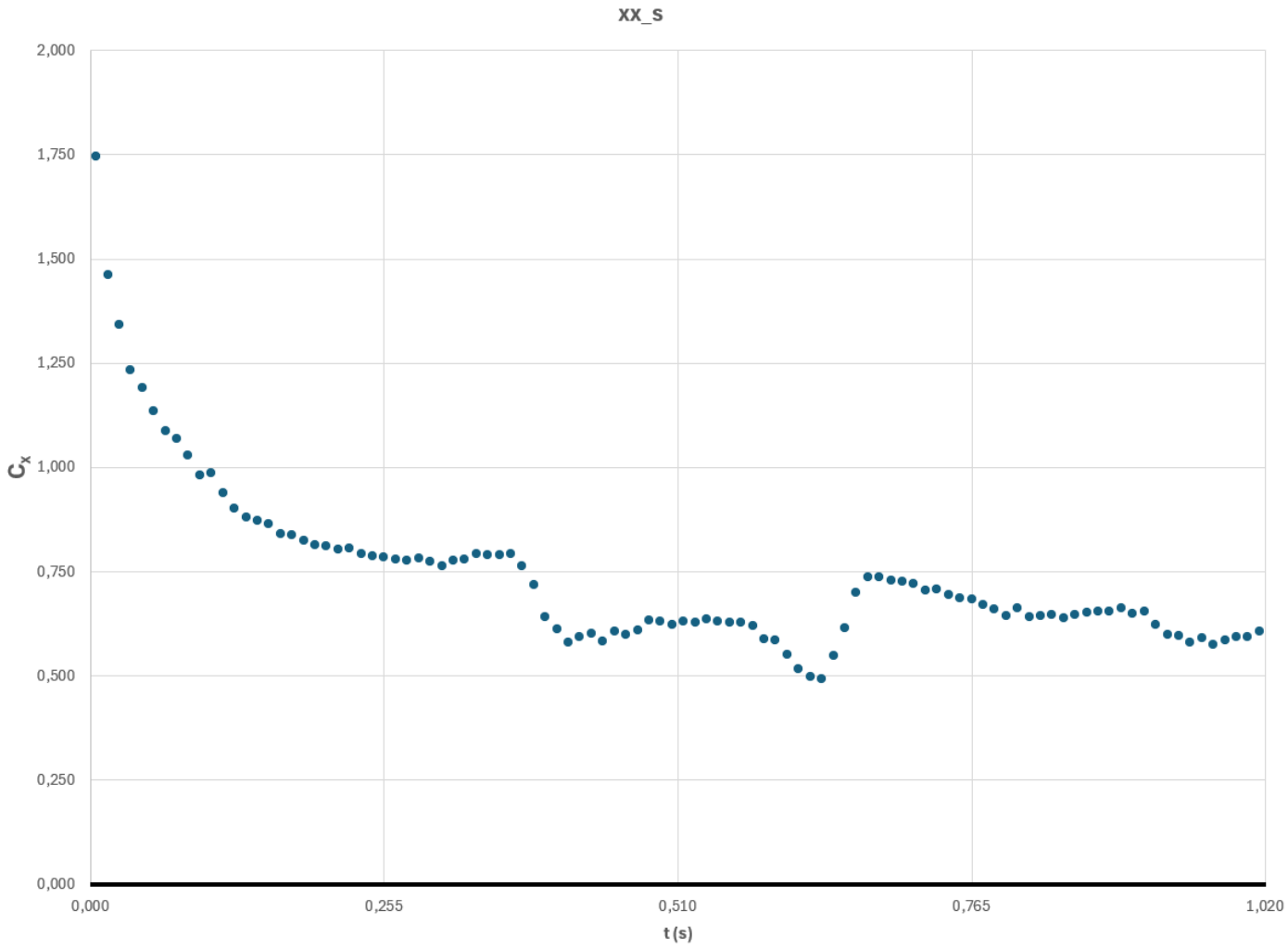


Figure E.2: Values of C_x over time for the secondary vehicle.

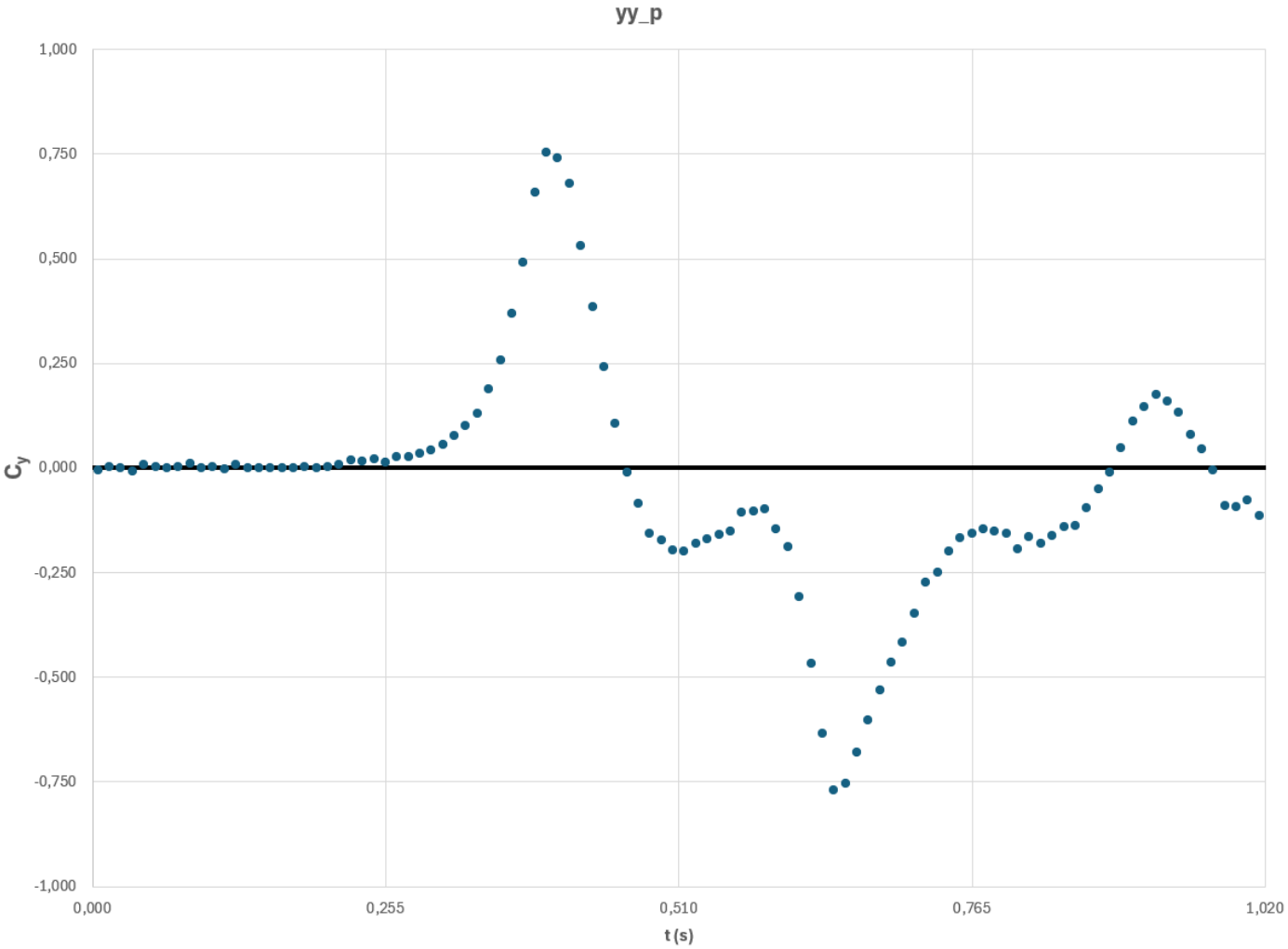


Figure E.3: Values of C_y over time for the main vehicle.

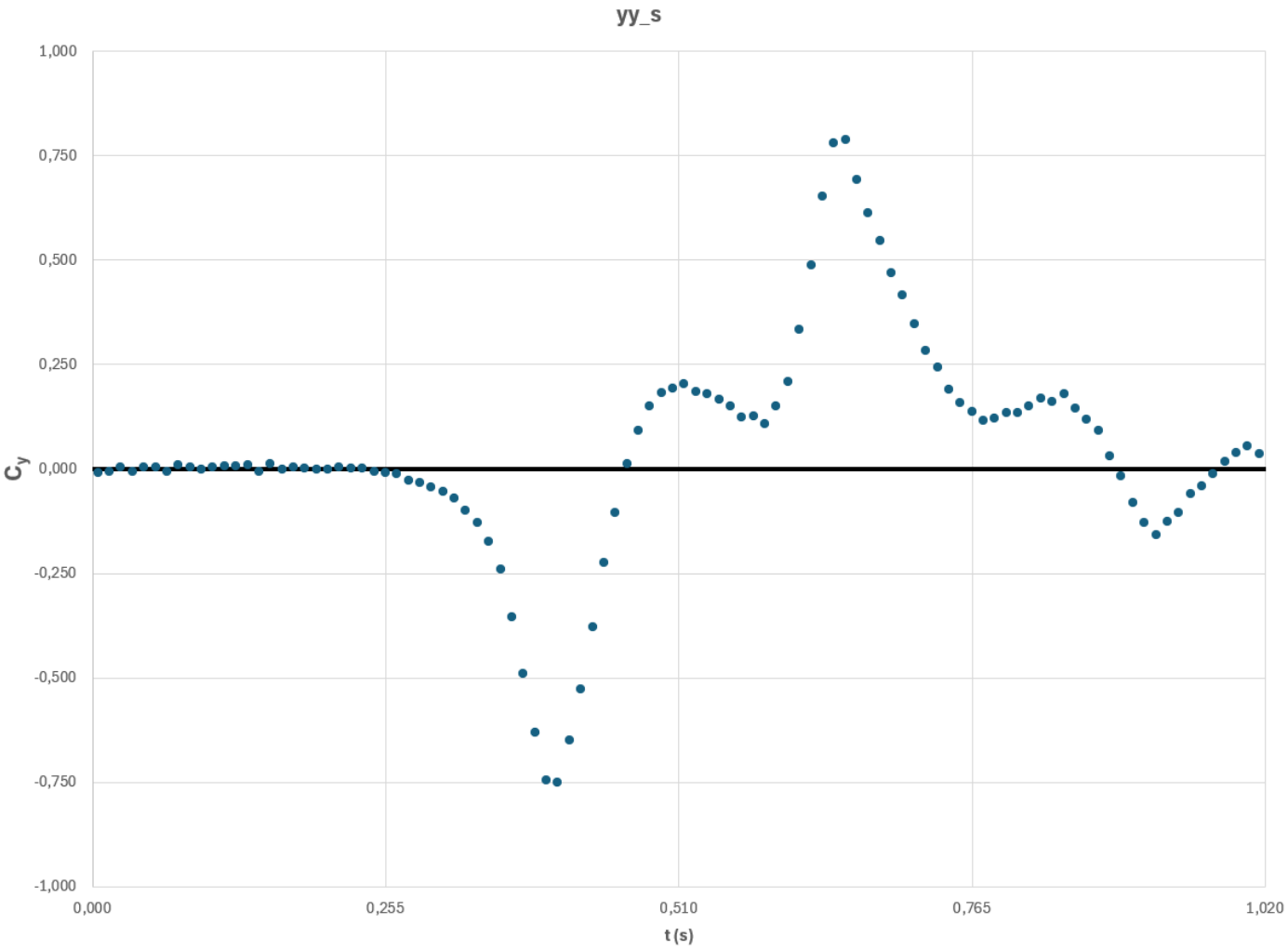


Figure E.4: Values of C_y over time for the secondary vehicle.

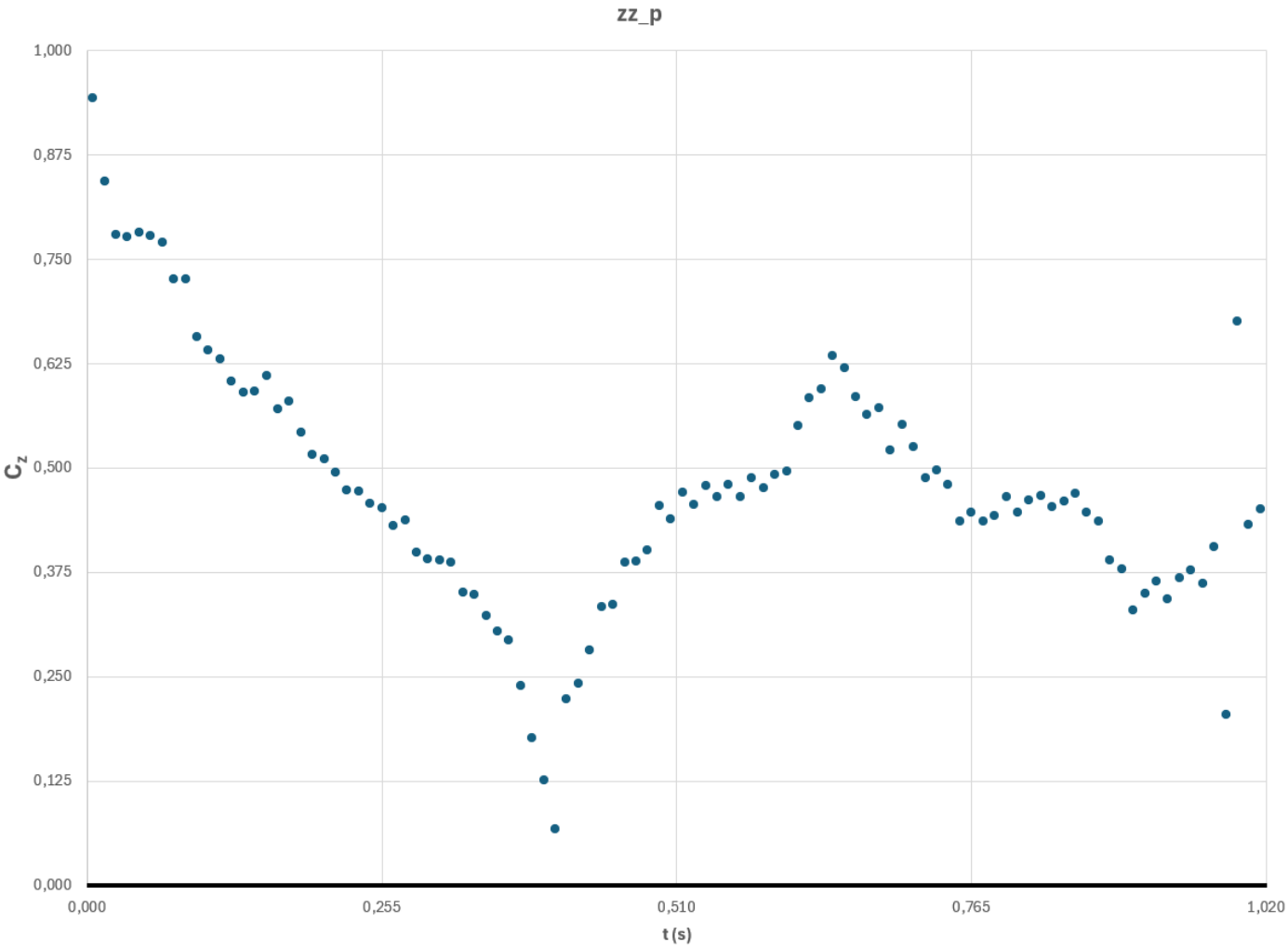


Figure E.5: Values of C_z over time for the main vehicle.

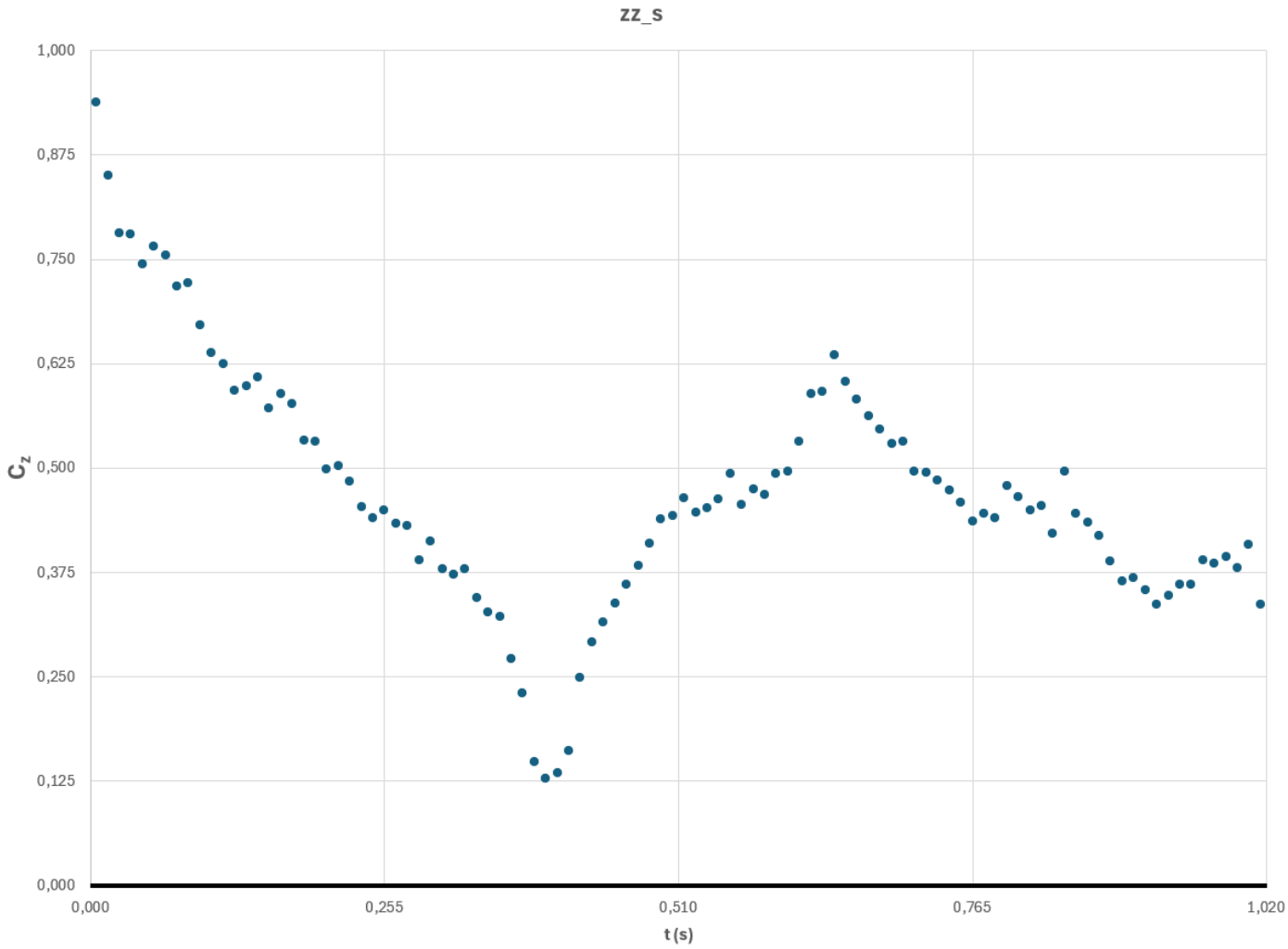


Figure E.6: Values of C_z over time for the secondary vehicle.

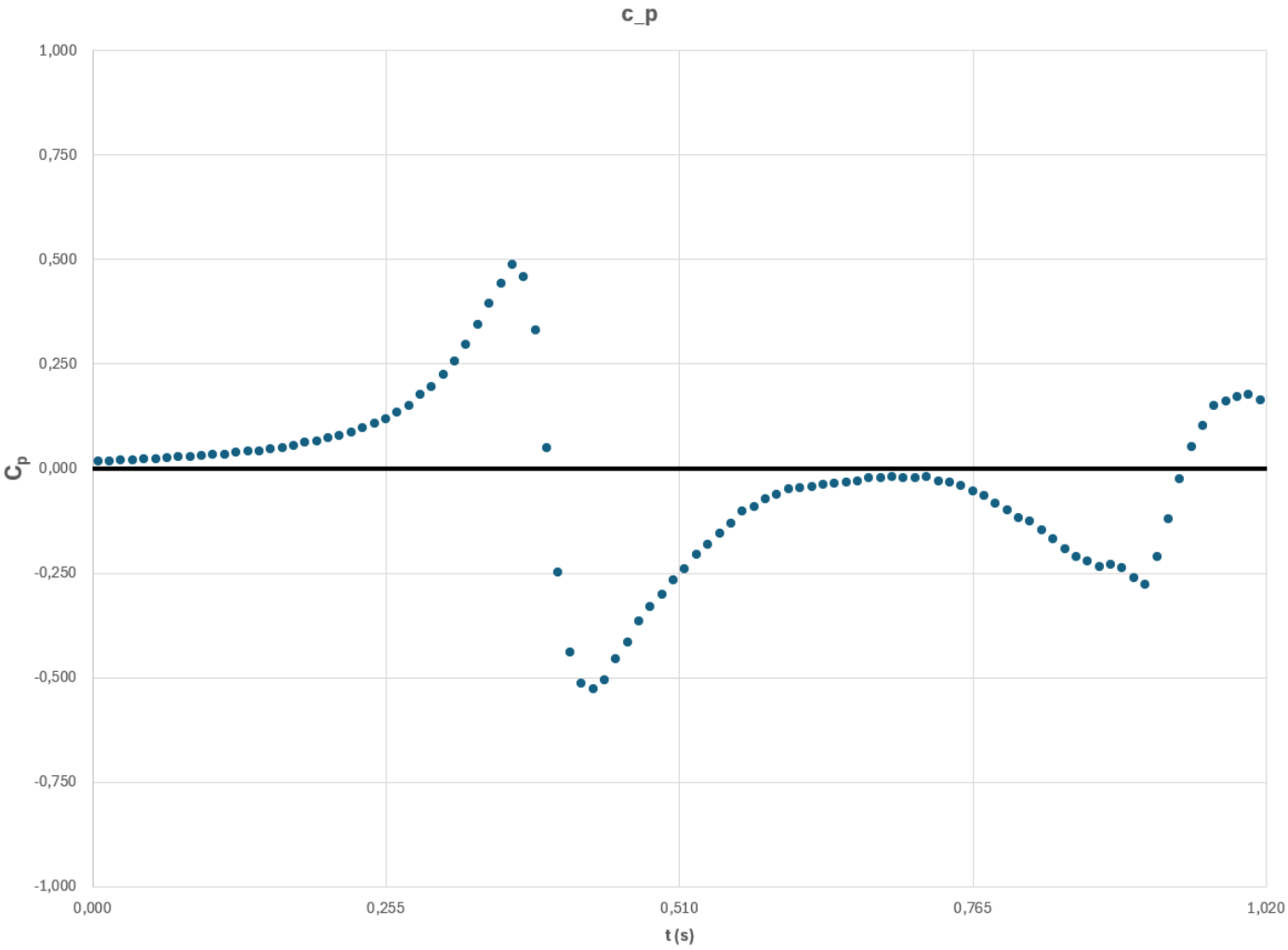


Figure E.7: Values of C_p over time for the midpoint of the intersection.

Appendix F

Graphical Results from the Passing Manoeuvre

F.1 Velocity Magnitude Contour on the XZ Plane

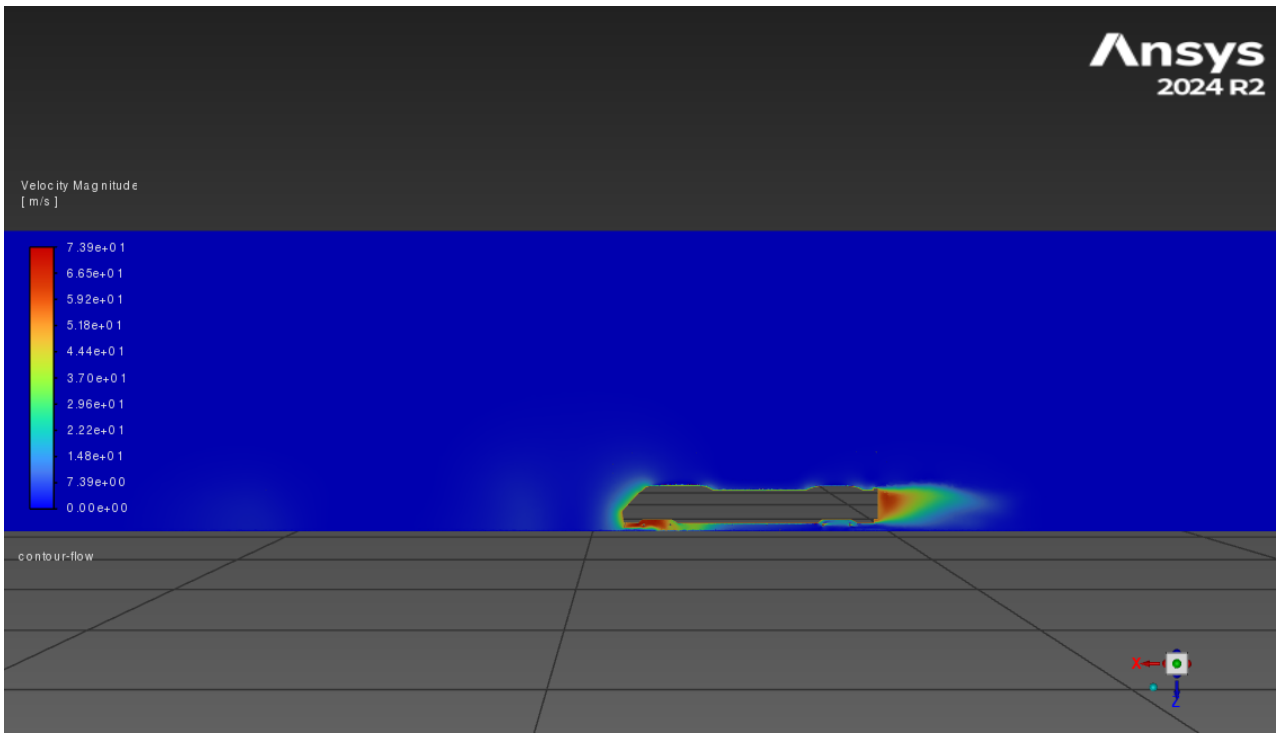


Figure F.1: Velocity magnitude contour on the XZ plane at $t = 0.305$s.

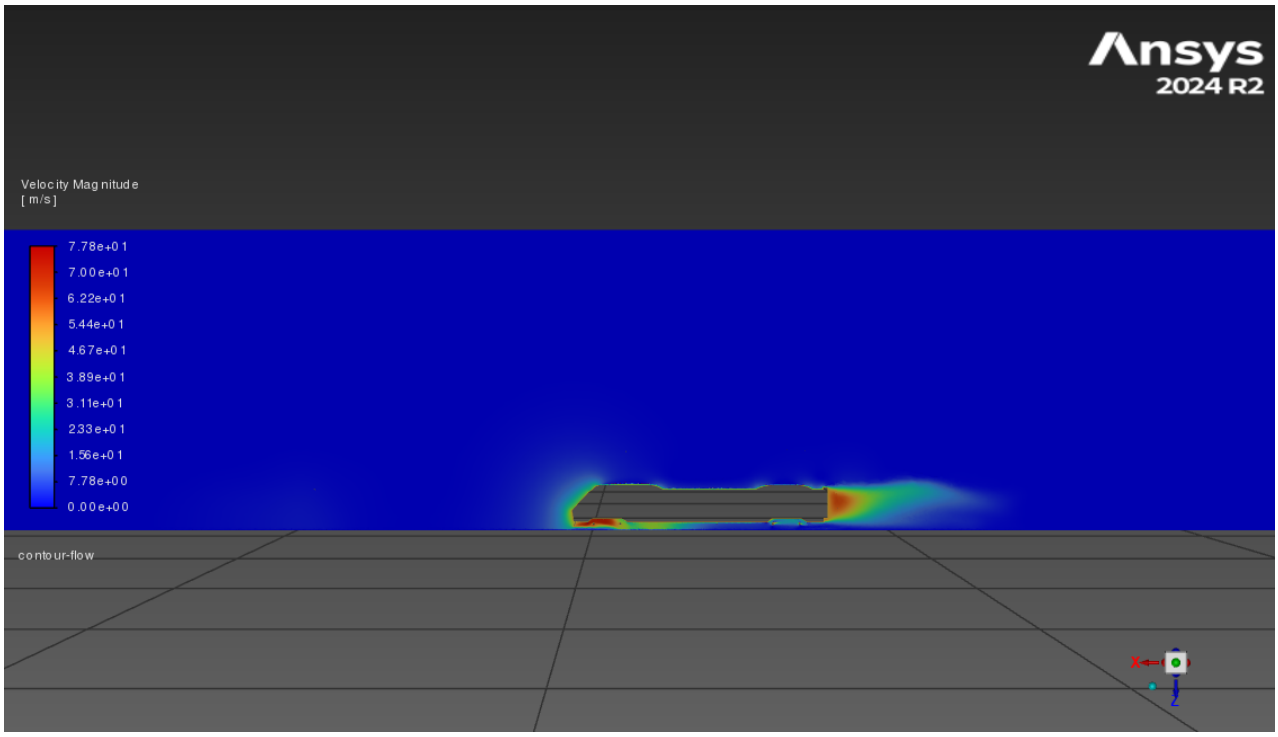


Figure F.2: Velocity magnitude contour on the XZ plane at $t = 0.395$s.

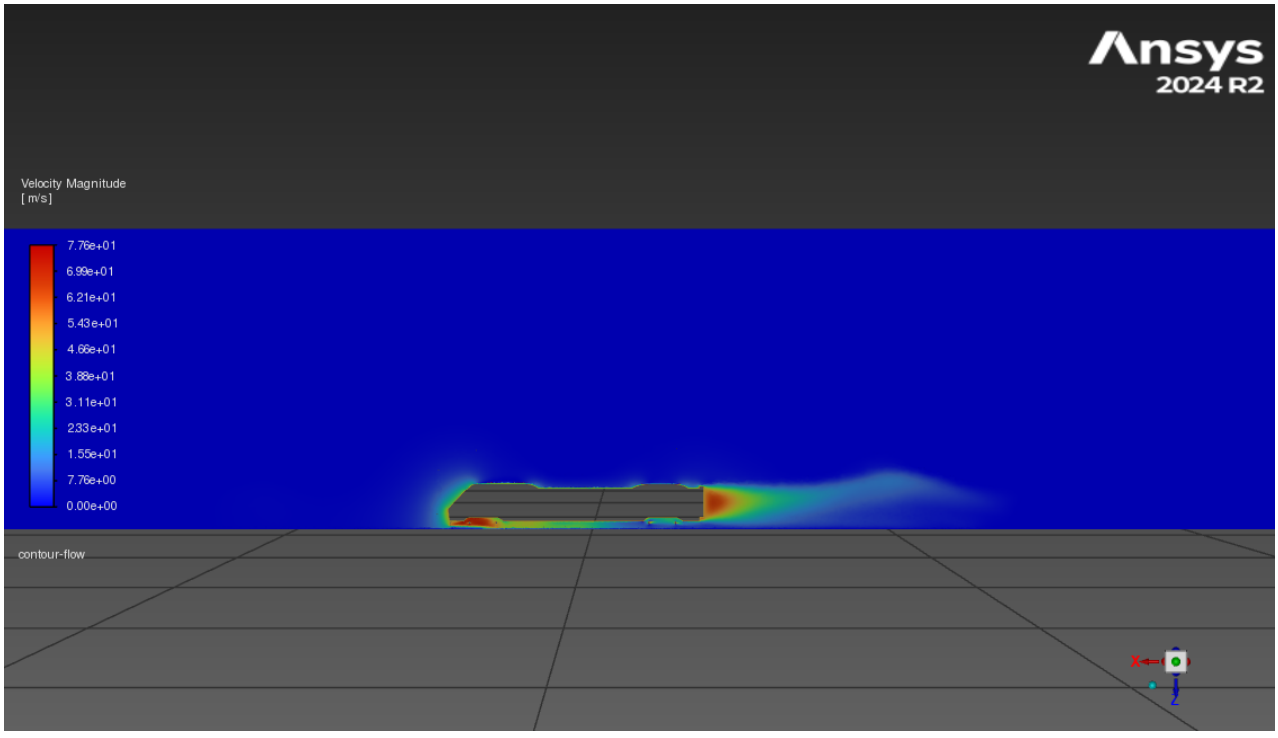


Figure F.3: Velocity magnitude contour on the XZ plane at $t = 0.652$s.

F.2 Pathlines Around the Train

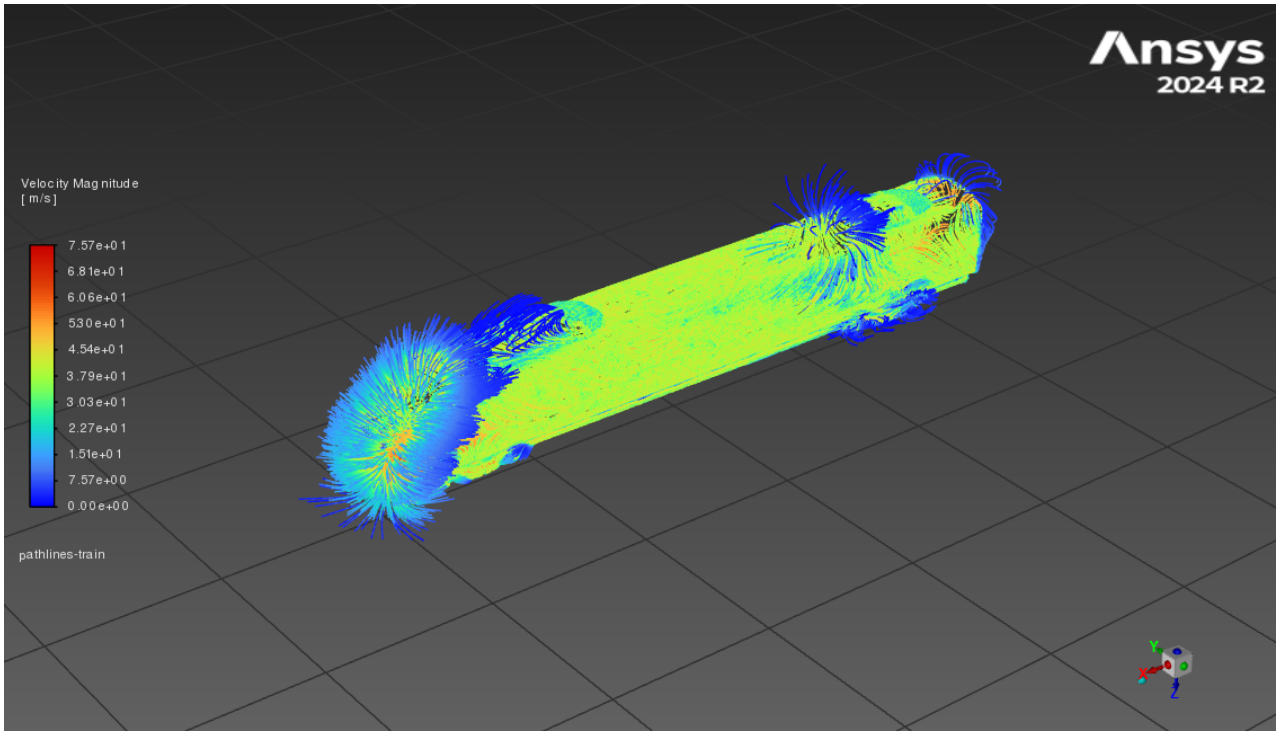


Figure F.4: Pathlines around the train at $t = 0.150$s.

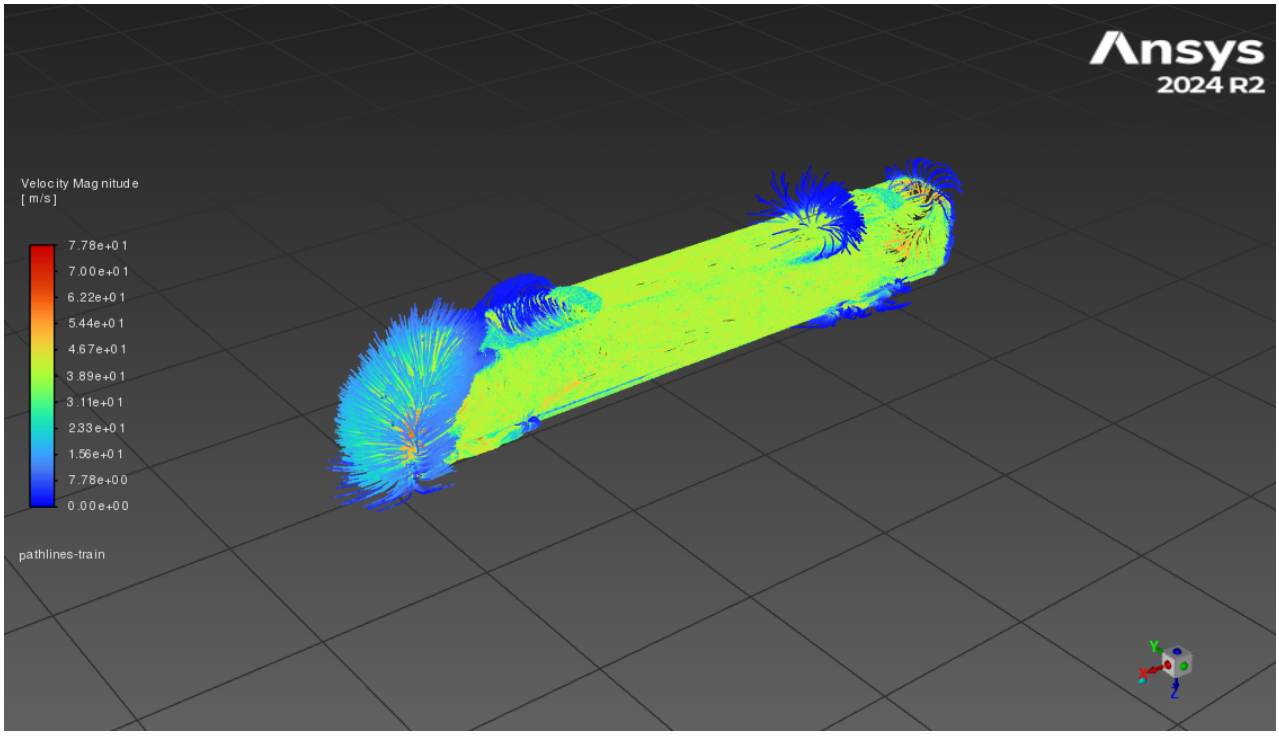


Figure F.5: Pathlines around the train at $t = 0.395$s (perspective view).

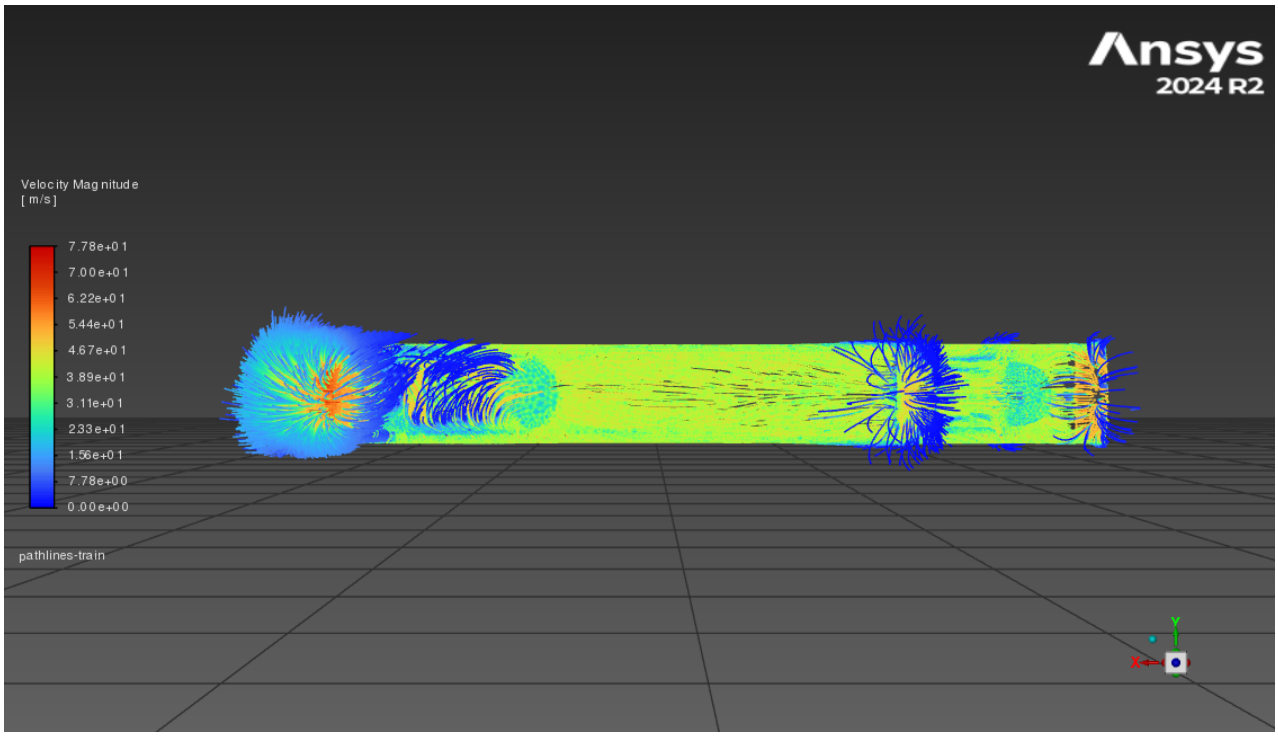


Figure F.6: Pathlines around the train at $t = 0.395$s (viewed from above the vehicle).

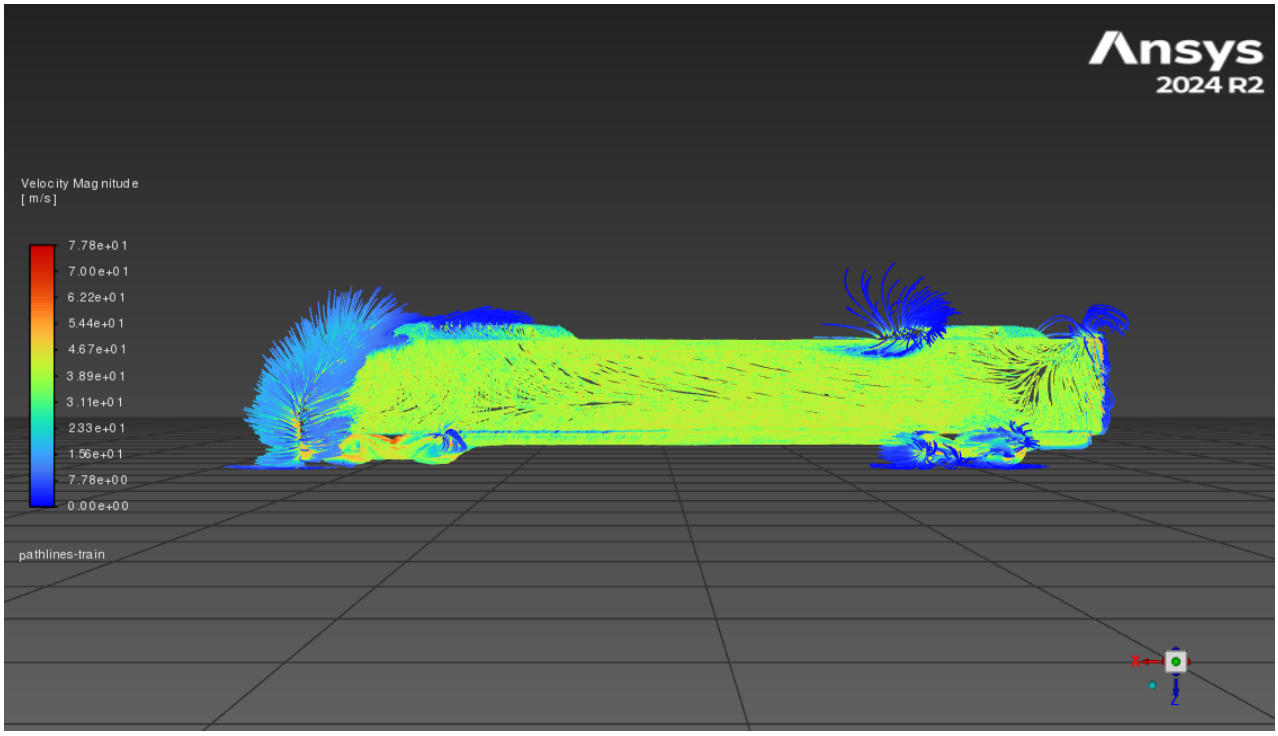


Figure F.7: Pathlines around the train at $t = 0.395$s (viewed from the vehicle's left side).

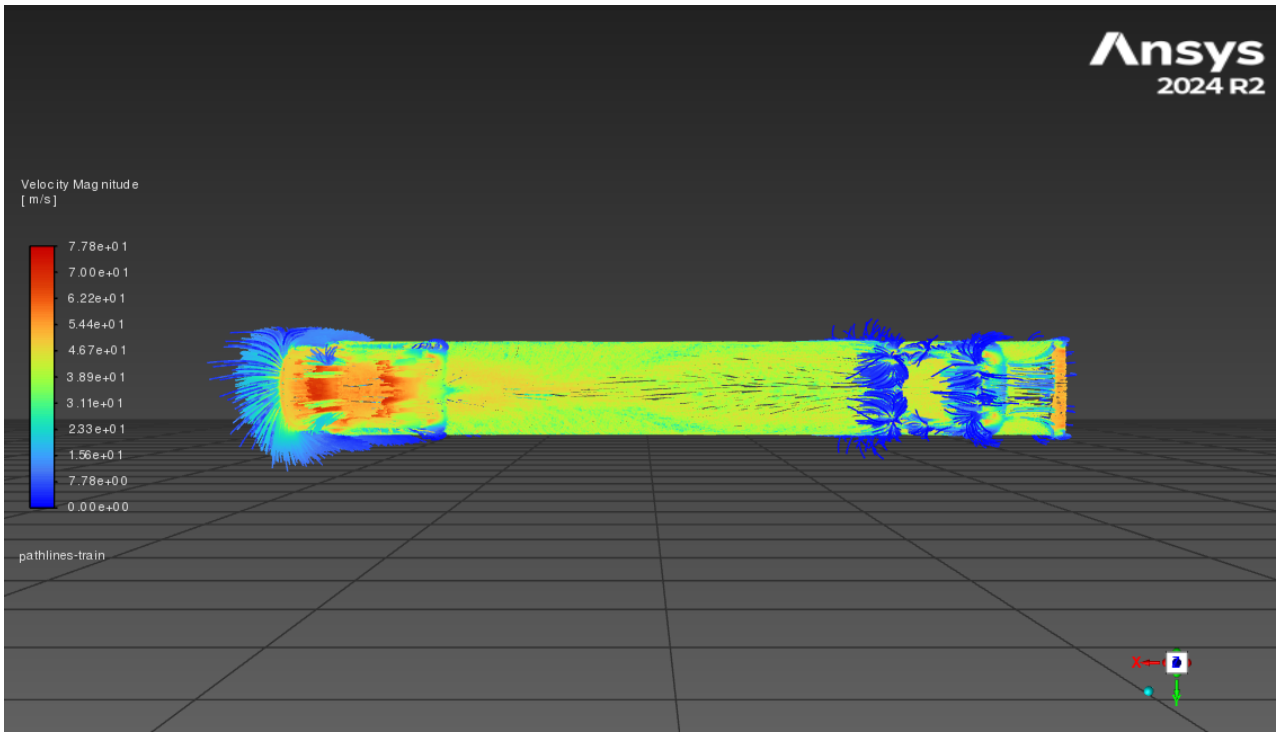


Figure F.8: Pathlines around the train at $t = 0.395$s (viewed from below the vehicle).

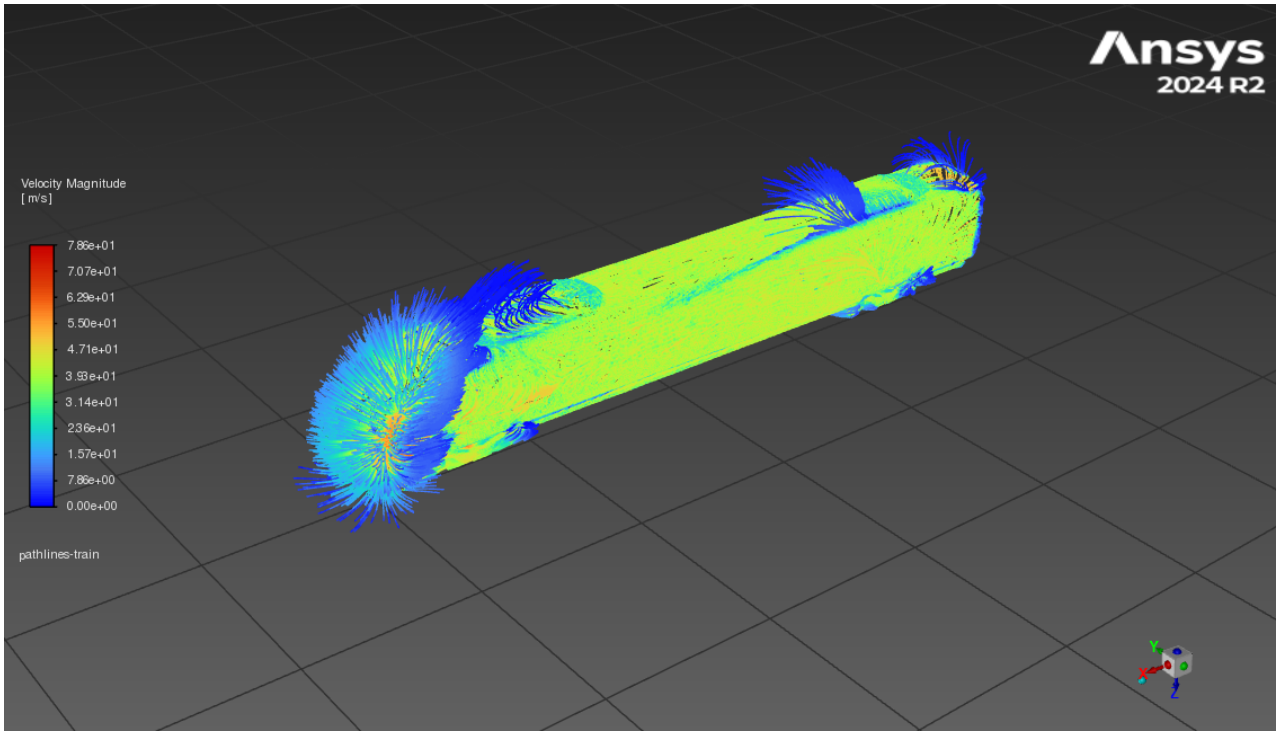


Figure F.9: Pathlines around the train at $t = 0.652$s.

F.3 Contour of Absolute Pressure on the XY Plane

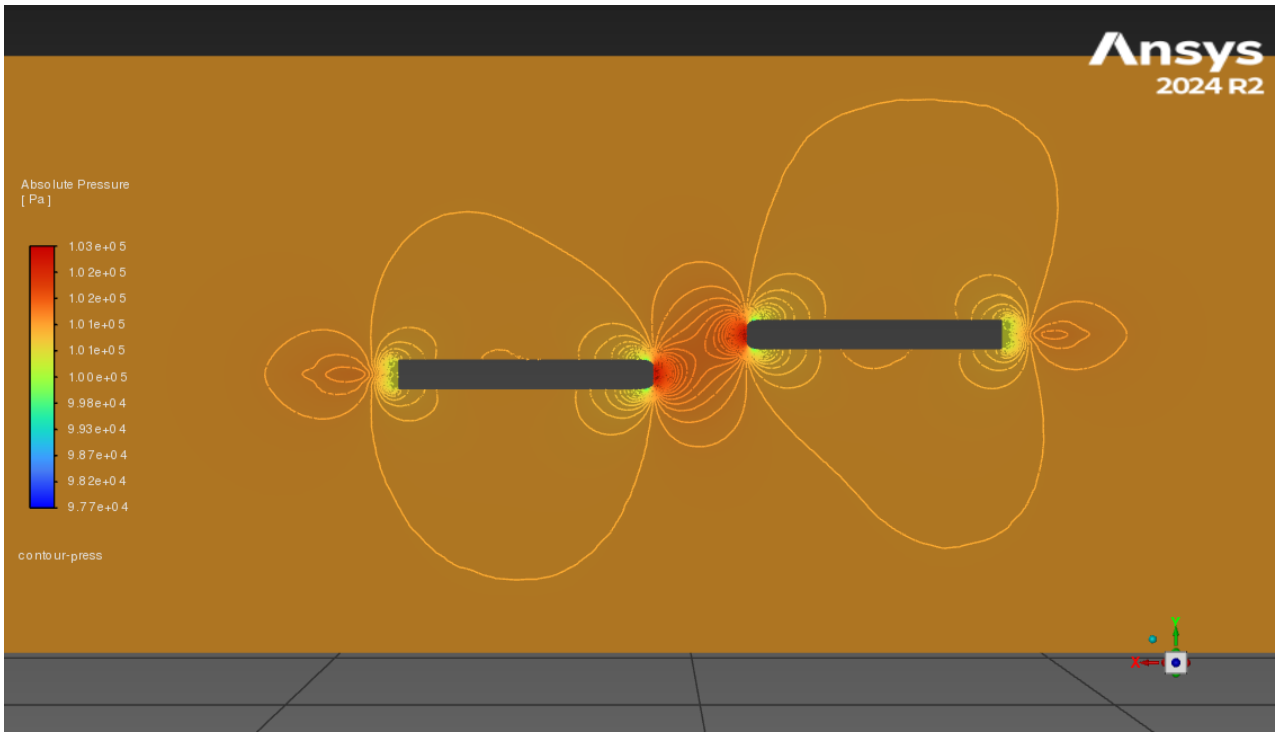


Figure F.10: Contour of absolute pressure on the XY plane at $t = 0.300$s.

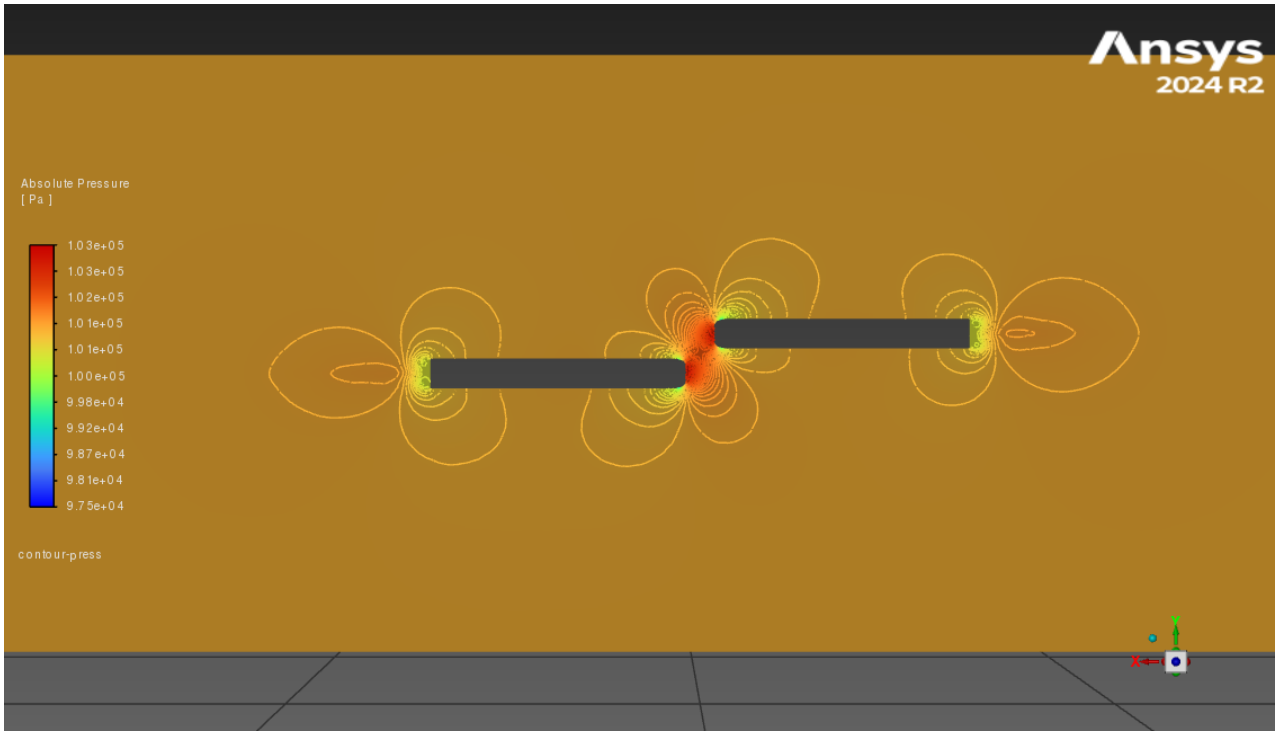


Figure F.11: Contour of absolute pressure on the XY plane at $t = 0.365$s - maximum value of C_p.

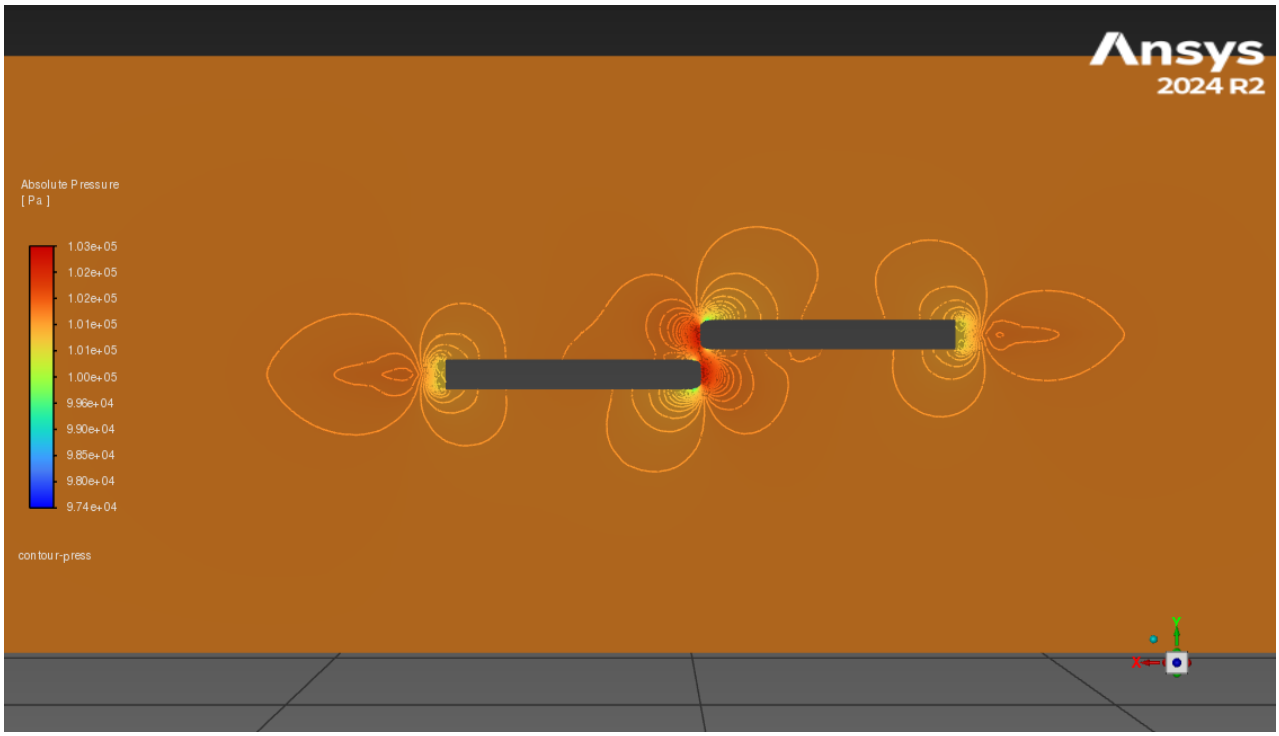


Figure F.12: Contour of absolute pressure on the XY plane at $t = 0.395$s.

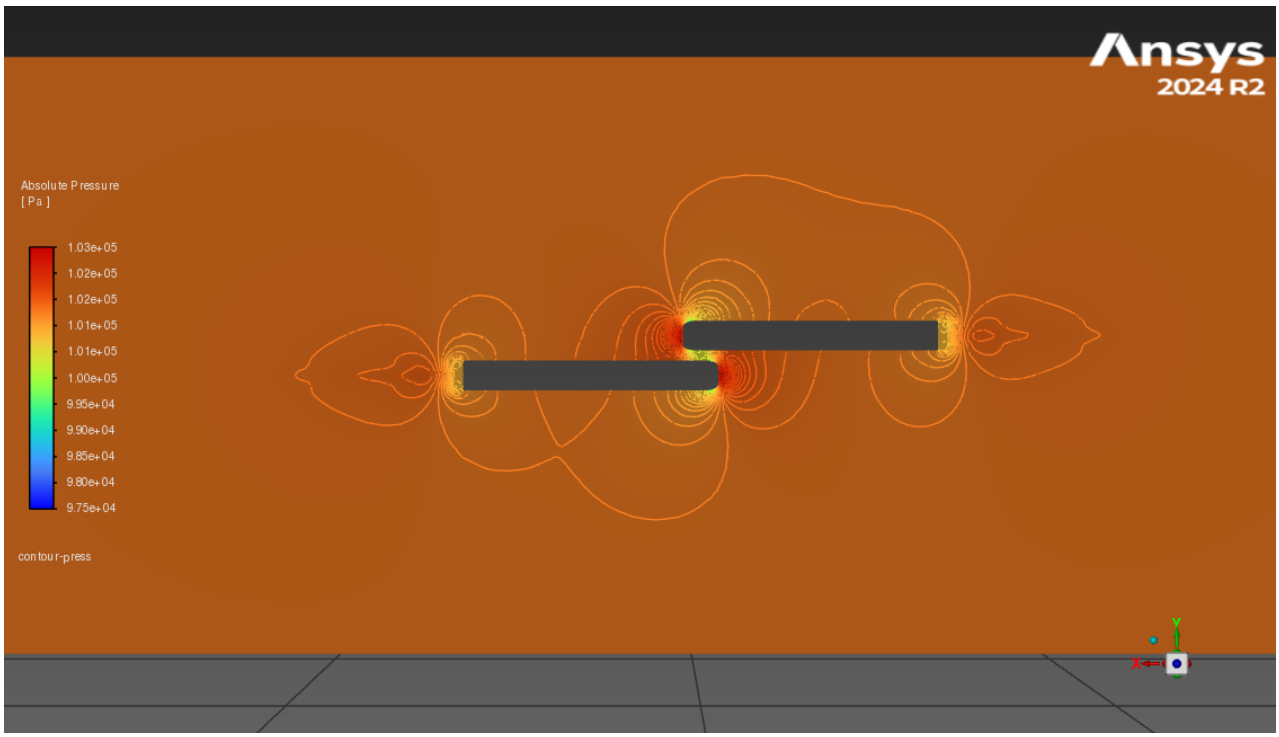


Figure F.13: Contour of absolute pressure on the XY plane at $t = 0.435$s - minimum value of C_p.

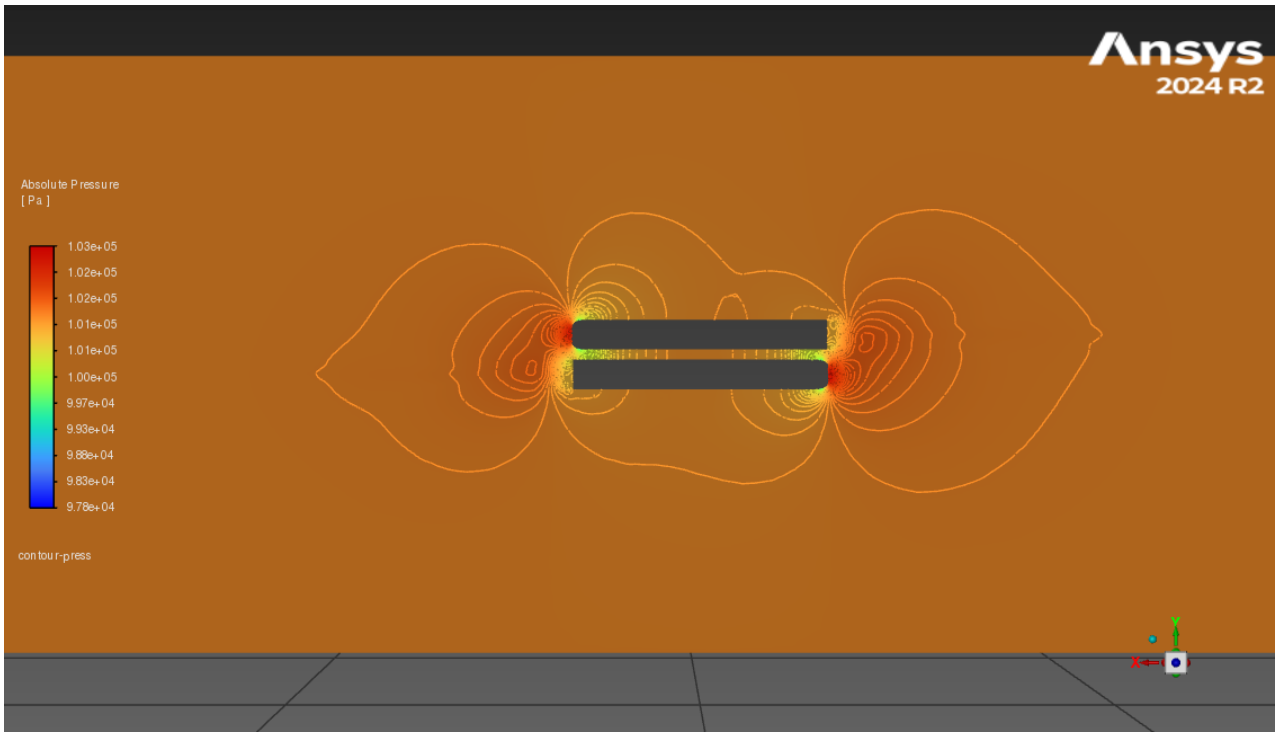


Figure F.14: Contour of absolute pressure on the XY plane at $t = 0.652$s.

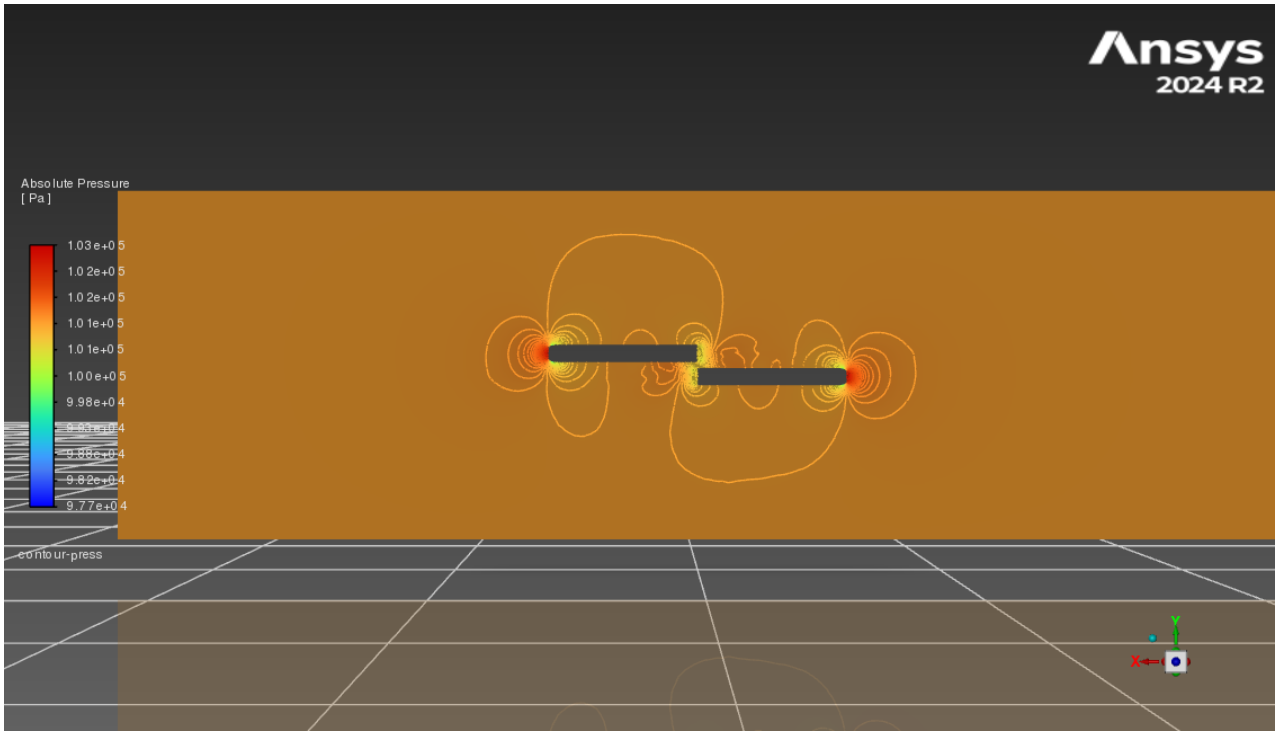


Figure F.15: Contour of absolute pressure on the XY plane at $t = 0.909$s.

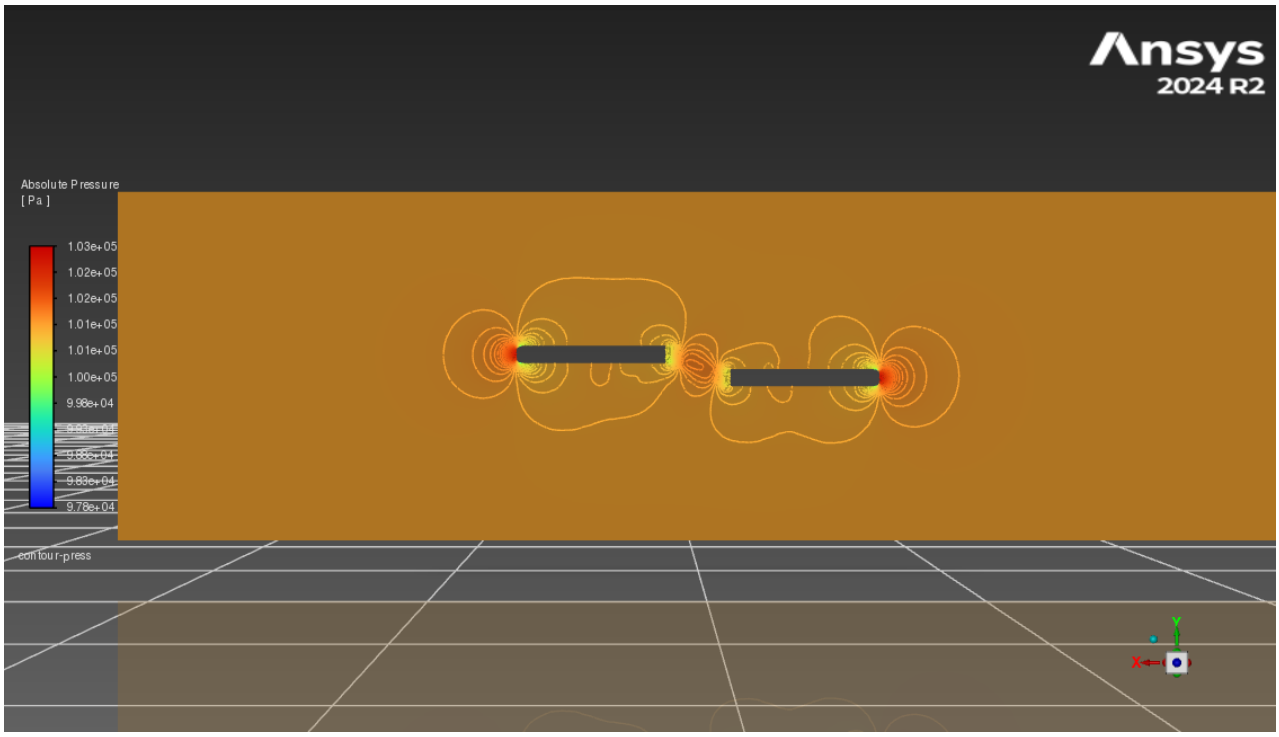


Figure F.16: Contour of absolute pressure on the XY plane at $t = 1.020$s.

F.4 Contour of Absolute Pressure Around the Trains

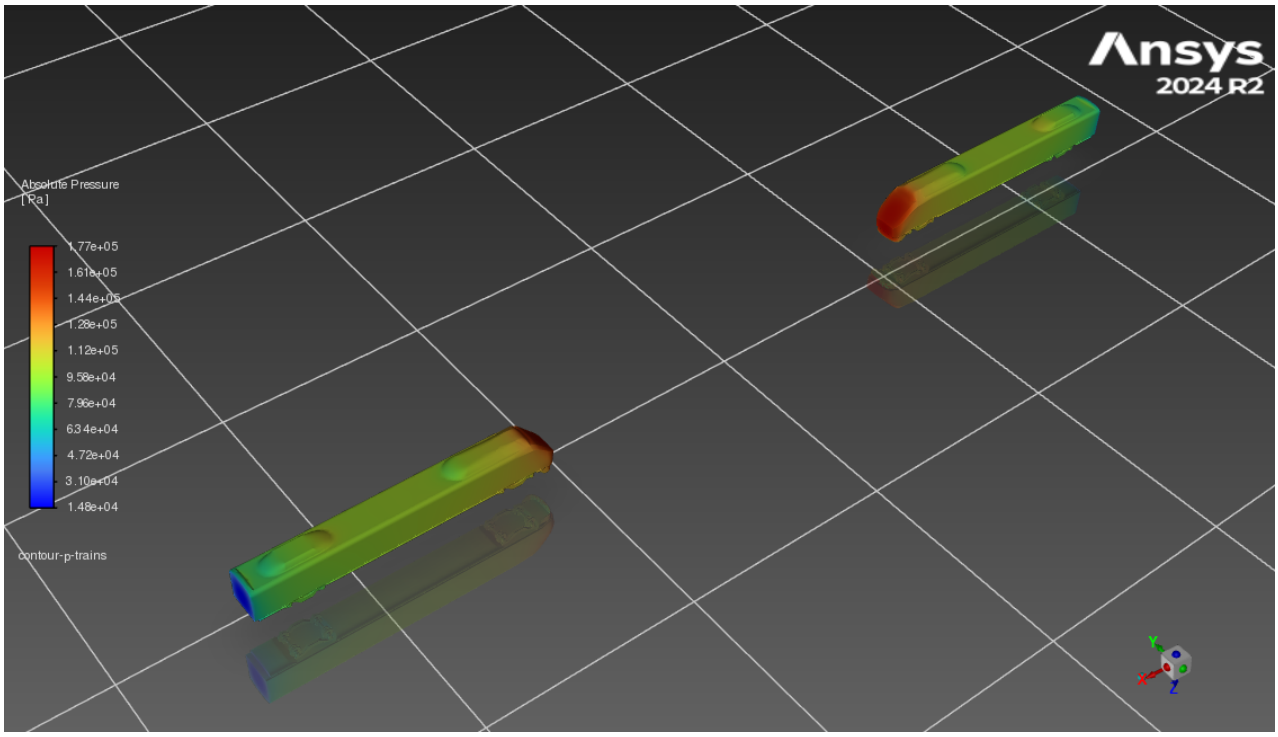


Figure F.17: Contour of absolute pressure around the vehicles at $t = 0$s. The unrealistic pressure distribution comes from the sudden movement initialization.

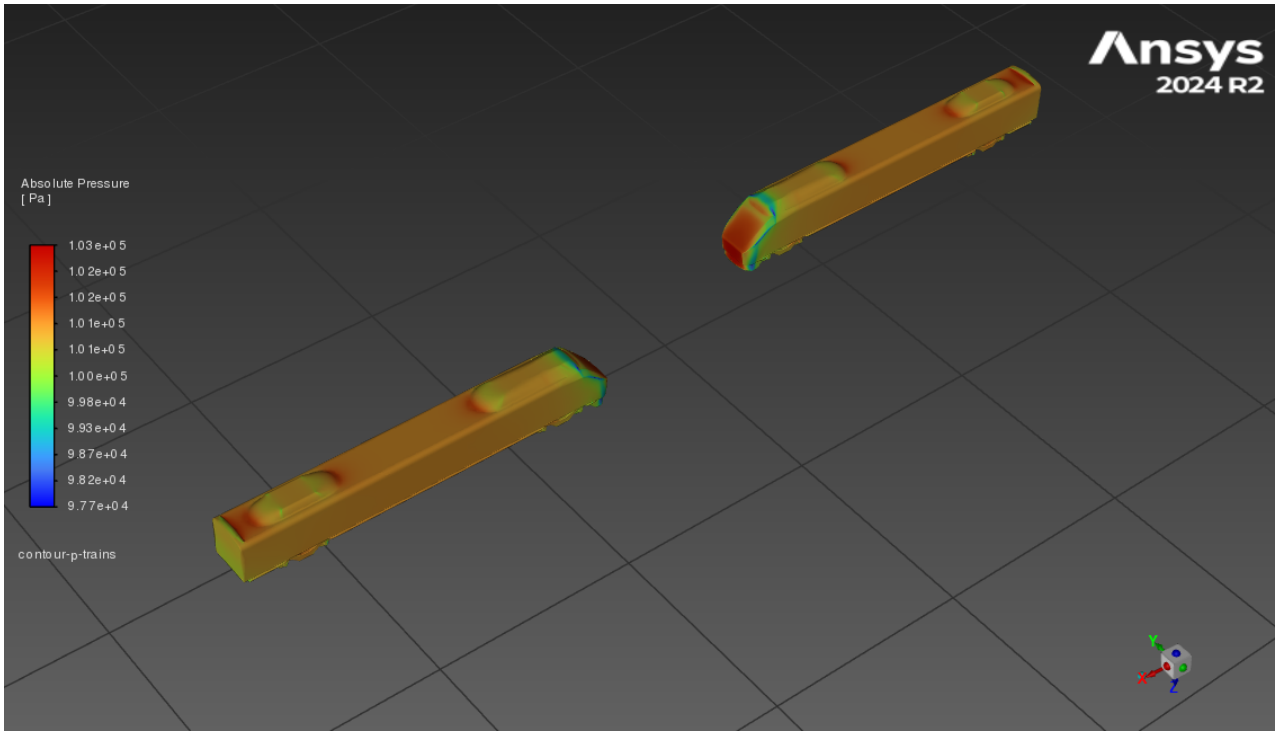


Figure F.18: Contour of absolute pressure around the vehicles at $t = 0.255$s.

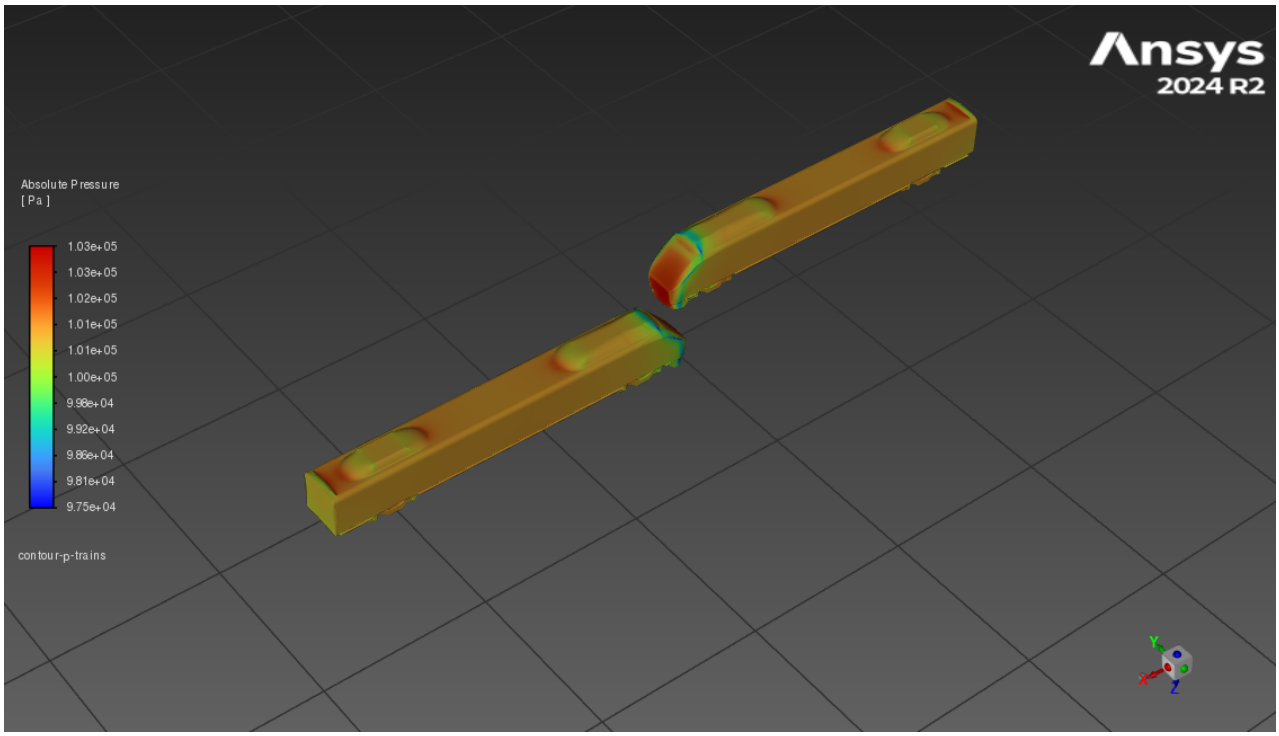


Figure F.19: Contour of absolute pressure around the vehicles at $t = 0.375$s (perspective view).

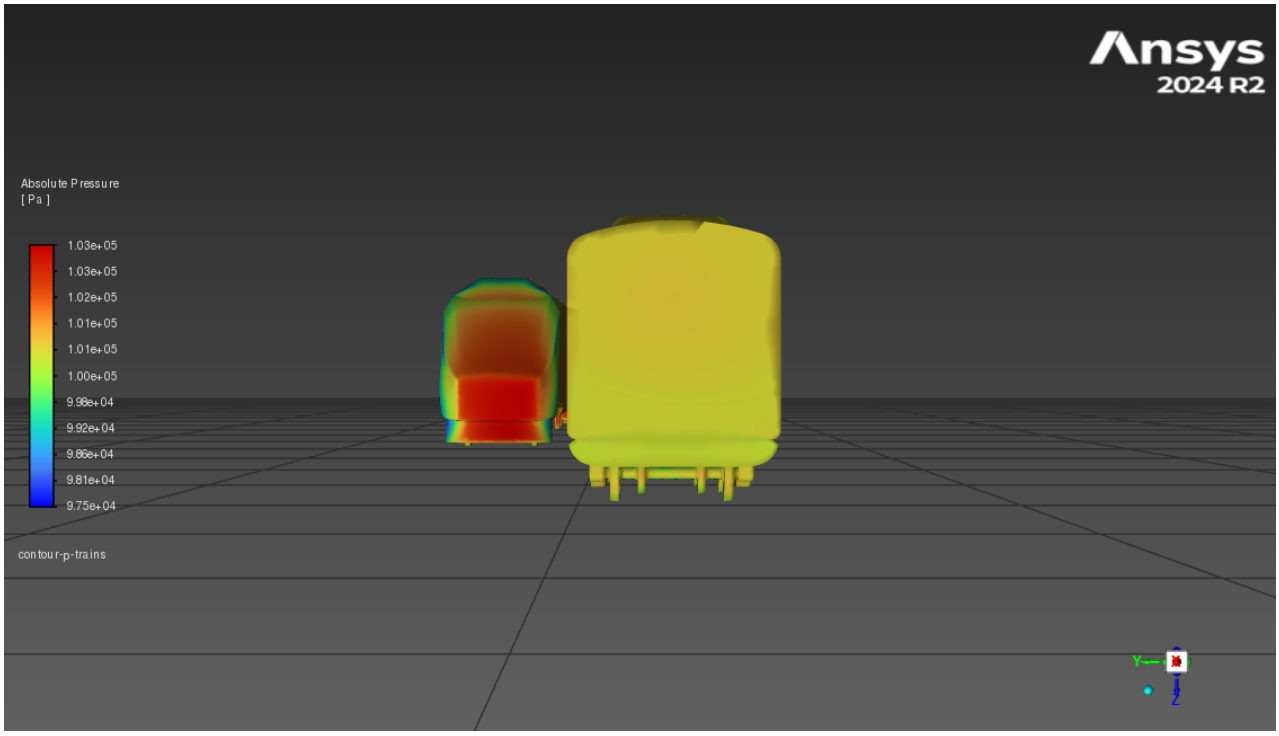


Figure F.20: Contour of absolute pressure around the vehicles at $t = 0.375$s (front view).

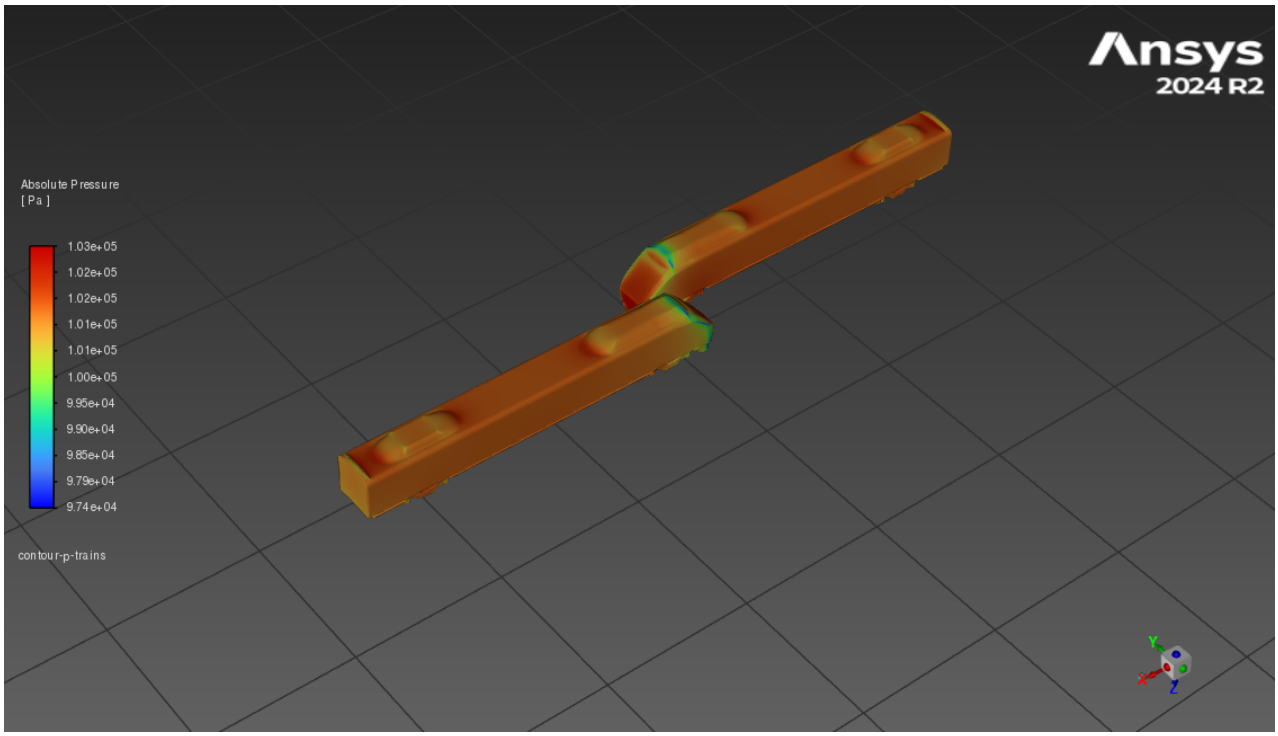


Figure F.21: Contour of absolute pressure around the vehicles at $t = 0.420$s (perspective view).

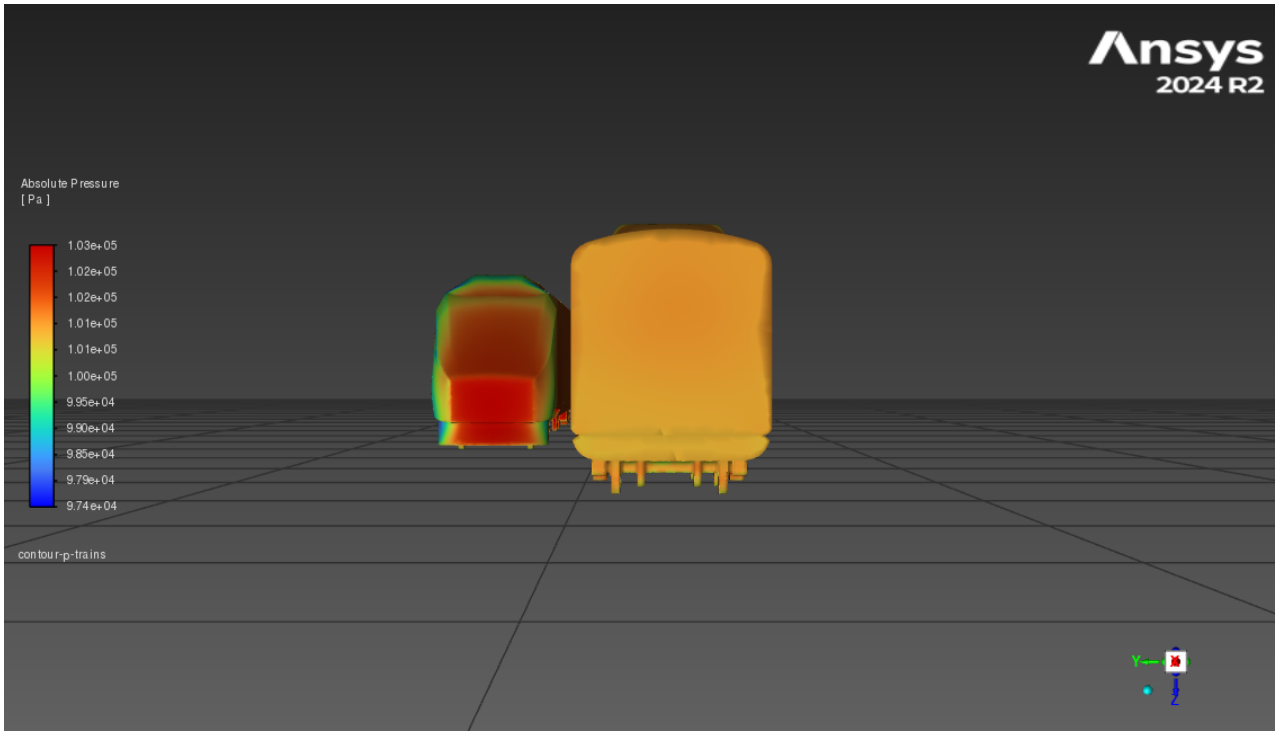


Figure F.22: Contour of absolute pressure around the vehicles at $t = 0.420$s (front view).

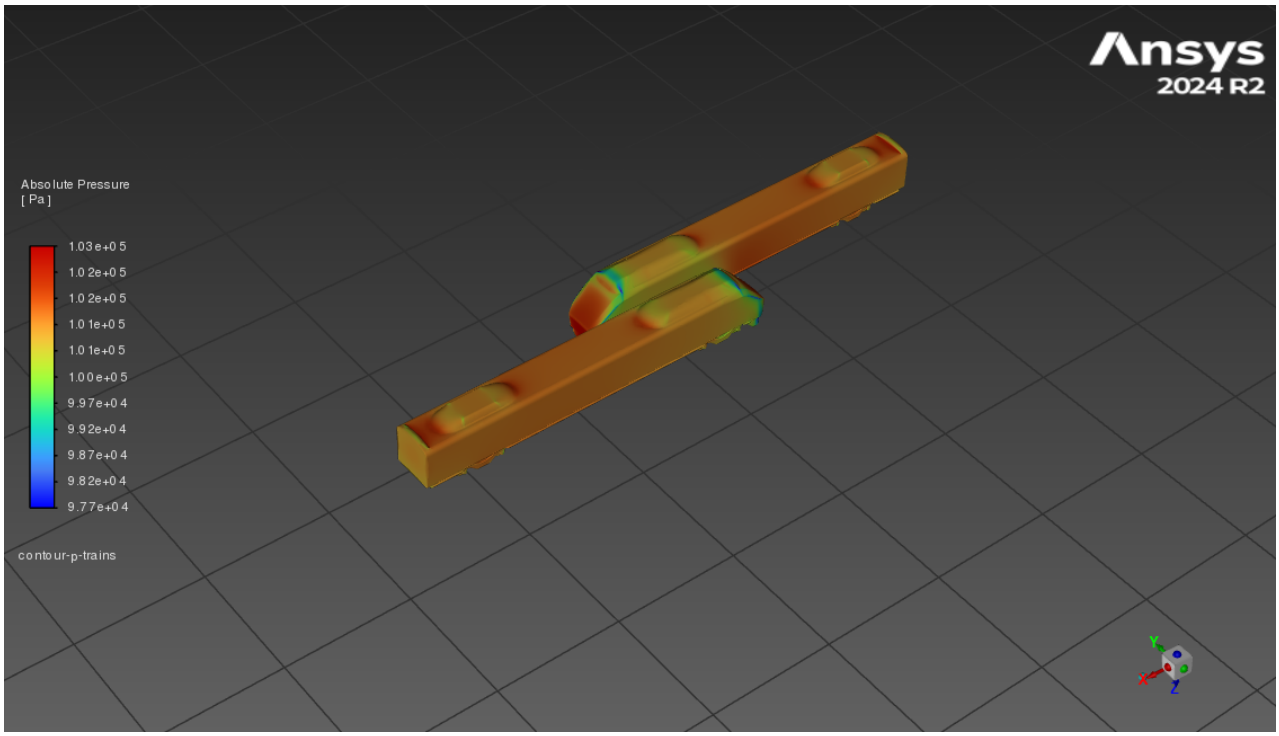


Figure F.23: Contour of absolute pressure around the vehicles at $t = 0.500$s.

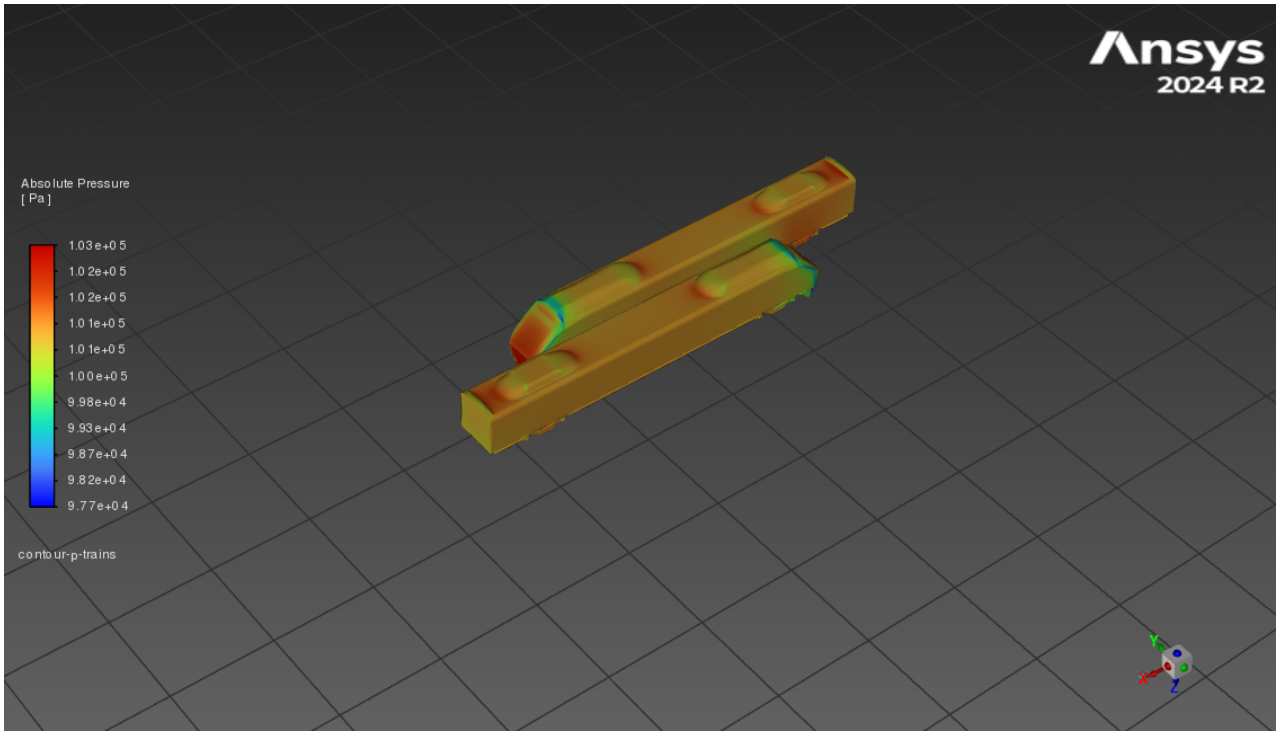


Figure F.24: Contour of absolute pressure around the vehicles at $t = 0.595$s.

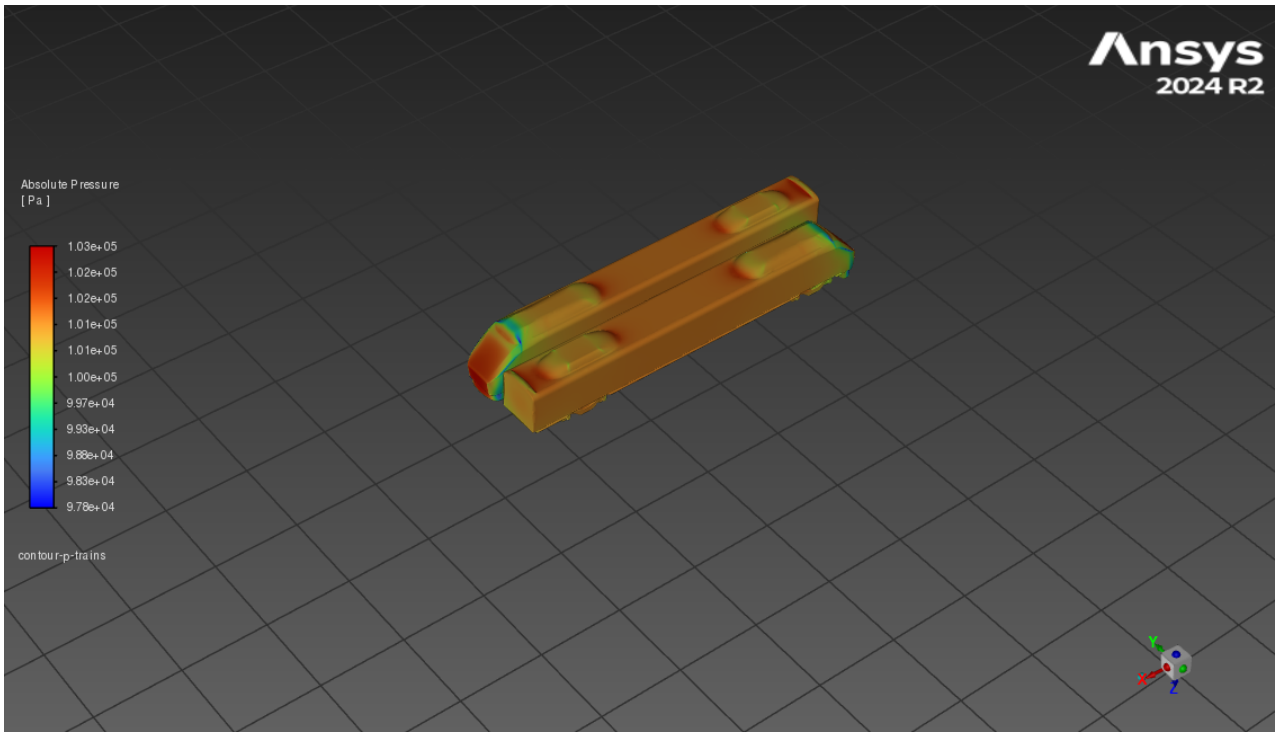


Figure F.25: Contour of absolute pressure around the vehicles at $t = 0.652$s.

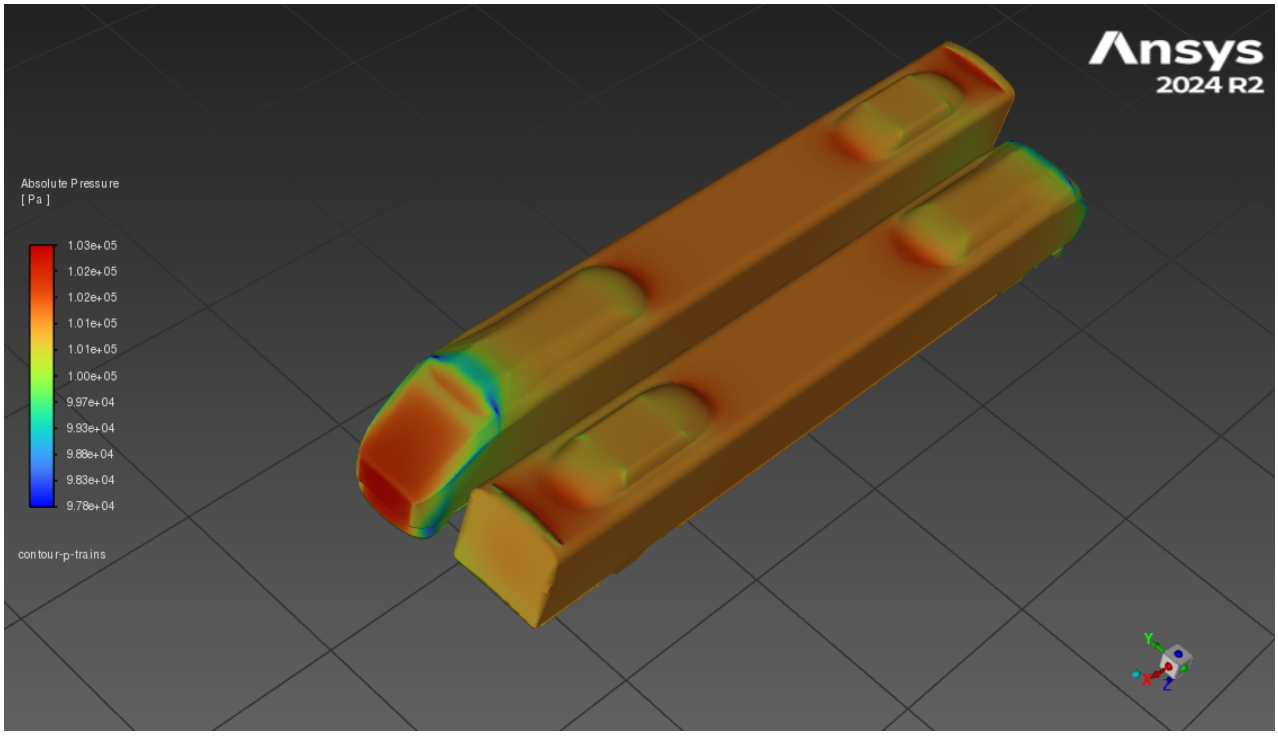


Figure F.26: Contour of absolute pressure around the vehicles at $t = 0.652$s (closer view).

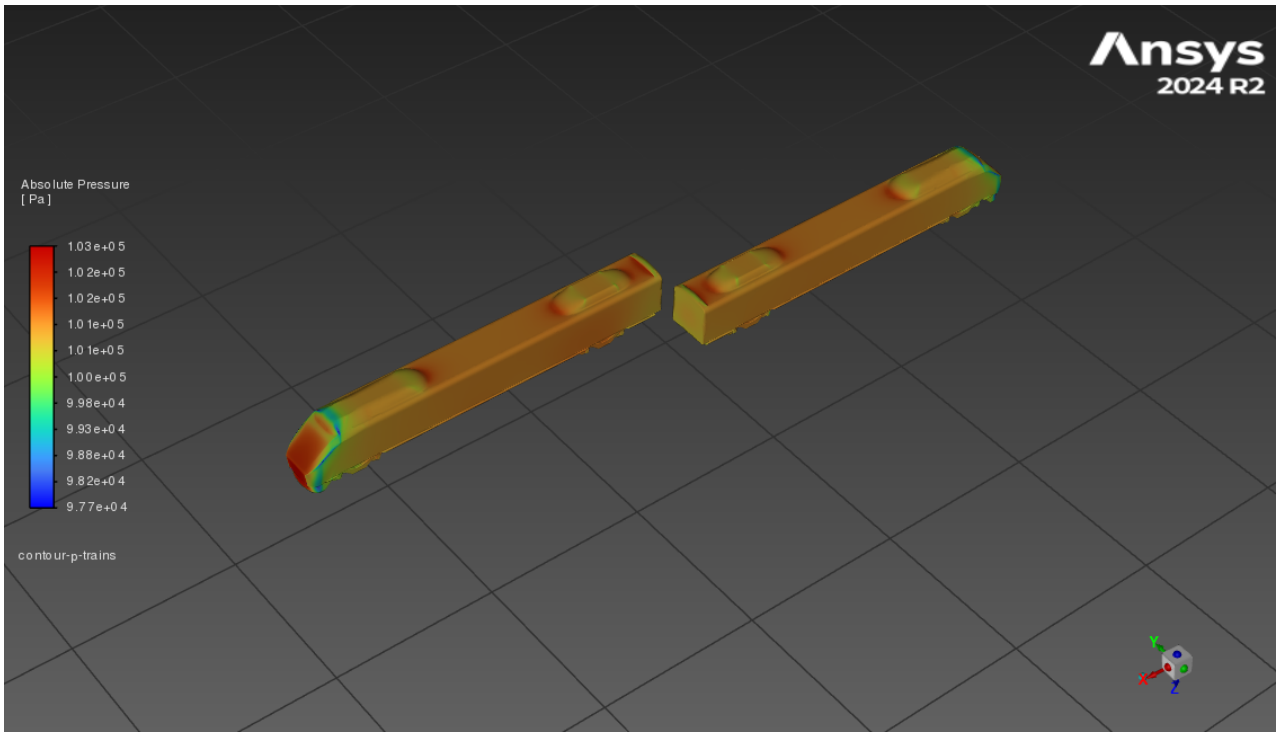


Figure F.27: Contour of absolute pressure around the vehicles at $t = 0.909$s.